Lawrence Berkeley National Laboratory
Recent Work

Title

CATALYTIC AND SURFACE SCIENCE STUDIES OF CLEAN AND MODIFIED RHODIUM, MOLYBDENUM AND PALLADIUM CRYSTAL SURFACES: HYDROGENATION OF CARBON MONOXIDE AND THE CYCLOTRIMERIZATION OF ACETYLENE TO FORM BENZENE

Permalink

https://escholarship.org/uc/item/3kp6d8nf

Author

Logan, M.A.

Publication Date

1985-08-01

eScholarship.org Powered by the California Digital Library
University of California

LBL-21414
c.2

Lawrence Berkeley Laboratory
UNIVERSITY OF CALIFORNIA

RECEIVED
LAWRENCE
BERKELEY LABORATORY

Materials & Molecular Research Division

OCT 1 3 1986

LIBRARY AND
DOCUMENTS SECTION

CATALYTIC AND SURFACE SCIENCE STUDIES OF CLEAN AND MODIFIED RHODIUM, MOLYBDENUM AND PALLADIUM CRYSTAL SURFACES: HYDROGENATION OF CARBON MONOXIDE AND THE CYCLOTRIMERIZATION OF ACETYLENE TO FORM BENZENE

M.A. Logan
(Ph.D. Thesis)

August 1985

TWO-WEEK LOAN COPY

This is a Library Circulating Copy which may be borrowed for two weeks.

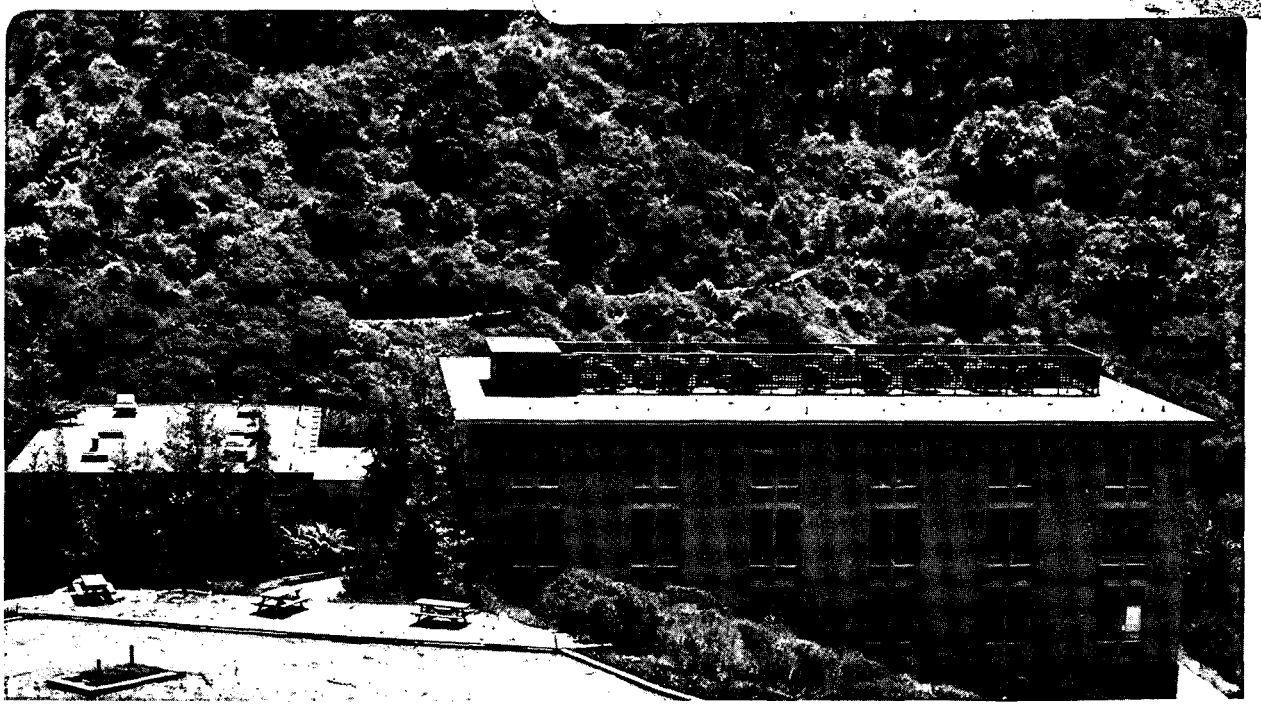

Prepared for the U.S. Department of Energy under Contract DE-AC03-76SF00098

LBL-21414
c.2

DISCLAIMER

This document was prepared as an account of work sponsored by the United States Government. While this document is believed to contain correct information, neither the United States Government nor any agency thereof, nor the Regents of the University of California, nor any of their employees, makes any warranty, express or implied, or assumes any legal responsibility for the accuracy, completeness, or usefulness of any information, apparatus, product, or process disclosed, or represents that its use would not infringe privately owned rights. Reference herein to any specific commercial product, process, or service by its trade name, trademark, manufacturer, or otherwise, does not necessarily constitute or imply its endorsement, recommendation, or favoring by the United States Government or any agency thereof, or the Regents of the University of California. The views and opinions of authors expressed herein do not necessarily state or reflect those of the United States Government or any agency thereof or the Regents of the University of California.

LBL-21414

CATALYTIC AND SURFACE SCIENCE STUDIES OF CLEAN AND MODIFIED RHODIUM, MOLYBDENUM AND PALLADIUM CRYSTAL SURFACES: HYDROGENATION OF CARBON MONOXIDE AND THE CYCLOTRIMERIZATION OF ACETYLENE TO FORM BENZENE

Mark Andrew Logan
Ph.D. Thesis

Materials and Molecular Research Division
Lawrence Berkeley Laboratory
University of California
Berkeley, California 94720

August 1985

This work was supported by the Director, Office of Energy Research, Office of Basic Energy Sciences, Material Science Division of the U.S. Department of Energy under contract number DE-AC03-76SF00098.

CATALYTIC AND SURFACE SCIENCE STUDIES OF CLEAN AND MODIFIED RHODIUM, MOLYBDENUM AND PALLADIUM CRYSTAL SURFACES: HYDROGENATION OF CARBON MONOXIDE AND THE CYCLOTRIMERIZATION OF ACETYLENE TO FORM BENZENE.

Contents

ABSTRACT vi

ACKNOWLEDGEMENTS ix

1. INTRODUCTION 1

1.1. Introduction 1

1.2. The Hydrogenation of Carbon Monoxide 3

1.3. The Cyclotrimerization of Acetylene 4

1.4. References 5

2. EXPERIMENTAL METHODS 6

2.1. Instrumentation 6

2.2. Surface Analysis Methods: Introduction 19

2.3. Auger Electron Spectroscopy (AES) 19

2.4. X-ray Photoelectron Spectroscopy (XPS or ESCA) 29

2.5. Temperature-programmed Desorption (TPD or TDS) 34

2.6. Work Function Measurements 37

2.7. Low Energy Electron Diffraction (LEED) 39

2.8. Materials 42

2.9. Catalyst Samples 44

2.10. Dosing Materials and Procedures 47

2.11. Low Pressure Studies 48

2.12. High Pressure Studies 52

2.13. References 54

INTRODUCTION TO CHAPTER THREE, FOUR AND FIVE: HYDROGENATION OF CARBON MONOXIDE 56

3. DEUTERIUM ISOTOPE EFFECTS ON HYDROGENATION OF CARBON MONOXIDE OVER RHODIUM 62

3.1. Introduction 62

3.2. Results and Discussion 63

3.3. References 72

4. HYDROGENATION OF CARBON MONOXIDE OVER OXIDES OF RHODIUM AND 3d TRANSITION METAL PEROVSKITES 73

4.1. Introduction 73

4.2. Results and Discussion 75

4.3. References 86

5. HYDROGENATION OF CARBON MONOXIDE ON Mo(100) SINGLE CRYSTALS AND POLYCRYSTALLINE FOILS 87

5.1. Introduction 87

5.2. Results 89

5.3. Discussion 100

5.4. References 109

6. MODEL CATALYTIC HYDRODENITROGENATION AND HYDRODEOXYGENATION REACTIONS OVER CLEAN AND SULFIDED MOLYBDENUM SINGLE CRYSTALS AND FOILS 111

6.1. Introduction 111

6.2. Clean Mo Surfaces 112

6.3. Sulfided Mo Surfaces 116

6.4. Discussion 118

6.5. References 119

7. THE CONVERSION OF ACETYLENE TO FORM BENZENE OVER PALLADIUM SINGLE CRYSTAL SURFACES 120

7.1. Introduction 120

7.2. Results: Introduction 122
7.3. Ultra-high Vacuum Studies: Pd(111) 123
7.4. Effect of Adatoms on Cyclotrimerization at Low Pressures: Pd(111) 127
7.5. Ultra-high Vacuum Studies: Pd(110) 131
7.6. Effect of Adatoms on Cyclotrimerization at Low Pressures: Pd(110) 133
7.7. Ultra-high Vacuum Studies: Pd(100) 136
7.8. Effect of Adatoms on Cyclotrimerization at Low Pressures: Pd(100) 138
7.9. Coverage Dependence of Additives 144
7.10. Conversion of Acetylene to Benzene at High Pressures . 146
7.11. Effect of Adatoms on Cyclotrimerization at High Pressures: Introduction 151
7.12. Effect of Adatoms on Cyclotrimerization at High Pressures: Pd(111) and Pd(100) 152
7.13. Effect of Adatoms on Cyclotrimerization at High Pressures: Pd(110) 155
7.14. Discussion of UHV and High Pressure Studies on Clean Pd Single Crystal Surfaces: Introduction 156
7.15. Discussion of UHV and High Pressure Studies on Clean Pd Single Crystal Surfaces 157
7.16. Discussion of UHV and High Pressure Studies on Promoted Pd Single Crystal Catalysts: Introduction 162
7.17. Discussion of UHV and High Pressure Studies on Promoted Pd Single Crystal Catalysts: Adatom Properties 163

7.18. Discussion of High Pressure Studies on Promoted Pd Single Crystal Catalysts: Introduction 169

7.19. Discussion of High Pressure Studies on Promoted Pd Single Crystal Catalysts: Pd(111) and Pd(100) 170

7.20. Discussion of High Pressure Studies on Promoted Pd Single Crystal Catalysts: Pd(110) 171

7.21. Discussion of UHV Studies on Promoted Pd Single Crystal Catalysts: Pd(100), Pd(111) and Pd(110) . . . 172

7.22. Comparison of Results of UHV and High Pressure Studies on Promoted Pd Single Crystal Surfaces 177

7.23. References 178

8. CONCLUSIONS 181

8.1. Overview 181

8.2. Hydrogenation of Carbon Monoxide 182

8.3. Cyclotrimerization of Acetylene 184

APPENDIX: CYLINDRICAL MIRROR ANALYZER SCHEMATICS AND PHOTOGRAPHS 185

A.1. Materials and Suppliers 185

A.2. Overview of Schematics 186

A.3. Abbreviations Used in Schematics 187

A.4. Figs. A.1 - A.12 188

A.5. Figs. A.13 - A.18 201

A.6. Figs. A.19 - A.22 208

A.7. Figs. A.23 - A.37 213

A.8. Photographs A.38 - A.52 229

CATALYTIC AND SURFACE SCIENCE STUDIES OF CLEAN AND MODIFIED RHODIUM, MOLYBDENUM AND PALLADIUM CRYSTAL SURFACES: HYDROGENATION OF CARBON MONOXIDE AND THE CYCLOTRIMERIZATION OF ACETYLENE TO FORM BENZENE

MARK ANDREW LOGAN

(Ph.D. Thesis)

Materials and Molecular Research Division
Lawrence Berkeley Laboratory
University of California
Berkeley, California 94720

ABSTRACT

The effect of modifying single crystal and polycrystalline foil catalysts, under both ultra high vacuum (UHV) and high pressure conditions, on catalytic reactions has been investigated. With the aid of UHV surface science techniques such as Auger electron spectroscopy (AES), X-ray photoelectron spectroscopy (XPS), temperature programmed desorption (TPD), and work function measurements the product distribution and activity of two catalytic reactions have been studied when the surfaces of crystalline catalysts modified with O, Si, P, S, Cl, and K were systematically varied. The high pressure reactions discussed are the hydrogenation of carbon monoxide over clean and modified rhodium and molybdenum crystalline catalysts and the cyclotrimerization of acetylene to form benzene over clean and modified palladium single crystal surfaces.

For the hydrogenation of CO over clean rhodium polycrystalline foil surfaces an inverse deuterium isotope effect was observed. The rate of CD_4 formation was found to be 1.5 times faster than the rate of CH_4 formation under the conditions used in this study ($CO:H_2$, 1:2, 6 atm total pressure, 520-720 K). The pressure dependence of the reaction is -1.0 ± 0.1 order in CO and $+1.0 \pm 0.1$ order in H_2, which implies competitive adsorption

of these two molecules on the surface. This data along with an activation energy of 25 kcal/mol for methane formation indicate that one of the final hydrogenation steps is rate-limiting.

Over Mo single crystals and polycrystalline foils the effects of adding K and S adatoms on the surface is discussed. The rates of formation of all products (methane, ethene, and propene) were found to be the same for both (100) single crystals and polycrystalline foils suggesting that the reaction is structure insensitive. The dependence of the rate of formation of methane on reactant pressure was found to be $r_{CH_4} = KP_{CO}^{+0.32} \cdot P_{H_2}^{+1.0}$. The unusual positive CO pressure dependence points to a mechanism of methanation that is different from that on other transition metal methanation catalysts (Fe, Ni, Ru) although the activation energy for the reaction is similar, 24 kcal/mol. Addition of K to the surface, at coverages of less than 0.3 ML, increased the overall rate of reaction and enhanced the olefin-to-paraffin ratio. The addition of S to the surface decreased the rate of hydrogenation but, for coverages up to 0.25 ML, increased the ratio of ethene to methane by a factor of as much as 5.

The cyclotrimerization of acetylene to form benzene has been studied over clean and modified Pd(111), (110), and (100) single crystal surfaces under both UHV and atmospheric pressure conditions. At low pressures Pd(111) was found to be the most active surface for the cyclotrimerization reaction, and the only surface studied in which benzene could be detected, by TPD, at less than 1 monolayer of acetylene coverage. The (110) surface produced 1/7 and the (100) surface produced 1/20 as much benzene as the (111) surface (for 6 L of acetylene dosed at 130 K). At atmospheric pressures Pd(111) and (100) gave similar rates of benzene formation (T.F.= 0.05 molecules/site • sec at 200 Torr acetylene and 575 K), while

the (110) surface had only 1/4 this rate of benzene formation. The percent open (not carbon covered) surface sites was found to correspond to these changes in the rate of formation of benzene. At high pressures, electropositive adatoms were found to enhance the rate of benzene formation, and electronegative additives reduced the rate. The rate of formation of benzene at atmospheric pressures was linked to the surface cleanliness. When using electropositive additives on the surface a lower amount of surface carbon was detected relative to using a clean single crystal surface. Low pressure stoichiometric results for additive-covered surfaces can be explained by a combination of surface structure and electronic interactions. The greatest enhancement in the amount of benzene produced was for Si on Pd(100), where evidence for the formation of a surface compound was found. Potassium was found to inhibit the reaction, possibly due to K blocking acetylene adsorption. Sulfur and chlorine decreased the decomposition of acetylene to hydrogen, and formed approximately the same amount of benzene as the clean surfaces.

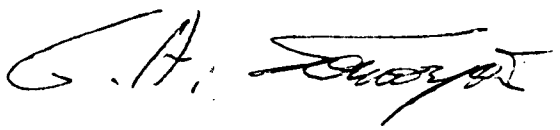

ACKNOWLEDGEMENTS

This research project could not have been accomplished without the assistance of many people, far too many to list completely here. Professor Gabor Somorjai provided support in many ways. He is truly a superior motivator and a constant source of encouragement, enthusiasm and inspiration. The research group under Prof. Somorjai's guidance was an invaluable source of ideas and insights into the many projects undertaken in this work, as well as a source of diversions - the Dawgs, foosball and, let us not forget, running. Thanks go especially to my lab partners and coworkers - Tom (the Buck) Rucker, Jose Carrazza, Andy Gellman, Francisco (Hose) Zaera, David Godbey, Kurt Seiber, Simon Bare, Mike Hilton, Brian Naasz (yes, I ran a tri), Brian Bent, Matthew Mate, Randy (the foos man) Yeates, Marc Levin, Mark (Whitey) Bussell, Dan (Tuna) Strongin, Greg (Relax) Blackman, Nic Spencer (who put up with teaching me to run a surface science apparatus) and all the other past and present members of the Somorjai family.

The building and repairing of this chamber and the associated electronics could not have been done without a lot of help from many technicians - Keith Frank, Dan Colomb, Glen Baum, Micheal Kujale, Weyland Wong, Jim Severns, Hank Brundel, Ron Hall (who patiently created x-ray source filaments), Emery Kozak and, of course, Will Lawrence and Bill Wilkie in the ceramics shop.

The other people at LBL and UC who must also be mentioned for their many hours of help include Ann Kahn, Tammy Learned, Cynthia, Winnie Heppler, John Holthius, Sandy Stewart, Cathy Sterling, Gloria Pelatowski and many of the TID people who brought new insights through clarity to this work.

Many thanks also go to my family at and away from home. Judith was especially good at timing care packages of cookies when they were needed most.

Mom and Dad certainly made all this possible and were always there to help out in anyway possible.

This thesis would be a whole lot less colorful, meaningful and certainly later in publication without the help, love and understanding of P. Donna Yoder.

You gotta love that!

This work was supported by the Director, Office of Energy Research, Office of Basic Energy Science, Material Science Division of the U.S. Department of Energy under contract number DEAC03-76SF00098.

CHAPTER ONE: INTRODUCTION

Section 1.1: Introduction

Additives have long been used to enhance the activity of catalysts. In 1912, researchers at B.A.S.F. added potassium oxide to an iron catalyst and found an enhancement in the rate of ammonia formation from hydrogen and nitrogen. Today, catalysts contain or are treated with many additives to enhance the rate of a certain reaction (as in the case of alkali metals) or reduce undesirable side reactions such as hydrogenation or dehydrogenation (as in the case of sulfur).

Although additives are used routinely in catalysis, there is still no definitive model of how they work. The additives used are said to effect the electronic or structural nature of the catalysts; however, determining the contribution of each for a given additive in a given catalytic reaction is very difficult. The work presented in this thesis was designed to improve the understanding of additives and oxidation state on catalytic reactions by using a combination of high pressure catalysis and surface science.

The investigations carried out in this laboratory are aimed at correlating real catalytic data, from industrial Fischer-Tropsch synthesis plants like SASOL or crude oil reforming plants, with the results obtained from well-characterized clean or additive-covered model catalysts. Under the conditions of ultra-high vacuum ($\leq 10^{-11}$ atm), the advanced spectroscopic tools of surface physics and classical chemical techniques can be used to analyze a catalyst surface before and after high pressure reaction studies. With the combination of high and low pressure capabilities, changes in reaction rates and product distributions are related to changes

in surface properties such as composition, oxidation state and/or crystal structure.

The reactions studied for the purpose of testing the effects of additives were the hydrogenation of carbon monoxide and the cyclotrimerization of acetylene to benzene.

Section 1.2: The Hydrogenation of Carbon Monoxide

The hydrogenation of carbon monoxide, or the Fischer-Tropsch synthesis (FTS), has been studied widely as a method of producing hydrocarbon fuels and many other industrially-important chemicals from gasified coal[1,2]. The only commercial application, at present is in South Africa, where the FTS is used to produce diesel fuel and waxes[3,4]. The catalysts used for this synthesis are aklali-promoted iron catalysts.

The research discussed in this thesis investigated the effect of oxygen, sulfur and potassium on molybdenum catalysts and the effect of changing oxidation state on rhodium catalysts. This work involved initial low pressure characterization of the surface (composition and oxidation state), followed by high pressure (6-20 atm) catalysis to obtain kinetic data, then followed by low pressure characterization of the surface. The surface composition and oxidation state are then related to changes in the overall reaction rate and changes in product distribution with the reaction time. These studies, provide evidence for a reaction mechanism and have aided in the understanding of how a catalyst works and what effect surface additives or contaminants have on the rates of formation of the many products of FTS.

Section 1.3: The Cyclotrimerization of Acetylene

The cyclotrimerization of acetylene to form benzene was first observed by Berthelot in 1866[5] at reaction conditions of ~ 775 K in a silica tube. Although the conversion of three acetylene molecules to benzene is highly exothermic, $\Delta H = -142$ kcal/mol[6] and symmetry-allowed[7], there are very few examples of purely thermal [2+2+2]-cycloadditions. It appears that entropic and, in some cases, enthalpic[8] activation barriers kinetically limit the reaction.

Many studies on homogeneous catalysis have shown that benzene and benzene derivatives can be formed under mild conditions[9,10]. Less work has been carried out on the heterogeneous catalytic formation of benzene. Some work has centered on the low pressure conversion of acetylene to benzene[11,12,13,14], but no studies have looked at the cyclic trimerization at high pressures over palladium single crystals and additive-covered Pd single crystals. Here we find the reaction to be extremely sensitive to the additive and the additive concentration on the metal surface.

Section 1.4: References

1. Poels, E.K., and Ponec, V., "Catalysis." Volume 6, eds. Bond, G.C., and Webb., G., The Royal Soc. of Chem. London 1983.

2. Bartish, C.M., and Drissel, G.M., "Kirk-Othmer Encyclopedia of Chemical Technology." Volume 4, p. 772, eds. Mark, H.F., et. al., John Wiley & Sons, New York 1978.

3. Dry, M.E., "Catalysis." Volume 1, eds. Anderson, J.R., and Boudant, M., Springer-Verlag, Berlin 1981.

4. Dry, M.E., Ind. Eng. Chem. Prod. Res. Dev. 15, 282 (1976).

5. Berthelot, M., C.R. Acad. Sci. 62, 905 (1866).

6. calculated using Benson's tables: Benson, S.W., "Thermochemical Kinetics.", Wiley, New York 1976.

7. Woodward, R.B., and Hoffman, R., "The Conservation of Orbital Symmetry." Academic Press, New York 1970.

8. Dower, W.V, and Vollhardt, K.P.C., J. Am. Chem. Soc. 104, 6878 (1982).

9. Vollhardt, K.P.C., Angewandte Chem. 23 (8), 539 (1984).

10. Maitlis, P.M., Acct. Chem. Res. 9, 93 (1976).

11. Gentle, T.M., Ph.D. Thesis, Univ. Calif. Berk, 1984.

12. Tysoe, W.T., Nyberg, G.L., and Lambert, R.M., J. Chem. Soc. Chem. Commun. 623 (1983).

13. Sesselmann, W., Woratschek, B., Ertl, G., and Kuppers, J., Surf. Sci. 130, 245 (1983).

14. Tysoe, W.T., Nyberg, G.L., and Lambert, R.M., Surf. Sci. 135. 128 (1983).

CHAPTER TWO: EXPERIMENTAL METHODS

Section 2.1: Instrumentation

The research described in this thesis was carried out in an ultra high vacuum/high pressure system[1] that was designed for combined surface analysis and high pressure (1-20 atm) catalysis studies, using small area (~ 1 cm^2) crystalline samples. A schematic diagram and photograph of this apparatus are shown in Fig. 2.1 and Fig. 2.2. Using this system, single crystal, polycrystalline-foil and powdered samples were cleaned in ultra high vacuum (UHV) and characterized by Auger electron spectroscopy (AES), X-ray photoelectron spectroscopy (XPS) and in the case of single crystal samples, low energy electron diffraction (LEED). The sample could then be enclosed in an internal isolation cell which could be pressurized (up to 20 atm) to function as a high-pressure batch reactor for catalytic studies. After high-pressure reactions, the cell could be evacuated and opened, such that the sample was exposed to UHV for further surface characterization.

The vacuum system consisted of a stainless steel belljar constructed at Lawrence Berkeley Laboratory (~ 40 ℓ internal volume) that was pumped by a high speed oil diffusion pump (Varian VHS-6) and a water-cooled titanium sublimation pump (Perkin-Elmer 224-0540). The oil diffusion pump was separated from the main chamber by a liquid nitrogen cold trap (Torr Vacuum Products LNB-62). Base pressures of ~ 2 X 10^{-10} Torr were achieved after 24-48 h bakeouts at 400-450 K. After high pressure experiments, a pressure burst to ~ 1 X 10^{-7} Torr was observed on opening the internal isolation cell to UHV. The pumping time to ~ 5 X 10^{-9} Torr was 10-100 min, depending on the gases being pumped (CO, H_2 being faster; and C ≡ C, benzene, furan, pyrridine being slower). During periods of continued use, the working pressure was ~ 1-2 X 10^{-9} Torr.

HIGH PRESSURE / LOW PRESSURE CHAMBER FOR CATALYST SURFACE STUDIES

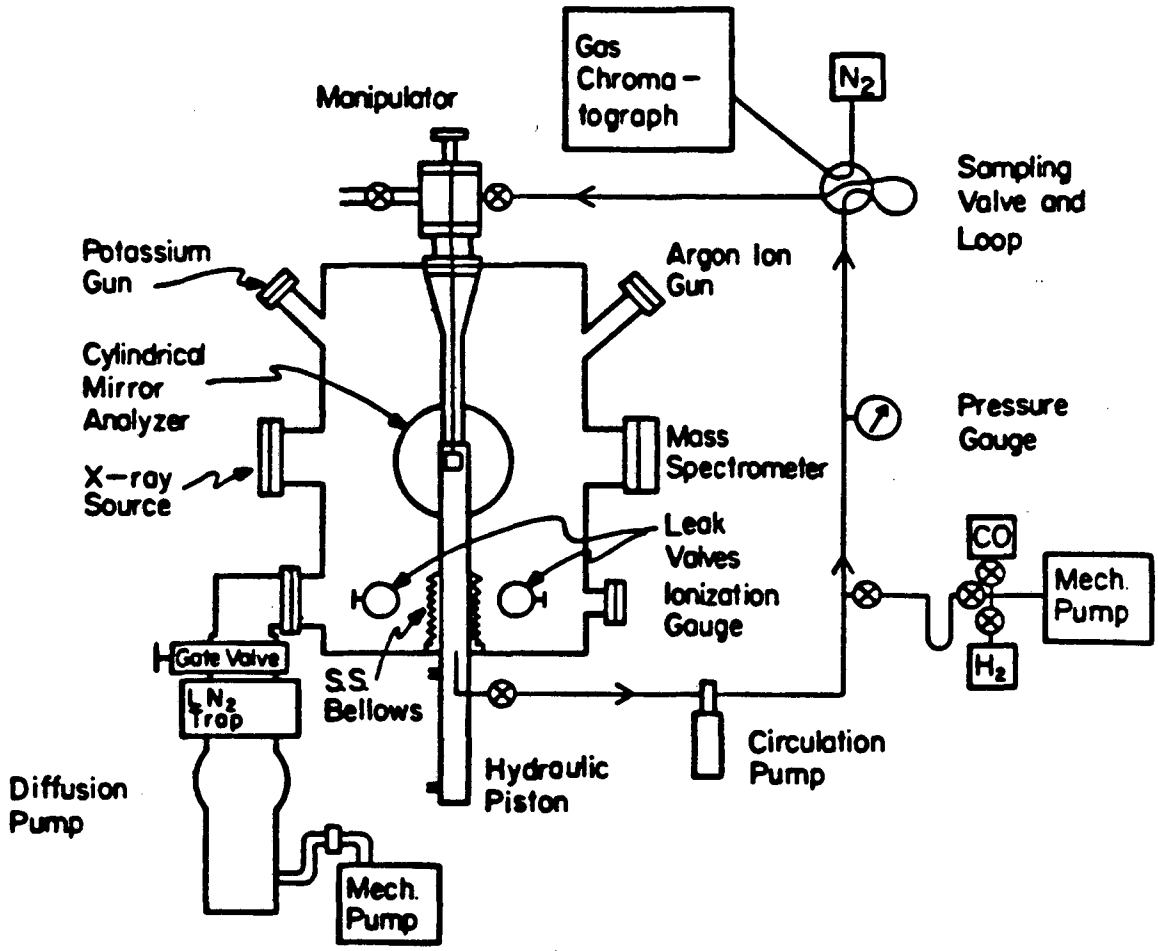

Fig. 2.1. A schematic representation of the ultra high vacuum/high pressure apparatus used for the studies described in this thesis.

Fig. 2.2 a) A front view of the UHV chamber with all the associated valves, gauges and cables.

Fig. 2.2 b) A back view of the UHV chamber with the pumps, x-ray water filter system and gas purification dewars.

Fig. 2.2 c) A view of the inside of the chamber through the CMA port. The K source, x-ray source, mass spectrometer, manipulator, high pressure cell (open) and LEED optics are shown.

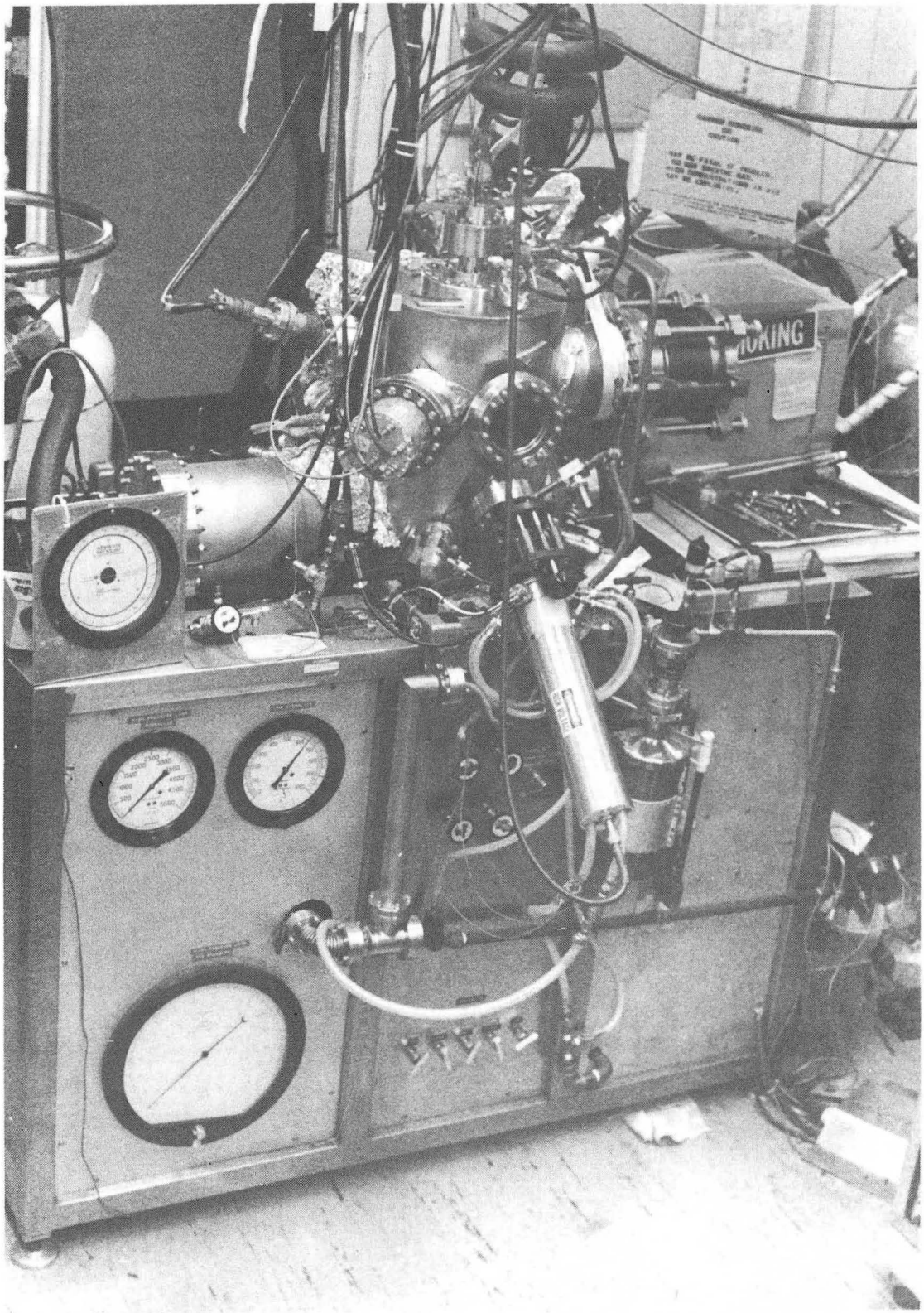

XBC 857-5541

Fig. 2.2a

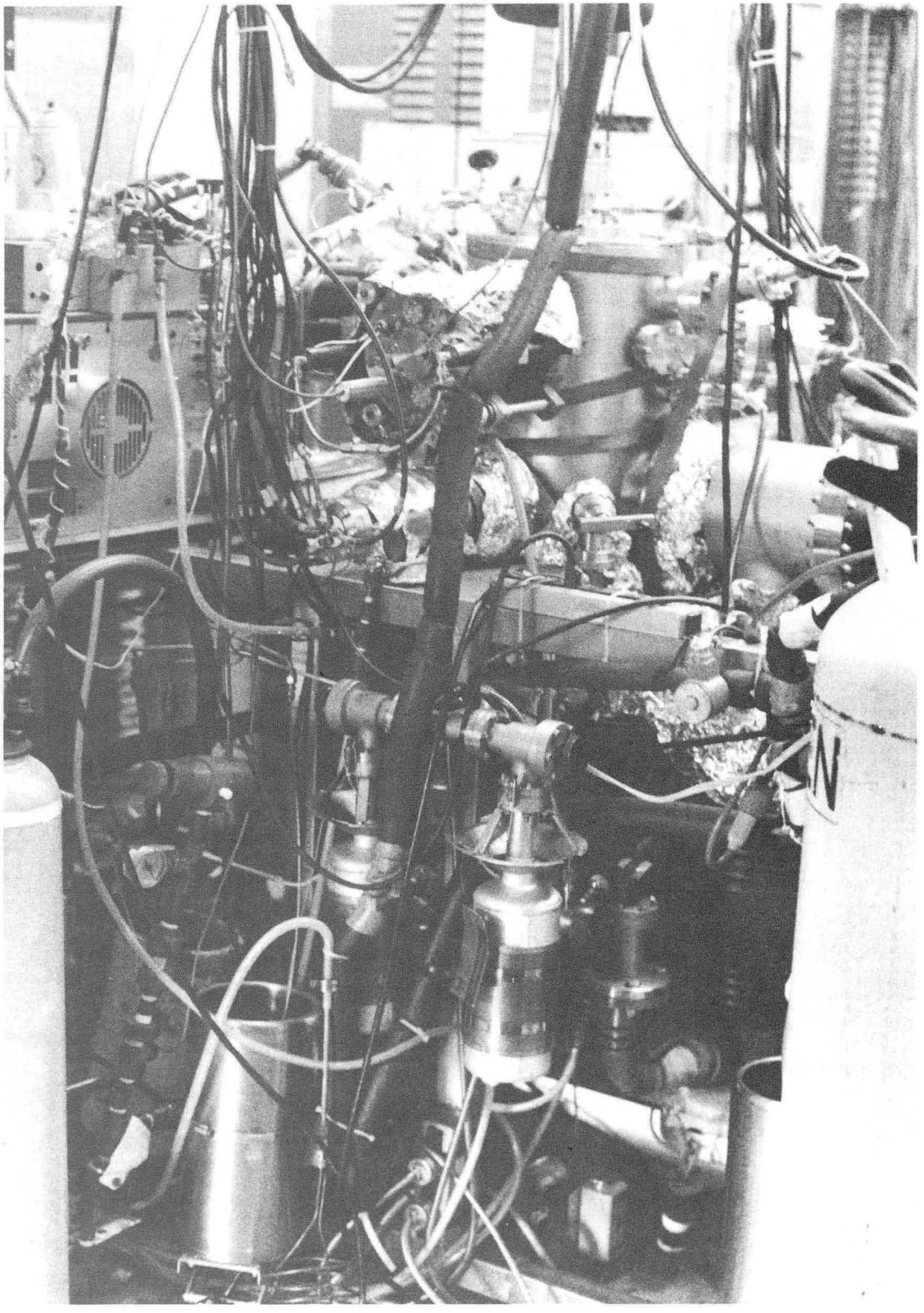

Fig. 2.2b XBC 857-5542

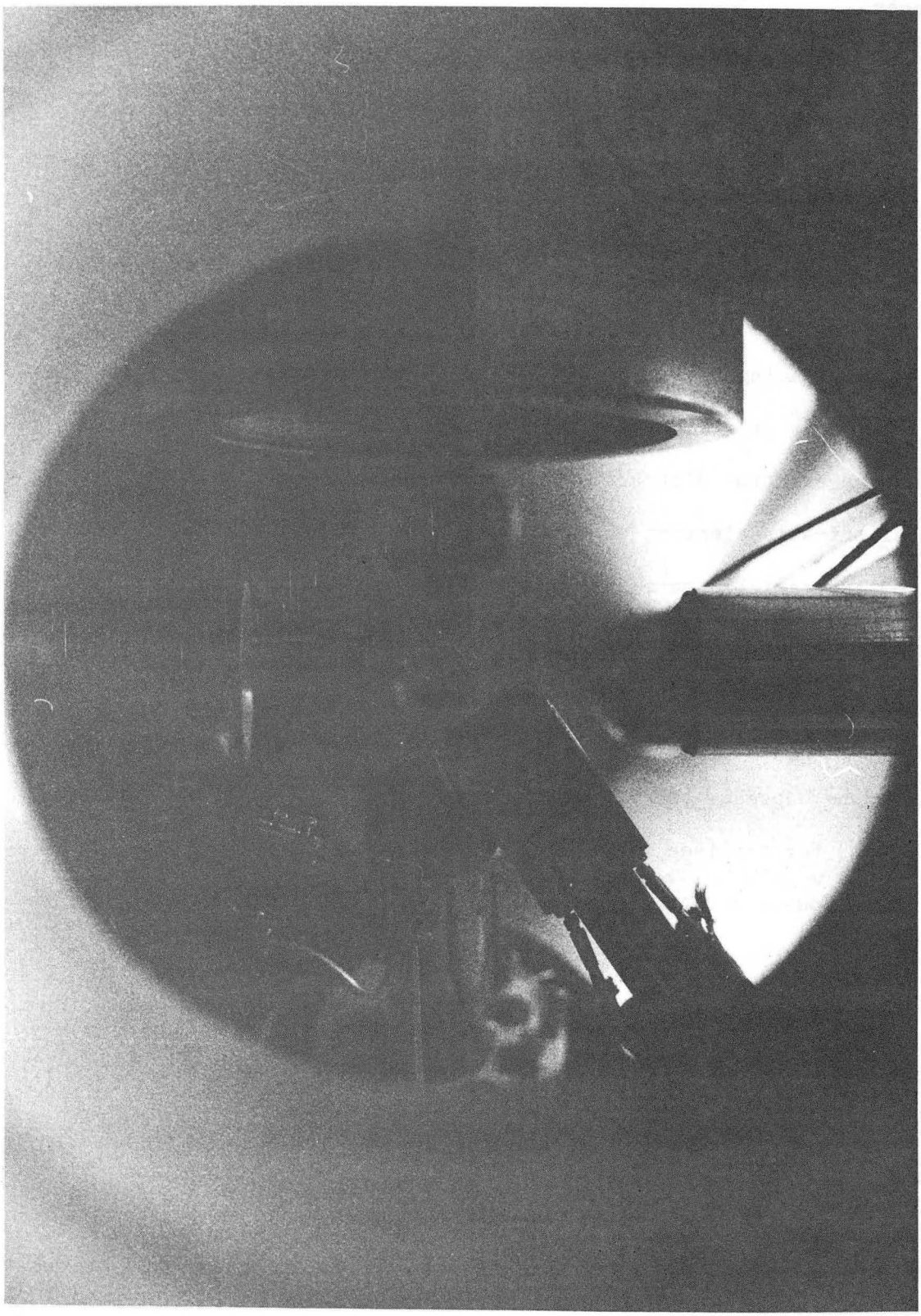

XBC 857-5517

Fig. 2.2c

The residual gases were composed of mainly H_2, H_2O, CO and CO_2. These pressures were adequate to routinely prepare well-characterized annealled surfaces.

The chamber was equipped with the following:

1) an ion sputtering gun (Varian 981-2043) for crystal cleaning;

2) a quadrupole mass spectrometer (EAI QUAD 240) for residual gas analysis and temperature programmed desorption studies;

3) a nude ion gauge (Varian 971-5008) and controller (Varian 845) for pressure measurement;

4) a glancing incidence CRT-electron gun for Auger excitation;

5) a four-grid electron optics energy analyzer (Varian 981-0127) for low energy electron diffraction and Auger electron spectroscopy, with a coaxial off-axis electron gun (Varian 981-2125) for the LEED experiments;

6) two variable rate leak valves (Varian 951-5106), one with 1/8 inch tubing pointing to the sample to act as a directional doser, for introducing gases at low pressures;

7) a differentially-pumped dual filament 15 kV x-ray source (originally designed by Ganschow and Steffens[2], improved by K. Franck and built by D. Colomb) for XPS (see Fig. 2.3);

8) a double pass cylindrical mirror analyzer (CMA) (built by K. Franck at Lawrence Berkeley Laboratory) for AES and XPS (see Appendix).

The single crystal, polycrystalline foil and powdered samples were mounted on a rotatable manipulator as shown in Fig. 2.4. This manipulator is an improved version of that discussed by Gillespie[3,4]. The mounting schemes allowed the sample to be cooled to 100 K and resistively heated to 2000 K (in the case of Mo) without significant heating of other parts of the chamber. For high pressure reactions the sample could be heated

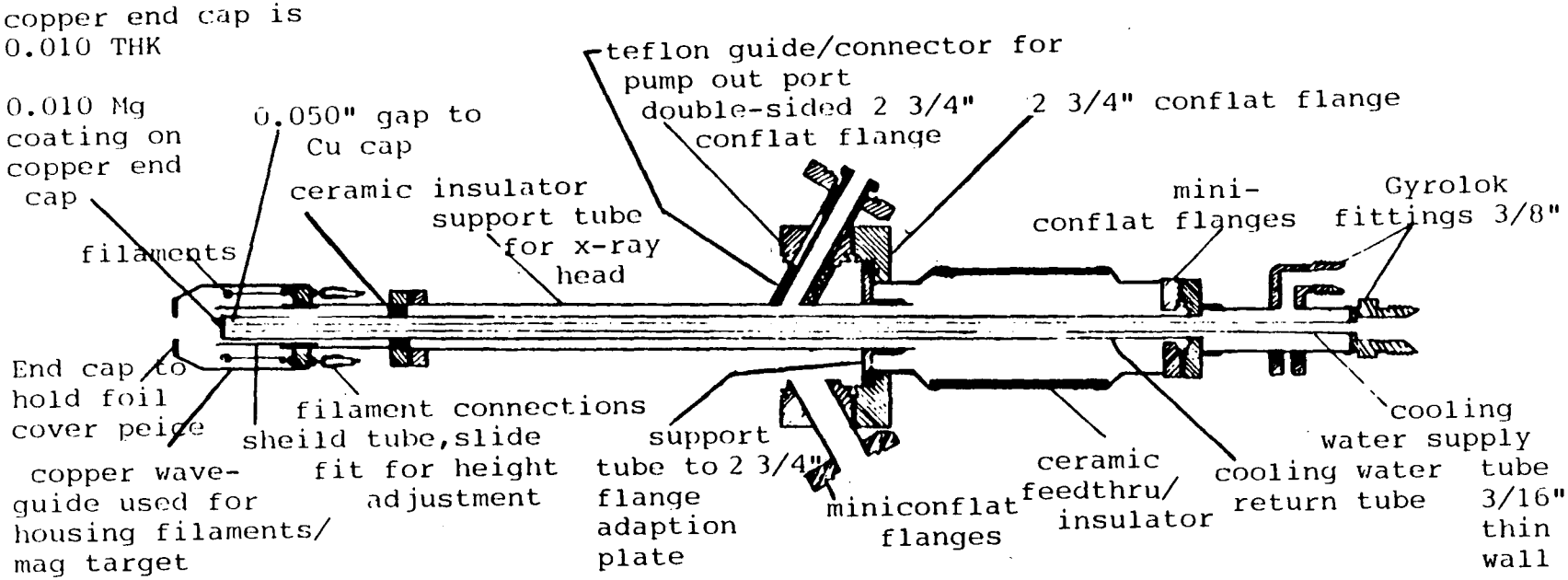

Fig. 2.3. A schematic of the x-ray source built by K. Frank.

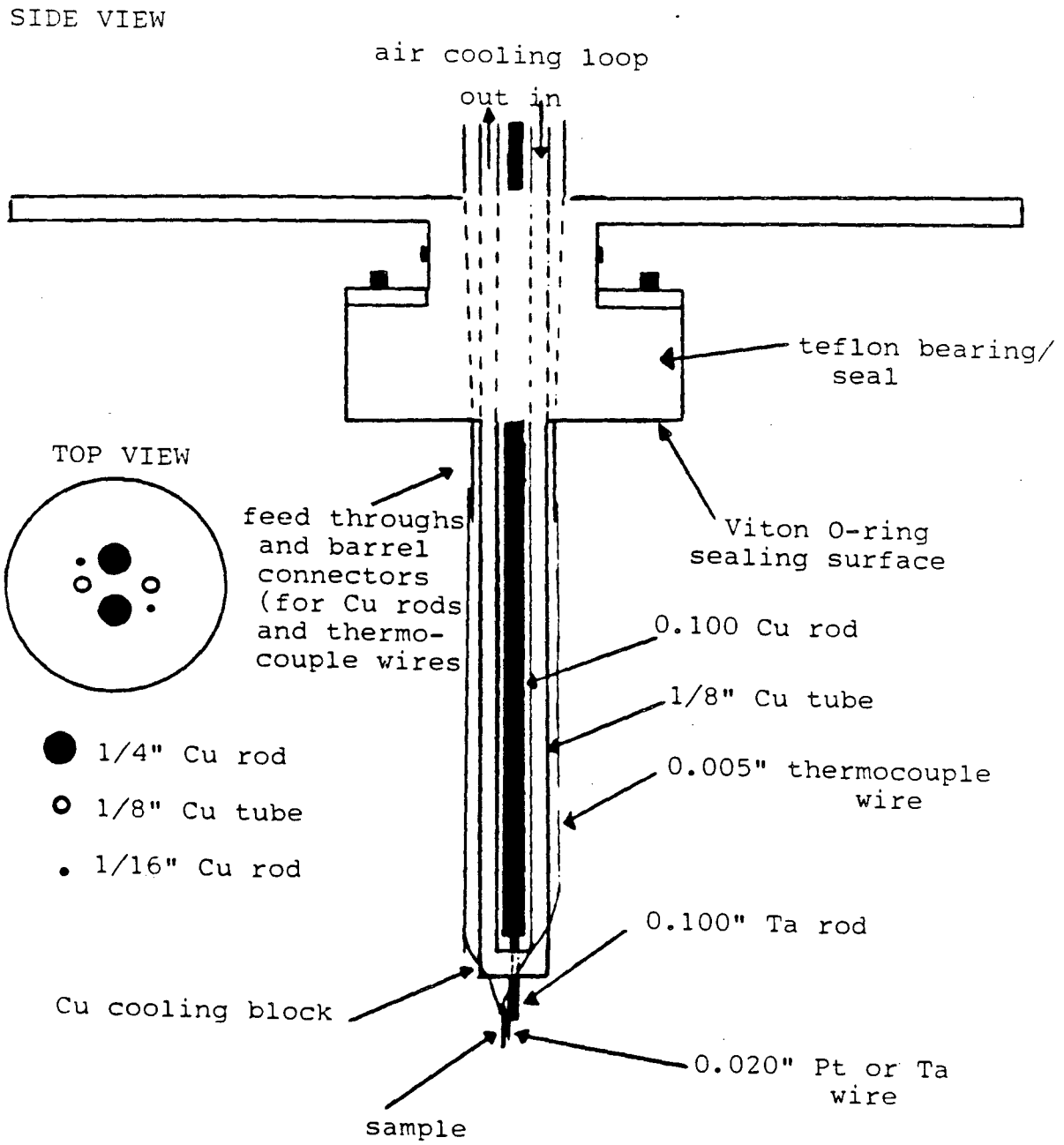

Fig. 2.4. A schematic of the high pressure precision manipulator used in these studies. The tested pressure limit was ~ 20 atm.

to 750 K without significant heating of the isolation cell or manipulator, thus avoiding any extraneous catalytic activity. The mountings were checked visually in vacuum for uniformity of heating at 750-1350 K. The samples were mounted and remounted until the heating was uniform and the contact points appeared to be no hotter than the sample itself. Powdered samples were pressed (5-50 kpsi) into gold mesh (60 X 60 X 0.004 inch), gold foil (0.003 inch) or between a foil and screen. The gold then was resistively heated to uniformly heat/cool the powdered sample.

A platinum/platinum 10% rhodium (used with Mo single crystals and foils) or chromel-alumel (used with rhodium and palladium catalysts) thermocouple, 0.005 inch wires, spot-welded tightly to an edge of the foil, screen or single crystal were used for temperature measurement. To check the accuracy of the temperature measurement, two tests were performed. First, a simple visual check of the minimum temperature of optical emission in UHV, as described in detail by Gillespie[3]. The threshold temperature for observing optical emission in a dark laboratory was found to be 785 ± 10 K. Second, for higher pressures, a check based on the equilibrium constant between isobutane and isobutene was developed. A comparison of the experimental and theoretical equilibrium was undertaken and this method was found very accurate for checking the sample temperature (570-630 K), as described in detail previously[5].

When the internal isolation cell was closed over the sample a batch reactor was formed. A diagram of the batch reactor is shown in Fig. 2.1. A teflon rotor micropump (Micropump model no. 120-000-100) was used to circulate continuously the reactant gases. Two gauges (Wallace-Tiernan 61C-1D-0410 and Heisse H33814) were used for measuring the pressure of the reactant gases. After a high pressure experiment, the diffusion

pump was isolated, and the reaction loop was pumped down to ~ 50 mTorr, using a mechanical pump (MP2). At this time the liquid-nitrogen-trapped (Varian M2) 2" oil diffusion pump (Varian VHS-2) was opened to pump out the reaction loop to ~ 10^{-5} Torr. The bypass valve, was opened during pumpout to increase the conductance of the recirculation loop, which was otherwise limited by the gas chromatographic sampling valve (1/16 inch). The total volume of the loop was 270 cm^3.

Product gas samples from the high pressure reaction loop were taken periodically be the use of a six port sampling valve (see Fig. 2.5) equipped with a 0.5 ml sampling loop. The sampling valve was controlled by a microprocessor in the gas chromatograph (HP 5793). The peak areas and retention times were calculated by an HP 3390 integrator. A typical chromatogram for CO/H_2 over $TiRhO_3$ is shown in Fig. 2.6. The sensitivity of the gas chromatograph was calibrated regularily using a primary standard gas mixture (Matheson) that contained 100 ppm (mole basis) of methane in nitrogen. All hydrocarbon products were calibrated relative to methane using published snsitivity factors[6]. Reaction products were separated using 1/8 inch packed columns which contained either Poropak™ N, Poropak™Q, Poropak™ QS, Chromosorb™ 102, Chromosorb™ 103 or Carboseive™ SII.

X-ray photoelectron and Auger electron spectroscopies were performed by moving the CMA in to ~ 1 cm from the sample by means of hydraulic bellows. The CMA and x-ray source could be moved close to the sample for analysis and then retracted when the internal isolation cell was to be closed for high pressure experiments.

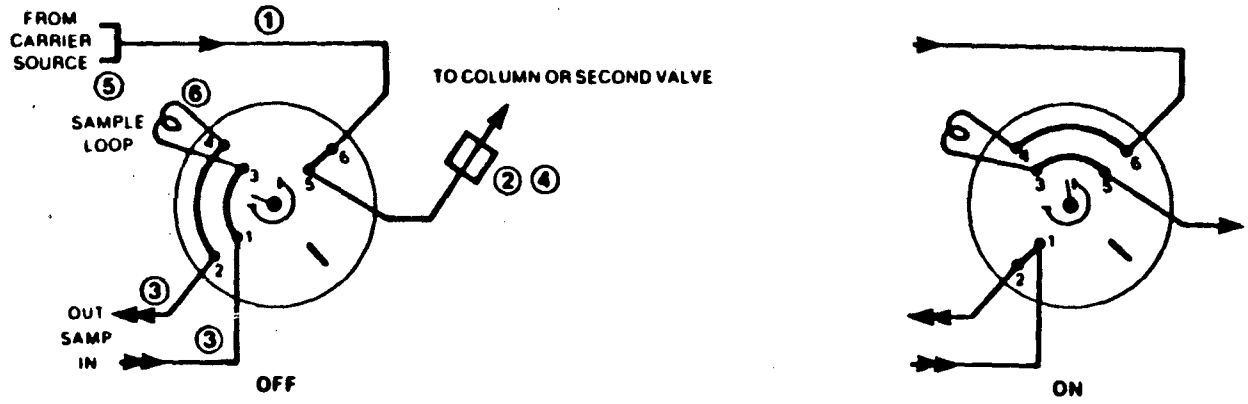

Fig. 2.5. The six port sampling valve is shown in the two configurations used in these studies.

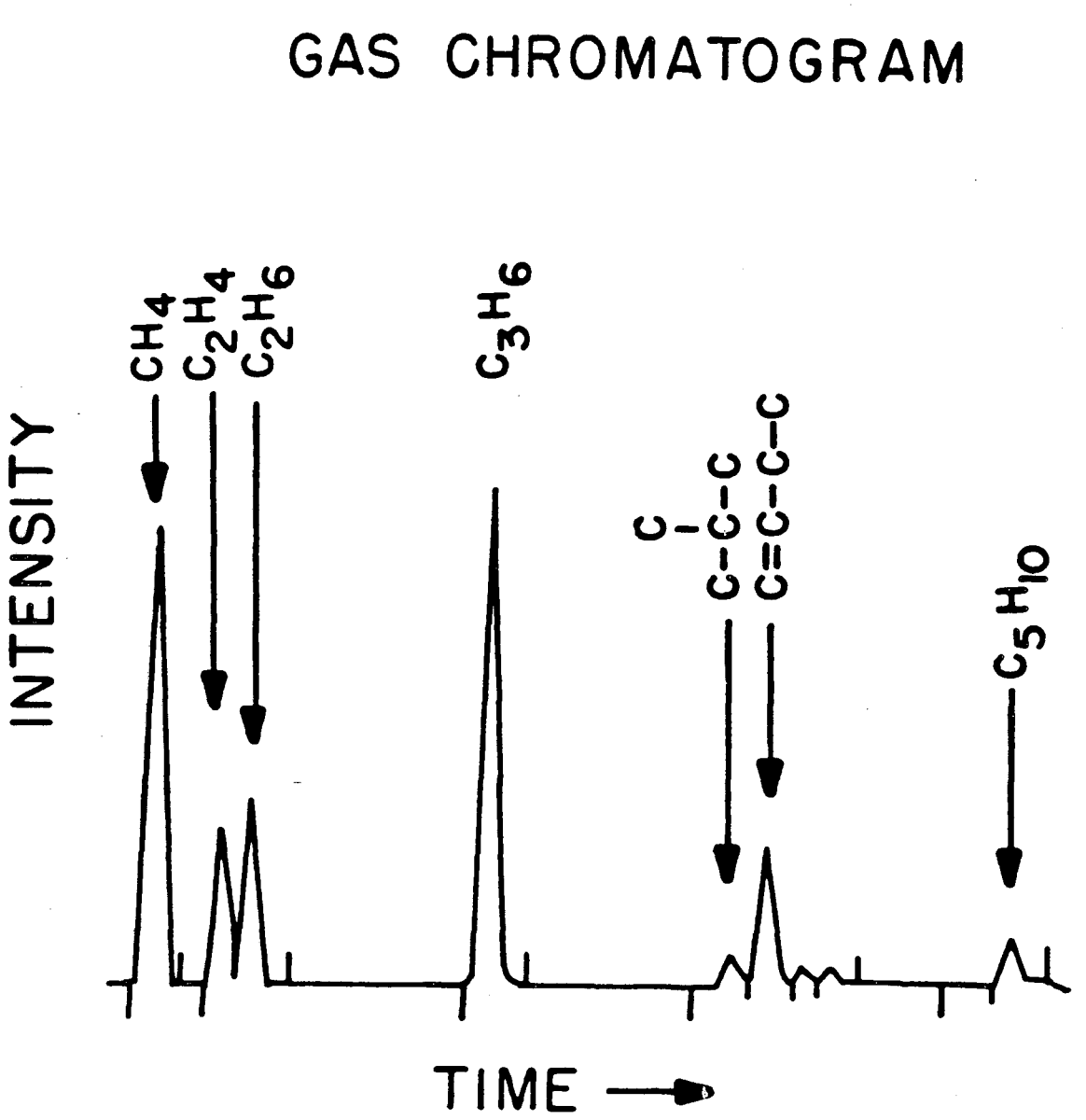

Fig. 2.6. A typical gas chromatogram from a CO/H_2 reaction over $TiRhO_3$ (CO/H_2 1:2, 6 atm, 300°C).

Section 2.2: Surface Analysis Methods, Introduction

Several surface-sensitive techniques have been used throughout the work presented in this thesis. They have been used to characterize the solid-gas interface of the catalytic samples studied. Low energy, < 2000 eV, electrons are extremely useful for this (see Fig. 2.7), sampling only the topmost layers of the surface. Most of the work described here is based on this surface sensitivity: AES, LEED and XPS. In addition to electron-based spectroscopies temperature programmed desorption (TPD or TDS) was also used in this work. Since the theory and application of these techniques have been discussed thoroughly in the surface science literature (viz. AES[7,8], XPS[7,9], LEED[7,10], TPD[11]) only a short description of each will be given here.

Section 2.3: Auger Electron Spectroscopy (AES)

AES was used extensively in the research reported in this thesis to monitor the elemental composition of the catalyst surface before and after low pressure chemisorption and high pressure reaction studies. The technique can be used to gather not only compositional information, but also electronic information about the chemical state of the atoms on the surface. This electronic information was used to determine the nature of carbon on the surface after reaction studies (see Fig. 2.8). The lineshape of the Auger spectra for graphitic and carbidic carbon are found to be quite different[12].

AES has several advantages for routine surface analysis: 1) every element, except H and He, has a unique spectrum which can be used as a fingerprint to identify small amounts of impurities on the surface; 2) excellent spectra can be taken very rapidly (1-5 min); and 3) AES is very surface-sensitive, since the electrons impinged on the surface and

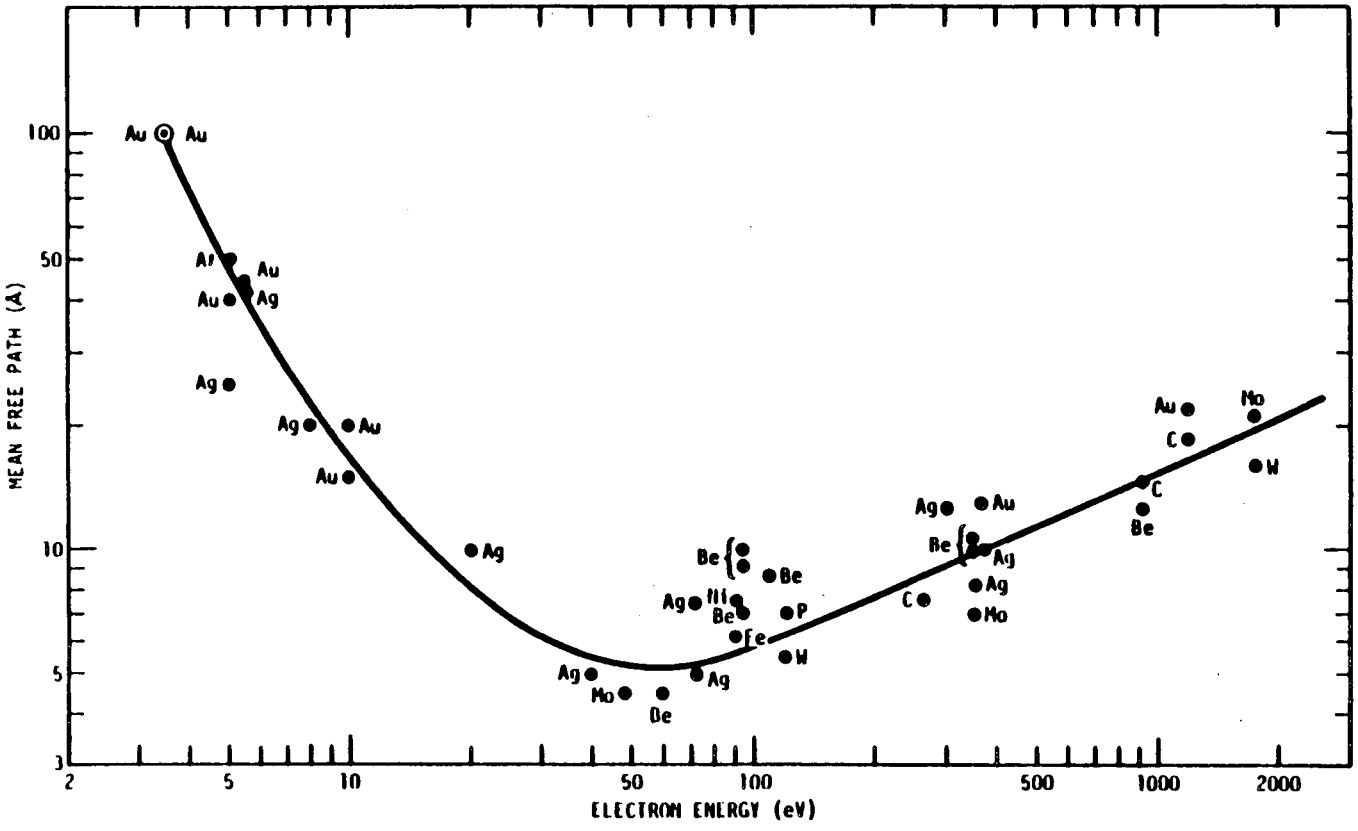

Fig. 2.7. "Universal curve" for the electron mean free path as a function of electron kinetic energy.

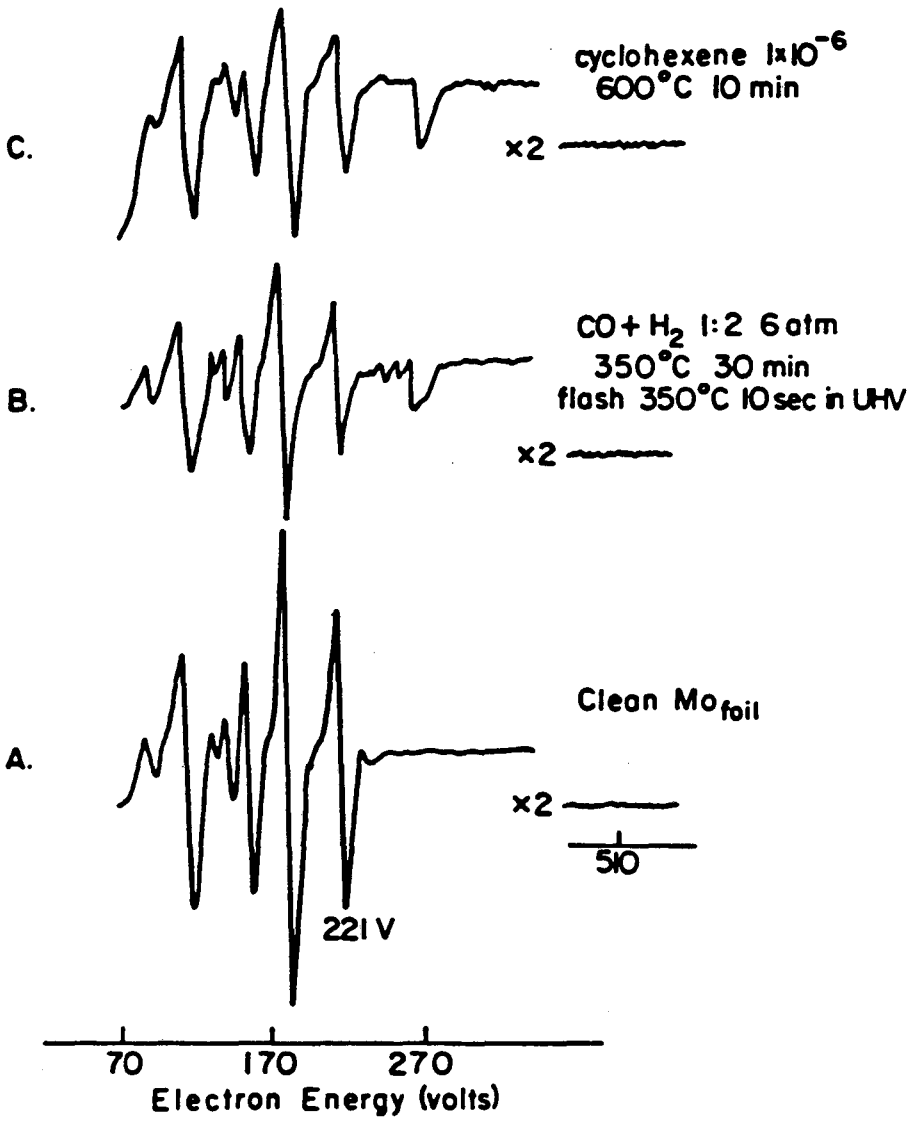

Fig. 2.8. The AES of clean (bottom), carbided, and graphite (top) covered Mo foil. The difference in the peak shape of the 270 volt carbon peak is apparant.

the Auger electrons have ~ 100-1000 eV (see Fig. 2.7).

The spectra obtained in this work used two electron analyzers: a four-grid retarding field analyzer (RFA) (see Fig. 2.9) and a double pass cylindrical mirror analyzer (CMA) (see Fig. 2.10). The second harmonic of the modulation voltage V_m was detected as a function of the the ramp voltage using a phase-sensitive lockin amplifier (EG&G Brookdeal 9503). The second harmonic corresponds to the first derivative of the Auger spectrum[13].

The Auger process, as depicted in Fig. 2.11, is inititated by impinging a high energy electron beam (1-3 kV) on the sample surface. This energy ionizes a core level electron. The resulting core level electron hole is filled by a higher-lying electron "falling" into this core hole. The energy from this transition goes into autoionization of the Auger electron, shown as KL_IL_{III} in Fig. 2.11. The energy of the Auger electron will have a characteristic energy for each transition which is given by

$$E_{ijk}(z) = E_i(z) - E_j(z) - E_k(z - \Delta) - \phi_e$$

where $E_j(z)$ and $E_k(z)$ are the energies of the outer shell electron involved in the transition, z is the atomic number of the atom, Δ is the effective charge (~ 0.5-0.8) due to the initial ionization and ϕ_e is the work function of the sample referred to the vacuum level of the spectrometer.

The other relaxation mechanism which can occur is x-ray fluorescence, in which a photon is emitted when the outer shell electron relaxes to the inner shell hole. Auger emission is dominant for low z elements or when initial ionization occurs in the L, M, N ... subshells[13] (see Fig. 2.12). Fig. 2.8 shows an AES of clean, graphite-covered and carbidic carbon-covered

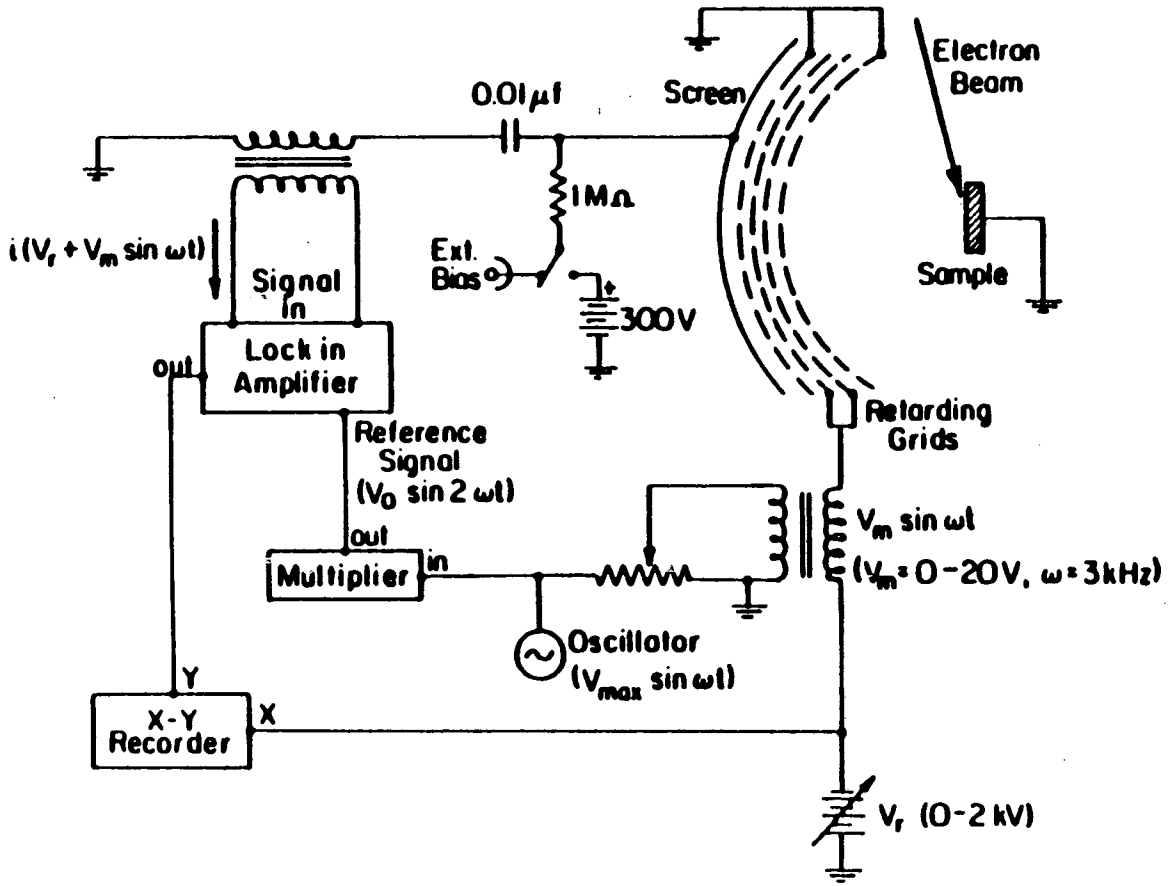

Fig. 2.9. Schematic of a retarding feild analyzer for AES and LEED.

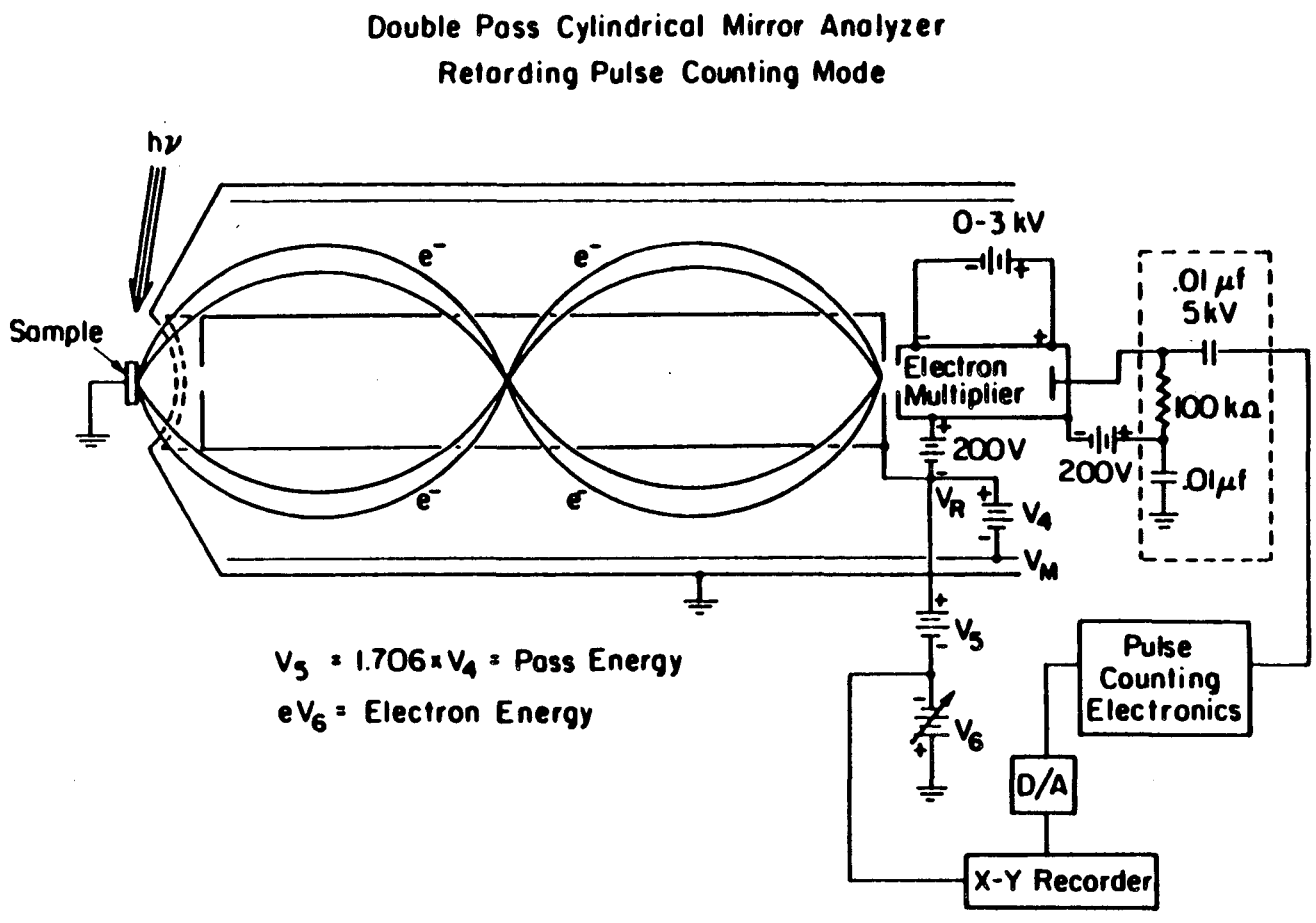

Fig. 2.10. Schematic of a double pass cylindrical mirror analyzer for AES and XPS.

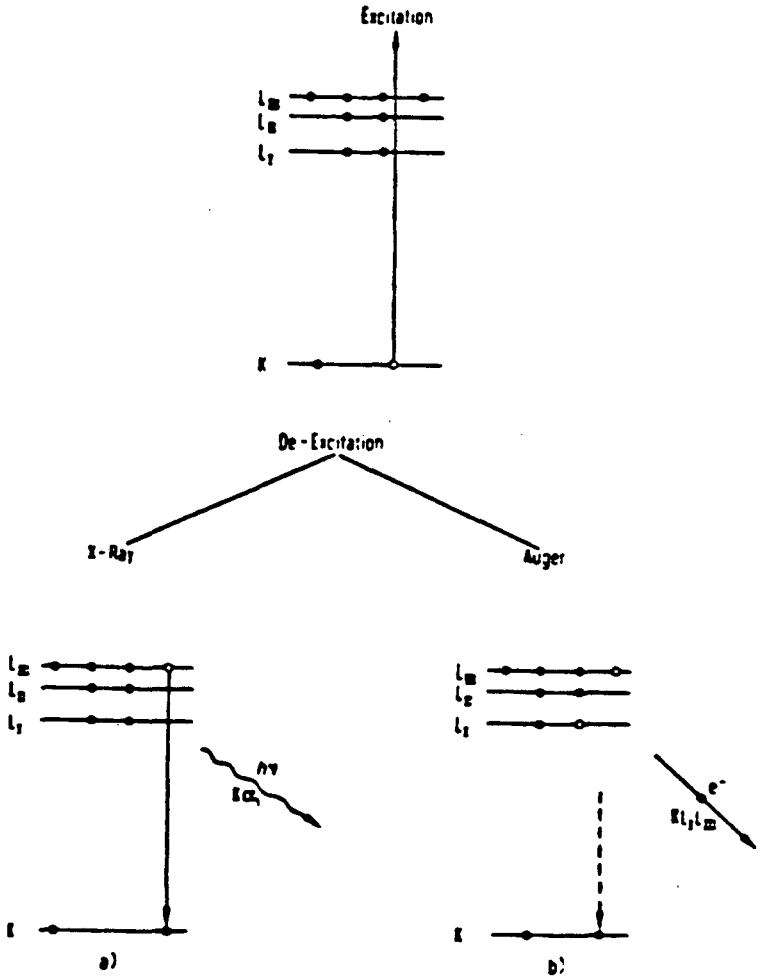

Fig. 2.11. The deexcitation pathways for an ionized atom are shown. The two pathways are x-ray fluorescence or emission of an Auger electron.

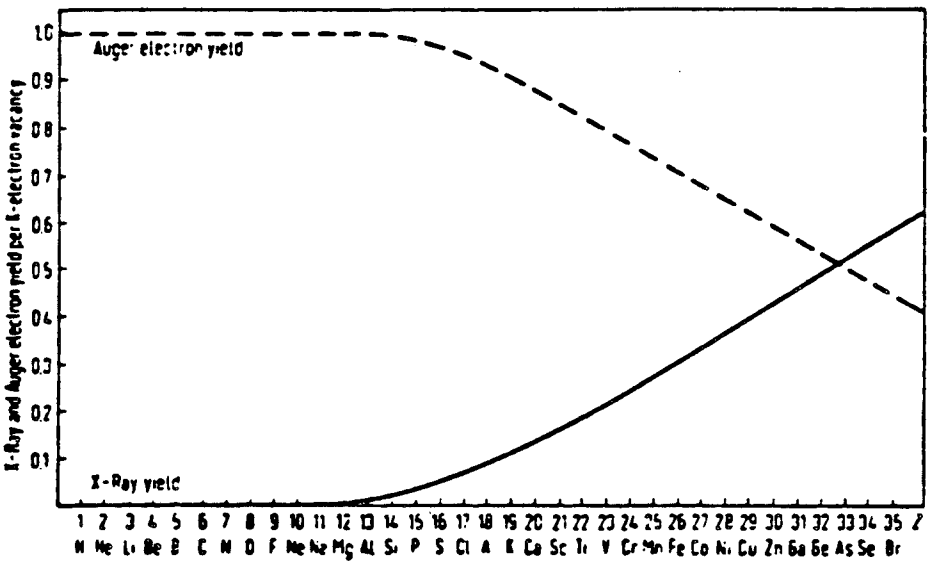

Fig. 2.12. Auger electron emission and x-ray fluorescence yields after ionization of a K-shell electron as a function of atomic number.

detect changes in chemical environment are displayed.

The surface sensitivity of AES is determined by the energies of the incident electron beam and the Auger electron. The most surface-sensitive electrons have energies between ~ 30-500 eV (see Fig. 2.7), where the mean free path of the electrons is only 2-3 atomic layers (and is independent of the incident beam energy). With increasing Auger electron energy the surface sensitivity is reduced; therefore, for the studies presented here the AES peaks used were between 60-510 eV to achieve the maximum surface sensitivity.

Adsorbate coverages can also be determined by AES. Several models have been developed in the literature: layer by layer growth[14],3-D crystallite formation[15], or monolayer growth followed by 3-D crystallite formation[15]. For the addition of additives to surfaces, less than one monolayer of additive was used generally. In this case the coverage approximation used is given by[16]

$$\Theta_x = \frac{h_A S_A}{h_A S_A + h_S S_S}$$

where h_A and h_S are the peak heights of the adsorbate and substrate and S_A and S_S are the Auger sensitivity factors for the adsorbate and substrate. Auger sensitivity factors[17] are shown in Fig. 2.13. This approximation is good for low coverages of additives and was used very often in determining the additive coverages in the acetylene cyclotrimerization work (see Chapter 7).

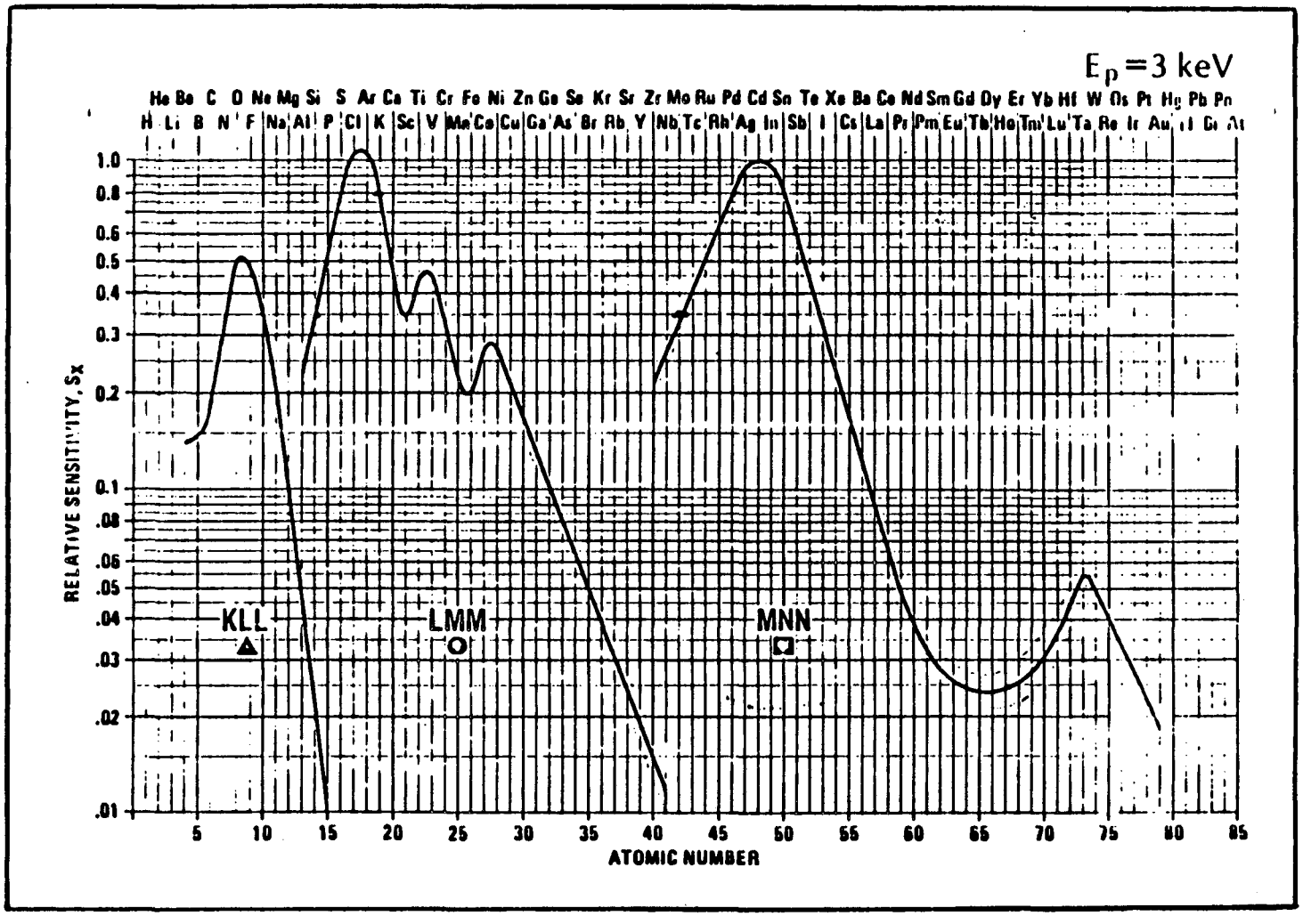

Fig. 2.13. The Auger electron sensitivity factors, for the three major types of Auger electrons, are plotted versus the atomic number at an electron beam energy of 3 keV.

Section 2.4: X-ray Photoelectron Spectroscopy (XPS or ESCA)

XPS was used mainly to obtain chemical state information on the catalyst sample before and after high pressure reactions or chemisorption studies from shifts in the binding energies of the ejected core photoelectrons (see Fig. 2.11). A typical XP spectrum of RhO_3 mounted on Au foil is shown in Fig. 2.14. Photoemission, as well as Auger electron emission, are observed when high energy electromagnetic radiation is impinged on a surface. The energy of the emitted electron, E_{kin}, can be obtained from the Einstein relationship

$$h\nu = E_{kin}(z) + E_i(z) + \phi_{sp}$$

where $h\nu$ is the energy of the monochromatic x-rays (for Mg anodes 1253.6 eV and for Al anodes 1486.6 eV), $E_i(z)$ is the binding energy of the emitted electron and ϕ_{sp} is the work function of the sample referred to the vacuum level of the spectrometer. An XP spectrum is taken by measuring the flux of electrons at a given energy, $J(E_{kin})$, versus the kinetic energy of the photoelectrons, E_{kin}. Fig. 2.10 shows a schematic representation of the experimental set-up and pulse-counting electronics for XPS.

The main advantage of XPS over AES is the resolution, due to the narrow energy spread of the photons emitted (0.7 eV for the Mg 1253.6 eV line and 0.85 eV (FWHM) for the Al 1486.6 eV line). AES uses a modulation voltage to pick the spectrum, and thus causes the inherently broader peaks; however, in XPS, electrons are retarded by a variable potential grid at the front of the detector (see Fig. 2.10), allowing only electrons of greater potential than the grid to enter the CMA. Electrons, once in the CMA, are filtered and focussed by applying a potential difference between the inner and outer cylinders, V_R and V_M. In this configuration,

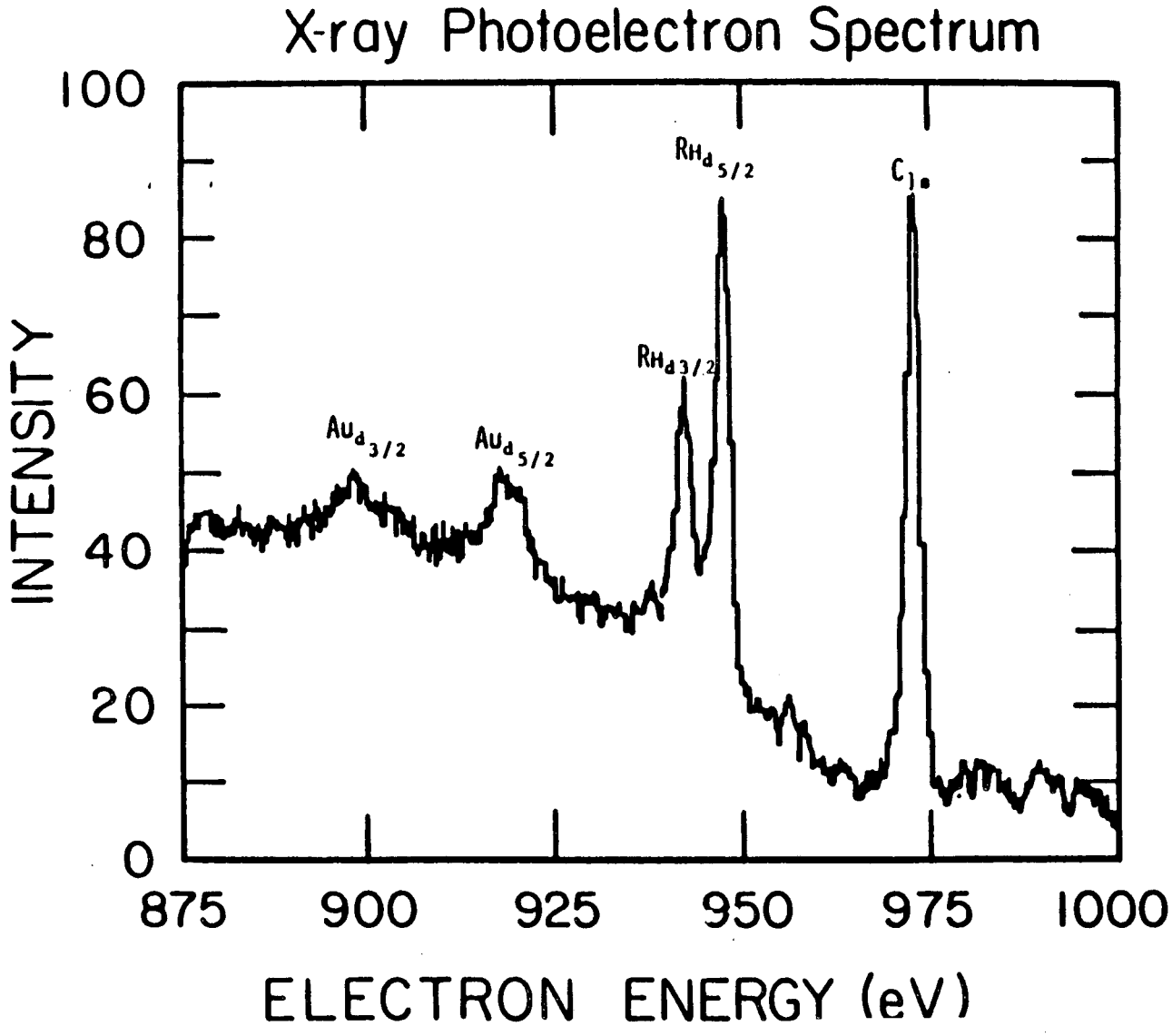

Fig. 2.14. A typical high resolution XP spectrum of carbon covered rhodium oxide mounted on Au foil.

the instrumental resolution, Δ_{sp}, remains constant across the spectrum and is given by

$$\Delta E_{sp}/eV_{pass} = K$$

where eV_{pass} is the pass (or kinetic) energy of the electrons in the CMA, and K is a constant. The term eV_{pass} can be written in terms of the spectrometer parameters

$$V_{pass} = V_4/[1.3 \ln(R_{out}/R_{in})]$$

where V_4 is the potential difference of the cylinders, and R_{out} and R_{in} are the radii of the outer and inner cylinders. Substituting the second equation into the first, rearranging, and using our actual spectrometer paramaters, we get the following equation for the instrumental resolution

$$\Delta_{sp} = 0.007\ eV_{pass}.$$

Therefore, for eV_{pass}=100 V, we calculate Δ_{sp}=0.7 eV; and for eV_{pass}=25 V, we get Δ_{sp}=0.18 eV.

The increased resolution results in a slower count rate. The area of the target from which photoelectrons are detected by the analyzer is reduced proportionally to the square root of the ratio of the pass energy to the kinetic energy of the emitted photoelectron, thus reducing the count rate (counting rate $\propto eV_{pass}/E_{kin}$). For example, when the pass energy is changed from 100 V to 25 V, the counting rate for a 1000 eV photoelectron is reduced by a factor of ~ 8. To achieve ~ 0.2 eV resolution using the set-up in our lab took 1-2 h.

Other features are also present in the XP spectrum. In some cases, these are due to the excitation sources. For instance, Mg sources have two additional x-ray lines, at 1262.0 eV (8% of the 1253.6 eV peak intensity) and at 1263.8 eV (4.1 % of 1253.6 eV peak intensity)[18], which lead to corresponding x-ray photoemission. Auger lines appear from the

relaxation of ionized electrons in the four main Auger series (KLL, LMM, MNN and NOO). The Auger lines have kinetic energies that are independent of the excitation energy and therefore appear to shift on a binding energy plot with different x-ray anodes, so these peaks can easily be detected.

Another type of feature which may arise in the XP spectrum is due to an ion being left in an excited state, several electronvolts above the ground state. In this event, the kinetic energy of the photoelectron would be reduced by the difference in energy between the excited state and ground state of the ion. These lines are termed shake-up lines and are most intense for paramagnetic compounds, which may approach that of the main line in intensity.

A third feature which can arise in the spectrum is due to emission of a core electron from an atom having a spin. The coupling of this new unpaired electron, left after photoemission from an s orbital, with other unpaired electrons in the atom can create an ion with either of two energies, which results in an asymmetrically split photoelectron line. Similar types of splittings can be observed for p and d level electrons.

As mentioned earlier, the main information obtained from XPS is the identification of the chemical or oxidation state of elements on the surface from the "chemical shift" of the photoemission lines. The simplist model of chemical shifts is based on the concept that ionization energy changes as a result of electron density being withdrawn or donated to the atom. Thus, more oxidized atoms will have higher binding energies for the photoelectron emitted. Unfortunately, other effects make this simplistic interpretation not valid entirely. As the oxidation state increases, the relaxation due to interaction of the ionizing electron with all the other

electrons in the same and neighboring atoms tends to decrease the binding energy.

Experimentally, x-rays are created by electron bombardment of a Mg or Al target (12-15 kV and 30-50 mA). The emitted radiation is filtered with a 1 μm Al window, to eliminate electrons escaping and to avoid contamination due to Mg or Al desorption from the anode. The sample to be be analyzed is placed as close to the x-ray source as experimentally practical (~ 0.1-0.5 cm) to get the maximum flux of photons to the surface.

The data was aquired and processed using a PET microprocessor, with software described elsewhere[19]. The energy scale was calibrated using a value of 83.8 eV for the Au $4f_{7/2}$ electrons[18]. Using this value, the spectrometer work function was found to be 5.1 V.

Section 2.5: Temperature-programmed Desorption (TPD or TDS)

TPD of adsorbed species from solid surfaces yields information on the interactive forces and reaction mechanisms between adsorbed molecules and surfaces, and between adsorbed molecules themselves. Another important use for TPD, in this work, was to determine relative coverages on clean and adsorbate-covered or partially poisoned surfaces.

The experiment consists of characterizing the sample to be studied in ultrahigh vacuum and leaking into the UHV chamber a known amount of well-characterized gas on the surface, while the sample is kept at a fixed temperature. The sample then is heated at a constant rate, usually 10-50 K/sec, and the partial pressure of each desorbed gas is plotted versus sample temperature. To identify each gas, a mass spectrometer (located in line of sight with the sample, ~ 2 cm away) is used. The resulting partial pressure versus temperature plot was analyzed using the method of Redhead[20]. Three TPD spectra showing possible surface reactions are shown in Fig. 2.15: the first is molecular desorption, the second is decomposition of a surface adsorbate, and the third is a surface reaction to make a new product.

The desorption rate, F(t), from a sample of area A, is related to the change in partial pressure of the desorbing gas, ΔP, by the expression

$$F(t) = (k \cdot s)\, \Delta P$$

where k is a constant and s is the pumping speed on the system (assumed to be much greater than the gas desorption rate). The desorption rate also can be described in the form of an Arrhenius expression

$$F(t) = \nu_N \cdot f(\Theta) \cdot \exp[-E_{des}/RT]$$

where ν is the preexponential factor, N is the desorption order, $f(\theta)$ is

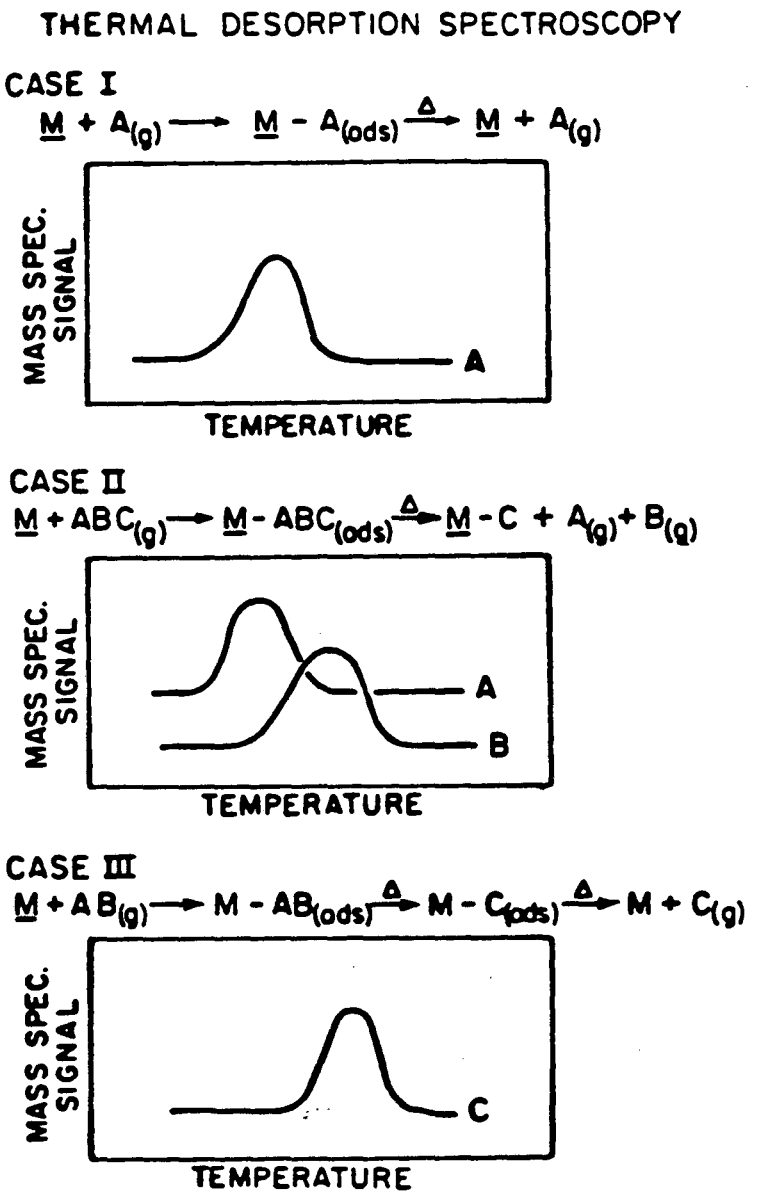

Fig. 2.15. Three possible thermal reactions are shown. Case I shows the molecular desorption of an adsorbate molecule A. Case II shows the decomposition reaction for ABC to form and desorb A and B, leaving a tyghtly bound metal-C residue on the surface. Case III shows a surface reaction where AB reacts with itself to form C, as is the case for the cyclotrimerization of C ≡ C.

an adsorbate coverage dependent function and E_{des} is the activation energy for desorption. When the temperature varies linearly with time ($T = T_o + \beta \cdot t$) and it is assumed that ν_N and E_{des} are coverage-independent, then Redhead has shown that for first order desorptions

$$E_{des}/(RT_p^2) = (\nu_1/ \beta) \exp[-E_{des}/RT_p]$$

and for second order desorptions

$$E_{des}/(RT_p^2) = (\nu_2/ \beta) \Theta_o \exp[-E_{des}/RT_p]$$

where T_p is the temperature of maximum desorption, β is the heating rate, and Θ_o is the initial coverage. Using this model, T_p is independent of coverage for first order desorption processes but T_p decreases with increasing coverage for second order desorption processes. Therefore, the molecular desorption and surface recombination followed by desorption can be differentiated by varying the initial coverage and monitoring T_p.

To find values for E_{des} and ν_N, the heating rate (β) and initial coverage (Θ) should be varied independently; however, this is very difficult experimently. In practice, a value of 10^{13} is assumed for ν_1 and ν_2, based on vibrational frequencies, and E_{des} is calculated from[20]

$$E_{des}/RT_p = \ln (\nu_1 \cdot T_p/ \beta) - 3.64$$

for first order desorption processes.

In our experiments, most TPD runs consist of cooling the sample to ~ 130-170 K, dosing 0.1-100 Langmuirs of the gas(es) of interest, then heating the sample by passing a constant current through it at a linear rate of 10-100 K/sec. The desorbed gases were recorded by the monitoring the change in partial pressure versus time or sample temperature, using an X-Y chart recorder, PET microcomputer[19] or a UTI mass programmer.

Section 2.6: Work Function Measurements ($\Delta\phi$)

Adsorption of additives or gases to surfaces is usually associated with changes in the surface electronegativity or work function ranging from ~ 0.1 eV to more than 1.0 eV. The sign of the work function change is related to the direction of electron transfer between the substrate and the adsorbate. The theoretical treatment of the work function and changes in work function are, at present[7], still far from providing quantitative information about charge distributions. Therefore, in this work, the use of $\Delta\phi$ has been limited to investigating the relative effect of additives and adsorbing gases.

The work function of a solid is defined by the energy which is necessary to take an electron in the Fermi level of the solid to the vacuum level. Many methods have been devised[7] to measure $\Delta\phi$ such as thermionic electron emission, photoemission, field emission, the vibrating capacitor method (Kelvin probe), the diode method and the onset of emission from an electron gun.

The method used herein was to measure the onset of the electron emission from a biased crystal (using 6-24 V). This method does not yield any absolute work function information but does give information on the relative amount of charge transfer to or from the surface. Figure 2.16 shows some of the data obtained using this method. The values obtained by this method were found to be within ± 50% of $\Delta\phi$ values obtained by other workers using the Kelvin method[7] (where values were available), and the direction of electron transfer was consistent.

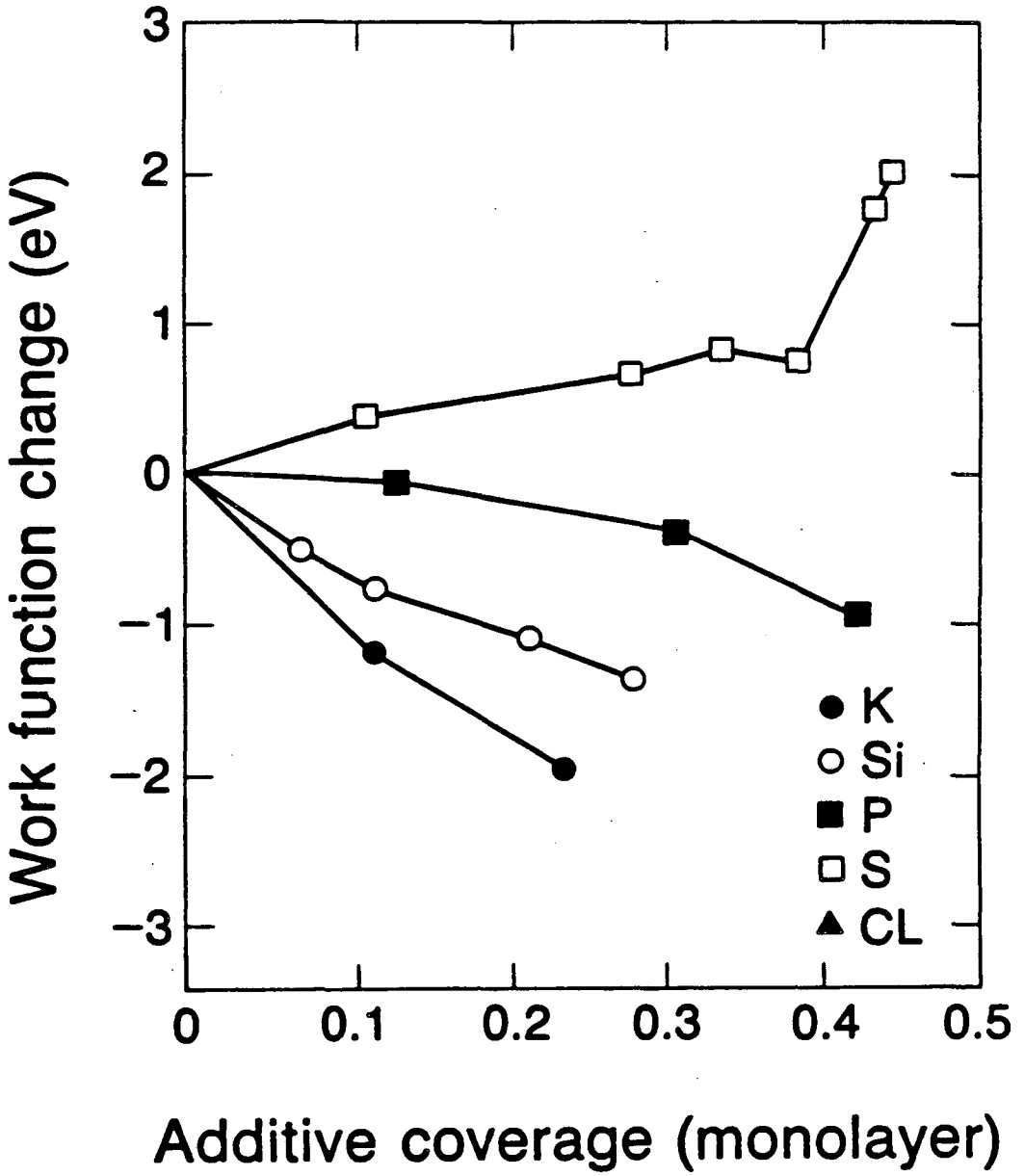

Fig. 2.16. The change in work function, $\Delta\phi$, vs. the amount of each additive on the Pd(100) surface. Potassium, Si and P are observed to donate electron density to the metal surface.

Section 2.7: Low Energy Electron Diffraction (LEED)

LEED is used to obtain information about the geometry of the top-most layers of solids. In this work, LEED was used mainly to identify the crystal structure of the substrate or substrate with adsorbate, to a lesser extent, and to check that the crystal was annealled after ion sputtering.

The technique is based on the wave properties of electrons. According to the de Broglie relation, electrons have a wavelength, λ , and

$$\lambda\ (\ \text{Å}\ ) = h/(m \cdot v) = \sqrt{150/V}$$

where h is Planck's constant, m is the rest mass of an electron with a velocity v and kinetic energy eV. If an electron beam of known energy is impinged on a crystal surface, some fraction of the electrons will be elastically scattered from the top-most 1-4 layers of the surface. Electrons with energies of 15-400 V, with de Broglie wavelengths of ~ 4-0.5 Å , are used for LEED, making them suited ideally for diffraction from the near surface (see Fig. 2.7). Braggs scattering equations govern where constructive scattering will occur[7]. For normal electron beam incidence, constructive scattering will occur at the angles, ϕ , where

$$\sin\ \phi = (N \cdot \lambda\ )/d_{h,k} \sim (N/d_{h,k})\ \sqrt{150/V}$$

where N is an integer (denoting the order of diffraction) and $d_{h,k}$ is the distance between parallel rows of scattering centers in the [h,k] direction. Information about the size and shape of the unit cell of adsorbates then may be determined and compared with the clean substrate, if the adsorbate orders on the surface.

A schematic representation of the experimental set-up is shown in Fig. 2.17 and shows a monoenergetic beam of electrons being impinged on the surface at normal incidence. The elastically scattered electrons then are filtered using

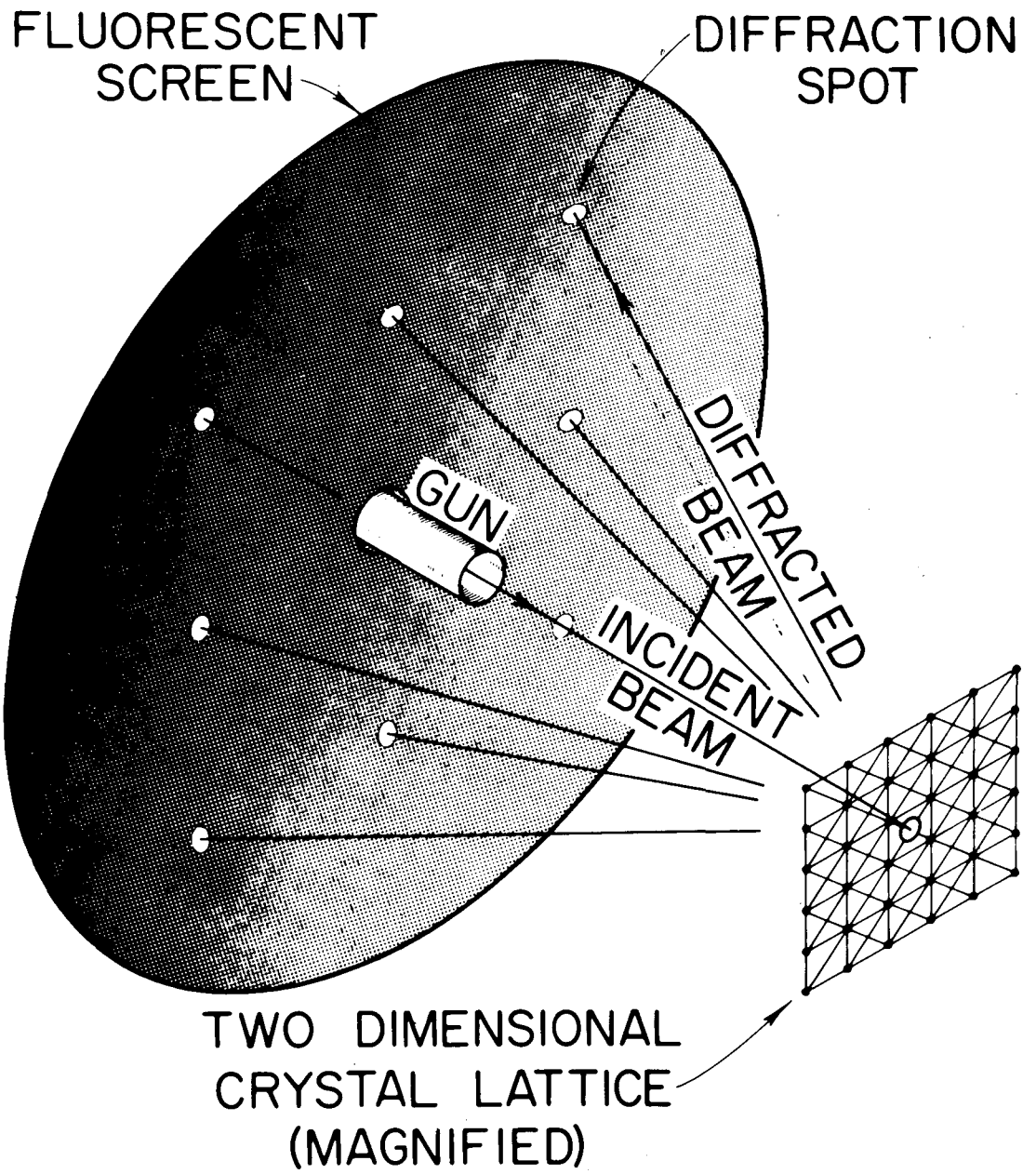

Fig. 2.17. A schematic representation of a LEED set-up is shown. The low energy electrons are diffracted from the (100) single crystal to form a square pattern on the phosphor screen.

a retarding field analyzer (Fig. 2.9) and finally accelerated into a phosphorescent screen. The patterns which are on the screen can be photographed through the UHV viewport, and analyzed.

Section 2.8: Materials

Hydrogen, carbon monoxide, additives (Na, K, Si, P, O, S, Cl) and hydrocarbons used in this research were the highest attainable research purity. A listing of reagents is given in Table 2.1 with sources, purities and major detectable or known impurities. Liquid hydrocarbons, distilled into teflon-sealed pyrex vacuum flasks were outgassed prior to use by repeated freeze-pump-thaw cycles at 77 K. Hydrogen was passed through a liquid nitrogen trap and carbon monoxide was passed through a dry ice/acetone trap prior to use. All other gases were used as supplied.

All reagents had very low contamination levels, < 1 ppm, as evidenced by the lack of contamination and/or poisoning of high pressure reactions during the course of these experiments. Only occasional low levels of sulfur, < 0.1 ML, were detected after CO/H_2 HDN and HDO experiments. The most important species deposited during high pressure reactions were carbon and hydrogen with some oxygen, forming carbonaceous overlayers characteristic of CO hydrogenation reactions.

Table 2.1. Materials

Reagent	Supplier	Purity[a]	Impurities[a]	Contaminants[b]
H_2	Matheson	<99.9995	ND[e]	ND
CO	Matheson	<99.99	propane, N_2	ND
N_2	LBL	<99.99	Ar, H_2O	H_2O
O_2	LBL	<99.9	CO	ND
Ar	LBL	<99.9598	CH_4, CO_2	carbon
D_2	Matheson	<99.95	HD, H_2	ND
C ≡ C[c]	Matheson	<99.6	acetone	
C = C	Matheson	<99.5	CO_2, C ≡ C	
C - C	Matheson	<99.0	ND	
He	LBL	<99.000	ND	
K	SAES getter		ND	
Na	SAES getter		ND	
SiH_4	Matheson	semiconductor purity	ND	
PH_3	Matheson	<99.999	ND	
H_2S	Matheson	<99.5	ND	S
Cl_2	Matheson	<99.96	CO_2, N_2	
cyclo-hexene	Phillips	<99.85	cyclohexane, benzene	S (2-4% ML)
furan[d]	MCB		ND	ND
tetrahydro-furan[d]	Mallinckrodt		ND	ND
pyridine[d]	Mallinckrodt		ND	S (~ 0.1 ML)
piperidine[d]	Aldrich		ND	ND
pyrrole[d]	Aldrich		ND	S (~ 0.1 ML)
pyrroli-dine[d]	Aldrich		ND	ND

[a]determined by GC, GCMS or MS. [b]determined by AES following high pressure experiments. [c]passed through dry ice/acetone trap, distilled into glass bulb prior to use. [d]anal.reag.grade, glass-distilled into teflon-sealed glass bulbs prior to use. eND ≡ not detectable by methods used.

Section 2.9: Catalyst Samples

Single crystals, foils and powders were used throughout this research. The samples are listed in Table 2.2, along with the supplier, major contaminants and the normal UHV cleaning procedure for each.

Molybdenum and palladium crystal catalysts used in this work were prepared by W. Heppler of LBL. The method used was to spark erosion cut a thin oriented disk (~ 0.3 - 0.9 mm thick) from the stock single crystal rods. The orientation was checked using Laue x-ray back diffraction, see Fig. 2.18, to insure that both crystal faces were within 0.5° of the desired orientation. The crystals then were polished to a mirror finish using standard metallographic procedures, with the final step using an aqueous slurry of 0.05 μm alumina powder in an ultrasonic vibrator. The samples then were dipped in acid, water, acetone and ethanol prior to mounting on the manipulator and inserted into the UHV chamber.

Powdered samples ($LaFeO_3$, $LaCrO_3$, $LaMnO_3$, $LaCoO_3$, $LaRhO_3$) were prepared by K. Seiber using La_2O_3, $La(NO)_3$, $Rh(OH)_3$ and nitrates of Fe, Co, Mn and Cr as reagents. The procedures have been published[22] and will not be discussed in detail here.

Table 2.2. Catalyst Samples

Catalyst	Supplier	Major Contaminant	Normal Cleaning Procedure
Rh_{foil}	Engelhard	C, B, Si, O	Argon ion sputter at 1000°C for B, O_2 at $5X10^{-7}$ Torr at 600°C for C, Argon ion sputter at 500°C for Si,O
Au_{foil}	Engelhard	C, S, Ca	Argon ion sputter at 600°C O_2 at $5X10^{-7}$ Torr at 500°C, repeat
Pd single crystal	Materials Research Corp. Lawrence Livermore Labs	C, S	Argon ion sputter at 500°C O_2 at $5X10^{-7}$ at 1000°C, repeat
Mo single crystal	Materials R.C.	C, S	a) heat to 1600°C for S b) O_2 at $5X10^{-7}$ Torr at 1000°C flash to 1600°C for C
$Rh_2O_3 \cdot 5H_2O$	Engelhard		flash in $5X10^{-7}$ Torr of O_2
$LaRhO_3$	Dr. K. Seiber[a]		"
$LaFeO_3$	"		"
$LaCrO_3$	"		"
$LaMnO_3$	"		"
$LaCoO_3$	"		"

[a] performed preparation and characterization

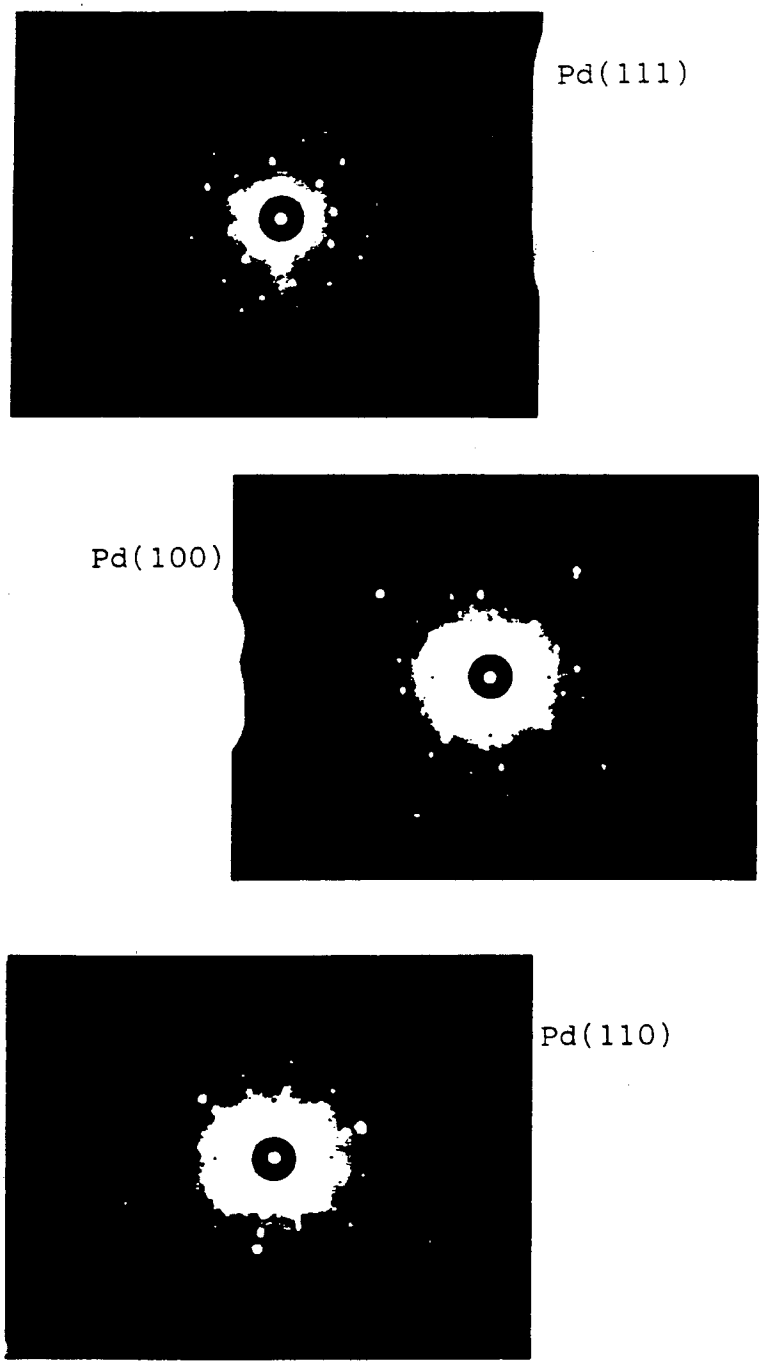

Fig. 2.18. Laue x-ray back diffraction for Pd(111), Pd(100) and Pd(110). From the symmetry of the pattern the orientation of the single crystal surface can be accurately checked (± 1.0°).

Section 2.10: Dosing Materials and Procedures

Volatile gases were dosed through a variable rate leak valve from the gas manifold into the vacuum chamber, either by backfilling the chamber or by introduction through a 0.125 in O.D. stainless steel tube doser pointed towards the sample. The crystal was cooled to 100-250 K (usually ~ 110 K) before backfilling the chamber with the volatile gas. Molecular gases were decomposed by rapidly heating the crystal to 600 K, thus desorbing H_2 from H_2S, H_3P and H_4Si.

All potassium and sodium dosing was done by heating a commercial SAES Getter source which consists of a powdered mixture of potassium chromate or sodium chromate and a zirconiium-16% aluminum alloy getter, enclosed in a tantalum dispenser. The doser was positioned about 5 cm from the sample, and heated by passing a 4-8 Amps. current through it, giving dosing rates of 0.05-0.20 ML per minute. The amount of potassium or sodium deposited was monitored by AES, and calibrated from the shape of the uptake curves, as described elsewhere.[5,21]

Procedures

Section 2.11: Low Pressure Studies

Low pressure chemisorption studies were carried out to determine approximate energies and surface coverages of additives or poisons. The single crystal, foil or powdered sample was cleaned in UHV as described in Table 2.2, then quickly cooled to the adsorption temperature (usually ~ 130-170 K). A leak valve, containing the gas to be adsorbed, was then opened to admit a flow which increased the pressure in the UHV chamber to ~ $2\text{-}5\text{X}10^{-8}$ Torr. The gas was dosed to provide 0.1-10 Langmuirs on the surface (1 Langmuir ≡ 1X10-6 Torr • sec of any gas used in these studies).

The surface was then heated at a linear rate, of 20-50 K/sec, and the mass spectrometer signal for a given mass was plotted or stored versus the time and/or temperature of the sample. Typical TPD spectra are shown in Fig. 2.19. The spectra contain four masses each and were aquired simultaneously with either a PET microcomputer of a UTI mass programmer. Areas under each curve correspond, after calibration, to the amount of each product desorbed and can be used to give kinetic information on the surface reaction.

TRIMERIZATION

ULTRA-HIGH VACUUM

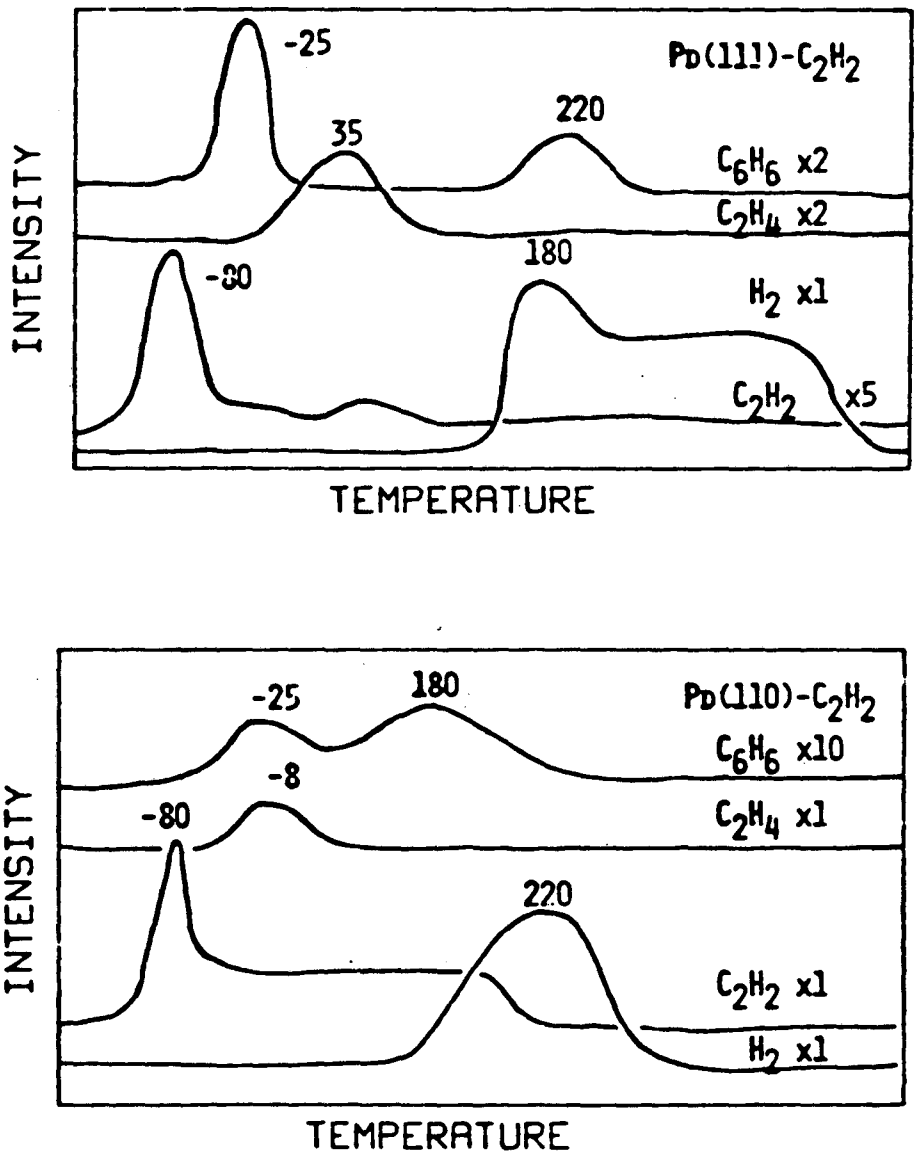

Fig. 2.19. TPD of acetylene from Pd(111) and Pd(110) (6 ℓ adsorbed at 130 K, heating rate of 25 K/sec) recorded in the UTI mass programmer.

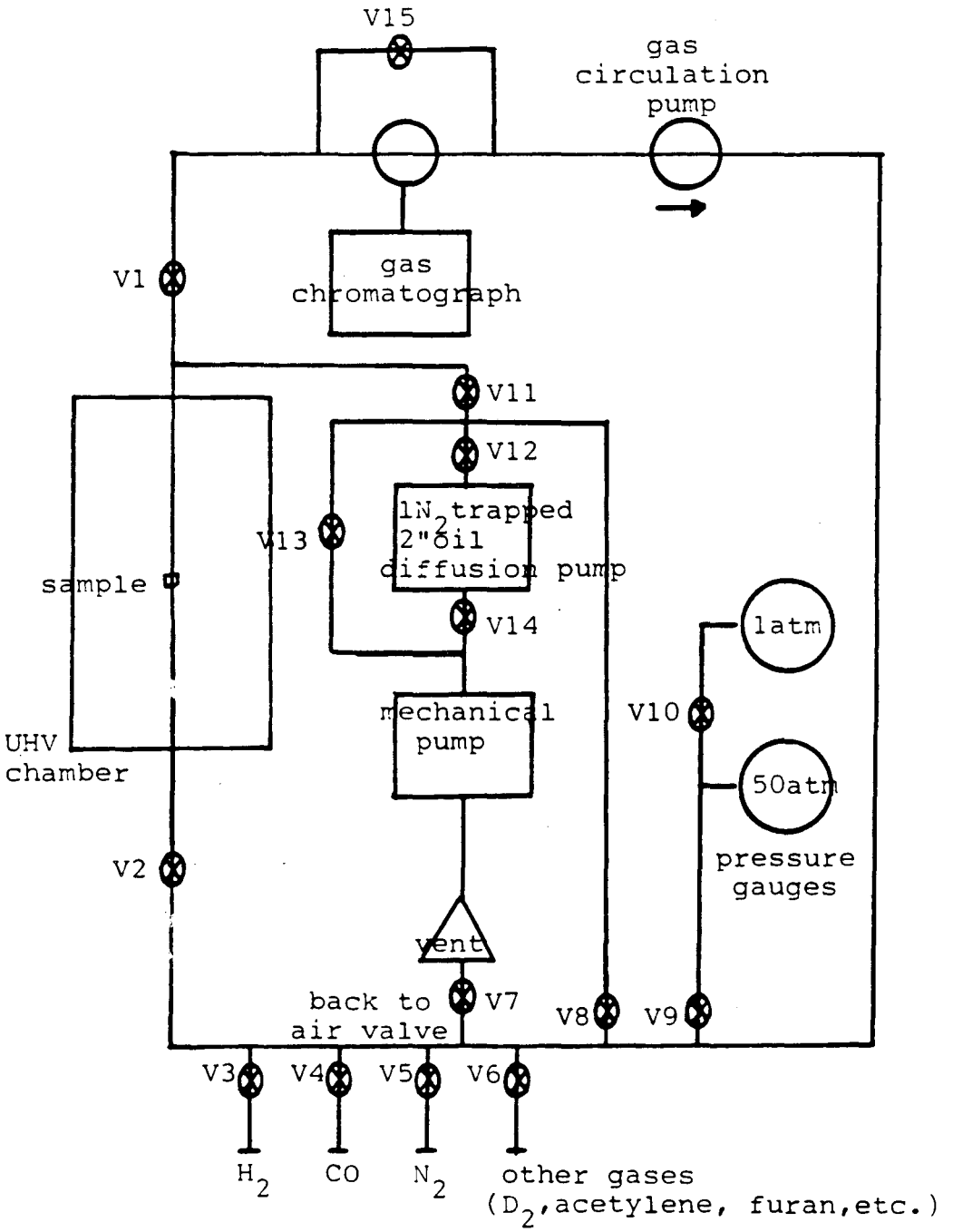

Fig. 2.20. A detailed schematic of the high pressure loop. All valves, except V12 and V14, are Nupro (4BK or 6BK). V12 is a 2 3/4" gate valve and V14 is a 1 1/2" brass bellows valve.

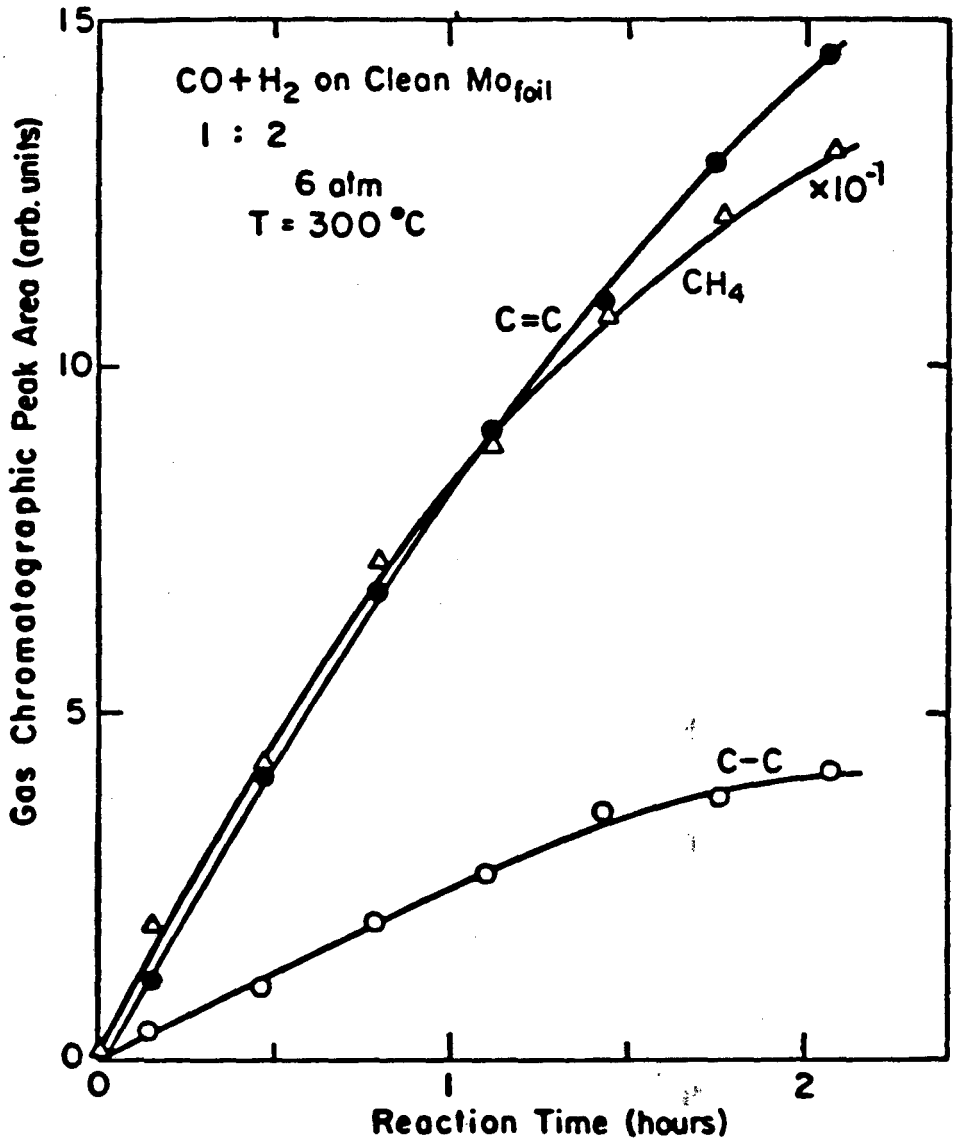

Fig. 2.21. A plot of the gas chromatographic peak area vs. reaction time for the typical reaction products of the hydrogenation of CO over clean Mo catalysts. Reaction rates for the individual products are determined graphically from the initial slope of the product accumulation curve.

Section 2.12: High Pressure Studies

Prior to each high pressure (1-20 atm) reaction study, the sample was cleaned in UHV using a combination of argon ion bombardment, high temperature oxygen treatments and annealing cycles, as described in Table 2.2 for each sample. The surface composition was characterized by AES and/or XPS. The well-characterized sample was then enclosed in the high pressure cell. The high pressure loop subsequently formed (see Fig. 2.20) has its own gas manifold, pressure gauges and pumping system. In normal high pressure operation valves V7, 8, 9, 11 and 15 were closed and V1 and V2 were opened to expose the sample to the reaction gases. The gases for reaction were bled in through valves 3-6, while the circulation pump was on and V14 was open, and mixed for 10 min prior to taking a gas chromatographic sample. After a background gas sample was taken, to insure uniform mixing, the sample was heated to reaction temperature and an automatic gas chromatograph sampling cycle (sampling every 15-120 min) was initiated. Time zero was taken as heating of the crystal began. The reaction temperature was continuously regulated to ± 3 K using a precision temperature controller (Eurotherm 919 PAP) with a digital voltmeter display referenced to the thermocouple. The data from the gas chromatograph was plotted in the form of product accumulation curves (see Fig. 2.21). Initial rates of reaction for each product were determined graphically by taking the initial slope of the gas chromatographic peak area versus time plot. Reactions were usually allowed to proceed 120-3000 min (CO/H_2 for 120-360 min, HDN/HDO for 120-240 min, C ≡ C cyclotrimerization for 1000-3000 min). When the reaction was to be stopped, the crystal was cooled and the gas mixture pumped out. First, in the case of CO/H_2 studies which involved two or more atmospheres of pressure, the gases were pumped out by opening

V7 to reduce the loop pressure to ~ 1 atm; then, in all cases, by using the mechanical pump (open V8, 11, 13 and 15 with V12 and V14 closed) and finally with the liquid nitrogen-trapped oil diffusion pump (open V12 and V14, close V13). The pumping sequence took ~ 30-60 min and reduced the pressure in the loop to ~ $1.0\text{-}10\text{X}10^{-4}$ Torr. After pumping, V1, 2 and 11 were closed and the high pressure cell opened, exposing the sample to UHV and the surface analytical techniques contained therein. The pressure burst upon opening the cell was ~ $5\text{X}10^{-8}\text{-}5\text{X}10^{-7}$ Torr and rapidly decayed to ~ $1\text{X}10^{-8}$ Torr in ~ 5 min. Subsequent Auger spectra were recorded for the sample, to provide an estimate of the surface carbon and other possible impurities (especially sulfur). The carbon deposits were studied further by using CO TPD, to determine the amount of clean surface area relative to a CO TPD prior to the reaction.

Section 2.13: References

1. Cabrera, A.L., Spencer, N.D., Kozak, E., Davies, P.W., and Somorjai, G.A., Rev. Sci. Instrum. 53 (12), 1893 (1982).

2. Ganschow, O., and Steffens, P., J. Vac. Sci. Tech. 21 (3), 845 (1982).

3. Gillespie, W.D., Ph.D. Thesis, Univ. Calif. Berkeley (1980).

4. Herz, R.K., Gillespie, W.D., Peterson, E.E., and Somorjai, G.A., J. Catal. 67, 371 (1981).

5. Davis, S.M., Zaera, F., and Somorjai, G.A., J. Am. Chem. Soc. 104, 7433 (1982).

6. Dietz, W.A., J. Gas. Chrom., Feb., 68 (1967).

7. Ertl, G., and Kuppers, J., "Low Energy Electrons and Surface Chemistry," Verlag Chemie, Weinheim (1974).

8. Somorjai, G.A., Szalkowski, F., Adv. High Temp. Chem. 4, 137 (1971).

9. Briggs, D., "Handbook of X-ray and Ultraviolet Photoelectron Spectroscopy," Heydon and Son, London (1977).

10. Van Hove, M.A., and Tong, S.Y., "Surface Crystallography by LEED," Springer-Verlag, Berlin (1979).

11. Schmidt, L.D., Catal. Rev. 9, 115 (1974).

12. Kelley, R.D., and Goodman, D.W., in "The Chemical Physics of Solid Surfaces and Heterogeneous Catalysis," D.A. King and D.P. Woodruff, eds., Elsevier, Amsterdam (1982).

13. Banbynek, W., Rev. Mod. Phys. 44, 716 (1972).

14. Biberian, J.P., and Somorjai, G.A., Appl. Surf. Sci. 2, 352 (1979).

15. Sachtler. J.W.A., Van Hove, M.A., Biberman, J.P, and Somorjai, G.A., Surf. Sci. 110, 19 (1981).

16. Mroczkowski, S., and Lichtman, D., Surf. Sci. 131, 159 (1983).

17. Palmberg, P.N., Riach, G.E., Weber, R.E., and MacDonald, N.C., "Handbook of Auger Electron Spectroscopy," Physical Electronics Ind., Minnesota (1972).

18. Wagner, C.D., Riggs, W.M., Davis, L.E., Moulder, J.F., and Muilenberg, G.E., "Handbook of X-ray Photoelectron Spectroscopy," Perkin-Elmer Corp, Minnesota (1978).

19. Garfunkel, E.L., Ph.D. Thesis, Univ. Calif. Berkeley (1983).

20. Redhead, R.A., Vacuum 12, 203 (1962).

21. Zaera, F., Ph.D. Thesis, Univ. Calif. Berkeley (1984).

22. Seiber, K., Personal Communication (1984).

INTRODUCTION TO CHAPTER THREE, FOUR AND FIVE: HYDROGENATION OF CARBON MONOXIDE

The hydrogenation of carbon monoxide is important for the long term world fuel requirements. Coal is a dirty and inconvenient material to handle, with an ash by-product. Also, approximately 1 1/2 tons of coal are need to supply the energy of 1 ton of oil. However, the world reserves of coal are estimated to be very large in comparison with those of oil and gas (see Table 1). Coal can be converted to ~ 1:1 $CO:H_2$. Most of the hydrocarbons produced by the hydrogenation of carbon monoxide are aliphatic, which creates high quality diesel and aviation fuel. Methanol can also be produced in high yields and can be converted to aromatics in zeolite catalysts[1], so all hydrocarbon products can be produced from H_2 and CO (see Fig. 1).

The hydrogenation of carbon monoxide, commonly called the Fischer-Tropsch synthesis, on metals has a long history. Methane formation was reported as early as 1902[2] and longer chain hydrocarbons were observed prior to 1910[3]. Table 2 contains a brief history of the developments in the hydrogenation of CO.

Thermodynamically, many products have a favorable free energy of formation, as can be seen in Fig. 2. Higher pressures are used to enhance products such as methanol and acetic acid.

The work described in the following three chapters investigated the effect of additives (O, S, K) on the hydrogenation of CO. The pressure dependence, activation energy and product distribution will be discussed in terms of the mechanism of the reaction.

Table 1. World energy reserves (1973 world energy production = 1).

	Proven Recoverable	Estimated Total
Gas	8	46
Oil	17	73
Shale and tar sands	47	250
Coal	66	730

Table 2. Milestones in the history of synthesis gas reactions.

Year	Author	Catalyst	Observed Products	Remarks
1902	Sabatier, Senderens[2]	Ni ; Co	CH_4	
1908	Orlov[3]	Ni/Pd	CH_4, C_2H_4, C_2H_6	
1913	BASF patent[4]	Co and Os oxide	'oil' (alkanes and oxygenates	100-200 atm; 575-675 K
1921	Patart[5]		CH_3OH	
1922	Fischer and Tropsch[6]	Fe (alkali)	oxygenated hydrocarbons	100 atm; 675 K
1923	BASF patent	$ZnO-Cr_2O_3$	CH_3OH (exclusively)	100-600 atm; 525-675 K
1923	Fischer and Tropsch[7]	Fe, Co	hydrocarbons	10-20 atm
1925	Fischer and Tropsch[8]	Fe-oxide/ZnO	hydrocarbons	1 atm
1938	Pichler[9,10,11]	Ru	waxes	10^3 atm
1974	Walker and Pruett[12]	Ru-complexes	glycol	U.S. patent
1978	Rabo[13]	Pd	CH_3OH	
1978	Ichikawa[14,15]	Rh-complexes	C_2H_5OH	
1979-1982	Leupold, et al.[16,17,18]	'Rh'	'oxygenates'	D.P. patents

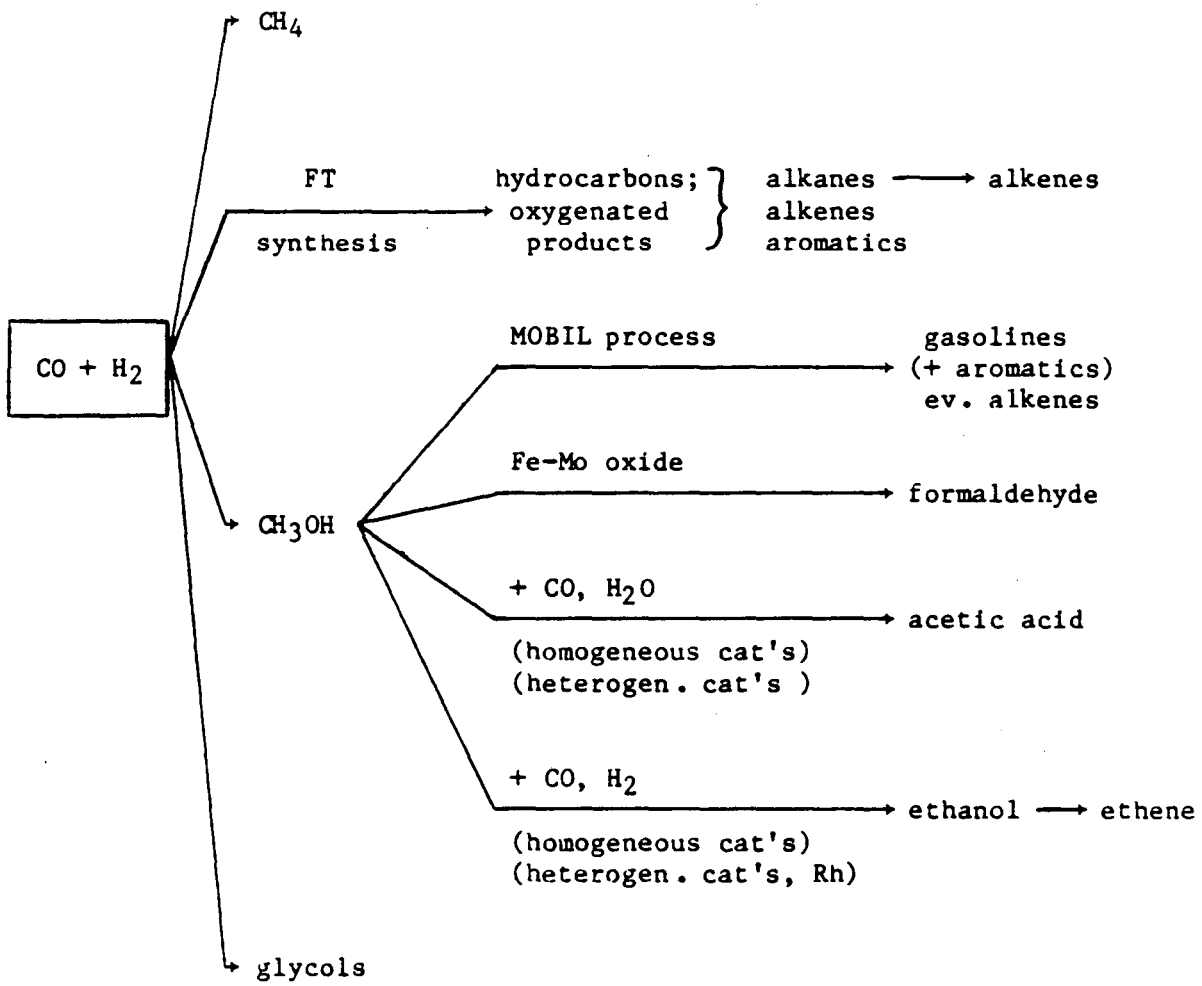

Fig. 1. Scheme of conversion of CO/H_2 gas mixtures.

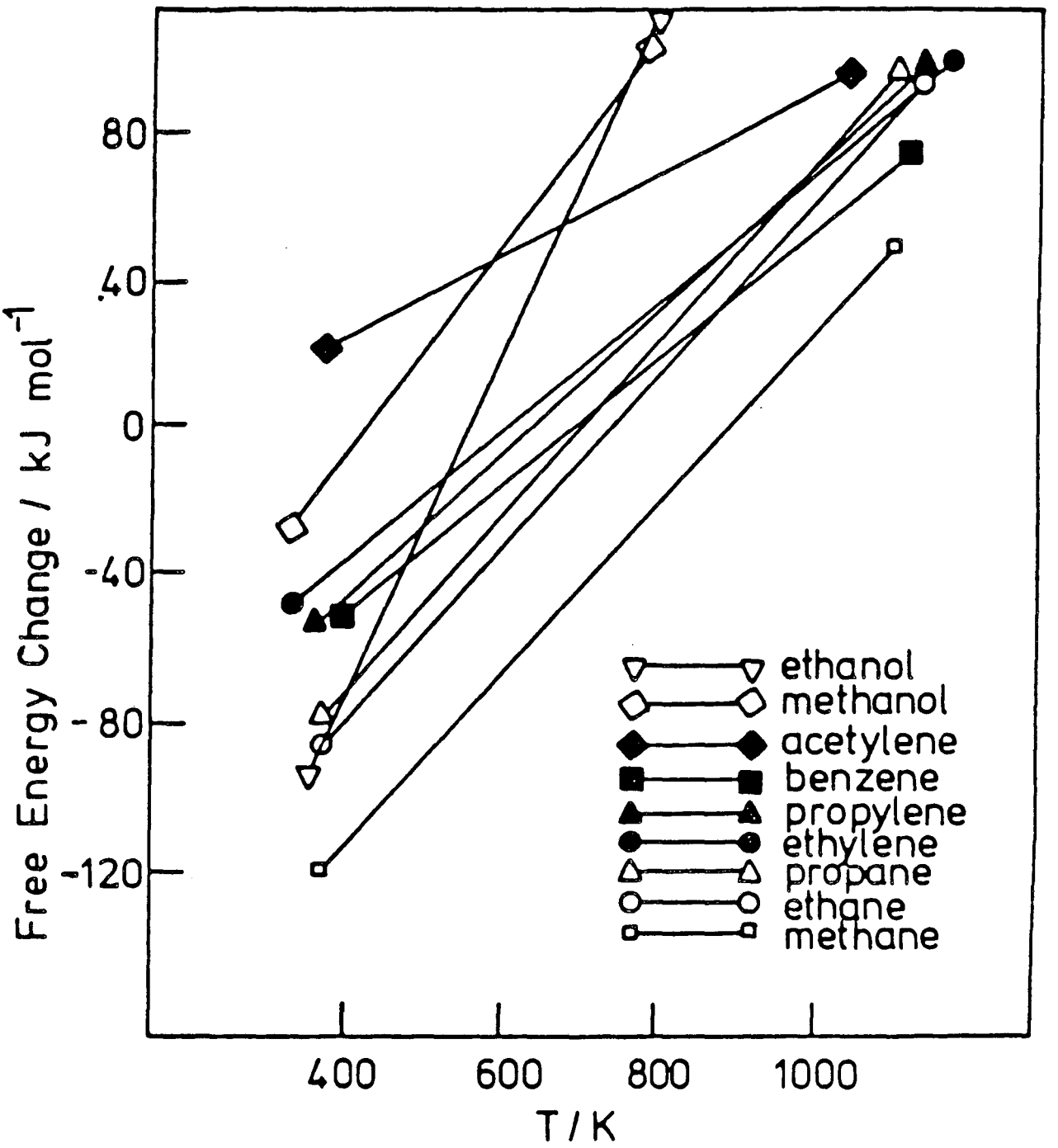

Fig. 2. Standard free energies of formation for synthesis of hydrocarbons and alcohols from carbon monoxide and hydrogen with water as by-product.

REFERENCES

1. Chang, C.D., and Silvestri, A.J., J. Catal. 47, 249 (1977).

2. Sabatier, P. and Senderens, J.B., C.R. Hebd. Seances Aced. Sci. Paris 134, 514 (1902).

3. Orlov, E.I., Zh. Russ. Khim. O-va., Chast Khim. 40, 1588 (1908). Transl.: Orlov, G., Ber. Dtsch. Chem. Ges. 42, 893 (1909).

4. D.R.P. 293, 787 to Badische Anilin und Sodafabrik (1913).

5. Patart, G., B.F. no 540, 343 (1921).

6. Fischer, F., and Tropsch, H., D.P.R. 411, 216 (1922).

7. Fischer, F., and Tropsch, H., Brennst.-Chem. 4, 276 (1923).

8. Fischer, F., and Tropsch, H., German patent 484, 337 (1925).

9. Pichler, H., Brennst.-Chem. 19, 226 (1938).

10. Pichler, H., Ges. Abh. Kenntn. Hohle 13, 417/74 (1957).

11. Pichler, H., Adv. Catal. 4 271, (1952).

12. Pruett, R.E., and Walker, W.E., U.S. patent 3,833,634 (1974).

13. Poutsma, M.L., Elek, L.F., Ibarbia, P.A., Risch, A.P., and Rabo, J.A., J. Catal. 52, 157 (1978).

14. Ichikawa, M., Bull. Chem. Soc. Jap. 51, 2273 (1978).

15. Ichikawa, M., J. Chem. Soc., Chem. Comm., 566 (1978).

16. Hoechst, A.G., Wunder, F.A., Arpe, H.J., Leupold, E.I., and Schmidt, H.J., D.P. 2814427 (1979).

17. Hoechst, A.G., Schmidt, H.J., Wunder, F.A., Arpe, H.J., and Leupold, E., D.P. 2814365 (1979).

18. Hoechst, A.G., Leupold, E.I., Schmidt, H.J., Wunder, F., Arpe, H.J., and Hachenberg, J., E.P. 791040090 (1979).

CHAPTER THREE: DEUTERIUM ISOTOPE EFFECTS ON HYDROGENATION OF CARBON MONOXIDE OVER RHODIUM

Section 3.1: Introduction

Isotopic substitution of deuterium for hydrogen can modify the rate of carbon monoxide hydrogenation[1-10]. Reports indicate that the rate of methane formation over ruthenium decreased[1], increased[2], or remained the same[4,5], over Ni increased[6-8] or remained the same[4,5], and over a Co/ThO_2 Kielselguhr catalyst increased upon substitution of deuterium.[9] In this note we report an "equilibrium" deuterium isotope effect during methanation over rhodium polycrystalline foils; that is, the rate of methane formation increased when D_2 was used as a reactant instead of H_2. The rate of CD_4 formation was found to be 1.5 times faster than the rate of CH_4 formation under the conditions used in this study ($CO:H_2$, 1:2, 6 atm total pressure, 520-720 K). This result is similar to that found on supported Ru catalysts by Kellner and Bell[2]. The pressure dependence of the reaction is -1.0 ± 0.1 order in CO and $+1.0 \pm 0.1$ order in H_2, which implies competitive adsorption[14] of these two molecules on the surface. This data along with an activation energy of 25 kcal/mol for methane formation indicate that one of the final hydrogenation steps is rate-limiting, as proposed by Kellner and Bell[2] over supported Ru catalysts.

Section 3.2: Results and Discussion

The catalytic hydrogenation of carbon monoxide has been investigated on rhodium polycrystalline foils. Typical turnover frequencies (defined as product molecules/Rh atom x second) for methane production were 0.26 at 570 K, CO/H_2=0.33, and 6 atm total pressure; and 1.0 at 520 K, CO/H_2=0.33, and 6 atm total pressure. These turnover frequencies were calculated using the surface atomic density of Rh(111) (1.6×10^{15} atoms/cm^2) and initial reaction rates. A typical product accumulation curve is shown in Fig. 3.1. A typical product distribution for the reaction is shown in Table 3.1.

Under all the conditions of this study, the main product from the reaction is methane with small amounts of ethane and propane also being produced. The only by-product of the reaction was found to be water.

Figure 3.2 displays an Arrhenius plot for CH_4 formation, from which an activation energy for methanation on Rh polycrystalline foils of 25 ± 0.5 kcal/mol was calculated. Also shown in Fig. 3.2 is the corresponding plot when deuterium was substituted for hydrogen in the reaction mixture. An isotope effect is observed clearly, the rate of methane formation increased by a factor of 1.5 when deuterium was used as a reactant.

The dependence of the methanation rate on the pressures of the reactant gases is shown in Fig. 3.3. This plot was determined by varying the partial pressure of each reactant gas while maintaining a constant temperature and total pressure, using argon as a buffer gas. Consequently, the observed rate law for methanation is given by

$$R_{CH_4} = kP_{CO}^{-1}P_{H_2}^{+1}.$$

The reaction begins to be poisoned after about 1-3 h, depending on reaction conditions (higher temperature and high CO/H_2 ratios lead to faster

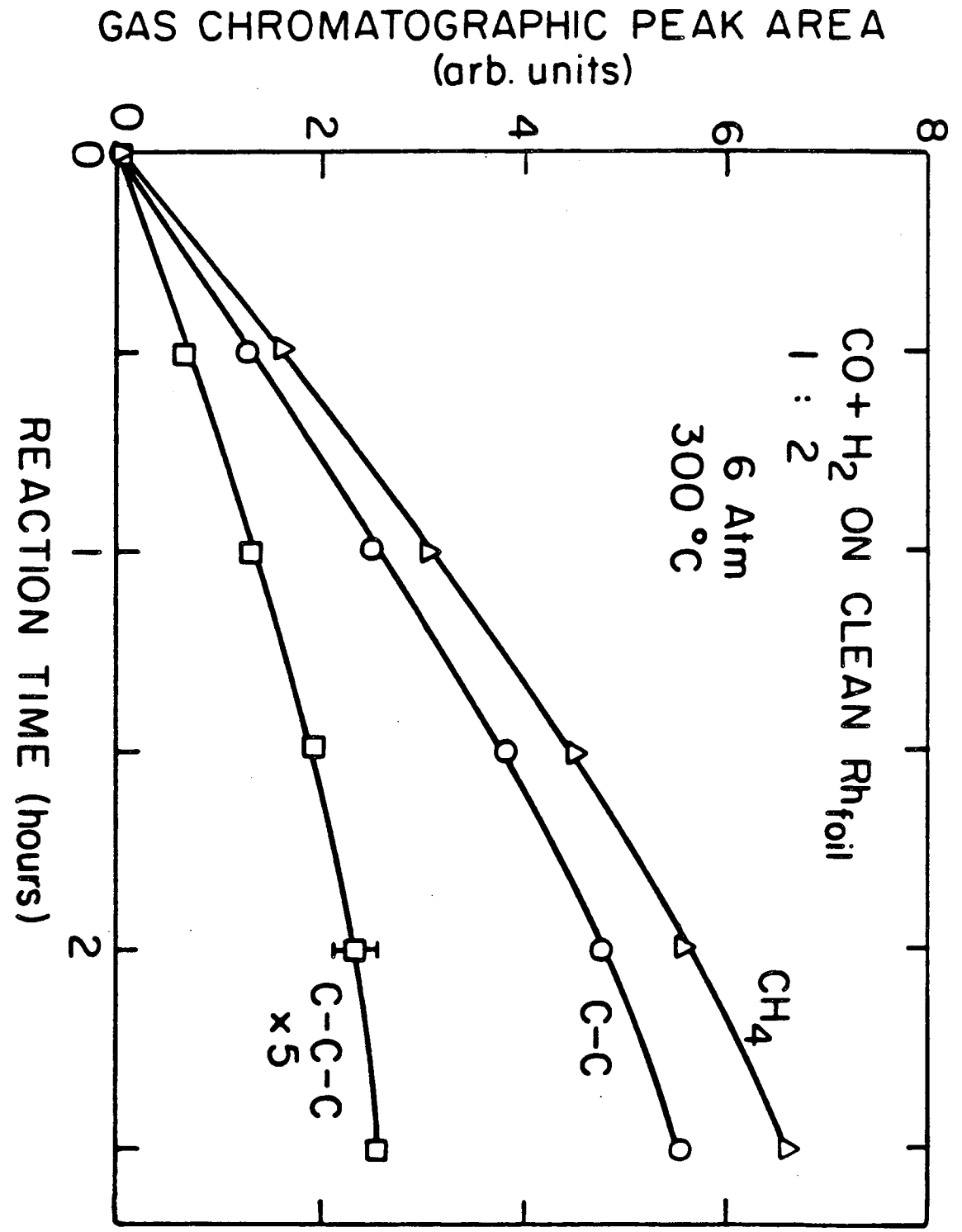

Fig. 3.1. Product accumulation vs. reaction time curves in closed-loop, batch reactor. The plot shows major products from CO + H_2 (1:1) at 6 atm total pressure and a clean Rh_{foil} catalysts temperature of 570 K.

Table. 3.1. Typical product distribution of the catalytic hydrogenation of CO.

Product	$CO:H_2$, 1:2, 570 K, 6 atm Turnover Frequencies (molecules/Rh atom • sec)	mole %
CH_4	0.26	95
C_2H_6	0.01	4
C_3H_8	0.003	1
C_4^+	0.00	0

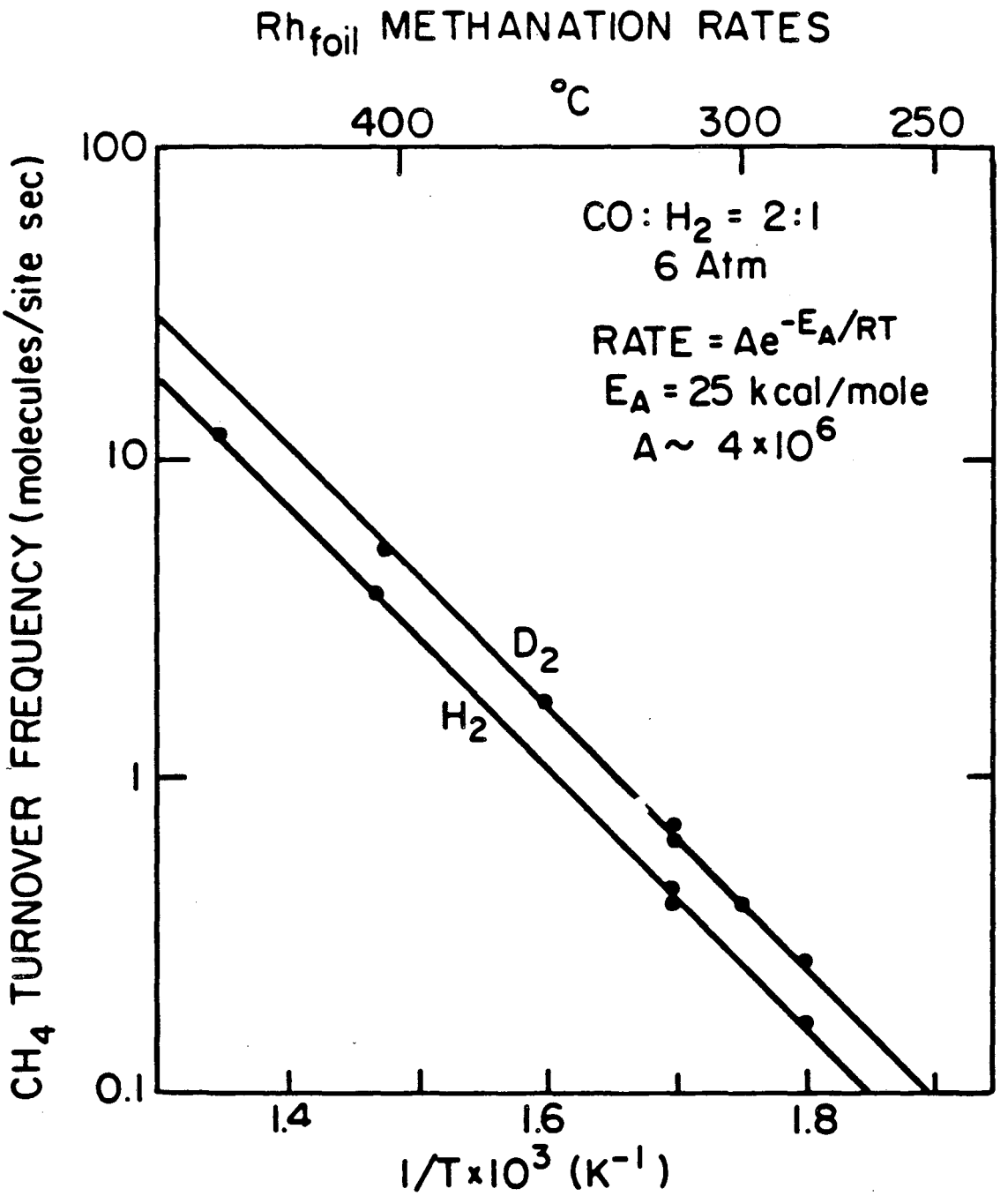

Fig. 3.2. Arrhenius plot for the initial rate of formation of CH_4 and CD_4 vs. inverse temperatures over Rh polycrystalline foils. As is shown, the rate of CD_4 formation is 1.5 times the rate of CH_4 formation over the entire temperature range of this study.

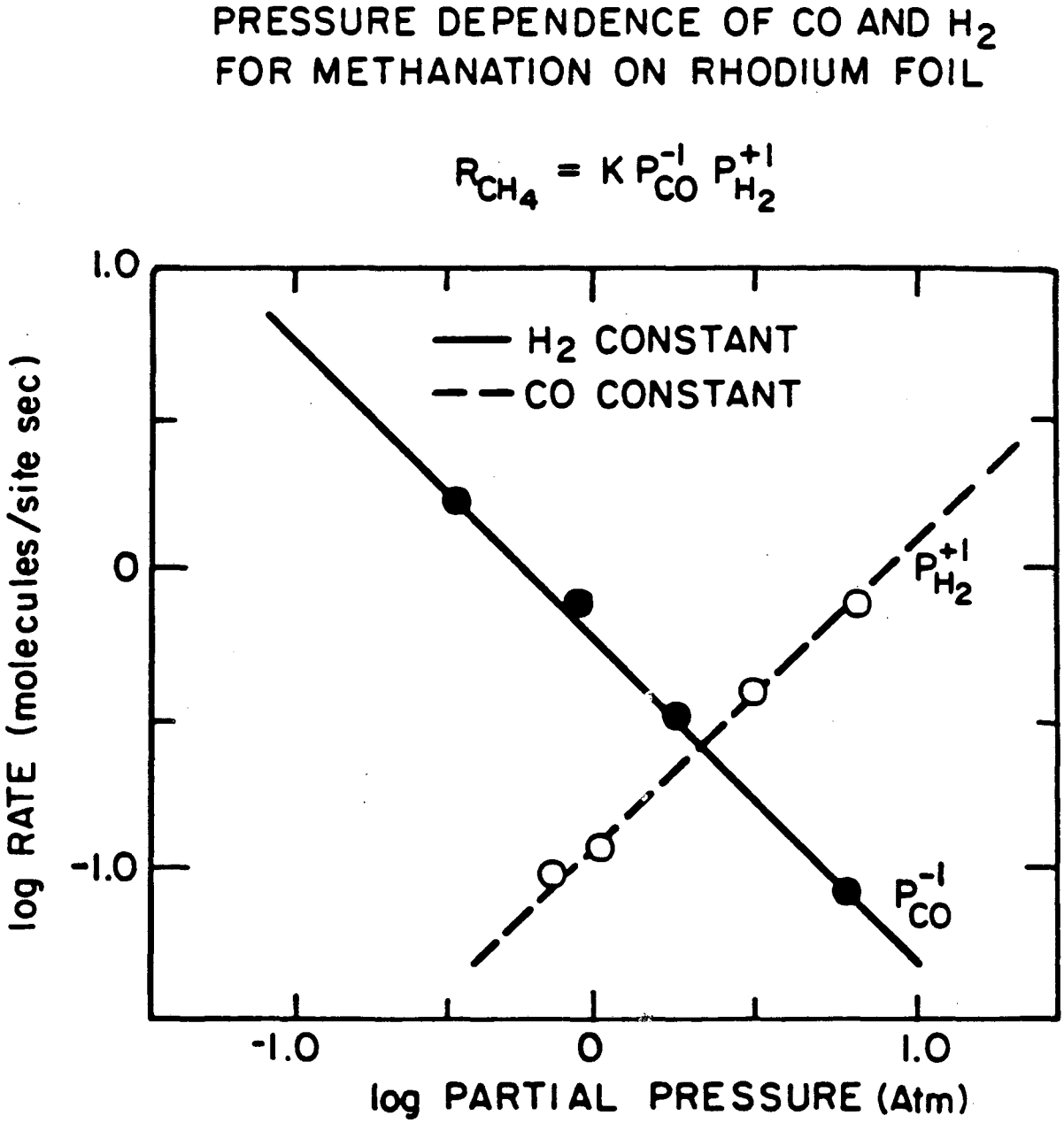

Fig. 3.3. Rate of methane formation vs. the partial pressure of each reactant at a constant total pressure of 10 atm and constant temperature of 570 K (constant H_2 pressure of 3 atm for determination of CO dependence and constant CO pressure of 3 atm for determination of H_2 dependence). The resulting rate expression has the form

$$r_{CH4} = KP_{CO}^{-1.0}P_{H2}^{+1.0}.$$

poisoning rates). After poisoning of the reaction, AES revealed a carbon-covered surface.

The products of the hydrogenation of CO on rhodium foils are alkanes[12], indicating that rhodium is a very good hydrogenation catalyst. The highest molecular weight hydrocarbon observed was propane, implying that the rate of carbon-carbon bond formation is slow relative to the rates of hydrogenation and desorption.

The substitution of deuterium for hydrogen in the reaction mixture provides further information about the rate-determining step. Fig. 3.2 shows an inverse deuterium isotope effect similar to that observed on Ru by Kellner and Bell[2]. Deuterium isotope effects arise from two sources[10,16]: first, the kinetic isotope effect, and second, the thermodynamic or equilibrium isotope effect. The kinetic isotope effect is the result of the difference in zero point energy associated with the dissociating bonds, k_H/k_D:

$$k_H/k_D \cong \exp[(E^*_{O(D)} - E^*_{O(H)}) - (E_{O(D)} - E_{O(H)})] \; / \; RT.$$

If the bond dissociating or forming is very weak, so that the zero point energy in the activated state can be ignored, then the ratio of the rate constants, k_H/k_D, is determined by the differences in zero point energies, $E_{O(D)} - E_{O(H)}$, for the reactants. The vibrational frequency of a C-H bond is greater than that of a C-D bond, $E_{O(H)} > E_{O(D)}$, so it is usually observed that $k_H > k_D$. The magnitude of $E_{O(H)} - E_{O(D)}$ can be evaluated from the vibrational frequency and for C-H/C-D it is ~ 1.1 kcal/mol, from which k_H/k_D could be as high as ~ 3 at 570 K. However, a large normal isotope effect is rarely observed, suggesting that some zero point energy is associated with the activated complex.

The thermodynamic isotope effect arises from a change in the surface concentration of a reaction intermediate. If the equilibrium constant for a reaction is given in terms of partition functions and expanded for methane formation it has the form of:

$$K_H = \frac{Q_{CH4}\ Q_{H2O}}{Q_{CO}\ Q^3_{H_2}}$$

and expanding for Q_H,

$$Q_H = M_H^{3/2}\ (I_A I_B I_C)^{1/2} \prod_i^6 \left(\frac{1}{1-\exp(-h\ \nu_i/kT)}\right) \exp(-E_o/RT)$$

where M = molecular weight, I_i = moments of inertia, ν_i = fundamental frequencies, E_o = zero point energies, h = Plank's constant and k = Boltzman's constant. The equilibrium constant ratio, k_D/k_H is determined largely by the energy difference

$$(E_{0(CH_4)} - E_{0(CD_4)}) + (E_{0(H_2O)} - E_{0(D_2O)}) - 3(E_{0(H_2)} - E_{0(D_2)})$$
$$= 7.01 + 3.39 - 3(1.67)$$
$$= 5.4 \text{ kcal/mol.}$$

At lower temperatures the value of K_D/K_H increases due to the last term in the partition function, which is highly temperature-sensitive. The observed inverse isotope effect results from a combination of the kinetic and thermodynamic effects. Since we have an inverse deuterium isotope effect, one of the hydrogenation steps is rate-limiting. From the size of the inverse effect, similar to the effect observed on Ru[2], it has been interpreted[2] as suggesting that one of the final hydrogenation steps is rate-limiting.

Pressure dependence studies for the reaction gave a negative 1.0 ± 0.1 order in CO and a positive 1.0 ± 0.1 order in H_2. These values are typical for Fischer-Tropsch catalysts[13,14] and generally explained by invoking competitive adsorption of CO and H_2 on the surface. Other

studies[15] on rhodium methanation catalysts have been carried out at total pressures of 75 atm. These studies found the pressure dependence of the reaction to be proportional to Rate = $P_{H_2}^{+1/2}P_{CO}^{-1/2}$, suggesting that in our lower pressure studies the RDS may shift from C* + H* → CH* to CH* + H* → CH_2*. This difference is in the direction expected from a decrease in the total pressure and an interesting set of future experiments would be to investigate the pressure dependence of the reaction at even lower pressures.

Pressure dependence studies on Rh foil combined with the magnitude of the inverse deuterium isotope effect and activation energy lead us to propose a mechanistic scheme (see Fig. 3.4) for the hydrogenation of CO to form methane. To obtain model kinetics three assumptions were made. First, the Rh surface is nearly saturated by adsorbed CO, which is an assumption supported by <u>in situ</u> infrared observations[17,18]. Second, water is the major oxygencontaining product, as seen in this study as well as others[19], and third, all the mechanistic steps indicated as reversible are at equilibrium. For the case where methane production is dominant, as it is for Rh, a limiting form of the rate expression is given by

$$R_{CH_2} = kP_{H_2}^{+1.5}P_{CO}^{-1}.$$

Our results support the second hydrogenation step as being ratelimiting, so then the rate of formation of methane can be expressed as

$$R_{CH_4} = kP_{H_2}^{+1}P_{CO}^{-1}.$$

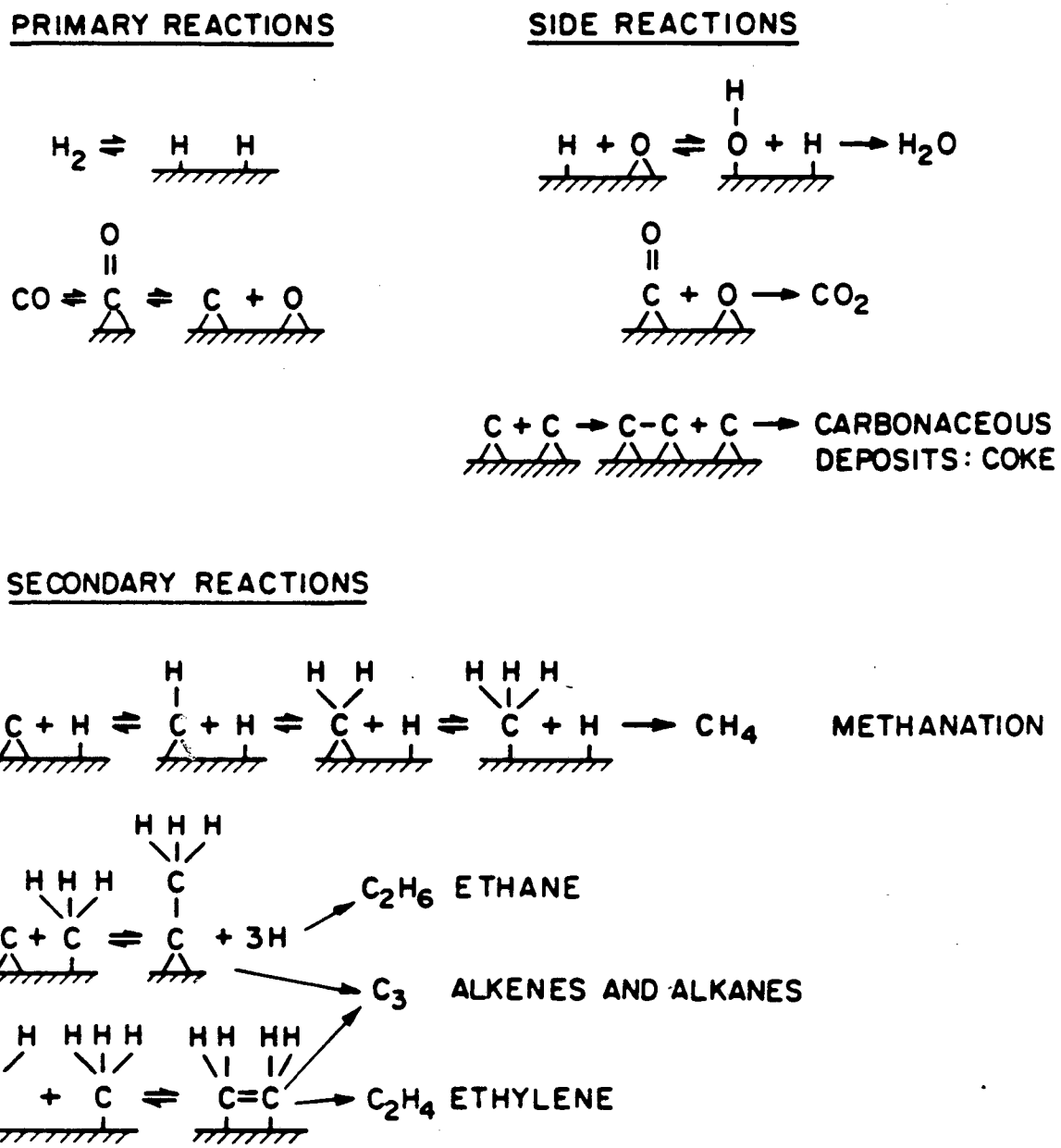

Fig. 3.4. Reaction mechanisms for the hydrogenization of carbon monoxide.

Section 3.3: References

1. McKee, E.W., J. Catal. 8, 240 (1967).

2. Kellner, C.S., and Bell, A.T., J. Catal. 67, 175 (1981).

3. Kobori, Y., Naito, S., Onishi, T., and Tamaru, K., J. Chem. Soc. Chem. Commun. 3, 92 (1981).

4. Dalla Betta, R.A., and Shelef, M., J. Catal. 49, 383 (1977).

5. Shelef, M., and Dalla Betta, R.A., J. Catal. 60, 169 (1979).

6. Mori, T., Masuda, H., Imai, H., Miyamoto, A., and Murakami, Y., Shokubai 22, 7 (1980).

7. Luytens, L., and Jungers, J.C., Bull. Soc. Chim. Belg. 54, 303 (1945).

8. Nicholai, J., Hont, M., and Jungers, J.C., Bull. Soc, Chem. Belg. 55, 160 (1946).

9. Sakharov, M.M., and Dokukina, E.S., Kinet. Katal. 2, 710 (1961).

10. Ozaki, A., "Isotopic Studies of Heterogeneous Catalysis." Academic Press, New York, 1977.

11. Davis, S.M., Zaera, F., and Somorjai, G.A., J. Amer. Chem. Soc. 104, 7453 (1982).

12. Sexton, B., and Somorjai, G.A., J. Catal. 46, 167 (1977).

13. Wilson, T.P., J. Catal. 60, 167 (1979).

14. Vannice, M.A., J. Catal. 37, 449 (1975).

15. Ellgen, P.C., Bartley, W.J., Bhasin, M.M., and Wilson, T.P., Adv. Chem. Ser. 178, 147 (1979).

16. Davis, S.M., Ph.D. Thesis, Univ. Calif. Berkeley (1981).

17. King, D.L., J. Catal. 77, 61 (1980).

18. Dalla Betta, R.A., and Shelef, M., J. Catal. 48, 111 (1977).

19. Ekerdt, J.G., and Bell, A.T., J. Catal. 58, 170 (1979).

CHAPTER FOUR: HYDROGENATION OF CARBON MONOXIDE OVER OXIDES OF RHODIUM AND 3d TRANSITION METAL PEROVSKITES

Section 4.1: Introduction

In an attempt to produce commercially valuable oxygenated feedstocks from nonpetroleum sources, the hydrogenation of carbon monoxide over transition metals in oxidation states of 0 - +4 has been studied. Other workers have found supported rhodium catalysts to be promising candidates[1-5]. The product distributions from different formulations range from high yields of methanol and ethanol[1,2] to ethanol and acetic acid[3,4,5] or solely non-oxygenated hydrocarbon products[6]. From these studies, it appears that the exact chemical environment of the catalytically active rhodium species on the surface plays an important role in determining the product distribution from FTS.

Previously, work in this group has investigated the characteristics of model, low surface area, unsupported rhodium catalysts for FTS in the pressure range of 1-10 atm[7-10]. These studies have found that the surface oxidation state of rhodium determines, to a great extent, the product distribution. The most significant finding of these studies was that $LaRhO_3$ could be used in FTS to form selectively up to 80% weight percent of oxygenated products and, more importantly, remained catalytically active indefinitely.

The work discussed in this chapter is intended to be a survey of other transition metals in stabilized oxidation states. For this purpose, a series of perovskites were synthesized of the type ABO_3, where A = La and B = Rh, Cr, Fe or Co. The hydrogenation of carbon monoxide was catalyzed by these perovskites at 10 atm and 570 K. To examine the stability of

the transition metals, the oxidation state XP spectra were taken before and after each reaction and compared.

Section 4.2: Results and Discussion

The catalytic hydrogenation of carbon monoxide on a number of oxides of rhodium (Na_2RhO_3, $TiRhO_3$, $CuRh_2O_4$ and $FeRhO_3$) and perovskites of the type ABO_3 (A = La, B = Rh, Cr, Fe, Co) has been studied. The perovskites used in this study can be divided into three catagories as shown in Table 4.1. Specific properties of each compound are listed in Table 4.2.

Typical conditions for the reaction were CO + H_2 1:2, 6-10 atm, and 570-620 K. Reaction times were generally 2-4 h. Turnover frequencies were calculated assuming 1.6 X 10^{15} active atoms per sample. Samples were prepared by pressing ~ 0.01 g of oxide powder between 0.03 inch Au foil and 100 X 100 X 0.005 inch Au mesh at ~ 20,000 psi. A typical product accumulation curve for $LaRhO_3$ is shown in Fig. 4.1. Initial rates of formation of each product for each catalyst sample (CO + H_2 1:2, 10 atm, 570 K) are shown in Figs. 4.2,3. The major product from every reaction was found to be methane. Alcohols were not detected, although several attempts were made to push the equilibrium toward their formation (lower reaction temperatures, increased CO:H_2 ratios, higher total reaction pressure).

The oxide catalyst product distribution for FTS can be compared with the product distribution of Mo, Rh and Fe shown in Fig. 4.4. The oxide catalysts appear to enhance the formation of higher molecular weight products and also alkene formation relative to alkane formation.

The overall activity was found to increase as B, in ABO_3, was changed from Cr to Fe to Co. This activity change was accompanied by lower carbon levels after high pressure reactions over $LaFeO_3$ and $LaCoO_3$. Carbon monoxide dissociated more readily on the transition metals on the left-hand side of the series, so this result is expected. No oxy-

Table 4.1. A list of properties of the five perovskites used in this study.

Catagory	Examples	Properties
1	$LaFeO_3$ $LaCrO_3$	a) B is in most stable oxidation state Fe^{+3} d^5 octahedral symmetry Cr^{+3} d^3 b) isostructural (orthorhombic perovskites) c) crystallized at 1300 K for 48 h in air in Pt crucible d) stoichiometric
2	$LaMnO_3$ $LaCoO_3$	a) B is in unstable oxidation state Mn^{+3} d^4 high spin (Mn^{+4},Mn^{+2} stable) Co^{+3} d^5 50% high spin 50% low spin (Co^{+2} stable) b) isostructural (monoclinic distortion of perovskites) c) crystallizes at 1300 K for 48 h in air in Pt crucible d) non-stoichiometric
3	$LaRhO_3$	a) B is in unstable oxidation state Rh^{+3} d^6 b) monoclinic distorted perovskite c) crystallizes above 1400 K in air in Pt crucible d) non-stoichiometric Rh^{+4},Rh^0

Table 4.2. Properties of the perovskites[a].

Compound	Formula Weight(g/mol)	Volume (Å^3)	z	a'(Å)	Density g/cm^3	MP(°C)
$LaRhO_3$	289.8	61.16	1	3.940	7.866	
$LaCrO_3$	238.9	234.20	4	3.883	6.773	
$LaFeO_3$	242.8	243.09	4	3.932	6.631	1888
$LaCoO_3$	245.8	55.906	1	3.824	7.300	

[a]The densities of perovskite-type compounds were calculated from x-ray data using the equation in a computer program

$$D = \frac{\text{Molecular weight} \times \text{No. of molecules per unit cell}}{\text{Volume of unit cell} \times 6.023\text{X}10^{23}\ \text{molecules/mole}}$$

In the program, the equation for the volume of a triclinic cell was used

$$V = a\ b\ c\ \sqrt{(1 - \cos^2\alpha - \cos^2\beta - \cos^2\gamma + 2\cos\alpha\cos\beta\cos\gamma)}$$

and the appropriate parameters from x-ray crystallographic data[11] were introduced for each compound. The molecular weight was obtained by introducing the periodic table with atomic weights into the computer and then inserting the data deck with the appropriate atomic symbols and multipliers. The cube root of

$$\frac{\text{volume of the unit cell}}{\text{no. of molecules per unit cell}}$$

was also calculated to obtain a', the unit cell edge of a cubic cell which represents the same volume allowed in the true unit cell for a molecule of a perovskite-type compound. This permits a comparison to be made between the ionic radii of the ions in these compounds even when they are indexed on cells with different symmetry.

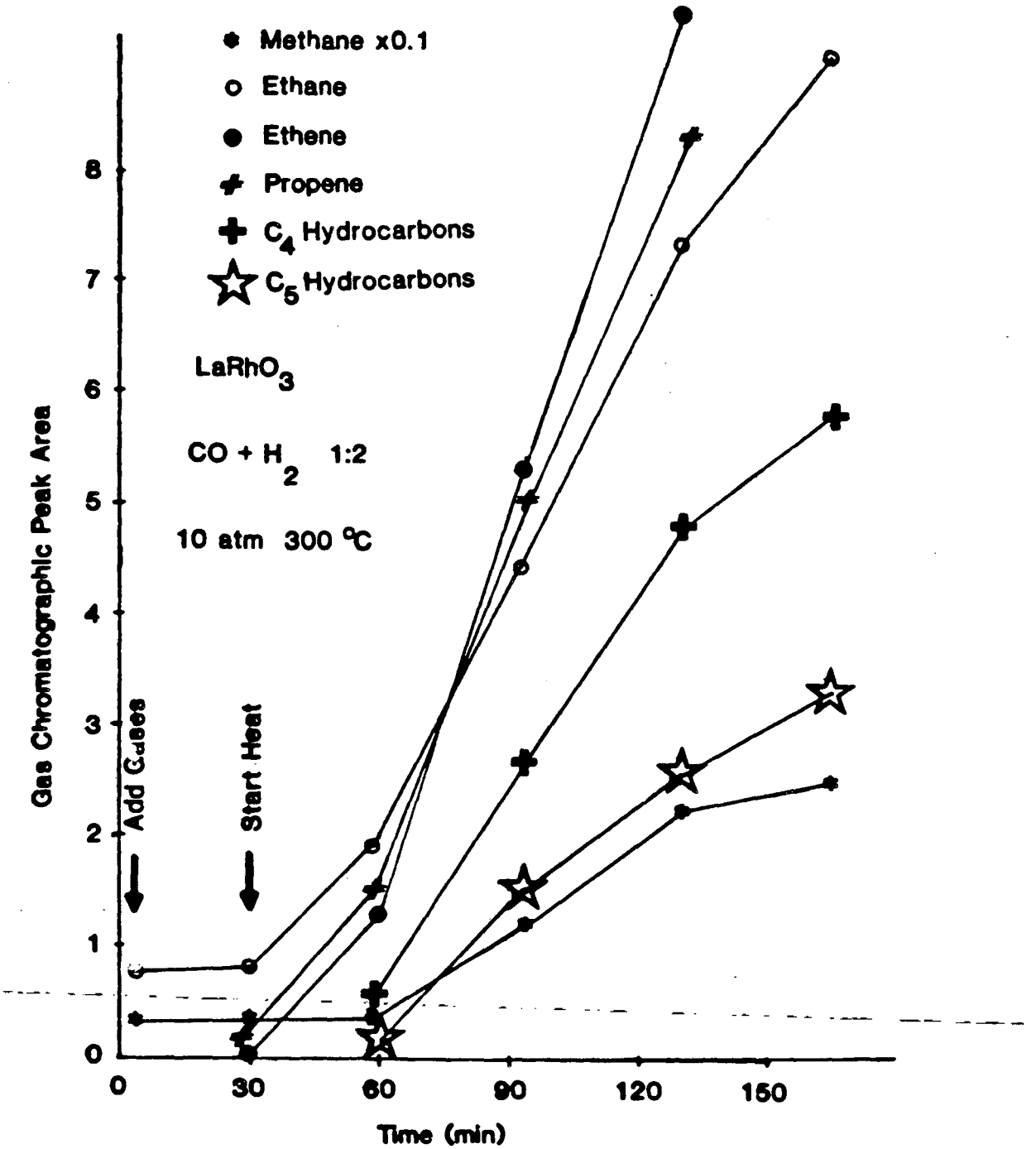

Fig. 4.1. Product accumulation versus reaction time curves in the closed-loop, batch reactor. The plot shows the major products from CO + H_2 (1:2), 10 atm total pressure and a $LaRhO_3$ catalyst temperature of 570 K.

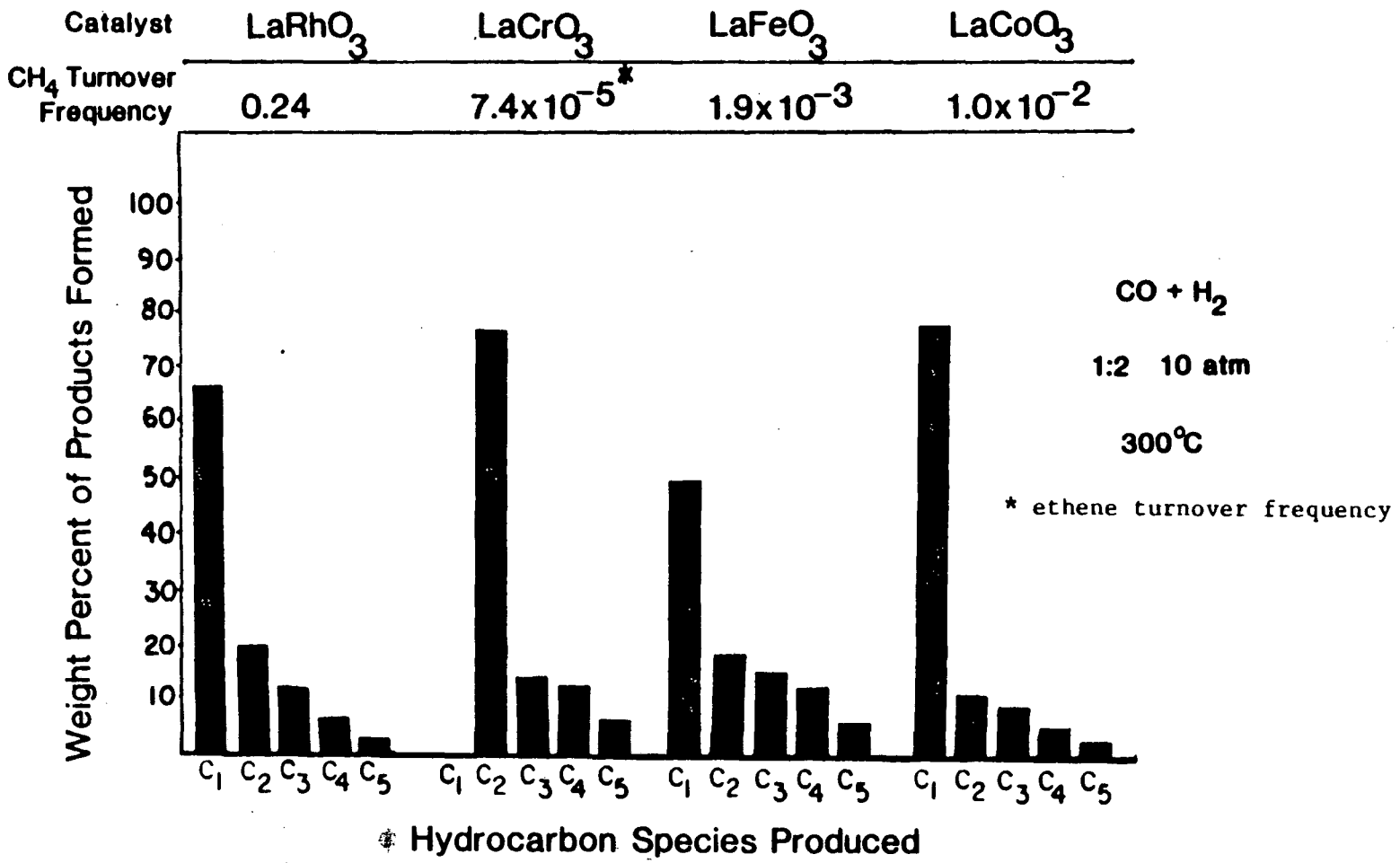

Fig. 4.2. Product distributions from CO hydrogenation over five perovskite catalysts (CO + H_2 1:2, 10 atm, 570 K).

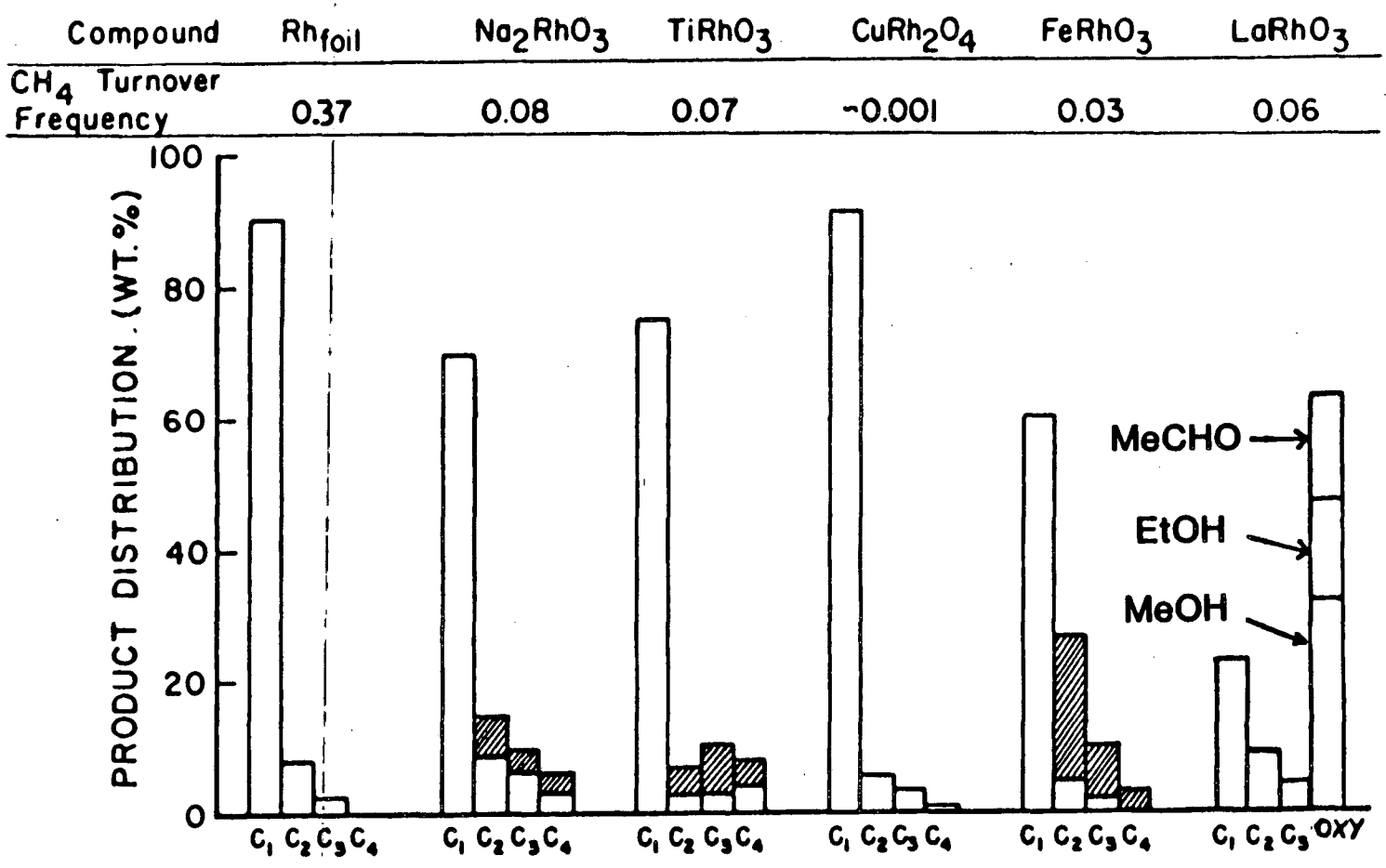

Fig. 4.3. Product distributions from CO hydrogenation over six Rh-containing catalysts (CO + H_2 1:2, 6 atm, 570 K). The $LaRhO_3$ product distribution is from Watson et al.[10]

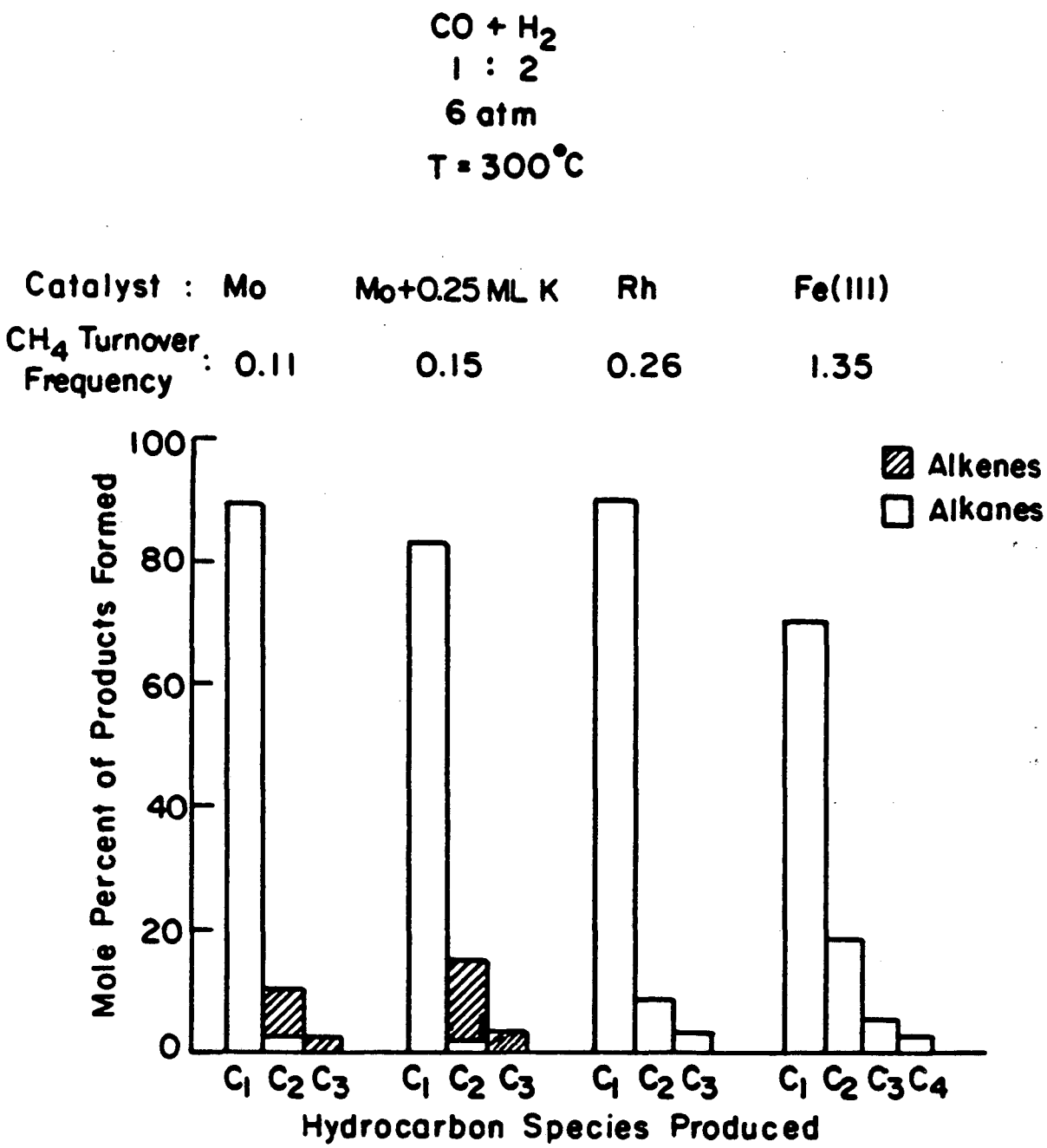

Fig. 4.4. The product distribution from FTS over metal and promoted metal catalysts. The methane turnover frequency is much higher for iron, the classical FT catalyst.

genated products from any of the reactions over any of the oxide catalysts studied were found. This result is contradictory to the results of Watson, et al.[10], who found up to 80% weight percent of the products from FTS over $LaRhO_3$. Further studies need to be undertaken to clarify this discrepancy.

To study the stability of the perovskite lattice in the reducing environment of the hydrogenation reaction, XP spectra were taken before and after each reaction. The spectra revealed that all perovskite catalyst samples appeared to reduce partially during the reaction (see Table 4.3). A typical wide scan, revealing the composition of the near surface region of $LaCoO_3$, is shown in Fig. 4.5. The Co $2p_{3/2}$ peaks are shown expanded at better resolution in a separate spectrum in Fig. 4.6. After reaction, the spectrum is shifted toward the lower binding energies by ~ 0.8 eV.

These initial results on the hydrogenation of CO over both perovskite samples and rhodium-containing mixed oxide catlysts showed that product distributions and activity can be altered significantly by changing either the oxidation state of the active metal center or the metal center itself. Future work on this system needs to be done to study in detail the relationship between oxidation state, transition metal catalyst, activity and product distribution.

Table 4.3. X-ray photoelectron spectroscopic results for perovskites (experimental values), metals, and ions (literature values).

Compound	Major XPS Peak Position (Binding energy in eV) Before Reaction	After Reaction
$LaRhO_3$	311.0	308.0
$LaCrO_3$	576.5	575.0
$LaFeO_3$	709.5	707.0
$LaCoO_3$	779.5	778.8

Metal/Ion[12]	Major XPS Peak Position (Binding Energy in eV)
Rh	307.1
Cr	574.0
Fe	706.8
Co	777.9
Rh^{+3}	309-311
Cr^{+3}	576-580
Fe^{+3}	709-712
Co^{+3}	779-782

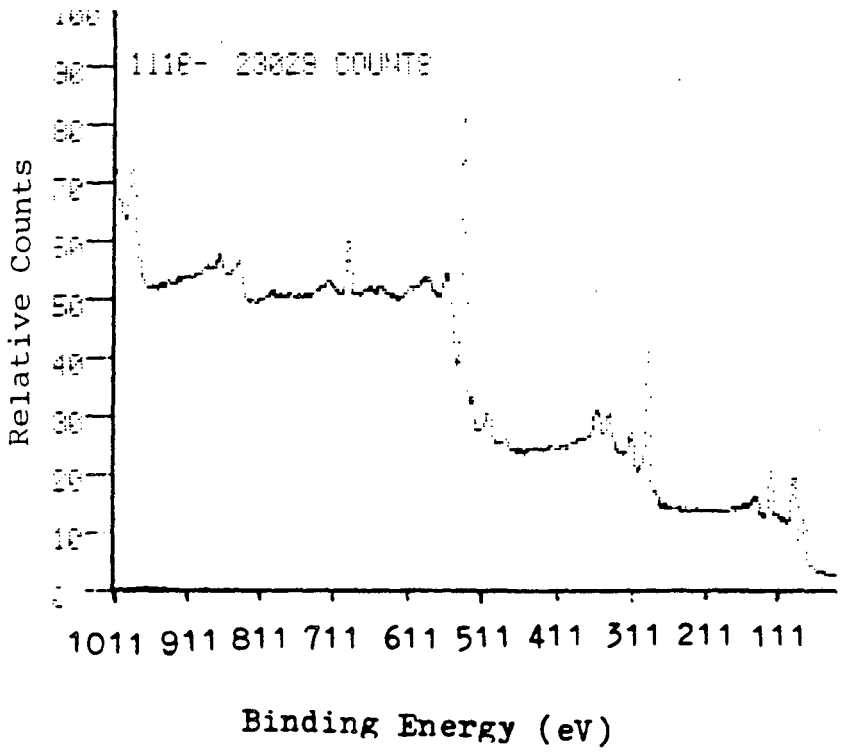

Fig. 4.5. A wide scan XP spectrum of $LaCoO_3$. The spectrum contains XP and AES peaks associated with Au, La, Co, O and C.

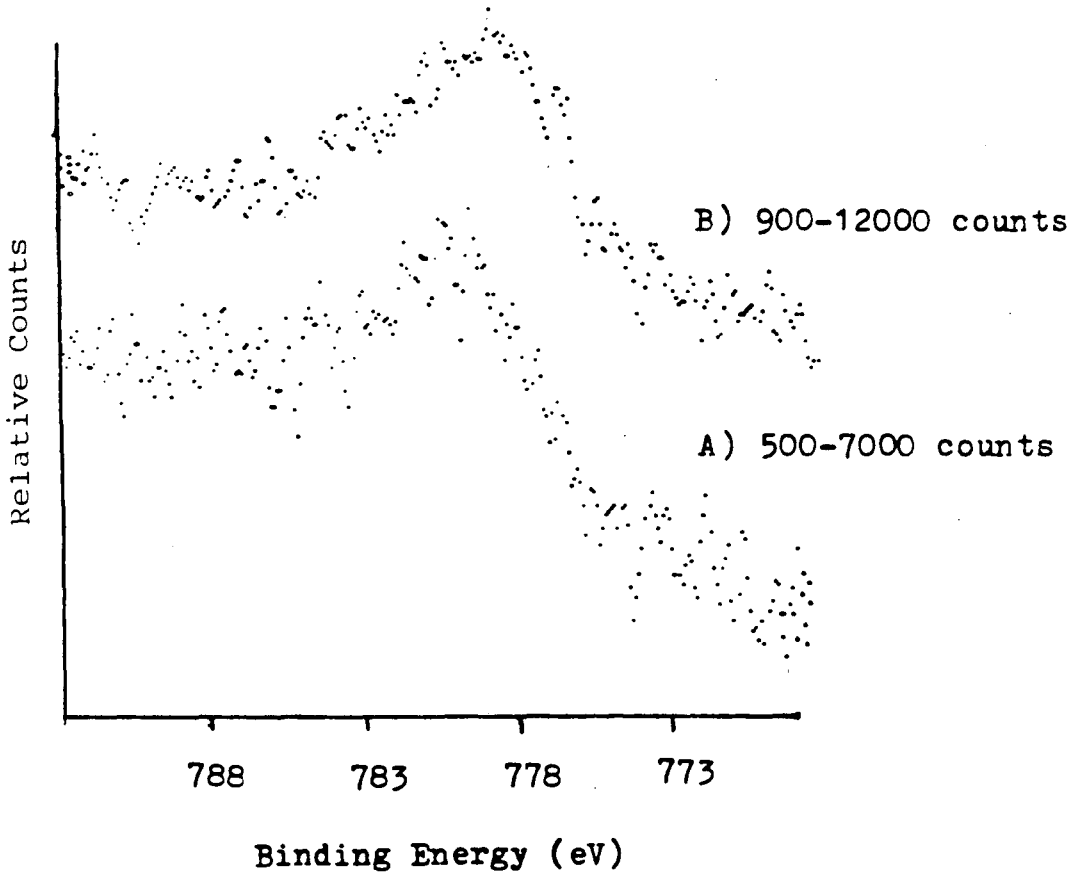

Fig. 4.6. The CO $2p_{3/2}$ photoelectron spectrum from (A) fresh $LaCoO_3$ and (B) after a high pressure reaction (CO + H_2 1:2, 10 atm, 570 K, 2 h). During the reaction, the surface reduces partially, as is indicated by the shift in binding energy from 779.5 to 778.8 eV.

Section 4.3: References

1. Ichikawa, M., Bull. Chem. Soc. Japan 51, 2268, 2273 (1978).

2. Ichikawa, M., J. Catal. 56, 127 (1979).

3. Ellgen, P.C., Bartley, W.J., Bhasin, M.M., and Wilson, T.P., Advan. Chem. Ser. 178, 147 (1979).

4. Bhasin, M.M., Bartley, W.J., Ellgen, P.C., and Wilson, T.P., J. Catal. 54, 120 (1978).

5. Wunder, F., Arpe, H.J., Leupold, E.I., and Schmidt, H.J., U.S. Patent 4,224,236 (Hoescht AC).

6. Vannice, M.A., J. Catal. 37, 449 (1975).

7. Sexton, B.A., and Somorjai, G.A., J. Catal. 46, 167 (1977).

8. Castner, D.G., Blackadar, R.L., and Somorjai, G.A., J. Catal. 66, 257 (1980).

9. Watson, P.R., and Somorjai, G.A., J. Catal. 72, 347 (1982).

10. Watson, P.R., and Somorjai, G.A., J. Catal. 74, 282 (1982).

11. Galasso, F.S., "Structure, Properties and Preparation of Perovskite-Type Compounds." Pergamon Press, Oxford, 1969.

12. Wagner, C.D., Riggs, W.M., Davis, L.E., Moulder, J.F., and Muelenberg, G.E., "Handbook of X-ray Photoelectron Spectroscopy." Perkin-Elmer Corporation, Minnesota, 1978.

CHAPTER FIVE: HYDROGENATION OF CARBON MONOXIDE ON Mo(100) SINGLE CRYSTALS AND POLYCRYSTALLINE FOILS

Section 5.1: Introduction

Many transition metals have been investigated as catalysts for the hydrogenation of CO, but, until recently, very little work had been carried out using Mo[1-4]. The research studies that have been performed, however, already point to several interesting and unique characteristics of Mo catalysts. Workers at the U.S. Bureau of Mines reported[1] that molybdenum catalysts had high activity for methane production although not as high as Fe, Ni, Co and Ru. Saito and Anderson [2,3] extended these studies and reported that Mo metal lost activity rapidly but produced about the same product distribution as iron. Most recently, Hou and Wise[4] have studied the kinetics of methane formation on MoS_2. They found a very low activation energy for the formation of methane (~ 7.4 kcal/mol) and the dependence of the rate on reactant gas pressures to be

$$r_{CH_4} = kP_{CO}^{+1}P_{H_2}^{+0.5}.$$

This pressure dependence is unusual since the rate of CO hydrogenation is usually of negative order with respect to CO pressure. The purpose of this study is to explore the catalytic activity of Mo for the CO/H_2 reaction. By using small-area (~ 1 cm^2) single crystals of (100) orientation and polycrystalline foils, we were able to determine the structure sensitivity of the reaction. Our low-pressure/high pressure apparatus permits surface analysis by Auger electron spectroscopy before and after the experiments. By adding potassium or sulfur in submonolayer quantities to the surface, we were able to study the influence of these products and thus, the product distribution.

The reaction produced mostly methane, ethane and propene. We found

positive pressure dependencies of the reaction rate on CO and H_2:

$$r_{CH_4} = kP_{CO}^{+.32}P_{H_2}^{+1.0}.$$

This points to a reaction mechanism that is different from that found for CO hydrogenation on many other transition metals (Ni, Fe, Ru). The reaction proved to be structure-insensitive under our conditions (pressure range 1-10 atm, temperature range 520-670 K). Both K and S, when added in submonolayer quantities, increased the olefin-to-paraffin ratio.

Section 5.2: Results

The catalytic hydrogenation of carbon monoxide has been investigated on Mo(100) single crystals and polycrystalline Mo foils. Typical initial turnover frequencies for methane production were 0.11 at 300°C, CO/H_2=0.33, and 4700 Torr total pressure and 0.011 at 275°C, CO/H_2=0.02, and 1320 Torr total pressure. We have defined turnover frequencies (product molecules/atom x second) using the surface atomic density of Mo(100) (1.0×10^{15} Mo atoms/cm^2). No correction has been made for the fact that Mo polycrystalline foil is not composed entirely of the (100) face. Using this definition, we observed no differences in either rates or product distributions between single crystal or polycrystalline surfaces. Thus, the reaction does not appear to be structure-sensitive. A characteristic product accumulation curve is shown in Fig. 5.1. The duration of the reaction varied from 30 min to 24 h but generally reactions were stopped after 4 h. Typical product distributions for the hydrogenation of CO are shown in Fig. 5.2. An interesting characteristic of the CO hydrogenation reaction on Mo is its high selectivity toward olefinic products under our low conversion ($\lesssim$ 1%) conditions. At a CO/H_2 ratio of 1/2, the rate of formation of ethene is four to six times greater than that of ethane. Of the products containing three carbon atoms, propene is observed almost exclusively.

The activation energy for the methanation reaction was determined by varying the temperature while holding the total pressure and reactant gas composition constant. On Mo it was found to be 24 ± 1 kcal/mol (Fig. 5.3). similar to that found on Ni, Rh, Ru and Fe[6-9]. Similarly, the activation energy for ethane production was found to be 23 ± 1 kcal/mol (Fig. 5.4). The dependence of the methanation rate on the pressures of the reactant

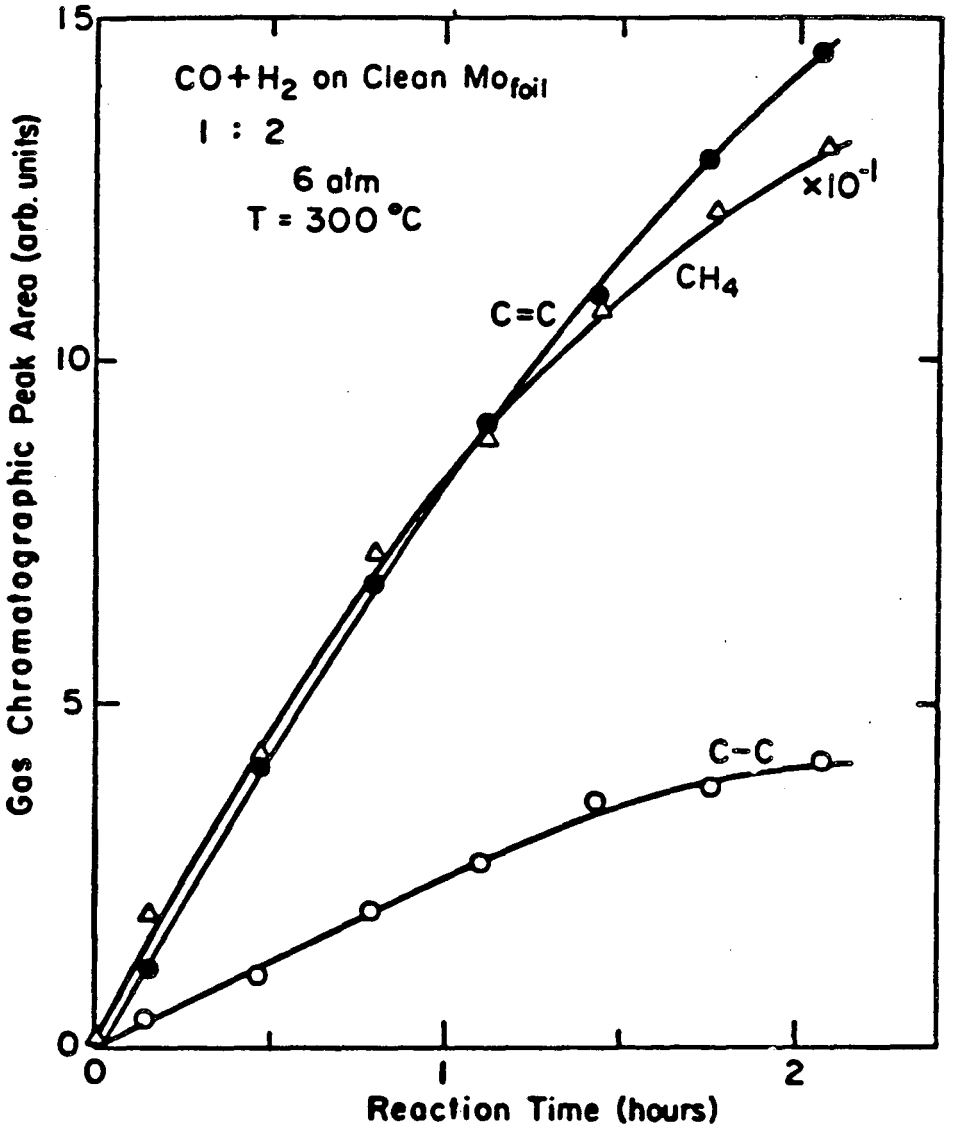

Fig. 5.1. Product accumulation vs. reaction time curves in closed-loop, batch reactor. The plot shows major products from CO + H_2 (1:1) at 6 atm total pressure and a clean Mo_{foil} catalyst temperature of 300°C.

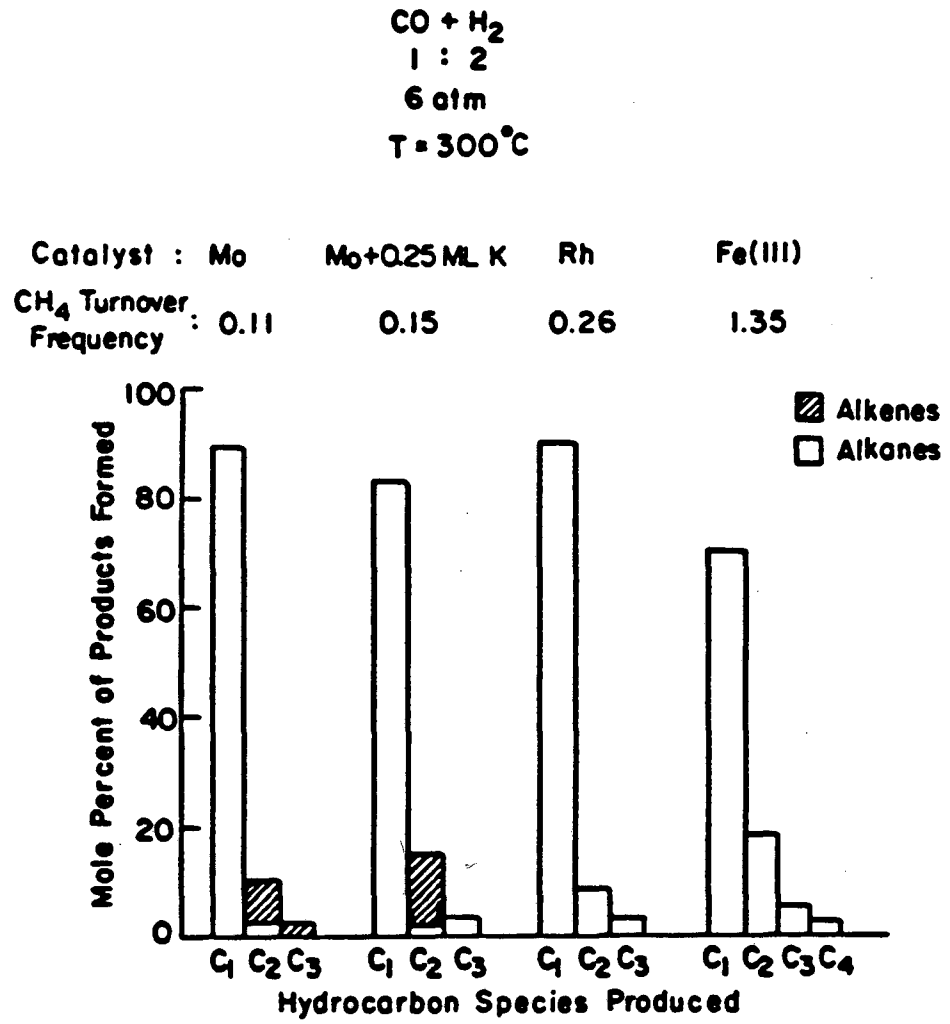

Fig. 5.2. Product distributions from CO hydrogenation over four different catalysts. The distributions for Rh and Fe(111) are taken from Refs. 6 and 8, respectively.

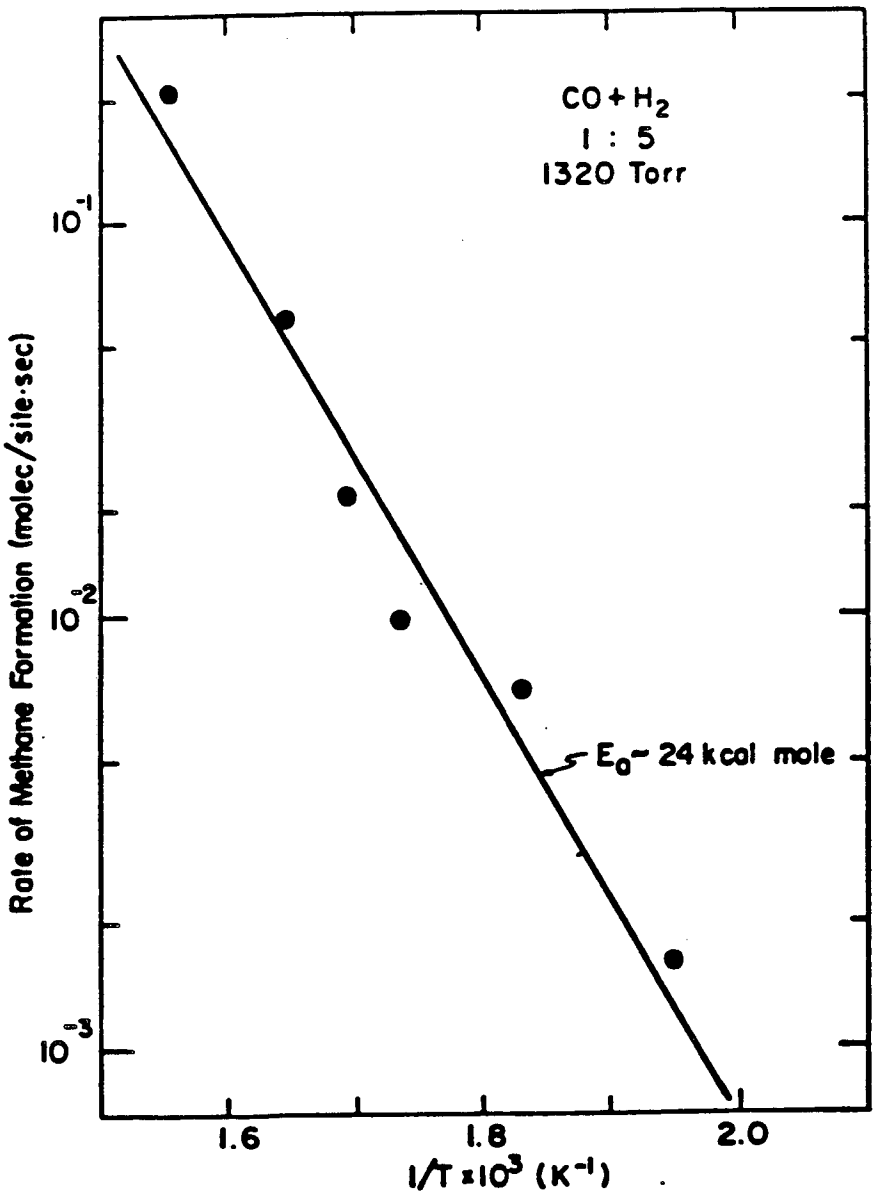

Fig. 5.3. Arrhenius plot for the initial rate of formation of methane vs. inverse temperature (CO + H_2, 1:2, 6 atm). The plot gives 24 kcal/mol as the activation energy for methane production over Mo(100) single-crystal catalysts.

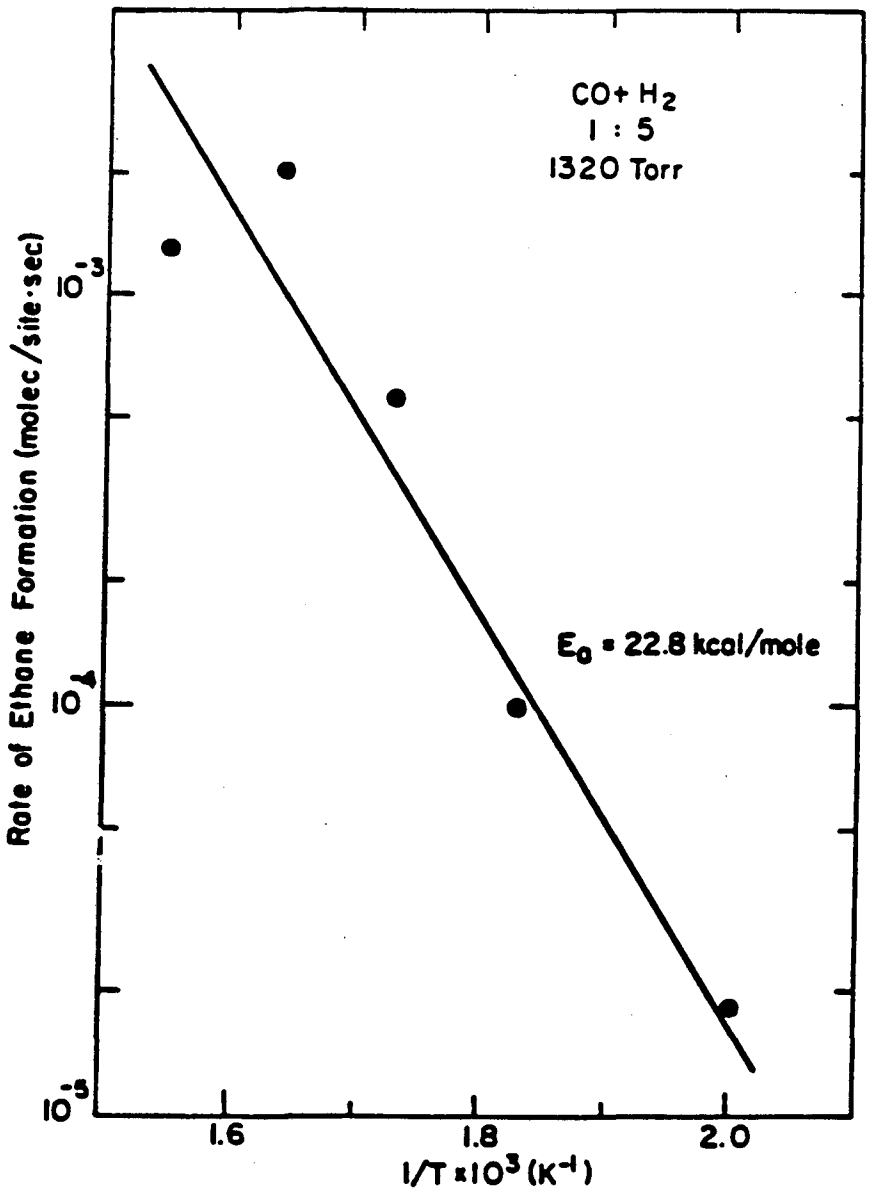

Fig. 5.4. Arrhenius plot for the initial rate of formation of ethane vs. inverse temperature over Mo(100) single-crystal catalysts.

gases was determined by varying the partial pressure of each reactant gas while maintaining a constant total pressure and temperature, using nitrogen or argon as a buffer gas. The observed rate law for methanation (see Fig. 5.5) is given by

$$r_{CH_4} = kP_{CO}^{+0.32}P_{H_2}^{+1.0}.$$

In an attempt to produce longer-chain ($\geq C_3$) hydrocarbons via secondary reactions, ethene was added to the reactant gas mixture. The primary result of this addition was the hydrogenation of ethene to ethane, while no production of longer-chain hydrocarbons was observed. Thus, it appears that the propene produced is not the result of ethene reacting with CH_x fragments on the surface.

Deactivation of the surface was observed when the catalysts were pre-treated by dosing with cyclohexene at 870 K, forming graphitic carbon on the surface. When the surface was completely covered by graphitic carbon, as determined by the lineshape of the C_{1s} peak of the Auger electron spectrum (see Fig. 5.6), the rate of methane formation was less than 3% that of the clean metal catalyst under identical conditions (CO + H_2, 1:2, 6 atm, 520 K). In other experiments, reactions were stopped before deactivation of the catalyst surface took place and in these cases sub-monolayer amounts of carbidic carbon were detected by AES on the surface (see Fig. 5.6b). Auger electron spectra taken after the surface was deactivated during the hydrogenation reaction were also studied. In these cases the lineshape of the C_{1s} peak signifies graphitic carbon on the surface (see Fig. 5.6c). These studies indicate that the "active" surface is covered by a carbidic carbon species and the reaction is poisoned as the carbidic species is converted to graphitic carbon on the

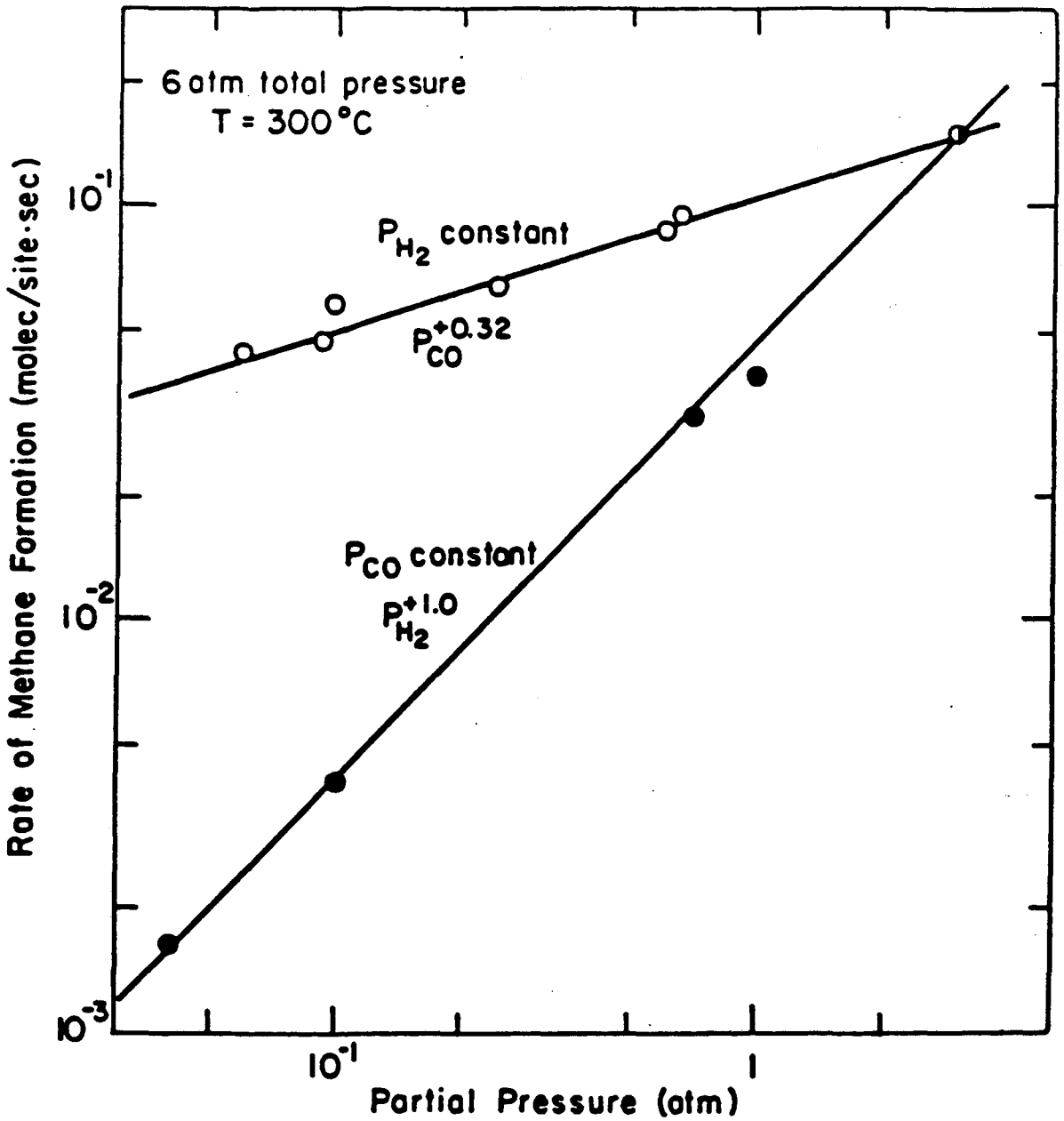

Fig. 5.5. Rate of formation of ethane vs. the partial pressure of each reactant at a constant total pressure (constant H_2 pressure of 3 atm for determination of CO dependence and constant CO pressure of 3 atm for determination of H_2 pressure dependence). The resulting rate expression has the form

$$r_{CH4} = KP_{CO}^{+0.32}P_{H2}^{+1.0}.$$

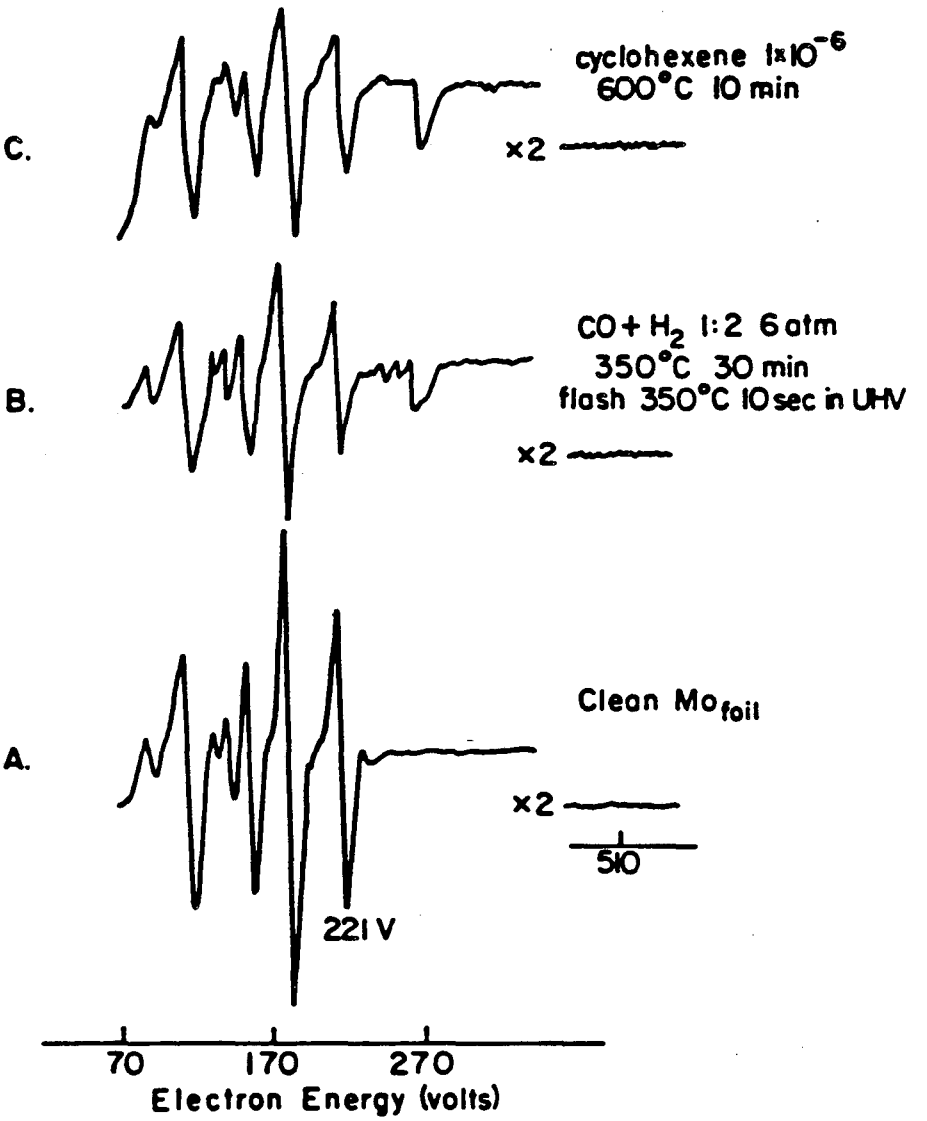

Fig. 5.6. Auger electron spectra of Mo_{foil} showing the difference between carbidic and graphitic carbon on the surface. (A) AES of clean Mo_{foil} after argon ion sputtering, oxygen treating (5×10^{-7} Torr O_2, 1000°C), annealing at 1600°C for 3 min. (B) AES of Mo_{foil} after running the hydrogenation of CO (CO + H_2, 1:2, 6 atm, 350°C) for 30 min, showing the formation of carbidic carbon on the surface. (C) AES of Mo_{foil} after forming a graphitic overlayer on the surface with cyclohexene. Similar spectra were obtained after the catalyst was poisoned during a reaction.

surface. The rate of poisoning is determined by the ratio of CO to H_2 in the reaction mixture and by reaction temperature (lower $CO:H_2$ ratios and lower temperatures prolong the active catalysts lifetime).

Studies were also performed to determine the effect of alkali doping on the catalytic activity and selectivity. Figure 5.7 shows the reaction rate as a function of potassium coverage, for $CO/H_2=1/2$ at a total pressure of 6 atm and a temperature of 570 K. For low coverages of potassium ($\Theta_K \sim 0.15$ ML) an overall rate enhancement was observed on Mo_{foil} samples samples. In addition, the product distribution shifted toward olefinic products. We see a four-fold increase in the rate of formation of ethene while the rate of formation of methane and ethane remain virtually unchanged. At higher potassium coverages, the total activity declines, signifing that the active sites for the reaction were partially blocked by over ~ 0.25 ML of K.

During the course of some of the reactions the surface was inadvertently contaminated by up to 0.5 ML of sulfur, as detected by AES after the reaction. In these circumstances it was noted that for a sulfur coverage of ~ 0.25 ML the rate of methane formation was attenuated by a factor of ~ 5, while the alkene production rate remained essentially unchanged relative to those rates observed on the clean Mo surface (see Fig. 5.8).

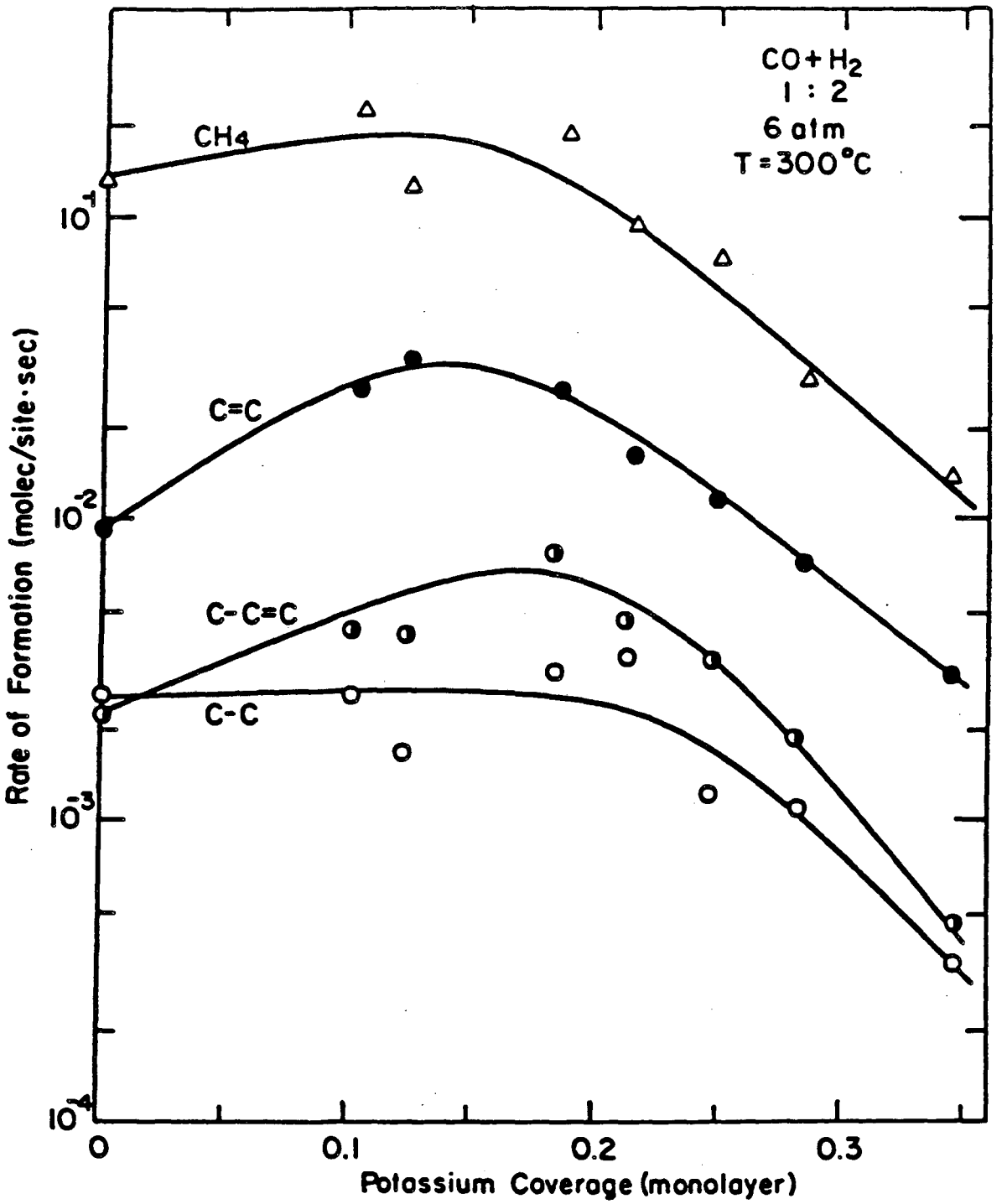

Fig. 5.7. A plot of the rates of product formation vs. potassium coverage showing the increase in the rate of alkene formation relative to the rate of alkane formation. This is due to an increase in the amount of dissociated CO on the surface as K is added to the surface (see Discussion).

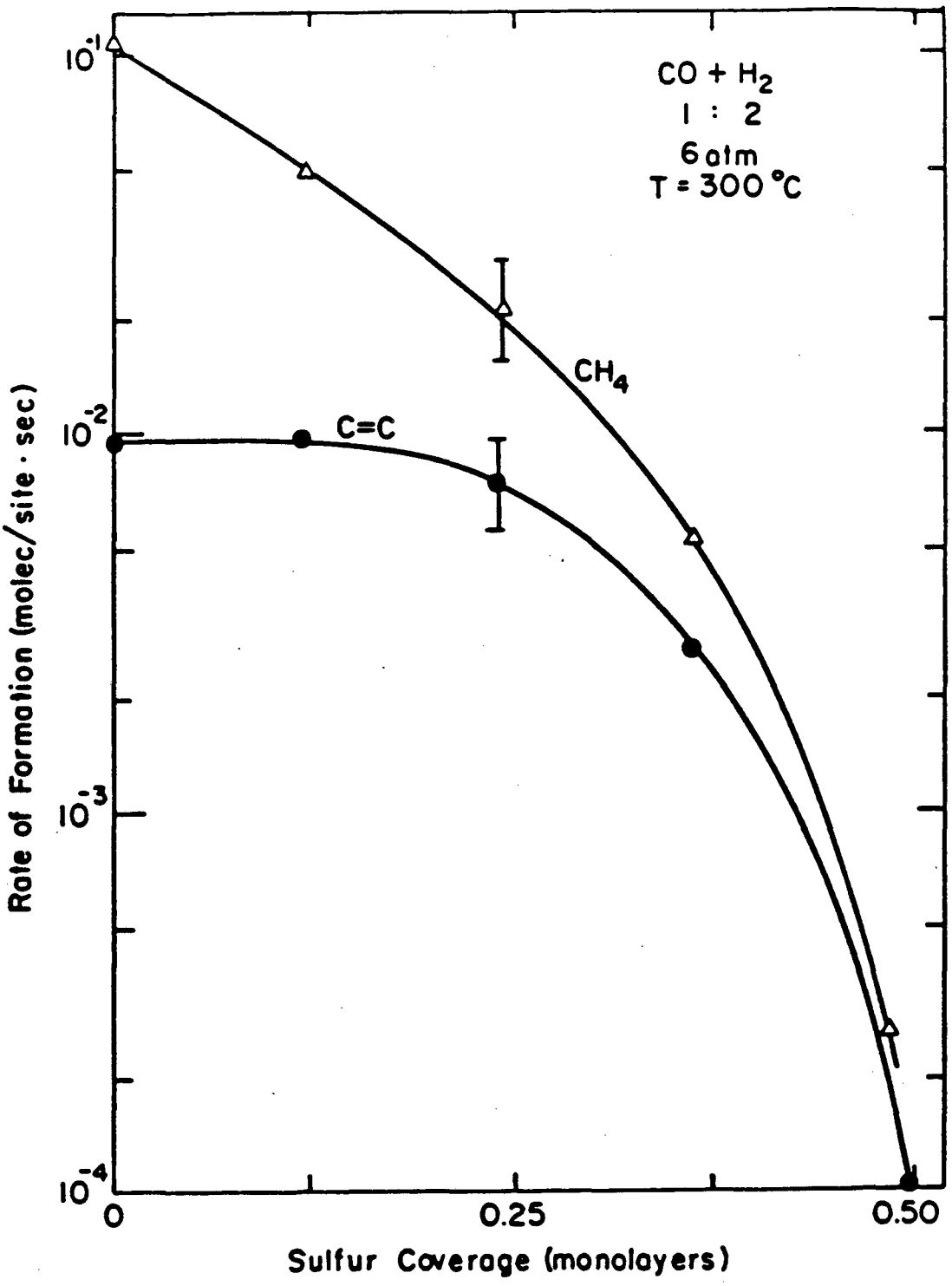

Fig. 5.8. Rates of product formation vs. sulfur coverage on Mo_{foils}, showing an enhancement in the rate of production of alkenes relative to the rate of production of alkanes. This is due to a decrease in the rate of hydrogenation as S is added to the surface (see Discussion).

Section 5.3: Discussion

Under our conditions for CO hydrogenation, Mo(100) crystals and Mo polycrystalline foil produced primarily methane, ethene, and propene. This is unusual when compared to the product distribution over other transition metals that produce solely methane (Ni) or a distribution of higher molecular weight paraffin products (Fe, Ru, Co) that form by a chain-growth mechanism[7-11]. Only Rh metal foils produce C_1-C_3 hydrocarbons exclusively under these experimental conditions.

The selectivity of the reaction on Mo showed a high proportion of olefinic products. This indicates that Mo is a poor hydrogenation catalyst. The hydrogenation of carbon monoxide on Mo produces less than 1% of hydrocarbons with more than three carbon atoms. This, and the high alkene-to-alkane ratio, leads us to conclude that the rates of carbon-carbon and carbon-hydrogen bond formation reactions are slow relative to the desorption rates of small hydrocarbons on Mo.

The positive power of rate dependence on the pressure of CO is unusual since the methanation rate has a negative-order dependence on CO partial pressure over Ni, Fe, Ru and Co[7,8]. Thus, on Mo the adsorption of CO does not inhibit the hydrogenation rate as it does on other transition metals. One explanation for the observed positive-order pressure dependence for CO is that the high carbon levels observed under typical reaction conditions strongly weaken the bonding of CO to the surface, so that the rate-limiting step of the reaction is the formation of "active", or carbidic carbon by CO dissociation. With this model an increase in the CO partial pressure results in an increase in the surface coverage of active carbon and thus to an increase in the concentration of the reaction-limiting species. The reaction proceeds through the same intermediate as

is assumed for other Fischer-Tropsch catalysts and therefore the activation energy is similar. This mechanism could be verified perhaps by the absence of a deuterium isotope effect. Another explanation for this observation can be made by proposing a mechanism similar to that suggested by Sinfelt[12] and later modified by Vannice[13]. In terms of this model the rate-determining step is the final hydrogenation of the $CO-H_2$ surface complex to rupture the C-O bond and all steps preceeding it are in quasi-equilibrium. The following set of elementary steps was proposed.

$$CO \overset{K_1}{\rightleftharpoons} CO_{(ad)} \qquad \text{I}$$

$$H_2 \overset{K_2}{\rightleftharpoons} H_{2(ad)} \qquad \text{II}$$

$$CO_{(ad)} + H_{2(ad)} \overset{K_3}{\rightleftharpoons} CHOH_{(ad)} \qquad \text{III}$$

$$CHOH_{(ad)} + y/2\ H_{2(ad)} \overset{K_4}{\rightleftharpoons} CH_{y(ad)} + H_2O \qquad \text{IV}$$

$$CH_{y(ad)} + H_2 \overset{\text{fast}}{\rightleftharpoons} CH_4 \qquad \text{V}$$

If the surface is covered predominantly by a strongly adsorbed CH_xOH species, whose surface coverage can be approximated by

$$\Theta_{CHOH} = \frac{KP_{CO}P_{H2}}{1 + KP_{CO}P_{H_2}} \sim (KP_{CO}P_{H_2})^N.$$

The sites remaining for hydrogen adsorption will be

$$1 - \Theta_C = \Theta \sim (KP_{CO}P_{H_2})^{-1}$$

and the fraction of the total surface covered by hydrogen will be

$$\Theta_{H_2} = \frac{\Theta K_{H2}P_{H2}}{1 + K_{H_2}P_{H_2}} \sim \Theta K_{H_2}P_{H_2}$$

Then for the case where hydrogen is weakly adsorbed, $K_{H_2} \ll 1$ and the rate of methanation is

$$r_{CH_4} = K \Theta_C \Theta_{H_2}{}^{v/2}$$

and upon substituting for the values of Θ_C and Θ_{H2} we obtain an equation of the form

$$r_{CH_4} = KP_{CO}^{N-y/2}P_{H_2}^{N}.$$

Then for our case, N=1 and y=1 would lead to a rate expression of the form

$$r_{CH_4} = KP_{CO}^{+0.5}P_{H_2}^{+1.0}.$$

It should be remembered that this mechanism for CO hydrogenation was first proposed in detail by Storch in 1948[14] and later extended by Kummer and Emmett in 1953[15].

It should be noted, however, that in spite of the different reaction mechanism that is proposed here, based on the unusual CO partial pressure dependence of the rate, the activation energy for methane formation is 24 kcal/mol, very similar to that found on other transition metals. In fact, the similar activation energy for ethane formation indicates that this hydrocarbon is formed by a mechanism similar to that for methane.

The production of ethene or propene can occur by the carbonylation of CH_x or C_2H_x fragments and their subsequent hydrogenation and dehydration by reaction steps similar to those proposed for methane formation. It should be noted that carbonylation is usually the chain-terminating step in CO hydrogenation as was added to the reaction mixture in the hope that propene or other higher molecular weight hydrocarbons would be produced. However, we found the ethene was either hydrogenated to ethane or did not react. This observation leads us to conclude that carbonylation is either a slow process or does not occur under our reaction conditions.

The hydrogenation of carbon monoxide uver Mo surfaces is structure-insensitive under our reaction conditions. This is indicated by the fact that rates and selectivities over foils and single crystal surfaces are similar. The structure-insensitivity of most Fischer-Tropsch catalysts

has been used to support the model that the reaction takes place on top of a carbidic overlayer on Fe, Ru and Co.

Our studies on carbon coverage and its relation to a catalyst deactivation revealed that the reaction probably takes place on top of a carbidic overlayer. This overlayer will deactivate by forming graphite on the surface and blocking the reaction sites (see Fig. 5.9). We found that with higher temperatures or higher partial pressures of carbon monoxide the rate of this deactivation process increased.

In an attempt to study the catalytic activity of molybdenum oxide we produced a surface layer of MoO_2 using the procedure described by Zhang et al.[5] Reactions performed over these surfaces exhibited the same rates and product distributions as those on clean surfaces. Auger spectra taken after the reaction indicate that the surface was reduced rapidly during the hydrogenation (see Fig. 5.10), suggesting that again the observed reaction takes place on a carbidic overlayer on the metallic surface.

Alkali doping of many metal surfaces facilitates carbon monoxide dissociation into carbon and oxygen[16,17]. It has been proposed that this is caused by lowering the dipole component of the work function at the surface thereby increasing back-donation of metal electrons into the CO 2 π^* antibonding orbital[16] (see Fig. 5.11). At reaction temperatures this accelerates the dissociation of CO, leading to higher coverages of carbon and oxygen on the surface. Assuming that hydrogenation is the rate-limiting step in the production of saturated hydrocarbons, K doping of the surface will increase the relative rate of production of unsaturated hydrocarbons[18,19], as we have observed. Our observation of the K promotion effects differs from the work of Bridgewater et al.[20] on supported Mo catalysts. Under reaction conditions similar to ours, Bridgewater

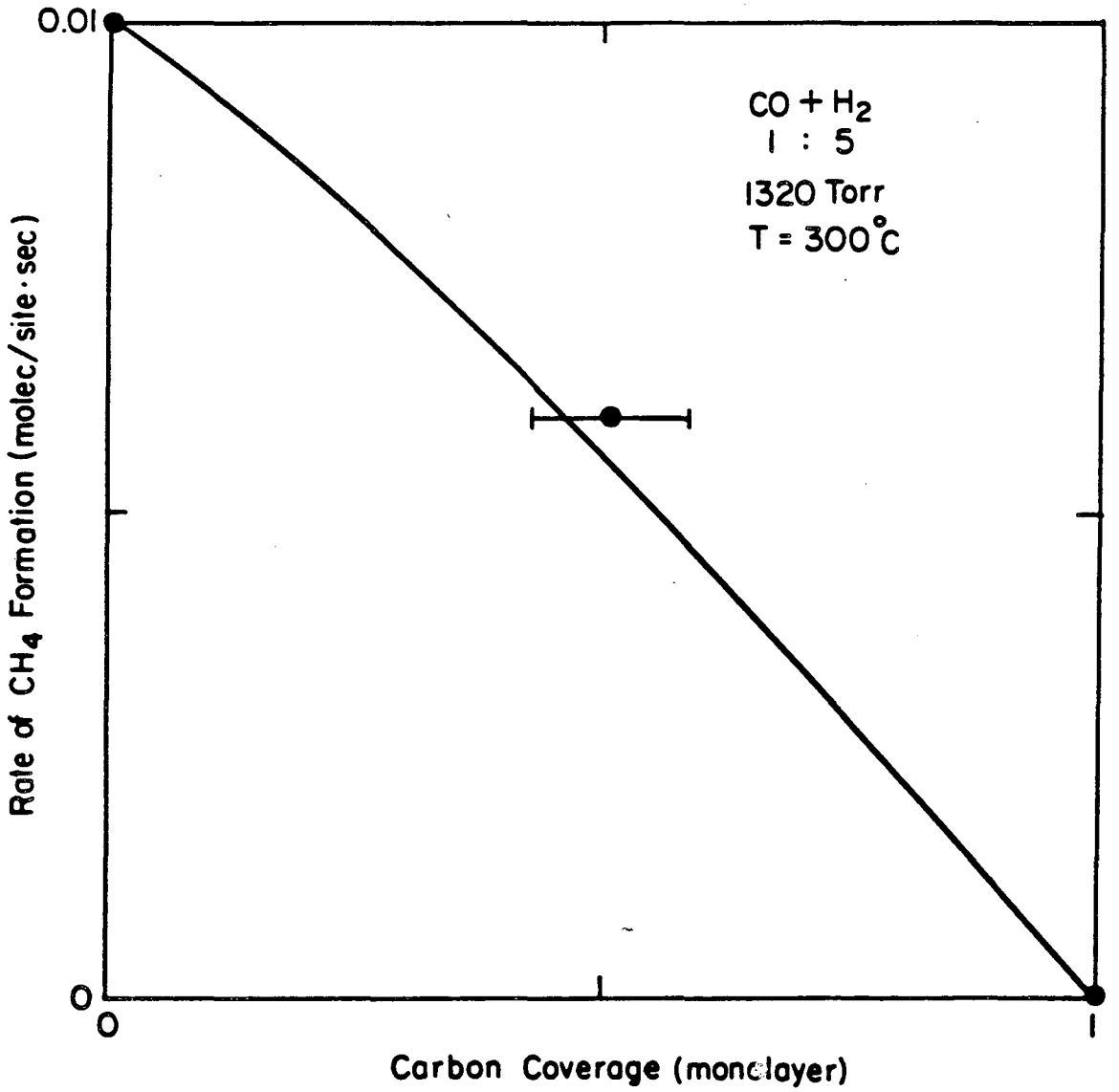

Fig 5.9. The rate of methane formation is plotted versus the carbon coverage, as determined by AES. The rate is observed to decrease linearly with increasing carbon coverage.

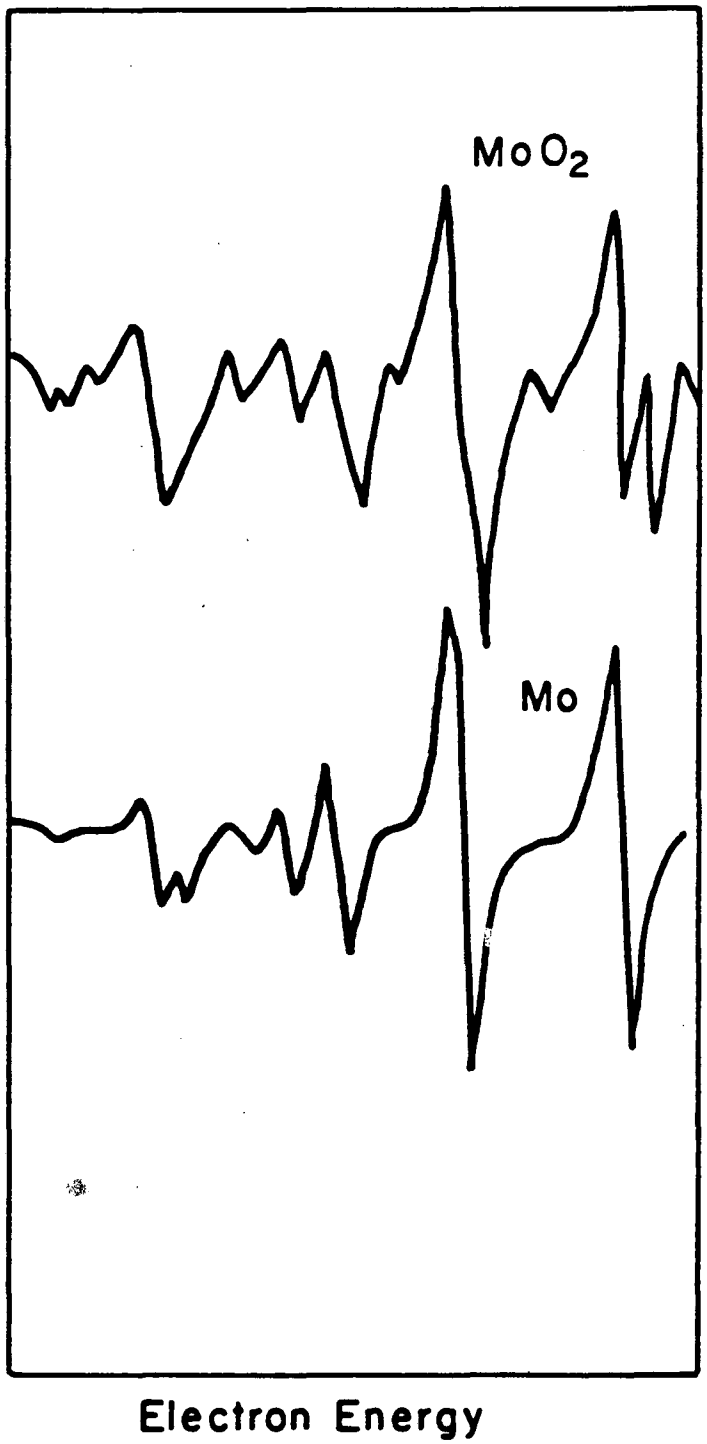

Fig. 5.10. The AES of Mo/O_2 ($Mo + O_2$, $5X10^{-7}$, 1150 K, 10 min), top, and Mo after a CO/H_2 reaction are shown. The oxide is observed to be reduced immediately during the high pressure reaction.

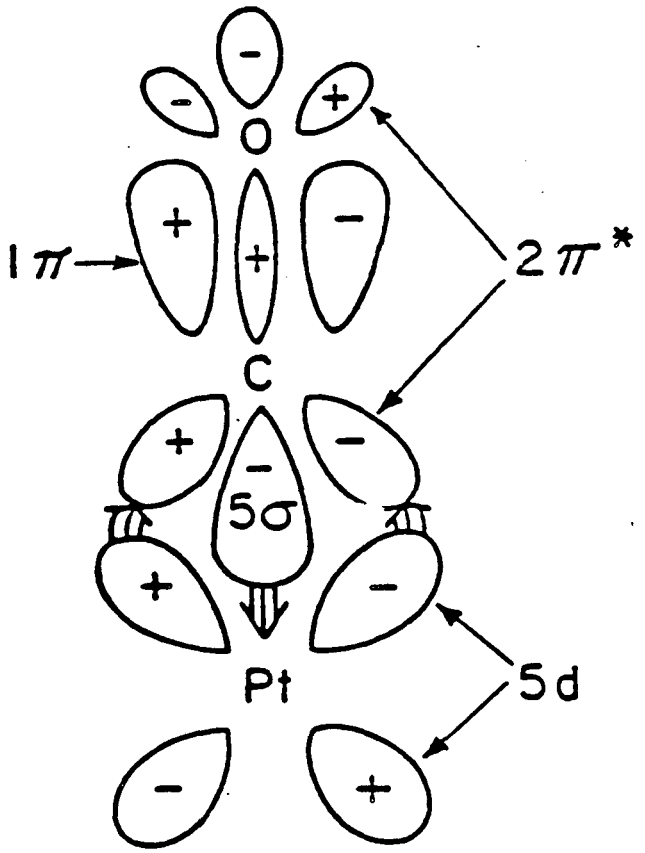

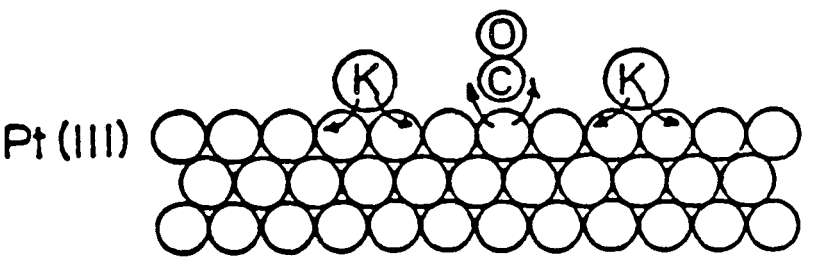

Fig. 5.11. The electron donating effect of K on metal surfaces is shown. In this example, with K on the surface, the electron donating capability of the 5d orbitals of Pt are shown to be enhanced, helping to dissociate CO.

found that doping of Mo catalysts with K to 17 atomic percent results in a 20-fold reduction in activity. It is possible that this discrepancy is caused by the segregation of K to the surface of the supported catalyst. This might be expected given the relative surface free energies of K_s (397 dyn/cm)[16] and Mo_s (1900 dyn/cm)[21]. A second explanation is that K is oxidized on the surface leading to altered catalytic properties. Since Bridgewater gave data for one particle size and did not use a surface-sensitive spectroscopic technique such as AES, it is not possible to determine the surface concentration of K on his catalyst.

The addition of S to the surface increases the olefin-to-paraffin ratio. We can rationalize our observation in terms of a selective blocking of H_2 adsorption sites. The work of Clarke[22] has shown that CO adsorption on the Mo(100) surface is blocked completely at sulfur coverages of 0.5 ML (see Fig. 5.12). Other work in this laboratory shows that H_2 adsorption is effectively blocked by ordered S overlayers at coverages as low as 0.25 ML[23,24]. If sulfur preferentially inhibits H_2 adsorption then its presence on the Mo surface will result in a decreased hydrogen-to-carbon ratio on the surface. Although there will be an overall decrease in reaction rate, the olefinto-paraffin ratio should increase, as observed.

EFFECT OF SULFUR OVERLAYERS ON DEUTERIUM AND CARBON MONOXIDE ADSORPTION AT CONSTANT EXPOSURE

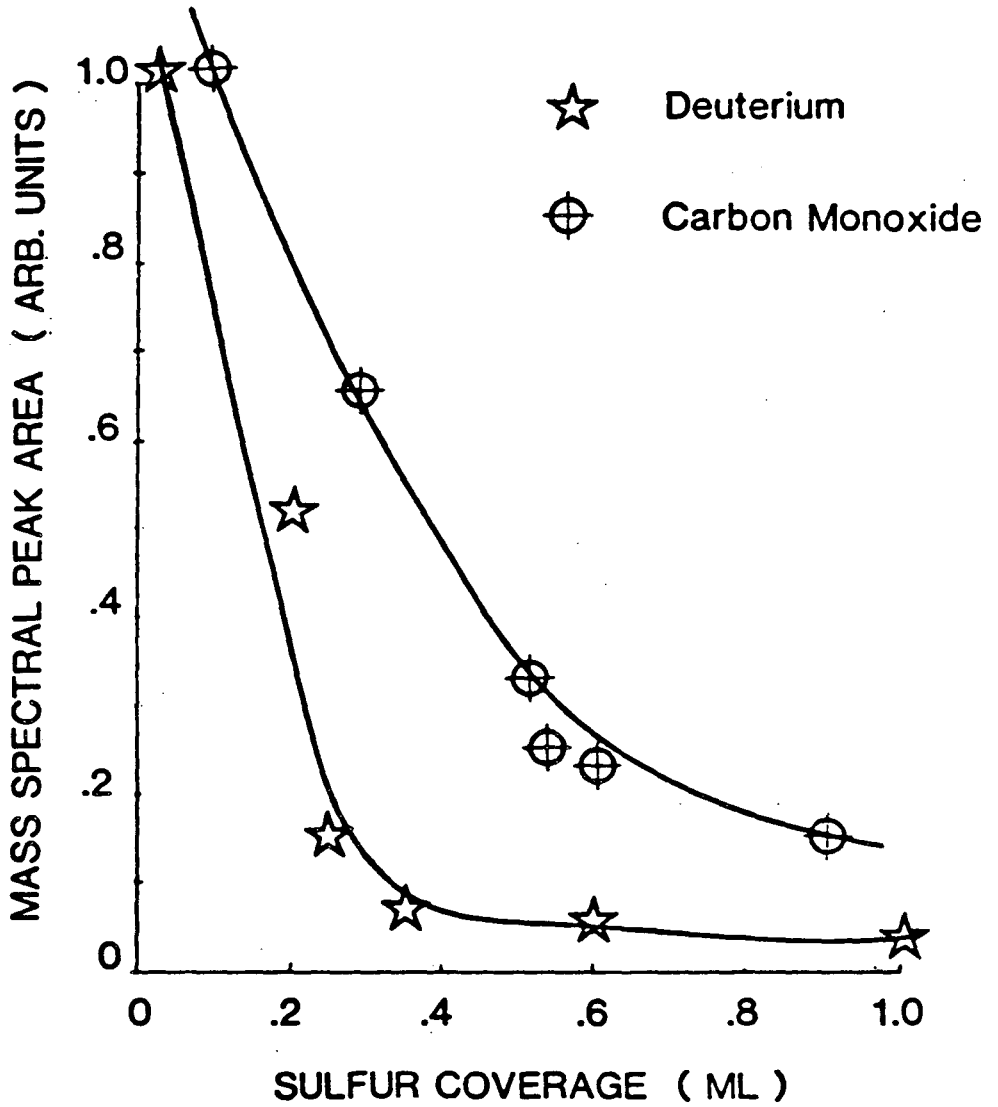

Fig. 5.12. The effect of S on D_2 and CO adsorption is displayed. D_2 is observed to be blocked from the metal surface at lower coverages of S than CO, leading to less hydrogenated products in the high pressure reaction.

Section 5.4: References

1. Shultz, J.F., Karn, F.S., and Anderson, R.B., U.S. Bur. Mines Rep. Invest., 6974 (19670).

2. Saito, M., and Anderson, R.B., J. Catal. 63, 438 (1980).

3. Saito, M., and Anderson, R.B., J. Catal. 67, 296 (1981).

4. Hou, P.Y., and Wise, H., to be published.

5. Zhang, C.S., Van Hove, M.A., and Somorjai, G.A., Surf. Sci. 149, 326 (1985).

6. Dwyer, D.J., Yoshida, K., and Somorjai, G.A., Adv. Chem Ser. 178, 65 (1979).

7. Vannice, M.A., J. Catal. 37, 449 (1975).

8. Sexton, B., and Somorjai, G.A., J. Catal. 46, 167 (1977).

9. Ekerdt, J.G., and Bell, A.T., J. Catal. 58, 170 (1979).

10. Kelley, R.D., and Semancik, S., J. Catal. 84, 248 (1983).

11. Fujumoto, K., Kamayama, M., and Kungi, T., J. Catal. 61, 7 (1980).

12. Sinfelt, J.H., Catal. Rev. 3, 175 (1969).

13. Vannice, M.A., J. Catal., 37, 462 (1975).

14. (a) Storch, H.H., "Advances in Catalysis." Vol. 1. Academic Press, New York, 1948;
(b) Storch, H.H., Golumliz, N., and Anderson, R.B., "The Fischer-Tropsch and Related Synthesis." Wiley, New York, 1951.

15. (a) Kummer, J.T., and Emmett, P.H., J. Amer. Chem. Soc. 75, 5177 (1953);
(b) Hall, W.K., Kokes, R.J., and Emmett, P.H., J. Amer. Chem. Soc. 82, 1027 (1960).

16. Nieuwenhays, B.E., Surf. Sci. 105, 505 (1981).

17. Luftman, H.S., and White, J.M., Surf. Sci. 139, 369 (1984).

18. (a) Mills, G.A., and Steffgen, F.W., Catal. Rev. 8, 159 (1973);
(b) Campbell, C.T., and Goodman, D.W., Surf. Sci. 123, 413 (1982).

19. Goodman, D.W., Kelley, R.D., Madey, T.E., and Yates, J.T., J. Catal. 63, 226 (1980).

20. Bridgewater, A.J., Brach, R., and Mitchel, P.C.P., J. Catal. 78, 116 (1983).

21. Allen, P.E., J. Less-Common Met. 17, 403 (1960).

22. Clarke, L.J., Surf. Sci. 102, 331 (1981).

23. Farias, M.H., and Somorjai, G.A., unpublished work.

24. Farias, M.H., Gellman, A.J., Chianelli, R., Liang. K.S., and Somorjai, G.A., Surf. Sci. 140 (1), 181 (1984).

CHAPTER SIX: MODEL CATALYTIC HYDRODENITROGENATION AND HYDRODEOXYGENATION REACTIONS OVER CLEAN AND SULFIDED MOLYBDENUM SINGLE CRYSTALS AND FOILS

Section 6.1: Introduction

Many workers have studied the hydrodesulfurization of model compounds[1-10]. These have included both ultra high vacuum surface studies and high pressure kinetic studies. The hydrodenitrogenation (HDN)[11-16] and hydrodeoxygenation (HDO)[17-20] reactions have received some attention, but due to the importance of HDS in crude oil refining, HDN and HDO, which accompany HDS in the refining process, have received much less consideration. In this study, catalytic HDN and HDO reactions are observed to occur over both clean and sulfided Mo single crystal and foil catalysts. Product distributions and reaction rates are reported for several model compounds.

Section 6.2: Clean Mo Surfaces

Table 6.1 shows the rates of product formation over clean Mo(100) single crystals and clean Mo polycrystalline foils. Table 6.1 expresses the rate of product formation as a turnover frequency (product molecules/metal site • sec) versus the hydrocarbon used in each experiment. No differences in selectivity or rate were observed between Mo(100) single crystals and polycrystalline foils. We found the rate of HDO reactions to be 10-100 times faster than HDN reactions for similar model compounds under identical reaction conditions.

Hydrodeoxygenation reactions over clean Mo mainly produced propene and CO and some methane. The HDO activity for furan was found to be ~ 10 times greater than for tetrahydrofuran (THF). The product distributions of furan and THF were found to be significantly different over the range of conditions used in this study. Furan produced propene and CO almost exclusively, while THF gave a product distribution similar to the HDN reactions studied. During THF HDO reactions, we found that furan was produced at approximately the same rate as the sum of the formation rates of the four carbon (Σ C_4's of Table 6.1) products combined.

Table 6.2 shows the product distribution in mole percent of C_3 and C_4 hydrocarbons produced from each model compound. The mole percent of propene was found to be approximately equal for THF and all the nitrogen-containing model compounds. The distribution of C_4 hydrocarbons produced from the THP and pyrrolidine HDO reactions was similar. Product distributions and overall rates for both the paraffinic and olefinic nitrogen-containing ring compounds were found to be the same. The rate of formation of C_5 hydrocarbons from pyridine and piperidine was found to be approximately twice the rate of C_4 hydrocarbon formation.

Table 6.1. Rates of product formation are shown. Conditions were 10 Torr hydrocarbon and 750 Torr H_2 at 610 K.

Reactants	Products[b]									
	C_3 //	/	//	//	/	//	$\sum C_4$	$\sum C_5$	CO	CH_4
furan	1.05	0.005	0.017	0.009	0.014	0.007	0.045		1.0	0.04
THF	0.07	0.006	0.019	0.013	0.017	0.004	0.049		0.05	0.02
pyridine	0.007	ND[a]	0.003	0.002		ND	0.005	0.10		0.10
piperidine	0.009	ND	0.002	0.004		ND	0.006	0.10		0.10
pyrrole	0.004	0.001	0.001	0.001		~ 0.001	0.002			0.04
pyrrolidine	0.009	0.001	0.003	<0.002		~ 0.001	0.005			0.09

[a]ND ≡ not detectable by methods used in this study. [b]Turnovover frequency ≡ molecules produced/metal site • sec.

Table 6.2. Product distribution of C_3 and C_4 hydrocarbons from each model compound over clean Mo are shown. Conditions were 10 Torr hydrocarbon and 750 Torr hydrogen at 610 K.

Reactants	Products (mole %)						
	C_3						overall rate[a]
furan	95	0.5	1.5	0.8	1.2	1.0	1.1
THF	54	5	15	10	13	3	0.13
pyridine	58	ND[b]	25	17		-	0.012
piperidine	60	ND	13	27		-	0.015
pyrrole	50	12	12	12		12	0.014
pyrrolidine	56	6	19	12		7	0.016

[a]units of molecules produced/site • sec. [b]ND ≡ not detectable by methods used in this study.

Experiments were performed to determine the effect of hydrogen pressure on the overall rate and selectivity of the HDO reaction. For the HDO reaction with furan, higher hydrogen pressures increased the overall rate and shifted the product distribution toward more C_4 hydrocarbons (see Fig. 6.1). All of the HDN reactions and also the HDO reaction with THF showed an increase in the overall rate of reaction but no change in selectivity.

We also studied the effect of temperature and partial pressure of hydrogen on the poisoning rate. Higher temperatures or a lower partial pressure of hydrogen increased the rate of poisoning of the reaction as shown in Fig. 6.2. The rate of poisoning, for the overall rate of product formation, can be fit to an Arrhenius curve which shows that the rate of poisoning (expressed as the half-life of the reaction rate) decreased exponentially with increased temperature.

Section 6.3: Sulfided Mo Surfaces

Addition of 0.5 ML of S to the Mo surface results in a decrease in the overall rate of reaction and an increase in the relative rate of production of C_4 hydrocarbons. Table 6.3 shows the product distribution (in mole percent) and overall rate (molecules produced/metal site • sec ≡ turnover frequency) of reaction for HDO and HDN reactions over a sulfided Mo surface. An increase in the olefin-to-paraffin ratio in the product distribution was noted. The HDO reaction was found to be more sensitive to addition of S to the Mo surface than was the HDN reaction. The overall rate of HDO reactions decreased 35-75% upon S addition, while the HDN reaction rates decreased by ~ 20%.

Table 6.3. Product distribution of C_3 and C_4 hydrocarbons from each model compound over sulfur-covered Mo (0.5 ML S) are shown. Conditions were 10 Torr hydrocarbon and 750 Torr hydrogen at 610 K.

Reactant	Products (mole %)					
	C_3					overall rate [a]
furan	88	1.3	4.6	2.1	3.5	0.37
THF	64	ND[b]	14	11	11	0.08
pyridine	50	ND	25	25		0.010
piperidine	50	ND	17	33		0.012
pyrrole	56	ND	22	22		0.010
pyrrolidine	82	ND	9	9		0.011

[a] units of molecules produced/metal site • sec. [b] ND ≡ not detectable by methods used in this study.

Section 6.4: Discussion

There has been a tremendous amount of work done on determining the mechanism and best catalysts for the hydrodesulfurization reactions because of their great economic value. Much less work has been done on the HDN and HDO reactions because under the conditions necessary for HDS these two reactions also occur. We have found that HDO and HDN of model compounds, in fact, do occur over clean and sulfided Mo catalysts.

The product distributions from HDN and HDO reactions appear similar to that found for the HDS reactions, using the sulfur analogues of the model compounds used in this work.[1-10] Sulfur on the Mo surface increased the C_4 to C_3 and the alkene to alkane mole ratios of the products. Increasing the hydrogen over-pressure also increased the C_4 to C_3 ratio of the products; but, decreased the alkene to alkane ratio.

The reaction mechanism for the HDO reaction using furan and THF, where the major products were propene and CO, was studied in more detail than the nitrogen HDN reactions. The rate of formation of propene from furan was found to be 10 times faster than from THF. A rate of production of furan was also observed from THF. The mechanism appears to involve dehydrogenation followed by ring opening and CO extraction to form propene and CO. The details of this simplistic scheme need more careful experiments designed to probe eacd step individually.

Section 6.5: References

1. Furinsky, E., Catal. Rev. Sci. Eng. 22 (3), 371 (1980).
2. Chianelli, R.R., Catal. Rev. Sci. Eng. 26 (3,4), 361 (1984).
3. Owens, P.J., and Amberg, C.H., Can. J. Chem. 40, 941 (1962).
4. Owens, P.J., and Amberg, C.H., Can. J. Chem. 40, 947 (1962).
5. Owens, P.J., and Amberg, C.H., Can. J. Chem. 41, 1966 (1963).
6. Owens, P.J., and Amberg, C.H., Can. J. Chem. 42, 843 (1964).
7. Owens, P.J., and Amberg, C.H., Can. J. Chem. 44, 2623 (1966).
8. Flening, J.E., and Lynton, H., Can. J. Chem. 45, 353 (1967).
9. Nag, N.K., Appl. Catal. 10, 53 (1984).
10. Rollmann, L.D., J. Catal. 46, 243 (1977).
11. Sonnemans, J., Van Den Berg, G.H., and Mars, P., J. Catal. 31, 220 (1973).
12. Ledoux, M.J., Puges, P.E., and Marie, G., J. Catal. 76, 285 (1982).
13. Ledoux, M.J., Appl. Catal. 9, 31 (1984).
14. Satherfield, C.N., and Gulfekin, S., Ind. Eng. Chem. Proc. Des. Dev. 20, 62 (1981).
15. McIlvried, H.G., Ind. Eng. Chem. Proc. Des. Dev. 10, 125 (1971).
16. Stern, E.N., J. Catal. 57, 390 (1979).
17. Furimsky, E., Ind. Eng. Chem. Prod. Res. Dev. 22, 34 (1983).
18. Furimsky, E., Ind. Eng. Chem. Prod. Res. Dev. 22, 31 (1983).
19. Krishnamurthy, S., Panvelker, S., and Shah, Y.T., Al. Ch. E. 27 (6) 994 (1981).
20. Furimsky, E., Appl. Catal. 6, 159 (1983).

CHAPTER SEVEN: THE CONVERSION OF ACETYLENE TO FORM BENZENE OVER PALLADIUM SINGLE CRYSTAL SURFACES

Section 7.1: Introduction

Palladium surfaces have been noted[1-12] to possess the distinctive property that catalytic reactions of various classes can be observed both at high pressures and under ultrahigh vacuum conditions. An example is the trimerization of acetylene, which has been shown to occur both in ultrahigh vacuum and at higher pressures over a number of Pd surfaces (single crystals[1-9], foils[6] and supported[6] catalysts) as well as over many homogeneous catalysts[10-12]. The low temperature formation of benzene has been observed using temperature programmed desorption (TPD)[1-6], high resolution electron energy loss spectroscopy (HREELS)[7-9], angle resolved ultraviolet photoemission spectroscopy (ARUPS)[1,2], metastable noble gas deexcitation spectroscopy (MDS)[4], X-ray photoelectron spectroscopy (XPS)[1,2], low energy electron diffraction (LEED)[1,2] and molecular beam measurements[2]. This paper deals with the effect of pressure and additives on Pd single crystal surfaces on the trimerization of acetylene to form benzene.

The cyclization of acetylene to benzene was first reported to occur in small yields by Berthelot in 1866 at elevated temperatures (300-400°C)[53]. In the 1940's, Reppe discovered that certain homogeneous nickel complexes produced benzene from acetylene in good yield under mild experimental conditions[54]. Since that discovery, other research groups gave found numerous homogeneous transition metal systems that catalyze substituted and functionalized acetylenes to form benzene derivatives[12]. For example, cobalt complexes such as $CpCo(CO)_2$ are used in cyclization steps in the

synthesis of natural products such as steroids and Vitamin B6. Also, it has been shown that palladium chloride will easily oligomerize acetylene[11].

Additives, such as potassium, silicon, phosphorus, sulfur and chlorine, have been shown to modify the behavior of catalysts for many different reactions[13-17], and their interaction with surfaces has been studied extensively by many surface-sensitive techniques[18-24]. Two effects are possible - (1) a geometric effects due to site blocking; and (2) an electronic effect due to electron donation (as in the case of K[18]) or electron depletion (as in the case of Cl[25]) of the near surface region.

In this chapter, a systematic study of both surface composition effects and pressure effects on the chemisorptive and catalytic properties of palladium (111), (100) and (110) single crystal surfaces on the cyclotrimerization of acetylene is described.

Section 7.2: Results: Introduction

This study investigated similarities and differences in the trimerization of acetylene to benzene using palladium single crystal catalysts under varying pressure conditions (10^{-12} atm - 1 atm) and with different additives on the single crystal surface. Under UHV condition, the cyclotrimerization of acetylene on all three surfaces ((111), (110) and (100)) was detected by observing the thermal desorption of molecular benzene after dosing with acetylene. All doses were at 130 K. Table 7.1 shows the dose molecules, desorption products, desorption temperature, E_A of desorption and relative areas for the products of acetylene adsorption for the clean (111), (100) and (110) surfaces in UHV.

Section 7.3: Ultra-High Vacuum Studies: Pd(111)

On the Pd(111) face, dosing 6 Langmuirs (L) of acetylene produced benzene with two distinct desporption peaks at 250 K and 490 K. The low temperature peak was 2.5 times larger than the high temperature (see Fig. 7.1). Acetylene, ethylene and hydrogen were also detected as desorption products. The acetylene and ethylene desorbed at 190 K and 305 K, respectively. Hydrogen, the only other product detected, had a broad desorption peak from 430-830 K, with a maximum at 450 K (Table 7.1). At low acetylene coverages (0.5 L), the benzene desporption maxima remained unchanged. The amount of benzene formed decreased, with the area under the high temperature peak decreasing more rapidly than the area under the low temperatture peak. No C_4 products were detected. In order to determine whether the product formation was desorption rate-limited or reaction rate-limited, C_6H_6, C_2H_4 and H_2 were adsorbed on clean Pd(111) and a TPD spectrum was taken. Benzene undergoes both reversible and irreversible chemisorption, with the fraction of reversibly bound benzene increasing with exposure. At low coverages (1.0 L), there was primarily decomposition as characterized by a broad hydrogen trace extending from 520 K to 720 K with a maximum at 545 K. Benzene had two weak desorption peaks at 260 K and 520 K. With exposures greater than 2 L, the hydrogen spectrum remained unchanged and the benzene maxima occured at 235 K and 510 K with a 1:10 intensity ratio (Fig. 7.2). No C_2H_2 or C_2H_4 fragments were detected. Hydrogen dosing yielded a desorption peak at 310 K with only the peak area changing at higher coverages. With ethylene (1.0 L), reversible desorption occured at 300 K with hydrogen desorbing at 370 K and 430 K in a 1:1 ratio. Higher coverages of ethylene (>2L) increased molecular desorption of ethylene only.

Table 7.1. Desorption products from acetylene, ethylene and benzene over Pd(111), Pd(100) and Pd(110) single crystal surfaces.

Crystal Face	Dose Molecule	Desorption Product	Desorption Temperature (K)	E_A(kcal/mol)	Relative Areas (for acetylene adsorption)
(111)	C_2H_2	H_2	450 (430-830)	26.3 (25.1-49.5)	4.3
		C_2H_2	190	10.8	1.0
		C_2H_4	350	20.3	0.22
		C_6H_6	250, 490	14.3, 28.7	0.9
	C_2H_4	C_2H_4	300	17.3	
	C_6H_6	H_2	545 (520-720)	32.0 (30.5-42.7)	
		C_6H_6	260, 520	14.9, 30.5	
(100)	C_2H_2	H_2	420 (495-625 sh)	24.5 (29.0-36.9 sh)	2.8
		C_2H_2	180 (250 sh)	10.2 (14.3)	1.0
		C_2H_4	305	17.6	0.1
		C_6H_6	260, 380, 470	14.9, 22.1, 27.5	0.04
	C_2H_4	C_2H_4	260, 310	14.9, 17.9	
	C_6H_6	H_2	575 (665 sh)	33.8 (39.3)	
		C_6H_6	220, 375, 525	12.5, 21.8, 30.8	
(110)	C_2H_2	H_2	490	28.7	1.43
		C_2H_2	180 (to 500 sh)	10.2 (to 29.3 sh)	1.0
		C_2H_4	260	14.9	0.09
		C_6H_6	250, 420	14.3, 24.5	0.06
	C_2H_4	C_2H_4			
	C_2H_6	H_2	475, 535	27.8, 31.4	
		C_6H_6	250 (to 425 sh)	14.3 (to 24.8 sh)	

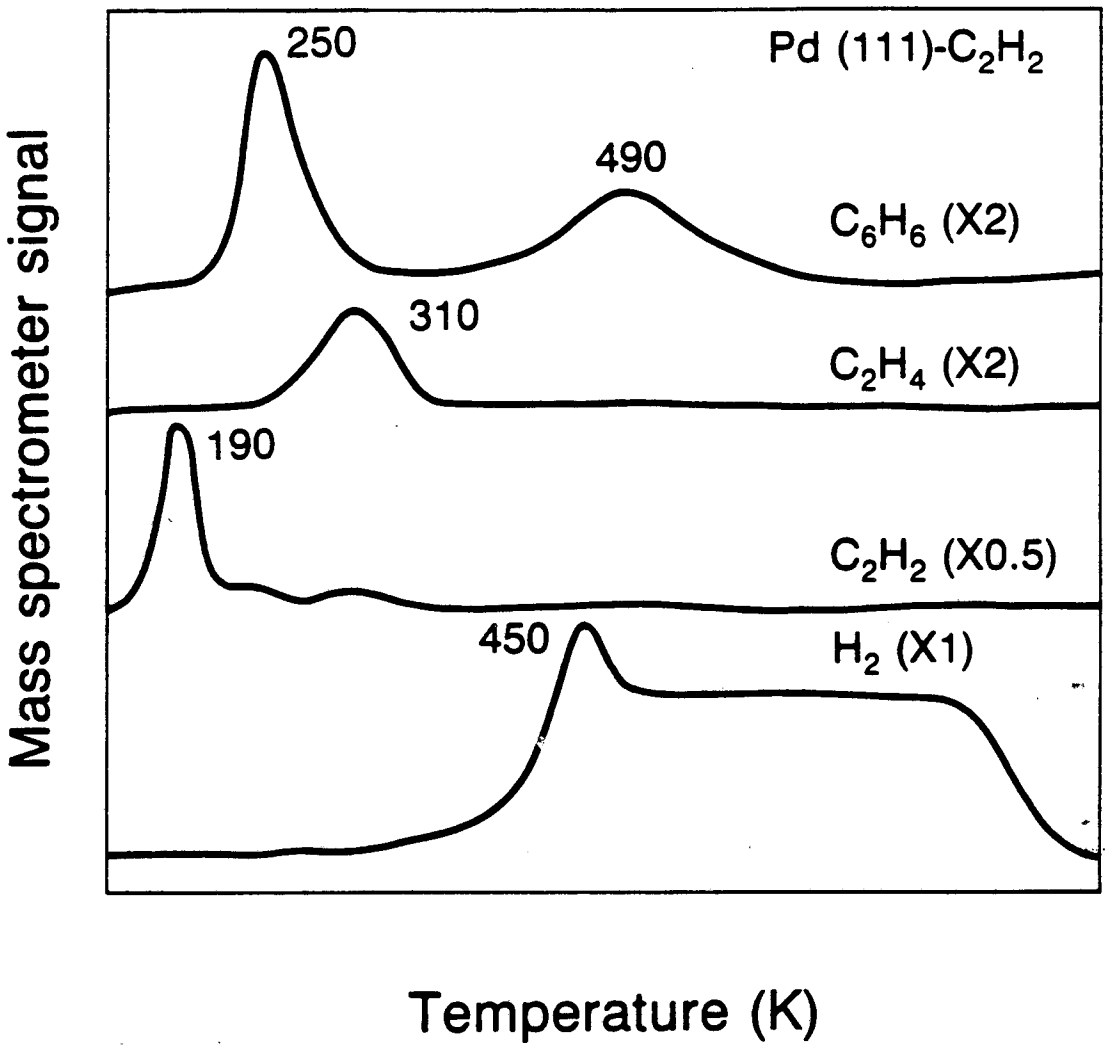

Fig. 7.1. The TPD spectra of acetylene on clean Pd(111) (6 L of acetylene dosed at 130 K) are displayed. The four products from the desorption are shown - benzene, from the trimerization of acetylene; ethylene, due to self-hydrogenation of acetylene; hydrogen, from acetylene decomposition; and molecular desorption of acetylene itself.

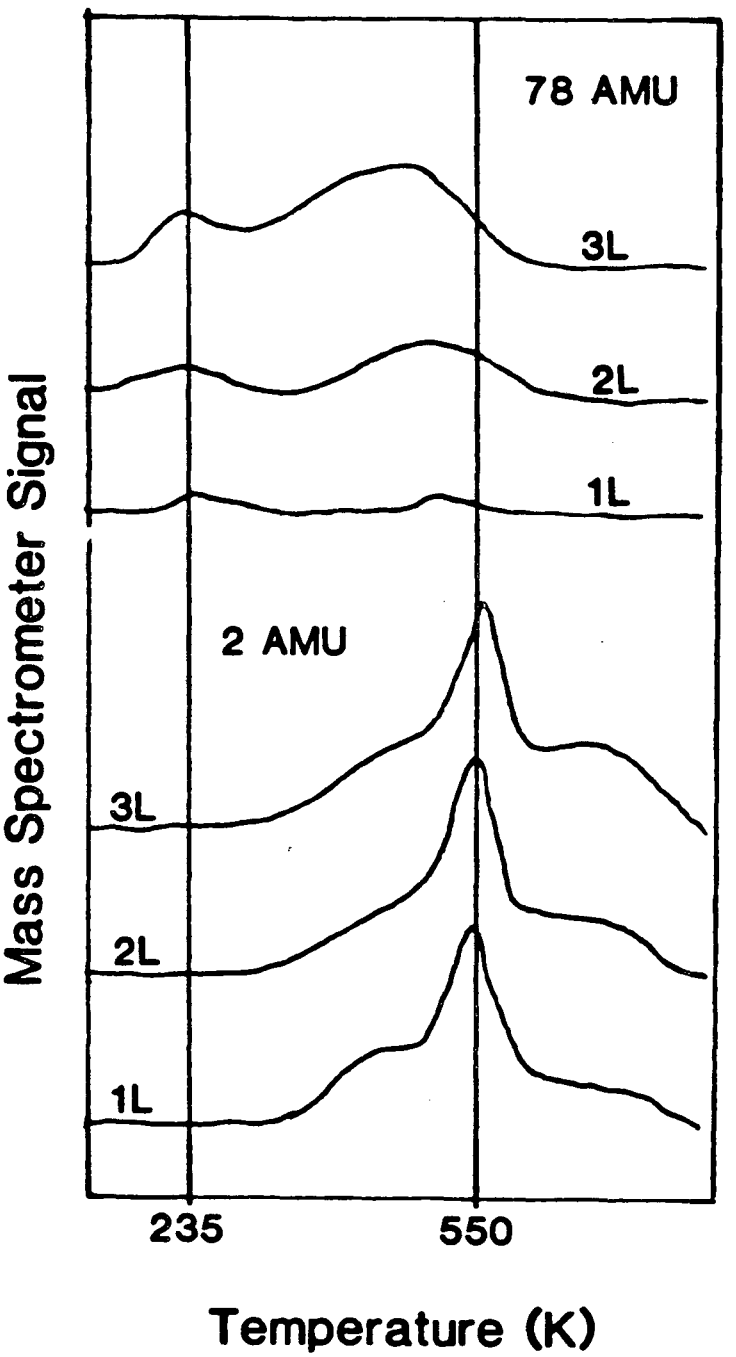

Fig. 7.2. Benzene was found to undergo both reversible and irreversible adsorption on clean Pd(111). The desorption signal of benzene and hydrogen from 1,2 and 3 Langmuir doses of benzene on Pd(111) at 130 K are shown. At higher exposures, a large increase in reversible desorption of benzene is observed.

Section 7.4: Effect of Adatoms on Cyclotrimerization at Low Pressures: Pd(111)

Adsorption of 0.25 monolayer (ML) of silicon on Pd(111) did not significantly perturb the chemisorption of acetylene, as shown by the thermal desorption results (see Fig. 7.3). As shown in Fig. 7.3, the only effect of Si was a slight decrease in the extent of acetylene decompostition (to form H_2 and C) and some enhancement of the high temperature desorption peak of benzene. Phosphorus, however, greatly suppressed the acetylene decomposition, increased the yield of ethylene, and yielded a complex thermal desorption spectrum of benzene (from the cyclotrimerization processes) with maxima at 200, 300, 400 and 470 K, while doubling the benzene yield.

Like P, S adatoms affected the thermal behavior of chemisorbed acetylene (see Fig. 7.3). At low coverages of S ($\lesssim$ 0.2 ML), the ethylene yield and decomposition to hydrogen decreased, but the benzene yield significantly increased. The low temperature benzene peak intensity increased and a new peak appeared at ~ 430K. At high S coverages (>0.25 ML), the formation of ethylene was fully suppressed and the decomposition to H_2 was also very low. At these high S coverages, the benzene desorption spectrum was comprised mostly of a broad peak with a single maximum at 260 K.

Like P and S, Cl adatoms also shifted the acetylene surface chemistry toward benzene formation (see Fig. 7.3); but, in contrast to S, the benzene desorbed largely in the high temperature regions with maxima at 415 and 490 K, although there was a smaller peak at 270 K. Chlorine also suppressed ethylene formation and acetylene decomposition to H_2 and carbon.

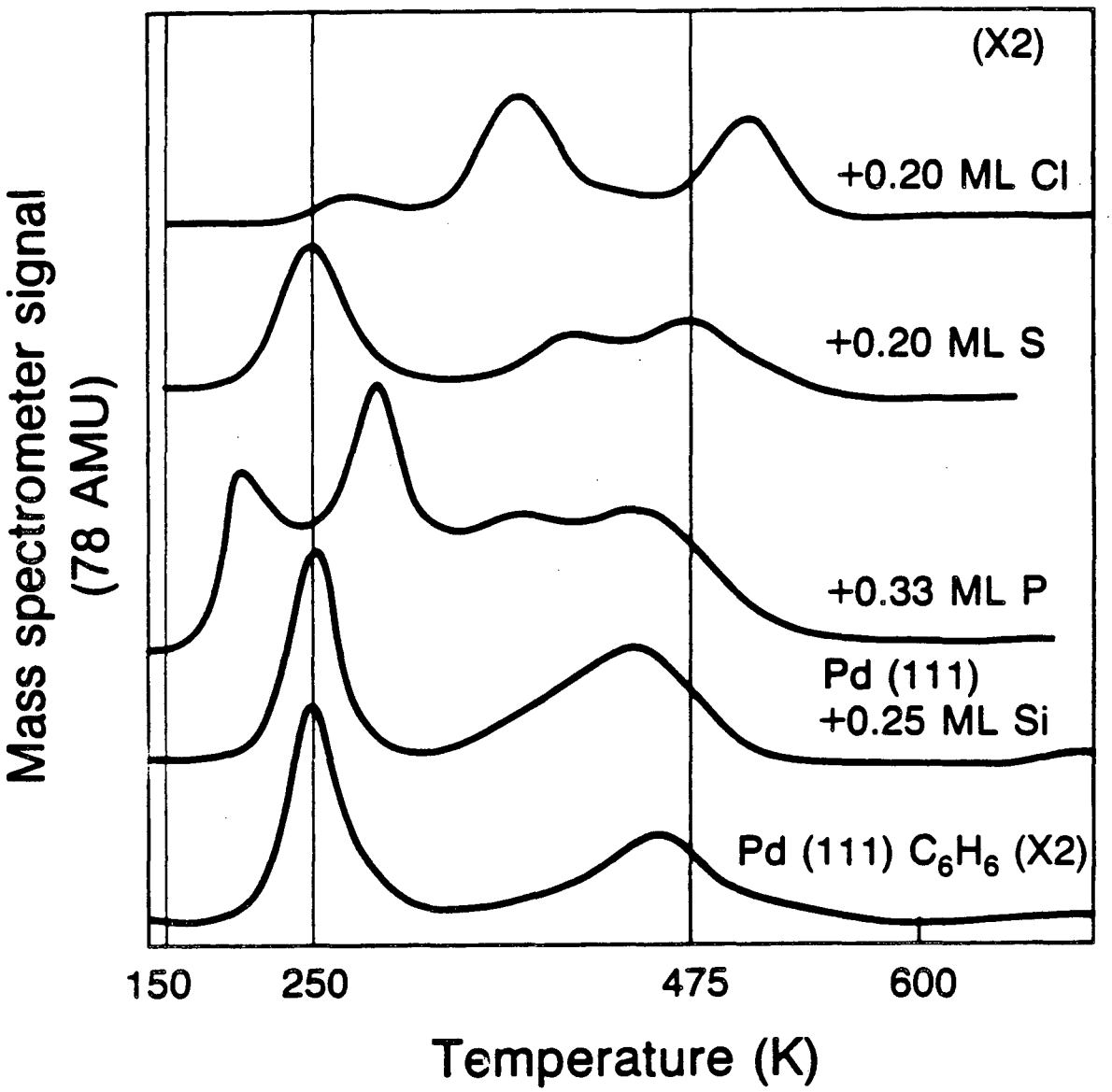

Fig. 7.3. Six L of acetylene were dosed on additive-covered Pd(111) at 130 K. The benzene TPD spectrum was then recorded and is displayed for each surface. The high temperature peak is observed to shift upwards from 470 K on the Si-dosed surface to 490 K on the Cl-covered Pd(111) surface. Phosphorus is observed to have a complex thermal desorption spectrum with four maxima.

The adatom effect upon the acetylene cyclotrimerization yield increased in the presence of adatoms in order from Si to P to S. Chlorine was not quite as effective as S, which basically fully suppressed all acetylene reactions except cyclotrimerization. Thus, Pd(111)-S is an impressively selective catalyst for benzene formation from acetylene under ultra-high vacuum conditions. The main difference in the TPD spectra between the Pd(111)-S and Pd(111)-Cl surfaces was that the Pd(111)-S surface mostly promoted the low temperature cyclotrimerization reaction and the Pd(111)-Cl surface promoted the high temperature process.

Using TPD studies to observe the effect of adsorbed benzene on adatom-covered palladium surfaces led to the same trends as found with acetylene adsorbed on adatom-coved Pd surfaces. For example, Fig. 7.4 shows the effect of 0.25 ML of Si on Pd(111). As in the case of acetylene adsorption, Si enhanced the high temperature TPD peak of benzene. Higher exposures of both acetylene and benzene led to an enhancement of the high temperature (470 K) benzene desorption peak.

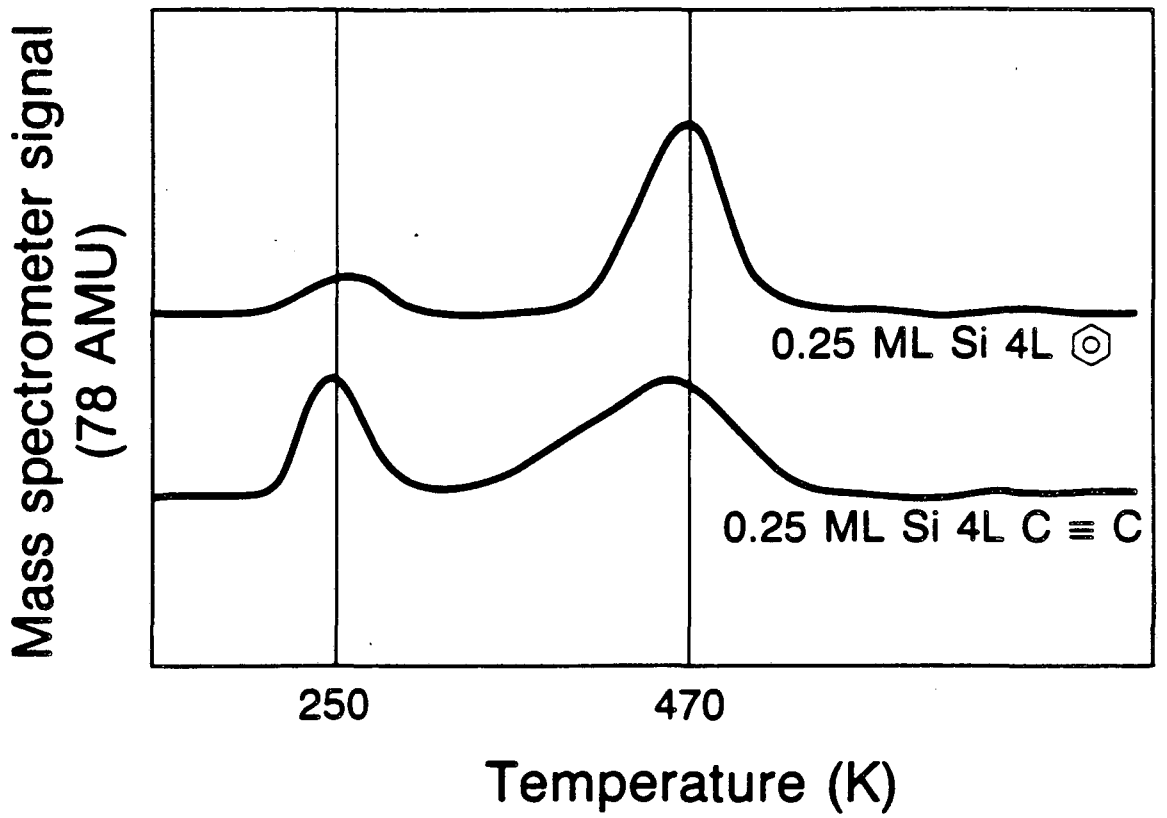

Fig. 7.4. Benzene TPD spectra are compared on a Si-doped Pd(111) surface after benzene or acetylene desorption (4 L adsorption at 130 K). Acetylene gives a broader high temperature peak. More acetylene exposure enhances the high temperature benzene peak, whereas more benzene exposure enhances the low temperature desorption maxima.

Section 7.5: Ultra-High Vacuum Studies: Pd(110)

The Pd(110) surface produced four times less benzene than the (111) face. On the (110) face, benzene desorbed at 250 K and 420 K in a 1:3 ratio after a 6L dose of acetylene (see Fig. 7.5). At coverages below 3L of acetylene, no benzene was detected. Molecular desorption of acetylene occured at 180 K with a broad shoulder plateau extending to 500 K. Ethylene desorbed at 260 K, and hydrogen desorbed in a broad peak centered at 490 K. When the surface was dosed with 6 L of benzene, molecular desorption occured at 250 K, with a shoulder extending to 425 K. At low coverages (1.0 L), a single peak at 260 K was observed. The hydrogen from decomposed benzene had maxima at 475 K and 535 K which increased in area with increasing amounts of benzene up to 3 L, after which they remained constant. Hydrogen desorbed at 310 K at all coverages, when adsorbed on the surface alone.

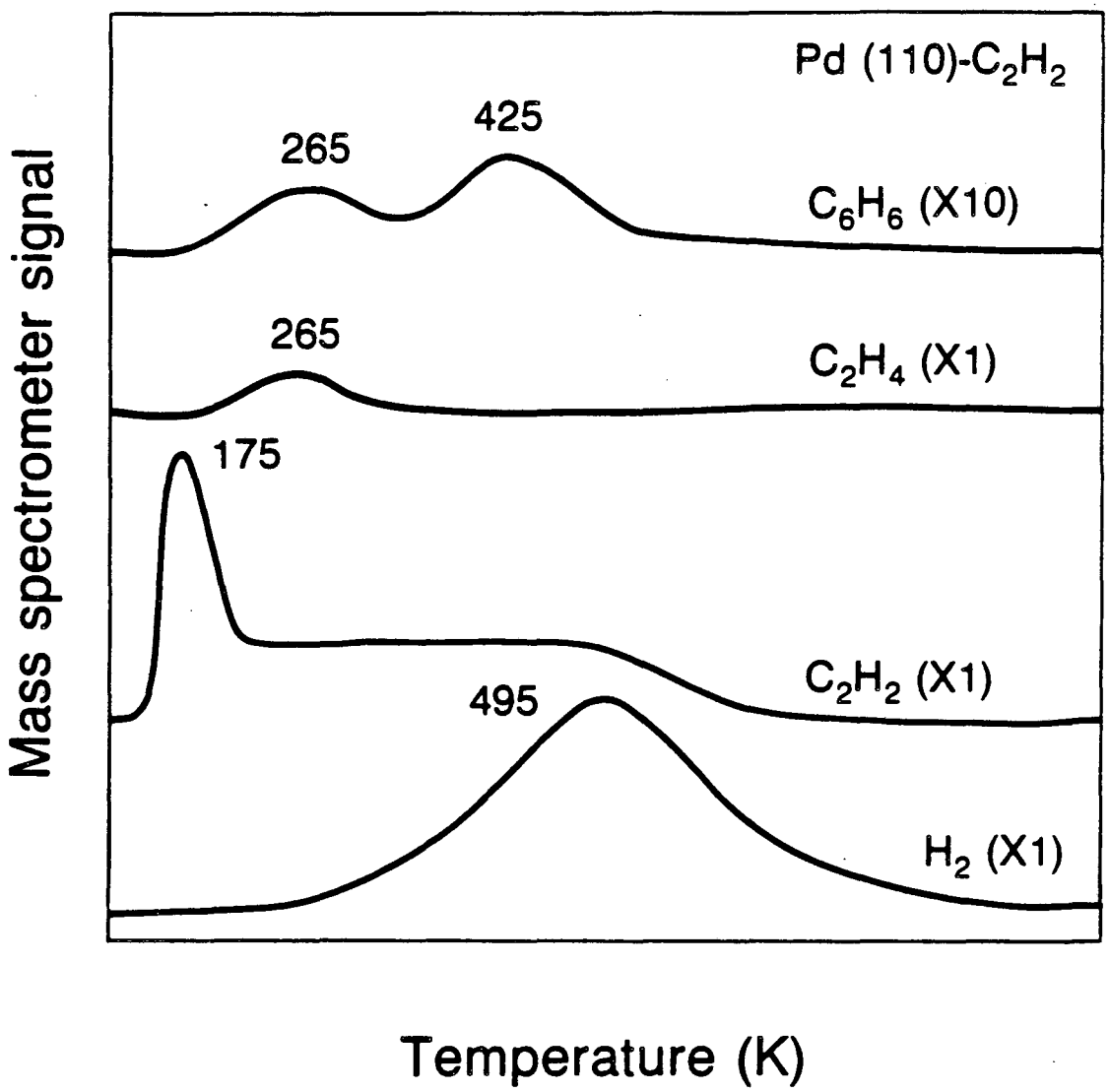

Fig. 7.5. The TPD spectra of acetylene on clean Pd(110) (6 L acetylene dosed at 130 K) are shown. The four products from the desorption are shown - benzene, ethylene, hydrogen and acetylene.

Section 7.6: Effect of Adatoms on Cyclotrimerization at Low Pressures: Pd(110)

Silicon at low surface coverages (<0.25 ML) enhanced the benzene yield through the high temperature desorption peak (see Fig. 7.6), and decreased the decomposition of hydrogen. At Θ_{Si}=0.37 ML, the yield of benzene increased further to a factor of 3.5 (relative to the clean surface), while the ethylene and hydrogen yields were less than that observed for the clean Pd(110) surface.

Phosphorus on the (110) surface of Pd also increased the cyclotrimerization and self-hydrogenation reactions of acetylene. Benzene desorption was found to increase at P coverages greater than 0.2 ML. As on Pd(111), the gain in benzene yield was in the high temperature desorption peak (see Fig. 7.6). At higher coverages of P, two benzene TPD maxima were observed at 270 K and 440 K. The high temperature maximum was increased by as much as a factor of 4 (Θ_P=0.42 ML) relative to the clean surface, while the ethylene yield remained at the level of the low coverage surface. A decrease in the amount of hydrogen desorbing from the surface was observed.

On sulfur-covered Pd(110), the yield of benzene showed a slight increase while the yield of ethylene decreased with increasing S coverage. The molecular desorption of acetylene increased with increasing sulfur coverage. At higher coverages of S, Θ_S=0.4 ML, no ethylene was detected, very little hydrogen desorbed, and the amount of benzene formed was approximately the same as on clean Pd(110).

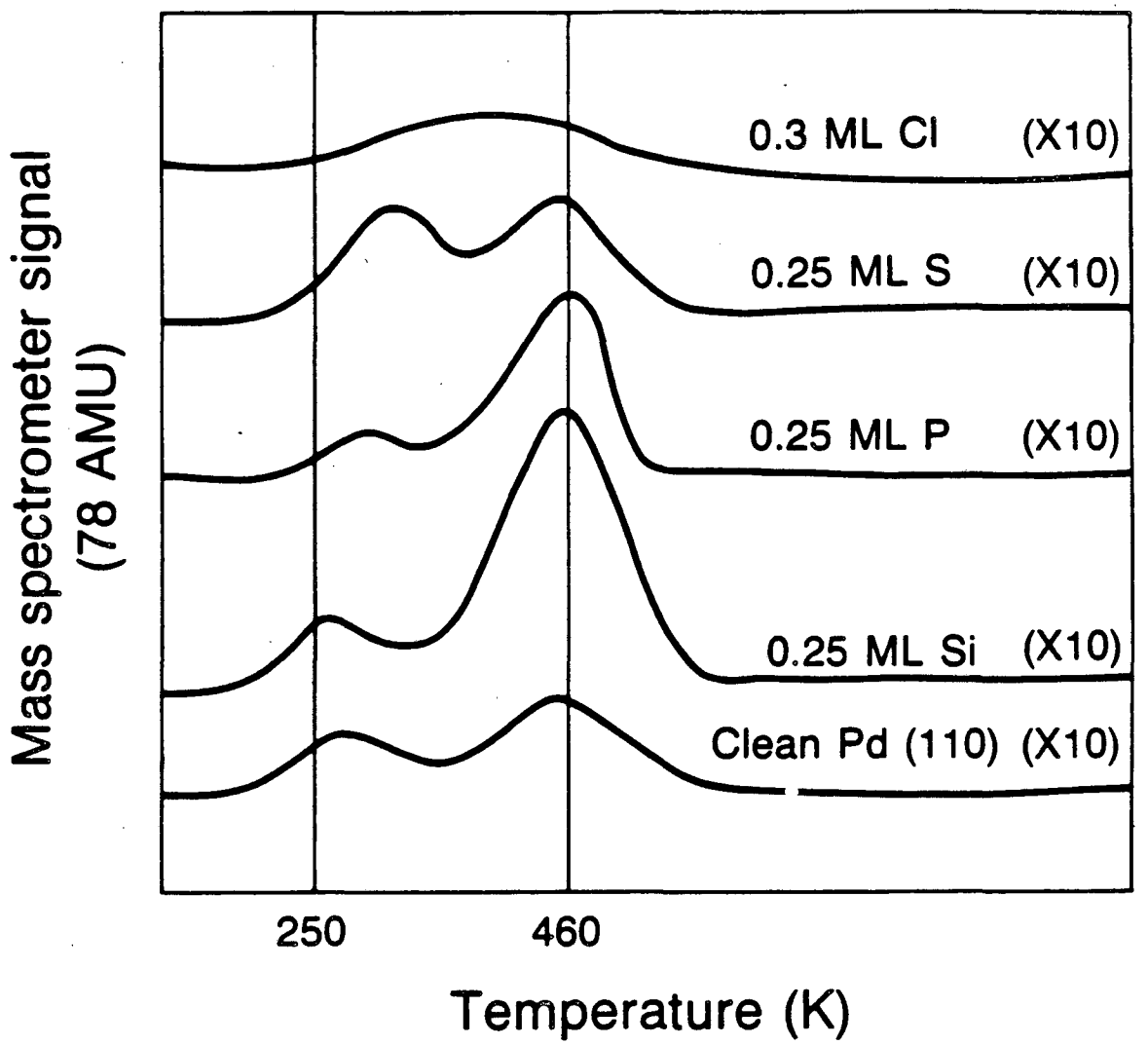

Fig. 7.6. The benzene TPD spectra from additive-covered Pd(110) after a 6 L exposure of acetylene at 130 K. Silicon and P add to the benzene yield in the high temperature peak, similar to their effect on Pd(111) and Pd(100). Sulfur, on the other hand, enhances the low temperature benzene desorption maximum slightly and Cl reduces the overall yield and broadens the two maxima into one peak.

Addition of Cl to Pd(110) resulted in decompositon, hydrogenation and cyclotrimerization of acetylene. At a Cl coverage of 0.30 ML, a very weak ethylene desorption was observed at 290 K and a broad benzene desorption maximum was observed at 370 K (see Fig. 7.6).

Section 7.7: Ultra-High Vacuum Studies: Pd(100)

On the Pd(100) surface, dosing 6 L of acetylene produced benzene continuously from 250 K to 490 K with three maxima at 260, 380 and 470 K. At exposures below 3 L, no benzene was detected. This surface formed 20 times less benzene than the (111) crystal face. With a 6 L dose of acetylene, in addition to trimerization, reversible desorption, hydrogenation and decomposition were also observed (see Fig. 7.7). Acetylene desorbed at 180 K with a shoulder at 250 K, and ethylene desorbed in a single peak at 305 K. The hydrogen desorption from the decompositon reached a maximum at 420 K, followed by a broad plateau from 495 to 625 K. At low coverages of acetylene (1.0 L), there was primarily decomposition. Benzene dosed on the crystal at low coverages (1.0 L) yielded a weak maximum at 310 K with a tail extending to 535 K. At an exposure of 6.0 L, three poorly resolved benzene maxima at 220, 375 and 525 K were observed, along with a hydrogen peak at 575 K, which had a high temperature shoulder at 665 K. When hydrogen alone was dosed on the surface, at all coverages, it desorbed in one peak at 310 K. Ethylene (0.5 L) gave molecular desorption at 260 K and 310 K in a 1:5 ratio with hydrogen desorbing at 365 K. Larger ethylene doses increased the low temperature reversible desorption peak without affection the hydrogen desorption.

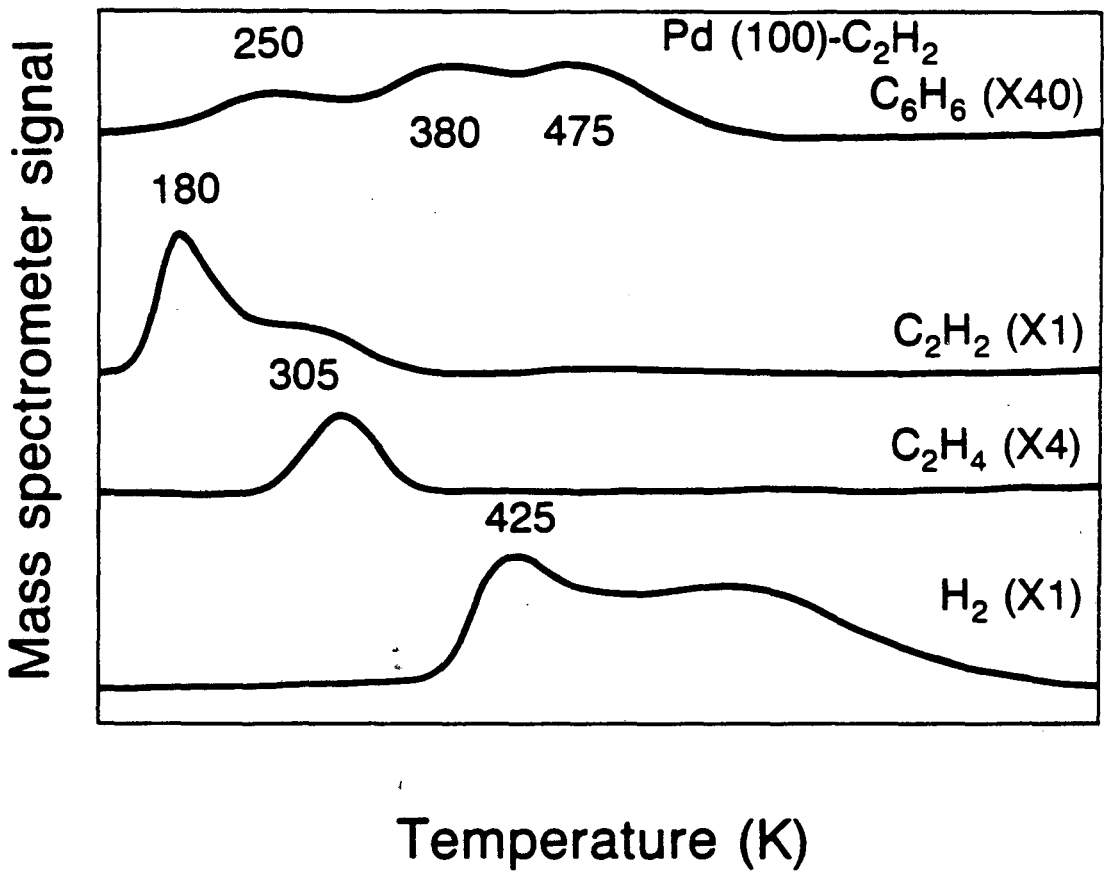

Fig. 7.7. The TPD spectra of acetylene from clean Pd(100) (6 L acetylene dosed at 130 K), showing the four products of the desorption reaction - benzene, ethylene, hydrogen and acetylene.

Section 7.8: Effect of Adatoms on Cyclotrimerization at Low Pressures: Pd(100)

Potassium on the (100) face of palladium had a large negative effect on the formation of benzene from acetylene (see Fig. 7.8). The yield of ethylene and hydrogen was decreased by ~ 95% (see Fig. 7.9,11). The molecular desorption of acetylene was slightly reduced, ~ 20-25% (see Fig. 7.10). At 0.25 ML (or higher) coverage of K, no benzene formation was observed.

Silicon has a substantial effect on acetylene chemisorbed on Pd(100). The yield of both ethylene and benzene was found to increase markedly (see Fig. 7.8,9). The two benzene TPD peaks were similarly affected by Si promotion on Pd(100) and Pd(111); that is, the high temperature peak increased and accounted for a six-fold increase in the yield of benzene at a Si coverage of 0.10 ML. Higher coverages of Si on Pd(100) further increased the yield of benzene, up to ~ 20 times that of the clean surface at Si coverages of 0.38 ML. Concommitantly, the ethylene yield was also enhanced by a factor of ~ 10. The decomposition reaction increased also, although the hydrogen desorption remained constant (see Fig. 7.11).

Phosphorus adsorbed on Pd(100) also influenced the chemistry of chemisorbed acetylene. The yield of benzene was enhanced, but not to the extent observed on silicon-covered Pd(100). At a coverage of 0.17 ML of P, two benzene maxima were observed, at 350 and 520 K. Low coverages of P, <0.2 ML, resulted in no change in the benzene or ethylene yields; however, at coverages of $0.3 < \Theta_P < 0.5$ ML, the yield of both benzene and ethylene was found to increase by a factor of 3-5 (see Fig. 7.8,9). With increasing P coverages, benzene desorption maxima were also observed

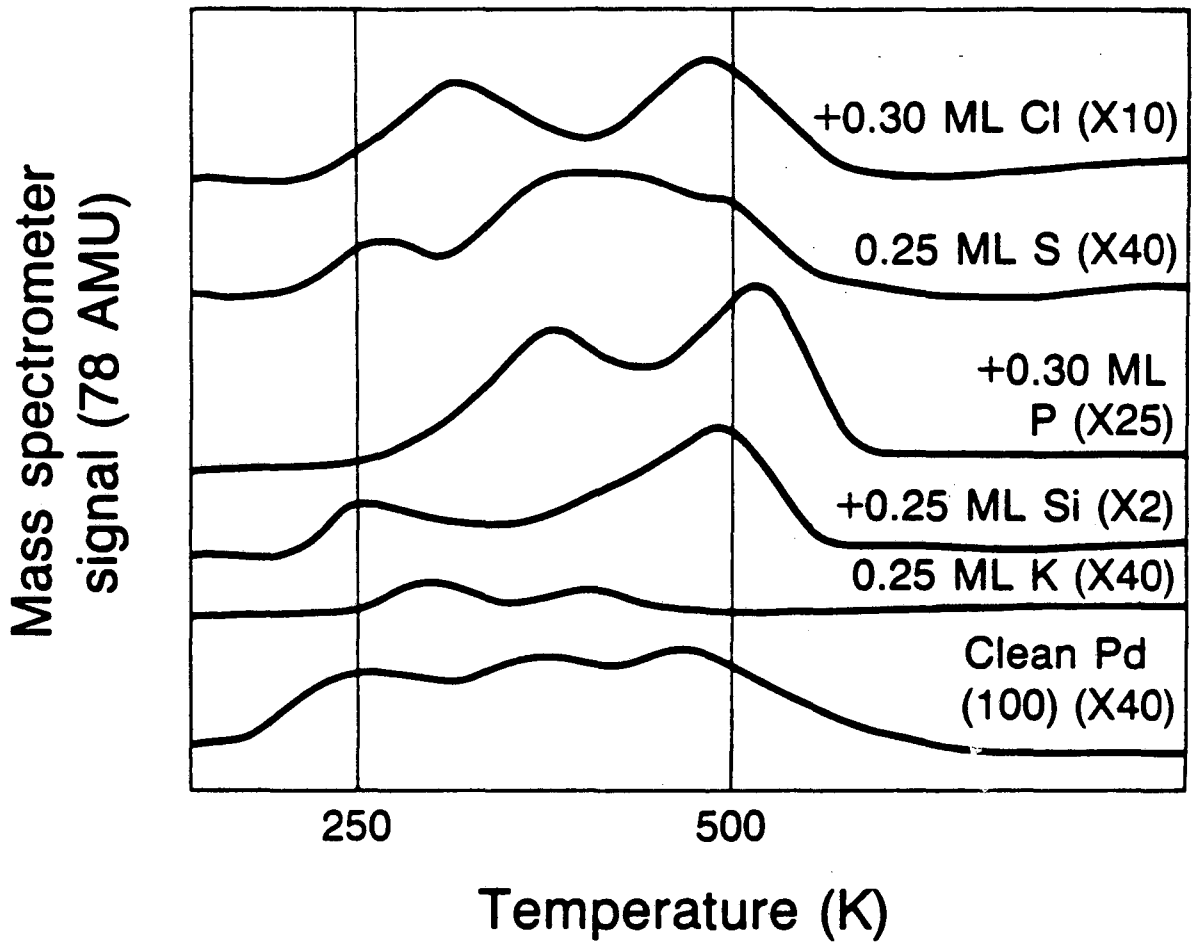

Fig. 7.8. Benzene TPD spectra from adatom-covered Pd(100), after a 6 L exposure of acetylene at 130 K, are displayed. Silicon, 0.25 ML, is found to enhance the formation of benzene ~ 15 times relative to the clean surface. For Si- and P-covered surfaces, the high temperature desorption maximum was enhanced further at higher additive coverages.

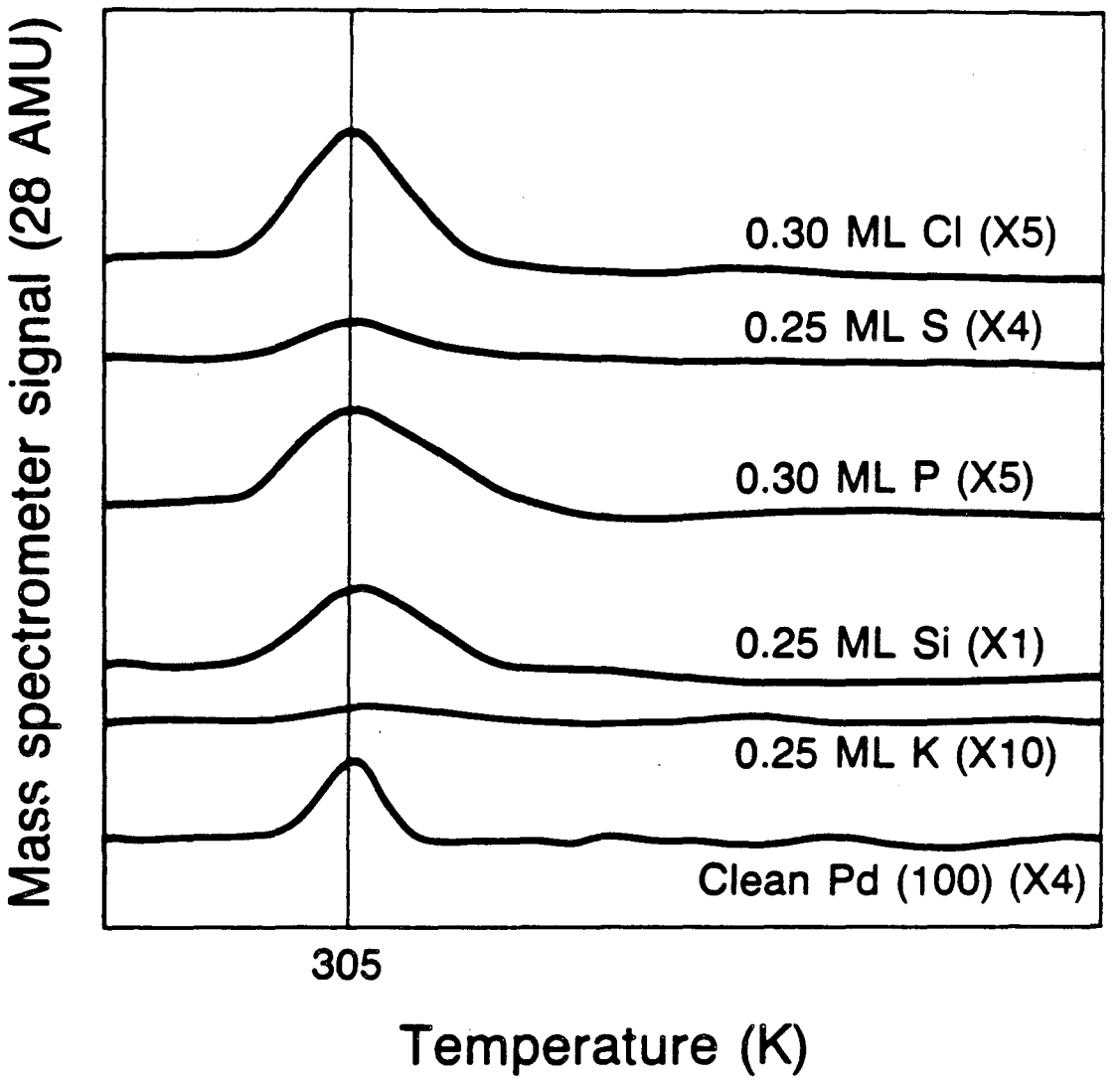

Fig. 7.9. Ethylene TPD spectra, after a 6 L dose of acetylene on Pd(100), are displayed. The more electron-withdrawing additives, S and Cl, completely block ethylene desorption at higher additive coverages. Potassium-covered surfaces produces very little ethylene. At coverages of more than ~ 0.1 ML, Si-covered Pd(100) enhances the formation of ethylene, as well as benzene, much more than the other additives.

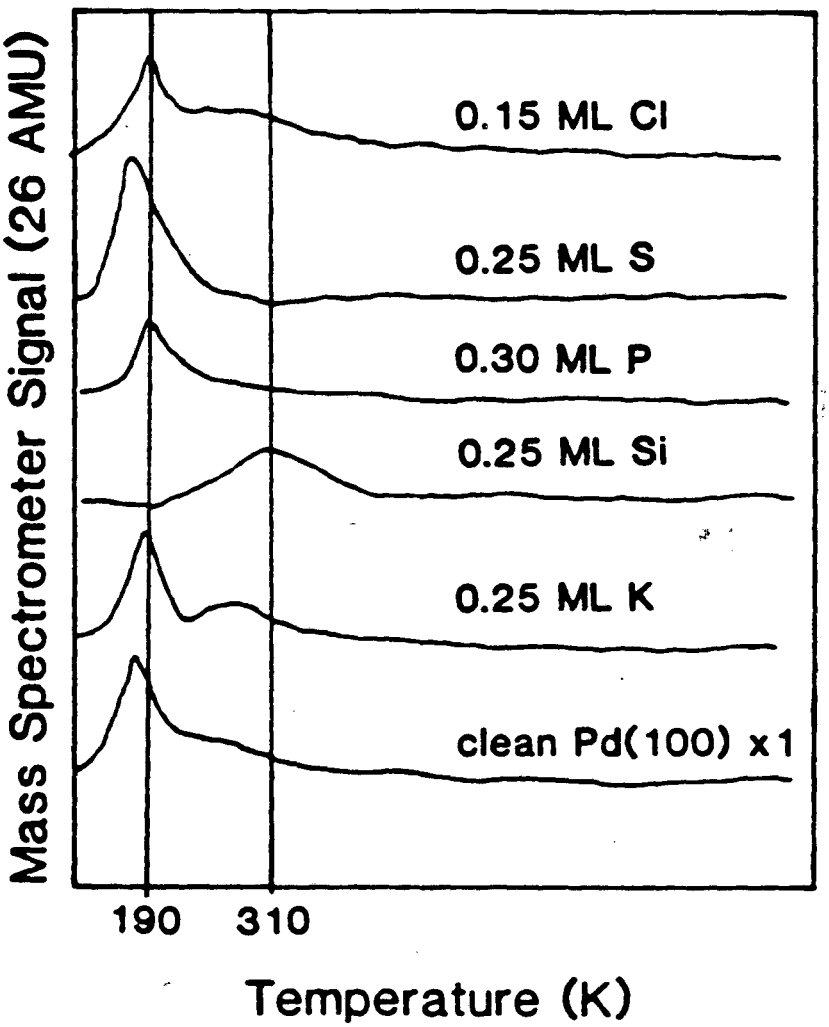

Fig. 7.10. Acetylene TPD spectra, after a 6 L dose of acetylene on Pd(100) at 130 K, are displayed. Clean Pd(100), K-, P-, S- and Cl-covered surfaces have similar TPD traces for acetylene desorption. Silicon appears to have the strongest binding site for acetylene.

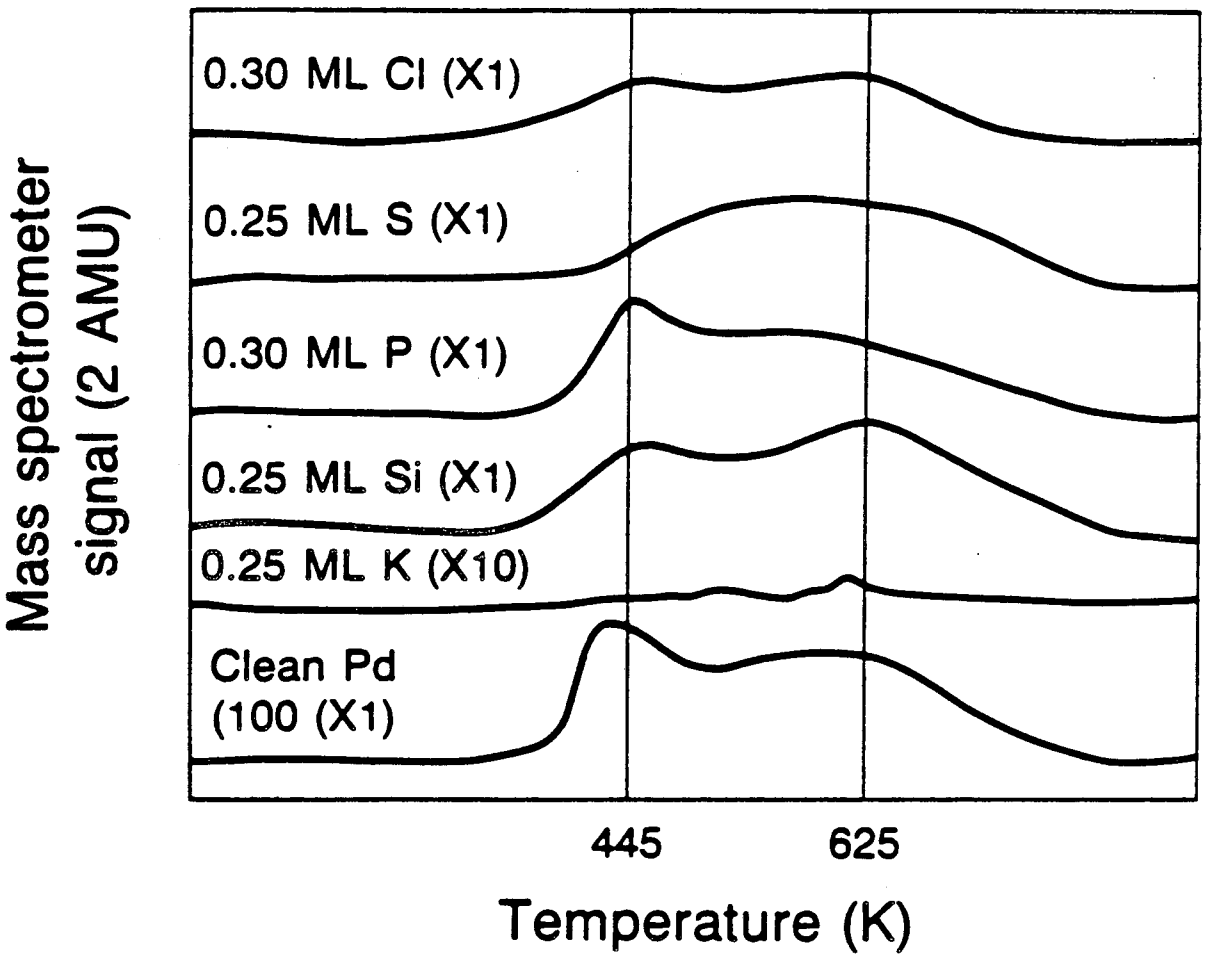

Fig. 7.11. The hydrogen TPD spectra, after a 6 L dose of acetylene at 130 K on Pd(100), are displayed. All the additives reduced the amount of H_2 desorption, K > Cl > S > P > Si > clean. Higher coverages of P, S and Cl further reduce the H_2 yield.

to shift to higher temperatures, with the increased yield coming mainly from the high temperature desorption peak, 470-490 K.

Low coverage sulfur on Pd(100) (Θ_S<0.25 ML) decreased the yield of ethylene and only slightly increased the benzene yield. The desorption of hydrogen was decreased markedly for all S coverages, and the desorption spectra was very broad, from 435-610 K (see Fig. 7.11). The major change observed at higher S coverages was the decrease in ethylene yield. For example, at Θ_S=0.25 ML, the ethylene yield was one-half that for the clean surface (see Fig. 7.9).

Chlorine was found to enhance the yield of both ethylene and benzene (see Fig. 7.8,9). The effect, however, was much smaller than that observed for either Si or P. For coverages of 0.3 ML of Cl, the yield of benzene was found to be 5 times higher than for the clean surface.

Section 7.9: Coverage Dependence of Additives

Coverage dependence of additives for the conversion of acetylene to benzene was studied on all three Pd surfaces. Fig. 7.12 shows the additive coverage for the formation of benzene on Pd(100). For coverages of S and Cl (>0.25 ML), the amount of benzene produced is decreased. Higher coverages of Si and P, up to 0.38 ML, increased the rate of benzene formation in this study.

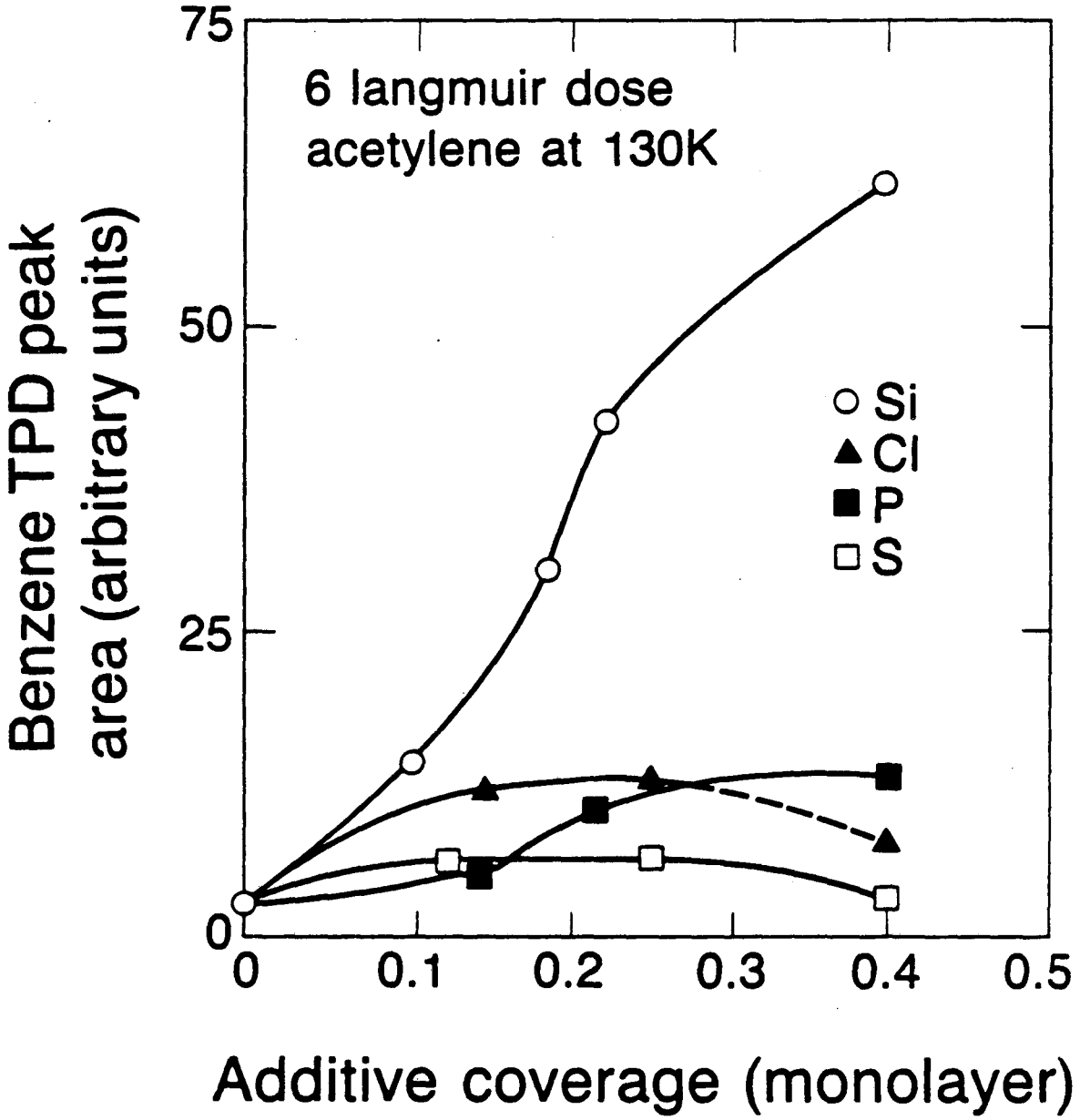

Fig. 7.12. The effect of varying the additive coverage at a constant exposure of acetylene, at 130 K, is shown. Electron-withdrawing additives, S and Cl, and electron-neutral P have similar overall effects on formation of benzene. Silicon, for coverages up to 0.38 ML, enhances the benzene yield in the high temperature peak. At 0.38 ML, the Si-doped surface increased the yield 20-fold over the clean surface.

Section 7.10: Conversion of Acetylene to Benzene at High Pressures

The cyclotrimerization of acetylene on three low Miller index planes of palladium ((111), (110) and (100)) was extensively studied at atmospheric pressures (200-1200 Torr). For all the temperature and pressure conditions used in this study, benzene was the only product detected. Due to the large acetylene peak in the gas chromatograms, trace ethylene could not be detected.

As also seen under UHV conditions, the reaction showed structure sensitivity for the formation of benzene (see Fig. 7.13) at atmospheric pressure. It was found that the (111) and the (100) surfaces were approximately equal in catalytic activity and the (100) surface was ~ 1/4 as active. The (111) and (100) surfaces had a turnover frequency (T.F. ≡ number of molecules produced/ metal atom • sec, assuming $1X10^{+15}$ metal atoms on the single crystal surface) of 0.014 molecules/site • sec (200 Torr acetylene, 850 Torr N_2 or Ar at 570 K). No correction was made for the slight differences in metal surface atoms on the various faces. On the more active surfaces, the reaction had up to 50% conversion of acetylene to benzene or roughly a 20 mole percent yield of benzene. At these conversions, the reaction was limited by either surface poisoning or product concentration. The slope of the turnover frequency versus 1/T plot, assuming Arrhenius kinetics, yields the apparent activation energy of the reaction, calculated as 2 kcal/mol on all three surfaces (Fig. 7.14). Plotting the reaction rate as a function of acetylene pressure showed that the reaction was first order in acetylene, with the rate law (Fig. 7.15):

$$\text{Rate} = kP^{+1}{}_{C \equiv C^{\bullet}}$$

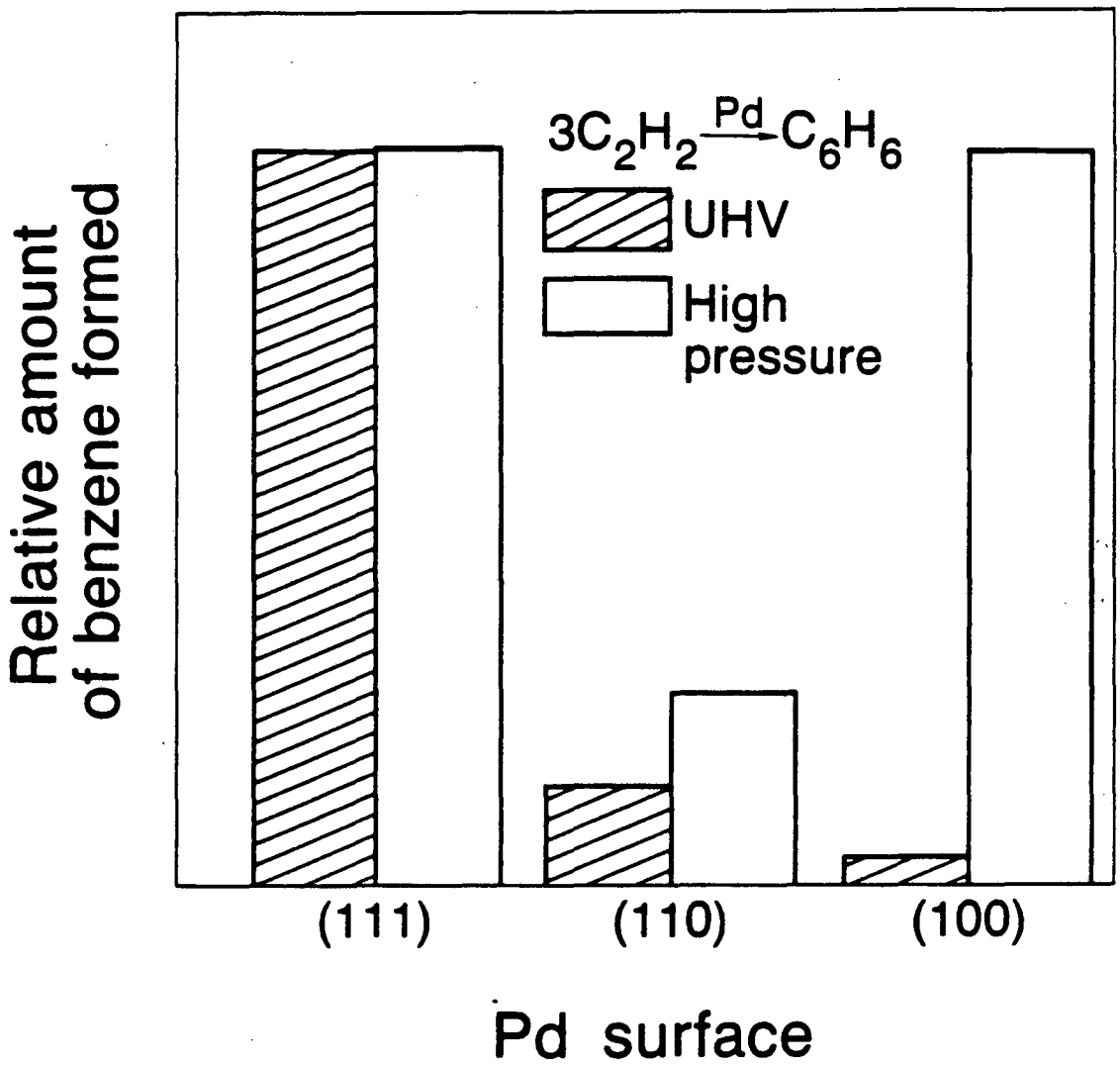

Fig. 7.13. The structure sensitivity for both atmospheric (high) and UHV studies for the conversion of acetylene to benzene over Pd(111), (110) and (100) surfaces is shown.

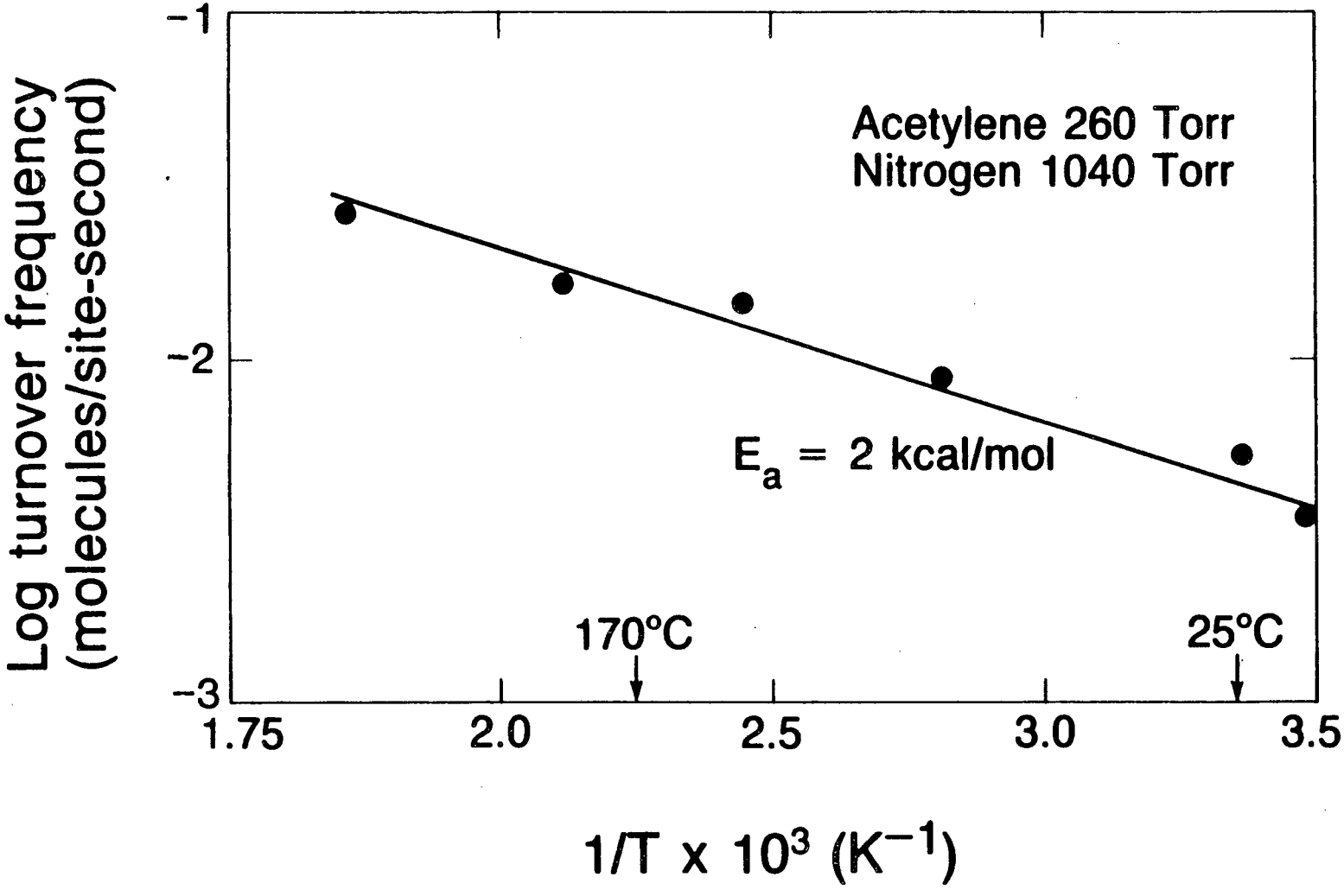

Fig. 7.14. The activation energy for the conversion of acetylene to benzene is determined by varying the reaction temperature at constant pressure.

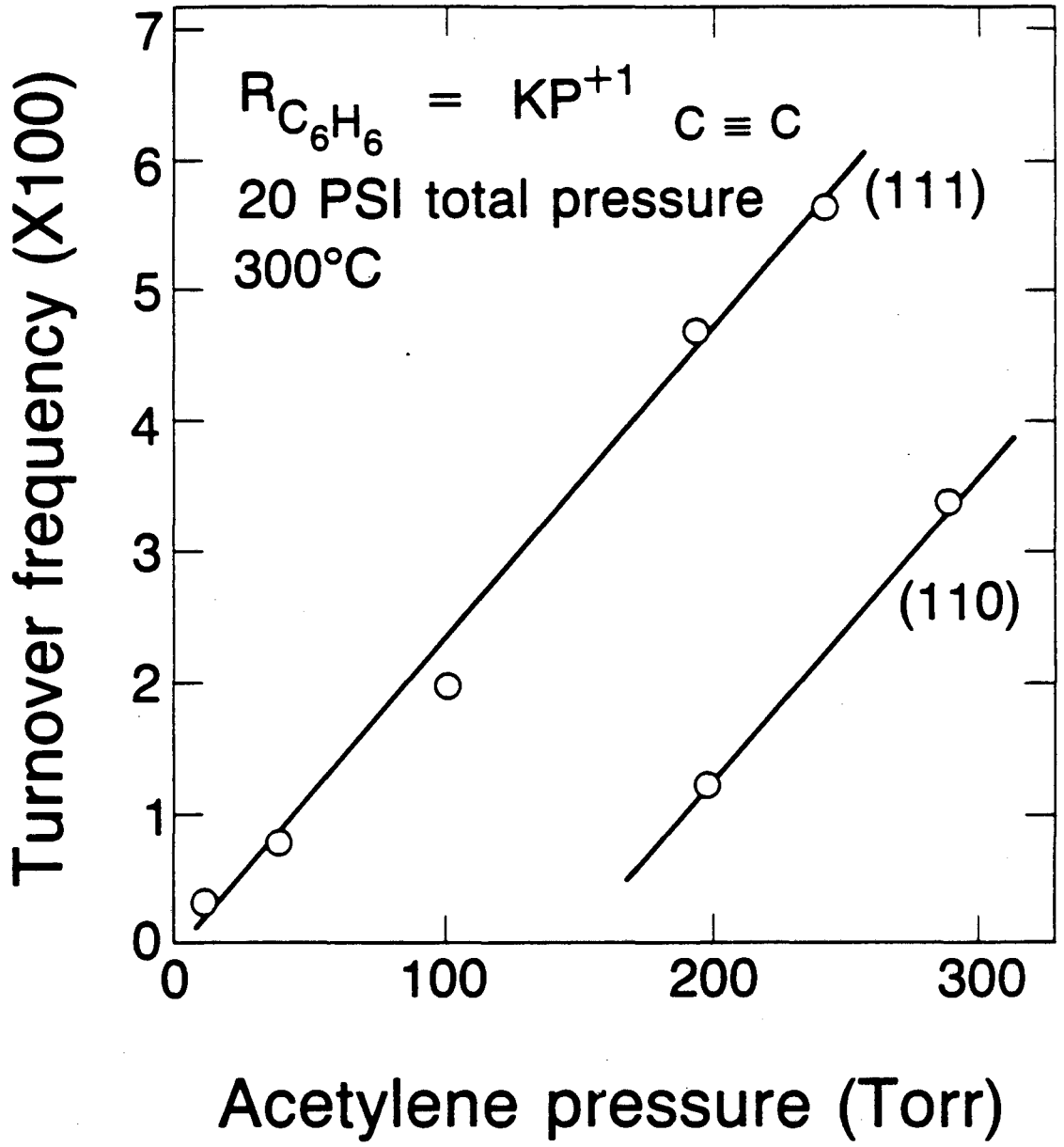

Fig. 7.15. The pressure dependence plot for the conversion of acetylene to benzene over Pd(111), (100) and (110) at high pressures. The plot is made by varying the partial pressure of acetylene at a constant total pressure and temperature.

Analysis by AES and CO titration after the reaction, found a partially carbon-covered surface. After heating the crystal to 650 K and exposing it to $1X10^{-6}$ Torr of H_2, the surface remained carbon-covered, suggesting a stabile graphitic overlayer. The CO titration technique determines the percentage of bare metal sites, as CO does not adsorb on carbon overlayers at low pressures. After the trimerization reaction (200 Torr acetylene, 850 Torr N_2 or Ar at 570 K for 3 h), it was found that 5-79% of the Pd(111) surface and 12-15% of the Pd(100) were composed of bare metal sites. The least active surface, Pd(110), contained less than 2% bare metal sites.

From TPD studies, it was determined that CO binds more tightly to the partially carbon covered metal than does C ≡ C. In order to determine if the reaction proceeded on the bare metal or carbonaceous overlayer, 200 Torr of CO was added into a room temperature reaction mixture 3 h after the start of the reaction. The reaction rate immediately decreased to ~ 0.00 T.F. Subsequent heating of the crystal to 485 K, which is above the desorption temperature of CO, restored the reaction rate to within 15% of its original value. This shows that the reaction proceeds on the bare palladium atoms. At lower reaction temperatures, the poisoning rate decreased.

Ethylene, as the reactant gas, instead of acetylene, produced small quantities of benzene (50 times less than did acetylene); and ethane, as the reactant gas, showed no activity for the formation of benzene. A mixture of methyl acetylene and acetylene produced only benzene.

Section 7.11: Effect of Adatoms on Cyclotrimerization at High Pressures: Introduction

High pressure catalytic studies were carried out over three Pd surfaces ((111), (100) and (110)) to determine the effect of adatoms on the cyclotrimerization of acetylene to form benzene. Reactions were, in general, carried out between 290 and 620 K at an acetylene pressure of 200 Torr. Reaction rates were calculated by assuming that each Pd surface atom was one reaction site, and no correction was made when adatoms were deposited on the surface. This leads us to report conservative values for the reaction rates. The products observed from all reactions were benzene and very small amounts of C_4 hydrocarbons. Small amounts of ethylene (<5% of the benzene formed) were not detectable by gas chromatography due to the large acetylene reactant gas peak tail.

Section 7.12: Effect of Adatoms on Cyclotrimerization at High Pressures: Pd(111) and Pd(100)

The initial rate of production of benzene over clean Pd(111) and Pd(100) at 570 K with 200 Torr of acetylene was found to be 0.05 molecules of benzene produced per Pd surface atom per second[6]. Potassium was observed to have the greatest positive effect on the rate of production of benzene over Pd(111) (see Fig. 7.16). With ~ 0.25 ML of K (200 Torr acetylene, 850 Torr N_2 at 570 K) the rate doubled to 0.10 molecule/site · sec. When K was present on the surface, less graphitic carbon appeared in AES (due to the decomposition reaction) and the rate of poisoning of the reaction was reduced, relative to reaction over the clean surface. The activation energy and pressure dependence for benzene formation on additive-covered surfaces did not appear to change from the values obtained on clean surfaces, being constant at ~ 2.1 kcal/mol and $Rate_{C_6H_6}=kP_C \equiv C^{+1}$. Silicon also had a positive effect on the reaction rate of benzene formation. For example, at a coverage of ~ 0.33 ML the rate was increased by 35%. Similarly, relative to the reaction over clean Pd(111), the amount of graphitic carbon deposition was reduced with Si present on the surface.

Phosphorus had a negative effect on the reaction rate. The reaction rate decreased with coverage of P (see Fig. 7.16). For example, at Θ_P= 0.33 ML, the rate of production of benzene was reduced by 37%. With P present, the graphitic carbon deposition rate and the poisoning rate were similar to that found over clean Pd(111).

Sulfur and chlorine had a large negative effect on the reaction rate. For coverages of greater than 0.20 ML, no benzene production could be detected. Reactions on chlorinated surfaces were carried out at room

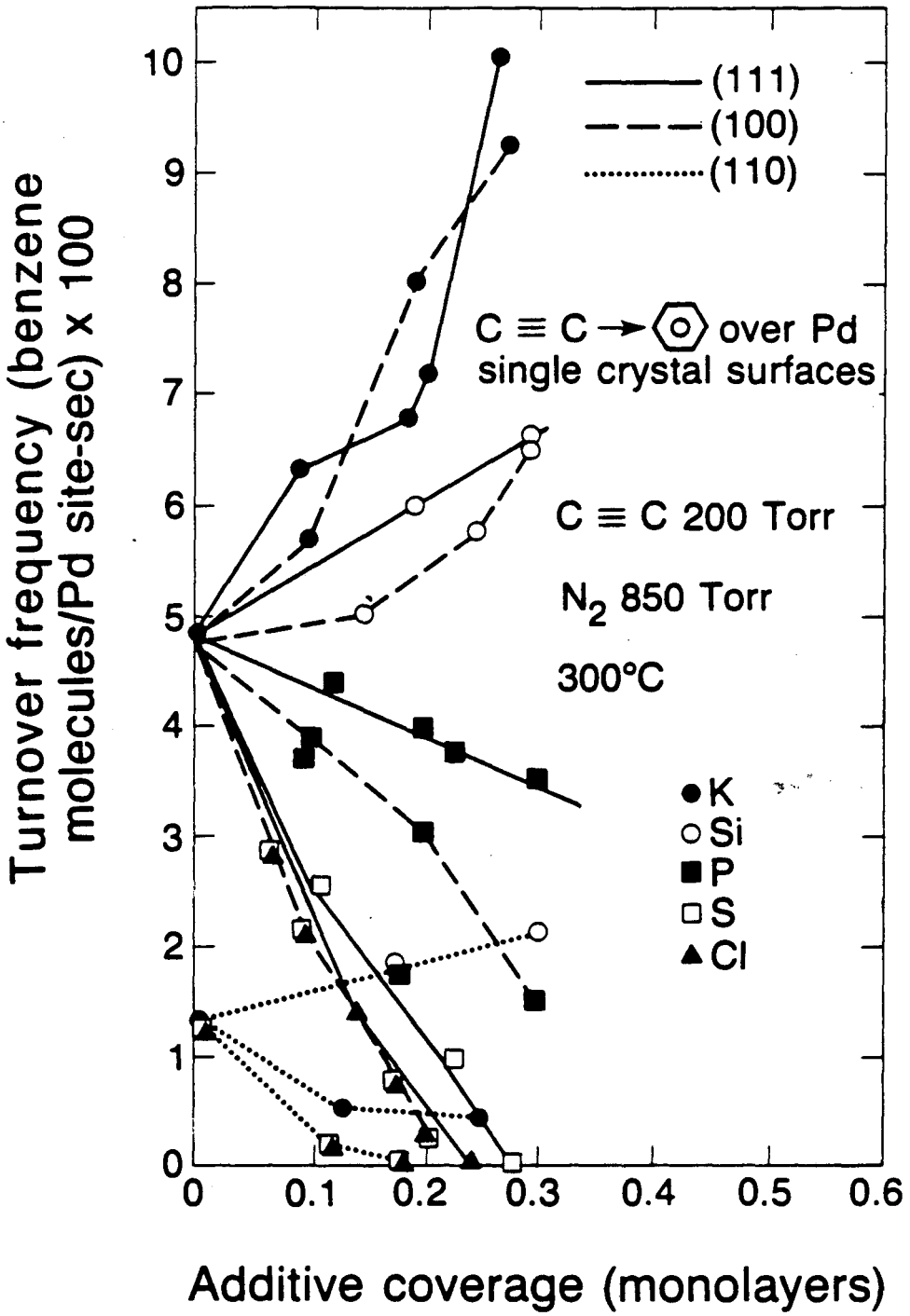

Fig. 7.16. The effect of additives at different coverages over Pd(111), Pd(100) and Pd(110) on the rate of benzene formation at high pressures (200 Torr acetylene, 850 Torr N_2 and 300 K) is shown. Pd(111) and Pd(100) appear to be affected similarly by the different additives. Potassium and Si enhance the rate of benzene formation, while P, S and Cl decrease the rate of benzene formation. On Pd(110), S and P increase the rate, while addition of K, S and Cl decrease the rate.

temperature, due to the low desorption temperature of chlorine from Pd surfaces. The rate of formation of benzene from chlorinated surfaces was very low, even for coverages as low as 0.1 ML, and for coverages over ~ 0.2 ML, no benzene formation was observed.

Section 7.13: Effect of Adatoms on Cyclotrimerization at High Pressures: Pd(110)

The rate of formation of benzene over clean Pd(110) was found to be ~ 1/5 that of Pd(111) for the same reaction conditions. Additives had less effect over the (110) surface. In contrast with K-doping of the (100) and (111) surfaces, adsorption of K on the (110) surface decreased the rate of benzene formation (see Fig. 7.16).

Silicon and phosphorus both enhanced the rate of benzene formation to the same extent. As on Pd(111) and Pd(100), sulfur and chlorine depressed the rate of benzene formation on the Pd(110) surface. It was also noted that the rate of poisoning was increased, at comparable coverages, as adatoms were changed from K to Cl.

Section 7.14: Discussion of UHV and High Pressure Studies on Clean Pd Single Crystal Surfaces: Introduction

The cyclotrimerization reaction of acetylene over clean Pd catalysts to form benzene proceeds readily in pressures ranging from $1X10^{-12}$-1 atm and on a variety of surfaces (single crystals, films and supported on alumina). The reaction is structure-sensitive at both low and high pressures. In UHV the stoichometric reaction over the (111) face is the most active. The (110) face is one-fourth as active, and the (100) is one-twentieth as active. At high pressures, the (111) and (100) surfaces show similar catalytic rates and the (110) face is four times less active (see Fig. 7.16).

The high activity at low pressures over Pd(111) has been attributed to a template effect[1], in which three acetylene molecules are oriented, in the six-fold symmetry of the Pd(111) surface in the Kekule benzene structure.

In addition to the cyclotrimerization reaction, hydrogenation, reversible molecular desorption and decomposition reactions are also detected[31] at all pressures. At high pressures the reaction has an apparent activation energy of 2 kcal/mol and is first order in acetylene pressure (Rate = $kP^{+1}_{C \equiv C}$).

Section 7.15: Discussion of UHV and High Pressure Studies on Clean Pd Single Crystal Surfaces

In UHV, benzene desorbs with two maxima at 250 and 450 K, on the Pd(111) when formed from acetylene. When the surface was dosed with benzene, there were desorption maxima at the same temperatures, suggesting that benzene formation is desorption rate-limited rather than formation rate-limited. Similar thermal desorption traces of H_2 from the C ≡ C and C_6H_6 doses further substantiate this proposition. In both cases, hydrogen desorbes in a broad high temperature peak centered around 450-540 K. These similarities between benzene desorption traces exist on the other two surfaces (see Table 7.2). The low and high temperature maxima in the benzene desorption show that benzene forms readily and also that some benzene formed decomposes on the metal surface.

Using Redhead's method[55] of calculating activation energies (E_A) for UHV reactions from desorption maxima, the activation energies for benzene formation are 15 and 30 kcal/mol for the low (260 K) and high (520 K) temperature peaks, respectively, on the (111) surface. Contrasting these values with those from high pressure studies, shows large differences in E_A. At high pressure the trimerization reaction has an E_A of 2 kcal/mol. For a high pressure reaction this is an extremely low value. For comparison, the formation of methane from CO and H_2, a facile reaction on Fe, has an E_A of 24 kcal/mol and hydrogen exchange on Pt has 8 kcal/mol activation energy[40,56]. This low energy could suggest formation of benzene on an overlayer of ethylidyne or other carbonaceous fragments, onto which it would be loosely bound.

From CO titrations, it can be seen that the reaction rate is dependent on the number of metal sites available. As mentioned previously, on the

Table 7.2. Relative catalytic rates, according to open active sites.

Crystal Face	Turnover Frequency[a]	Percentage of Open Sites	Catalytic Rates
(111)	0.048	7	0.96-0.68
(100)	0.048	12-15	0.40-0.32
(110)	0.014	~ 2	0.7

[a]units of molecules/site • sec

(111) and (100) surfaces, approximately 5-7% and 12-15%, respectively, of the surface was bare after 1 h of reaction and on the least active (110) surface only 1-4% of the surface was bare. The differences in bare metal sites on the (111) and (100) surfaces which have similar turnover frequencies are most likely due to different poisoning rates. Also, when CO was added to the room temperature reaction 3 h after the start of the reaction, the rate decreased to almost zero. Subsequent heating to 485 K, which is above the desorption of CO, restored the rate to within 15% of its original value. Carbon monoxide binds only to the metal surface and since it binds more strongly than acetylene, it displaces acetylene. The CO titrations, CO poisoning experiments and structure sensitivity show that the bare metal atom is the active site for the reacting at high pressure.

The (110) surface, the least active face, is the roughest surface and leads to the highest decomposition rate of both acetylene and benzene as seen by the low percentage of bare Pd atoms. Therefore, the amount of irreversibly-bound carbon in the catalytic steady state reaction limits the rate by blocking sites.

If the percent of open or active surface sites is taken into account, the reaction still exhibits structure sensitivity (see Table 7.2). The (111) surface is still the most active, followed by the (110) and then the (100) face. This is the same activity ordering as seen in UHV. The relative values of the activity differ; however, this may be due to the inability to determine perfectly the percentage of open sites with CO titrations.

The product distribution at low and high pressure are different. In UHV, in addition to benzene formation, approximately 20% as much ethylene

forms. At high pressure on single crystals, less than 5% ethylene forms, which is the detection limit of our gas chromatograph. Hydrogen could not be detected at high pressures.

The low activation energy for this reaction can be explained by incorporating an adsorption equilibrium constant into the rate law. The apparent activition energy, which is determined from the slope of the $\ln(K_{exp})$ versus 1/T plot, then equals the combination of the surface process activation energy and the heat of chemisorption. We were unable to extend the experimental parameters to regions of high acetylene coverage to test this hypothesis.

The most difficult question to address is that of possible mechanisms for the cyclotrimerization reaction. It is possible that at high and low pressures two or more mechanisms exist. Since benzene is detected in all pressure regions investigated, there may be a gradual transition from one path to another.

There are a few possible mechanisms which could occur on the surface. One scheme involves the concerted reaction of three acetylene molecules simultaneously joining[11,31]. Another mechanism involves formation of a cyclobutadiene ring on the surface, which is bound roughly parallel to the surface[11]. This ring would not be tightly bound to the surface, since no C_4 products were detected either at low or high pressure, thus this type of mechanism seems improbable. This type of mechanism has been ruled out in the homogeneously catalyzed reaction[10,12]. The third mechanistic scheme involves a metallacyclopentadiene as an intermediate[12]. In organometallic chemistry, numerous studies have investigated possible schemes for [2+2+2] cycloadditions[12]. Spectroscopic evidence (NMR, IR) suggest that two acetylenes sequentially displace two ligands to form a

metallacyclopentadiene intermediate. This is followed by the insertion of another acetylene to form a metallacycloheptane or a Diels-Alder type addition to form benzene. The first portion of the scheme has been proven, but the addition of the final acetylene is very rapid and the pathway has not been determined.

Analysis of product distribution and yields did not give enough information to propose a mechanism. Current electron energy loss spectroscopy studies will shed some light on this intriguing problem.

Section 7.16: Discussion of UHV and High Pressure Studies on Promoted Pd Single Crystal Catalysts: Introduction

The cyclotrimerization of acetylene has been observed over promoted (111), (100) and (110) single crystal surfaces of palladium at both high and low pressures. The difference in benzene yield at low pressures, relative to the rate of production of benzene at high pressures, was quite dramatic over the different promoted surfaces. Potassium was found to eliminate virtually all benzene formation at low pressures, whereas at high pressures, it was found to be the best promoter studied for the formation of benzene. Sulfur and chlorine, on the other hand, slightly enhanced the low pressure formation of benzene, while at higher pressures, even very low coverages (<0.1 ML) of S or Cl poisoned the reaction, and above ~ 0.25 ML, no benzene formation was observed.

The effects of the different additives will be discussed in terms of steric and electronic interactions with surfaces and the cyclotrimerization of acetylene. Also, the high pressure catalytic results will be compared and contrasted to the low pressure stoichiometric results.

Section 7.17: Discussion of UHV and High Pressure Studies on Promoted Pd Single Crystal Catalysts: Adatom Properties

To facilitate understanding of the results presented in this study, some of the important properties of the adatoms are considered first.

The four adatoms (Si, P, S and Cl) decrease slightly in atomic radius[35a] (see Table 7.3) with increasing atomic number, from 1.32 Å for Si to 0.90 Å for Cl. The atomic radius of Cl, however, ranges from 0.90 Å for the neutral Cl atom to 1.80 Å for Cl^-. The ionic radius of K is 1.33 Å. Palladium is slightly larger, with an atomic radius of 1.38 Å. Although structural data is not available for these adatoms on Pd surfaces, there is some structural data for S and Cl on Ni(111) and Pt(111)[25]. These studies show adatoms to reside generally in threefold hollow sites. Therefore we expected that Si, P, S and Cl would also chemisorb in the threefold sites of the close-packed Pd(111) surface. Due to insufficient data for the Pd(100) and Pd(110) surfaces, no conclusions can be drawn on the nature of the binding sites for the adatoms, but it is known that S on Ni(100) resides in the highest coordination site[30].

Electronegativity is another empirical parameter that differs significantly for the adatoms used in this study. To observe how the surface electonegativity changes with the addition of different adatoms to the surface, we performed work function measurements on Pd(100) (see Fig. 17). The change in work function varies linearly with the coverage of each additive. The decrease in work function is greatest for K, indicating that it donates the most electron density to the surface per unit coverage, followed by Si and then P. Conversely, S increases the work function, implying that it withdraws electron density from the surface.

Table 7.1. Pauling electronegativity[35a] and atomic radius[35a] of each adatom, palladium and hydrogen.

Element	Pauling Electronegativity	Atomic Radius (Å)
H	2.1	0.37
K	0.8	1.33[a]
Si	1.8	1.32
P	2.1	1.28
S	2.5	1.27
Cl	3.0	0.90
Pd	2.2	1.37

[a]ionic radius

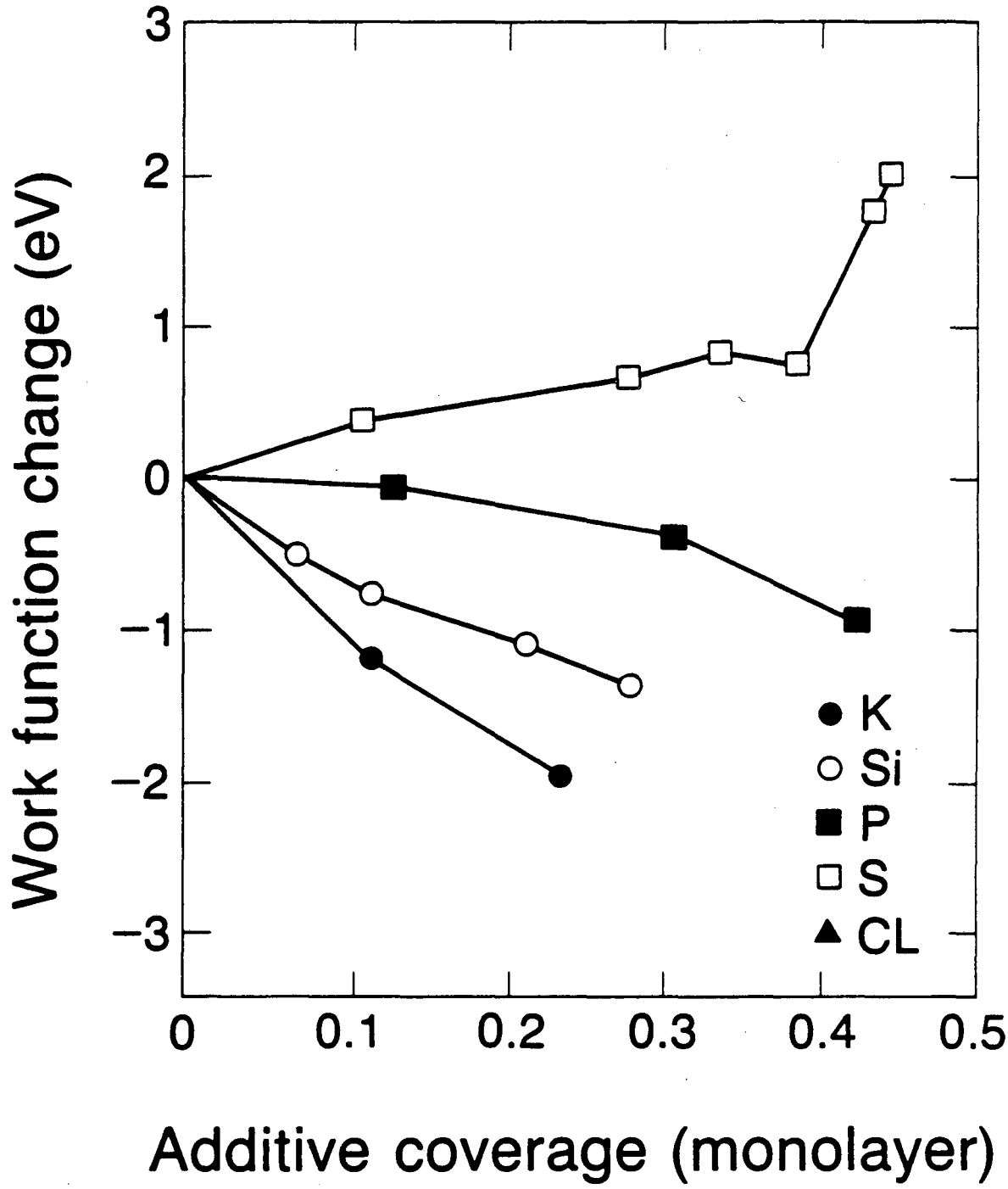

Fig. 7.17. The change in work function, $\Delta\phi$, is plotted vs. the coverage of different adatoms on Pd(100). Sulfur withdraws electron density from the surface, $\Delta\phi \sim 1$ eV at 0.33 ML of S, whereas P, Si and K donate electron density to the surface, $\Delta\phi \sim -1.5$ eV at 0.25 ML of Si.

While the atomic radii of the adatoms vary only slightly, there is a large difference in electronegativity (see Table 7.3) for the addtives. Therefore we expect that electronic interactions will have the greatest influence on the surface chemistry. The work function changes observed in our study fit with the electronegativity data very well and will be used to explain the results of the cyclotrimerization reaction studies.

Adatoms on all metal surfaces, under conditions of low pressure, have several effects on surface reactions - the additives can (1) donate or withdraw electron density from the surface, (2) form islands on the surface, (3) form surface compounds and (4) block certain reaction pathways. Studies have found K to be uniformly dispersed on metal surfaces[32,33] (except at higher monolayer coverages), and to donate electrons to the surface[19]. Sulfur and chlorine are known to form ordered islands at low coverages[30] and withdraw electron density from the surface[34]. From our work function measurements, we found P and Si to be electron donors, but not to the same extent as K (see Fig. 18). Phosphorus and silicon were found to form ordered LEED structures over some metal surfaces. For example, K forms a $\sqrt{7}$ X $\sqrt{7}$ R17° over Pd(111). Also, structures have been observed over C_g and Si[30]. Phosphorus and silicon are known to form stable compounds with many metals (Pd_2Si, PdSi, Ni_2Si, Ni_2P and Ni_5P_2)[35a,b,36].

Both acetylene and benzene are known[37-39] to donate electrons to metal surfaces. Acetylene has a low-lying antibonding orbital which is partially filled in the presence of electron donors on the metal surface, such as K[38], destabilizing the carbon-carbon bond. Benzene's antibonding orbitals have lower binding energy and thus are not filled even in the presence of K, as evidenced by the TPD and EELS work of this group[40,41].

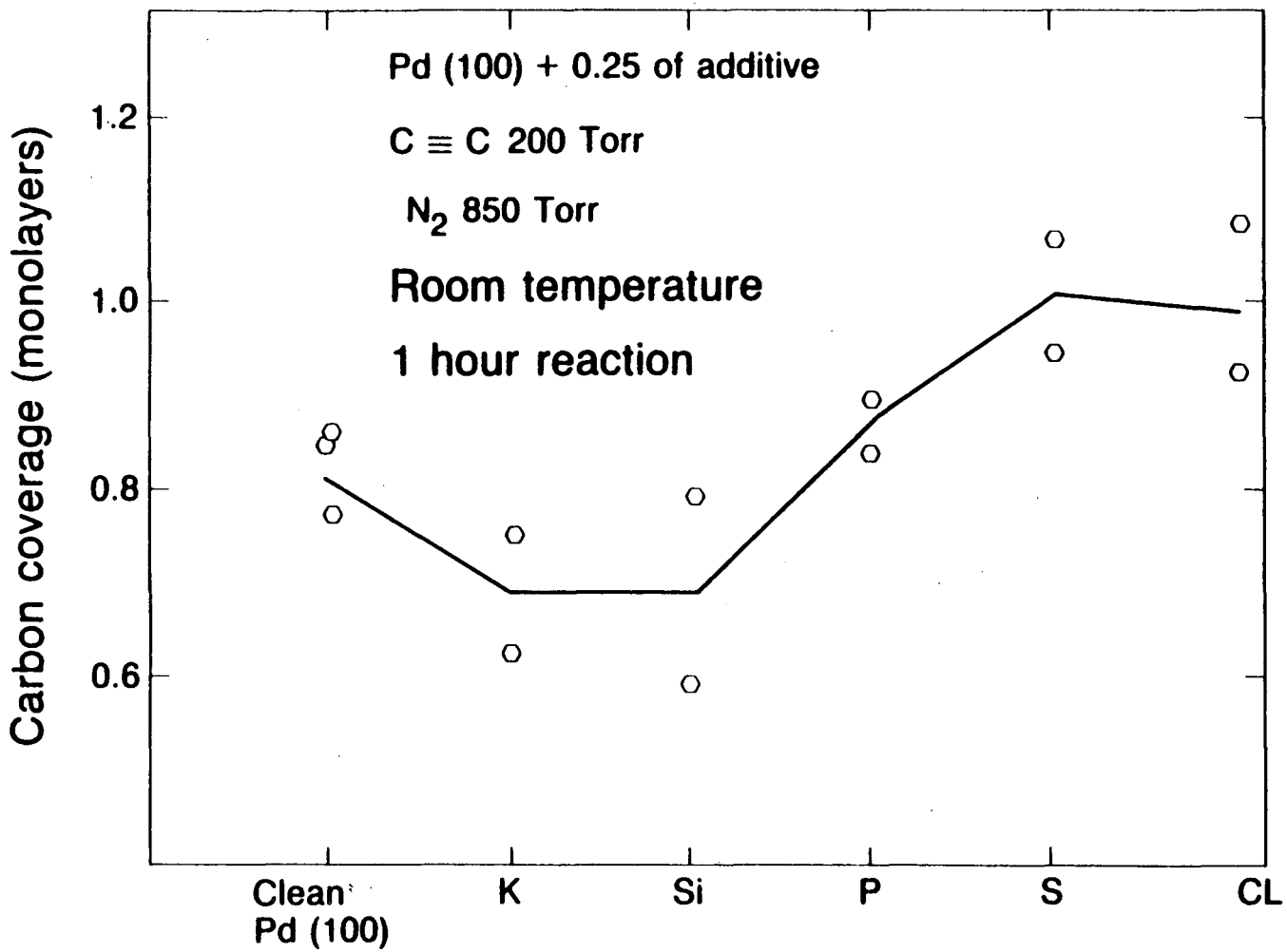

Fig. 7.18. The effect of additives on Pd(100) on final carbon coverage. Electron-donating additives (K, Si) appear to keep the palladium surface cleaner than starting with an initially clean Pd surface. Electron-withdrawing additives on Pd(100) have higher carbon levels and faster rates of poisoning relative to clean Pd(100).

From the theoretical work of Anderson[37,38] on Ni, Pt and Ag surfaces, S and Cl would be expected to poison the surface toward acetylene chemisorption. No other work has been completed on the effects of Si and P on the bonding of acetylene and benzene to metal surfaces, so no comparisons can made at this time.

Section 7.18: Discussion of High Pressure Studies on Promoted Pd Single Crystal Catalysts: Introduction

The effect of promoters at atmospheric pressures on the reaction of acetylene over single crystals of palladium has been investigated. We have previously published[6] the rate (Turnover frequency=0.05 molecules benzene/site • sec, 200 Torr acetylene, 850 Torr N_2, 570 K on Pd(111)), pressure dependence (rate of benzene=$kP_C \equiv C^{+1}$) and activation energy ($E_A \cong 2$ kcal/mol) for the formation of benzene from acetylene over Pd single crystals. In these earlier studies, we found Pd(111) and Pd(100) surfaces to have the same rate of benzene production, but on the Pd(110) surface the rate was about 25% of the rate on the (111) and (100) surfaces.

Section 7.19: Discussion of High Pressure Studies on Promoted Pd Single Crystal Catalysts: Pd(111) and Pd(100)

The additives investigated had the same effect on each of these two surfaces. Electron-donating additives were observed to enhance the rate of formation of benzene. As can be seen from Fig. 7.16, the electron-donating additives, K and Si, had a large positive effect on the rate of formation of benzene. Electron-withdrawing additives decreased the rate of production of benzene and increased the amount of carbon present on the surface after each reaction. We found that the activation energy and pressure dependence for the formation of benzene did not change, from the clean surface values, for all the modified surfaces studied.

The difference in rate of benzene formation for the different modified surfaces may be caused by the amount of open Pd surface area. The surface formed an equilibrium amount of carbon, which appeared to block reaction sites. This surface carbon could be in the form of graphite or a polymer of acetylene. It is possible that the electron-withdrawing additivies enhance the polymerization process, by acidifying the metal surface[51], thereby decreasing the rate of benzene formation. Figure 7.18 shows the amount of carbon present on the (100) surface after flashing the modified surface to 520 K in UHV. Electron-donating additives appear to keep the surface cleaner, and the rate of poisoning for surfaces modified with electron-donating additives was much slower than for the surfaces modified with electron-withdrawing additives.

Phosphorus did not fit the trend of electron donors acting to enhance the rate of benzene formation. It appears to have slightly more carbon at equilibrium than the clean Pd(100) surface, so the electron-donating power of P is not enough to stop either polymerization of decomposition.

Section 7.20: Discussion of High Pressure Studies on Promoted Pd Single Crystal Catalysts: Pd(110)

The clean Pd(110) surface was shown to have only ~ 2% open surface at equilibrium, which was used to explain the diminished rate of benzene production. The (110) surface of fcc metals can be thought of as a monotonically-stepped surface. This high density of steps is expected to be more reactive towards decomposition of acetylene. High carbon coverages on the surface under reaction conditions are therefore expected.

Additives on Pd(110) had less effect on the rate of formation of benzene than on Pd(111) and Pd(100). Potassium was found to inhibit the reaction rate and P enhanced the rate as much as Si. One explanation for K decreasing the rate of formation of benzene is that K on Pd plus acetylene induces faceting on the surface. Alkali metals are known to induce a 2 X 1 reconstruction in Ag(110) surfaces[43,44]. If K, or K + acetylene, induces a reconstruction in Pd(110) then K would be expected to sit in a deeper trough and therefore have less effect on the surface reaction, possibly just acting to block reaction sites.

Section 7.21: Discussion of UHV Studies on Promoted Pd Single Crystal Catalysts: Pd(100), Pd(111) and Pd(110)

Low pressure results for additive-covered surfaces can be explained by a combination of surface structure and electronic interactions. Potassium-covered Pd surfaces produced less benzene and less decomposition products than Si-, P-, S- and Cl-covered surfaces. Potassium is the least likely of the additives studied to form islands on the surface. At low coverages, K is known to be disordered on metal surfaces and only at coverages approaching saturation does a LEED pattern form[30]. If the adsorbate interaction is short range, then well-dispersed adatoms will produce a greater overall effect than adatoms with a clustering tendency. Less metal sites would be covered by additives such as Si, P, S and Cl, which form islands on compounds on the surface. This would help explain our results, since acetylene was not found to chemisorb to multilayers on K, due possibly to K atoms blocking sites. With dispersed K on the surface, three acetylene molecules would be less likely to be close enough together on the surface to form benzene. Our results seem to indicate that the electronic effect, as correlated to the change in work function, is not the major promotor function for K under UHV.

Ultra-high vacuum studies are summarized in Fig. 7.19, which shows the effect of each additive on the benzene yield on each surface, at a coverage of 0.25 ML. The most pronounced effect observed was that of Si on Pd(100), where at a coverage of 0.38 ML, the yield of benzene increased twenty-fold.

Significant effects on the formation of benzene from acetylene were observed from Si on Pd(100) surface and P on the Pd(111) surface. The greatly increased benzene formation over these two surfaces may be attributed

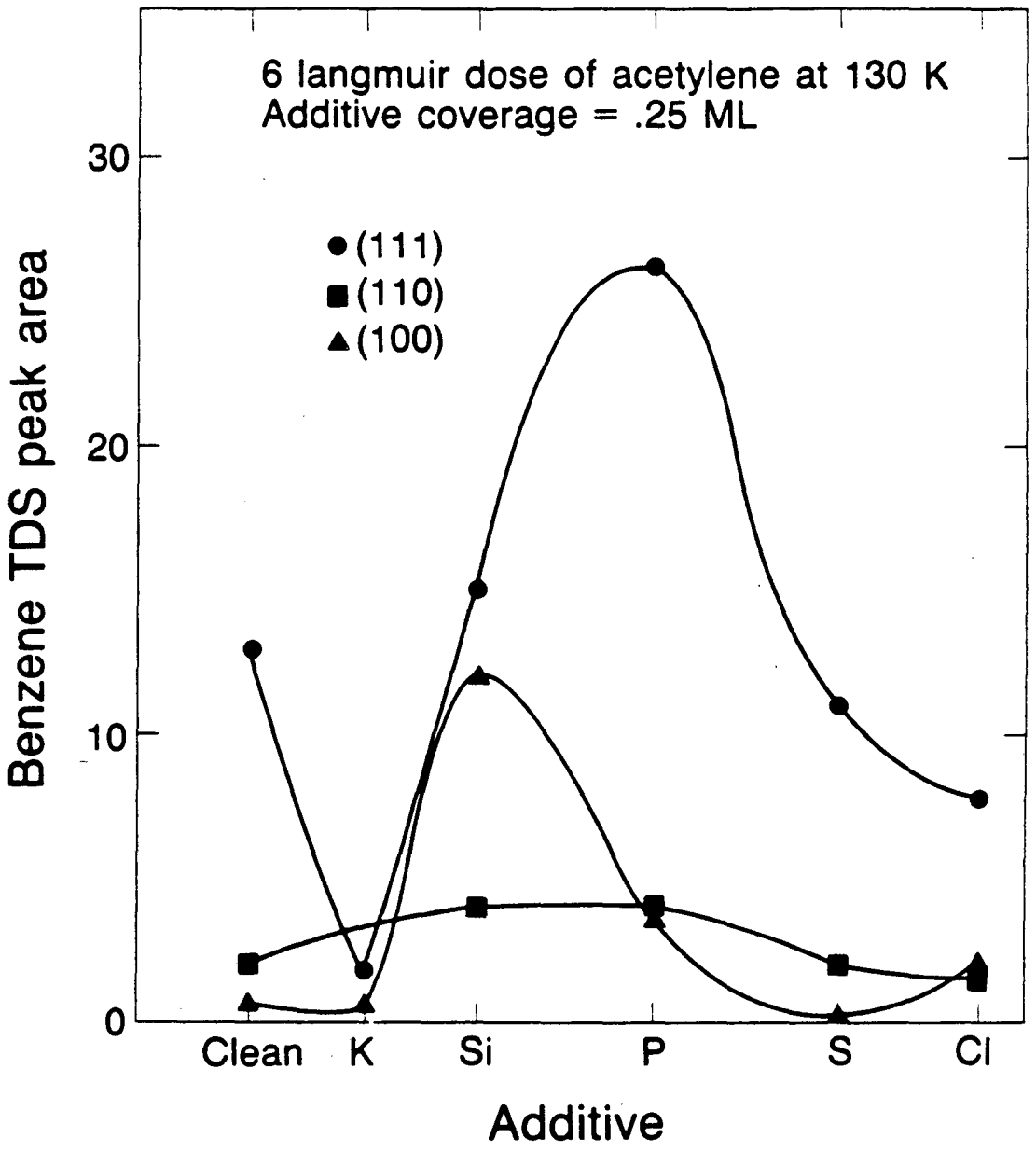

Fig. 7.19. The effect on the rate of benzene formation by additives at constant 0.25 ML coverages on different Pd single crystal surfaces is displayed. Benzene TPD spectra were recorded after a 6L dose of acetylene at 130 K. Phosphorus on Pd(111) and Si on Pd(100) have the greatest enhancement on benzene formation.

to the formation of surface compounds. The PdSi compound is known to be stable[35], and although no palladium phosphides are known, they are well know for nickel[35] (Ni_2P, melting point of 1385 K; and Ni_5P_2, melting point of 1458 K). Figure 7.20 shows evidence for the formation of a surface palladium silicide. As the temperature of the Si-covered Pd(100) surface is raised, the work function shifts dramatically, indicating a reversal of dipole moments. This shift corresponds to Si dissolution, as also shown by the slight change of the AES Si signal (no Si desorption was observed). This work function shift has been shown to indicate surface compound formation[26,45-51].

Phosphorus on Pd(111) was found to have similar changes in the work function, showing a change upon annealing the crystal. These changes were not observed for any of the other additives on any other Pd surface. In general, the work function versus coverage plot was reversible with annealing/flashing of the crystal to desorb some of the additive. Future work is planned to test the hypothesis os surface compound formation with Si and P on Pd(111) and (100).

Sulfur on Pd suppressed the decomposition reaction. Relative to the three clean surfaces, only ~ 5-10% as much H_2 and ethylene were observed (see Figs. 7.11) in the TPD experiment. As noted previously, Anderson and coworkers[37,38] predicted electron-withdrawing additives would block most acetylene adsorption and weaken the acetylene-metal bond. The weakened acetylene-Pd surface bond can account for the large decrease in decomposition observed. Benzene formation remained approximately unchanged and molecular desorption was enhanced somewhat (see Fig. 7.2,4,9). It appears that S selectively blocks hydrogenation, as has been seen previously for S on Mo in the hydrogenation of CO (see Chapter 5), as well as dehydrogenation reactions.[14,52].

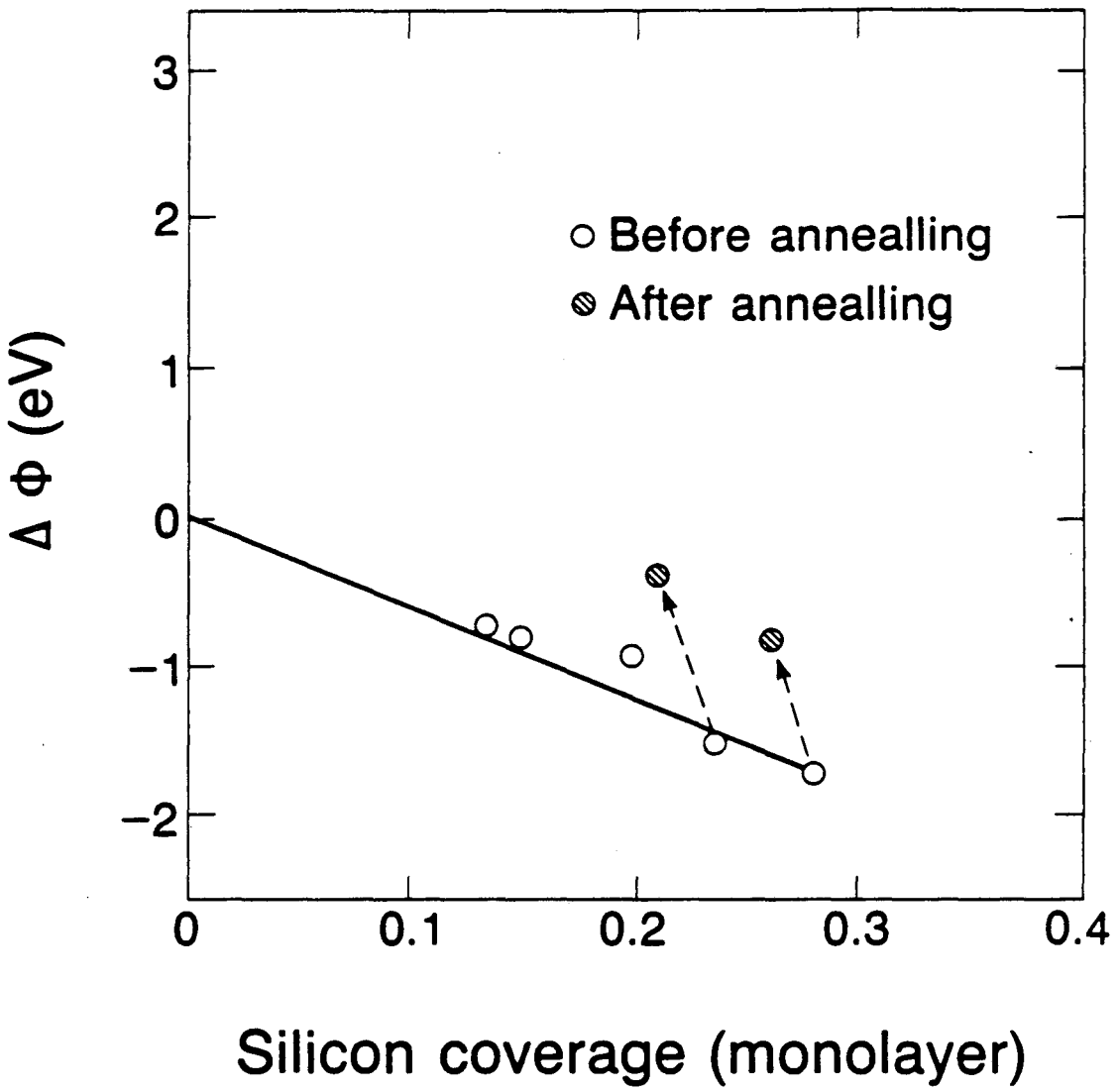

Fig. 7.20. The effect of annealing the Si-covered Pd(100) surface is displayed. Upon annealing at 700 K for 3 min., the work function shifts 0.75 - 1.25 eV, while the Si surfaces coverage remains almost constant (as measured by AES).

Chlorine also reduced the amount of acetylene decomposition, but not to the same extent as does S. Molecular desorption of acetylene was enhanced. Benzene formation was enhanced slightly on Pd(100) while it declined slighty on Pd(111) and Pd(110). Chlorine should act very much like S, because additives withdraw electron density from the surface and become enlarged as electron density is removed from the metal. Both Cl and S are known to form ordered structures at low coverages, indicating island formation. It is interesting that for similar coverages of S and Cl 2-10 times more hydrogen was formed on the chlorinated surfaces. In general, the trend from K → Si → P → S → Cl seems to indicate that increasingly electron-withdrawing additives lead to decreasing decomposition, but the most electron-withdrawing additive, Cl, breaks this trend.

The site blocking contribution to the surface reaction appears to be greatest for K and decreases as the additive atoms become more electronegative. The electron interactions increase as the additives become more electronegative.

Section 7.22: Comparison of Results of UHV and High Pressure Studies on Promoted Pd Single Crystal Surfaces

Our results for additive effects on the conversion of acetylene to benzene are quite different at high and low pressures. The high pressure catalytic results appear to depend on the amount of bare palladium exposed. At high pressures, the surface is saturated with acetylene and the formation of benzene competes with the decomposition and polymerization reactions which poison catalytic sites. Additives which keep the surface cleaner, such as K and Si, enhance the rate of benzene formation; but, S and Cl appear to enhance to polymerization or decomposition reactions, poisoning the catalytically active sites. The low pressure stoichiometric results correlate with site-blocking for electropositive additives and shifting to more of an electronic interaction for electronegative additives.

Section 7.23: References

1. Tysoe, W.T., Nyberg, G.L., and Lambert, R.M., J. Chem. Soc. Chem. Commun., 623 (1983).

2. Tysoe, W.T., Nyberg, G.L., and Lambert, R.M., Surf. Sci. 135, 128 (1983).

3. Gentle, T.M., and Muetterties, E.L., J. Phys. Chem. 87, 2469 (1983).

4. Sesselmann, W., Woratschek, B., Ertl, G., and Kuppers, J., Surf. Sci. 130, 245 (1983).

5. Gentle, T.M., Grassian, V.H., Klarup, D.G. and Muetterties, E.L., J. Am. Chem. Soc. 105, 6766 (1983).

6. Rucker, T, Logan, M.A., Gentle, T.M., Muetterties, E.L., and Somorjai, G.A., to be published.

7. Gates, J.A., and Kesmodel, L.L., J. Chem. Phys. 76, 4281 (1982).

8. Gates, J.A., Kesmodel, L.L., Surf. Sci. 124, 68 (1983).

9. Kesmodel, L.L., Laddell, G.D., and Gates, J.A., Surf. Sci. 138, 464 (1984).

10. Parshall, G.W., "Homogeneous Catalysts." Wiley, New York 1980, p. 165.

11. Maitlis, P.M., Acct. of Chem. Research 9, 93 (1976).

12. Vollhardt, K.P.C., Angewandte Chem. 23 (8), 539 (1984).

13. Broden, G., Gafner, G., and Bonzel, H.P., Surf. Sci. 84, 295 (1979).

14. Logan, M.A., Gellman, A.J., and Somorjai, G.A., J. Catal., 94, 60 (1985).

15. Ertl, G., Lee, S.B., and Weiss, M., Surf. Sci. 114, 527 (1982).

16. Kiskinova, M.P., Surf. Sci. 111, 584 (1981).

17. Campbell, C.T., and Goodman, D.W., Surf. Sci. 123, 413 (1982).

18. Luftman, H.S., and White, T.M., Surf. Sci. 139, 369 (1984).

19. Nieuwenhays, B.E., Surf. Sci. 105, 505 (1981).

20. Erley, W., Surf. Sci. 94, 281 (1980).

21. Fischer, T.E., and Kelemen, S.R., Surf. Sci. 74, 47 (1978).

22. Norskov, J.K., Holloway, S., and Lang, N.D., Surf. Sci. 137, 65 (1984).

23. Lang, N.D., Holloway, S., and Norskov, J.K., Surf. Sci. 150, 24 (1985).

24. Kiskinova, M., and Goodman, D.W., Surf. Sci. 108, 64 (1981).

25. Bartholmew, C.H., Agrawal, P.K., and Katzer, J.R., Adv. Catal. 31, 135 (1982).

26. Ertl, G., and Kuppers, J., "Low Energy Electrons and Surface Chemistry." Verlag Chemie, Weinheim 1974, p. 175.

27. Cabrera, A.L., Spencer, N.D., Kozak, E., and Davies, P.W., Rev. Sci. Instrum. 53 (12), 1893 (1982).

28. (a) Palmberg, P.W., Riach, G.E., Weber, R.E., and MacDonald, N.C., "Handbook of Auger Electron Spectroscopy." Physical Electronics Inc. 1972.

(b) Mroczkowski, Lichtman, Surf. Sci. 131, 159 (1983).

29. Davis, S.M., Zaera, F., and Somorjai, G.A., J. Amer. Chem. Soc. 104. 7453 (1982).

30. Somorjai, G.A., "Chemistry in Two Dimension: Surfaces." Cornell University Press, New York 1981.

31. Gentle, T.M., Ph.D. Thesis, Univ. Calif. Berk. 1984.

32. Pirug, G., Bonzel, H.P., and Broden, G., Surf. Sci. 122, 1 (1982).

33. Garfunkel, E.L., and Somorjai, G.A., Surf. Sci. 115, 441 (1982).

34. Maurice, V., Peralta, L., Bertlier, Ouden, J., Surf. Sci. 148, 623 (1984).

35. (a) "Handbook of Chemistry and Physics." 64th ed., CRC Press 1983.

(b) Dubois, L.H., Nuzzo, R.G., J. Am. Chem. Soc. 105, 365 (1983).

36. Calandra, C., Bisi, O., and Ottaviani, G., Surf. Sci. 4, 271 (1985).

37. a) Mehandru, S.P., and Anderson, A.B., to be published.
b) Anderson, A.B., McDevitt, M.R., and Urbach, F.L., to be published.

38. Anderson, A.B., J. Catal. 67, 129 (1981).

39. Somorjai, G.A., "Chemistry in Two Dimensions: Surfaces." Cornell University Press, New York 1981, p. 248.

40. Garfunkel, E.L., Ph.D. Thesis, Univ. Calif. Berk. 1983.

41. Crowell, J., Ph.D. Thesis, Univ. Calif. Berk. 1982.

42. Satherfield, C.N., "Heterogeneous Catalysis in Practice." Ch. 7, McGraw-Hill, New York 1980.

43. Heyden, B.E., Prince, N.C., Davies, P.J., Paolucci, G., and Bradshaw, A.M., Solid State Commun. 48, 325 (1983).

44. Francis, S.M., and Richardson, N.V., Surf. Sci. 152/153, 63 (1985).

45. Bauer, E., Poppa, H., and Viswanath, V., Surf. Sci. 58, 517 (1976).

46. Kramer, H.M., and Bauer, E., Surf. Sci. 92, 53 (1980); 93, 407 (1980).

47. Zingermann, Y.P., and Ishchuk, V.A., Fiz. Tver. Tela. 9, 2529 (1967).

48. Holloway, P.H., and Hudson, J.B., Surf. Sci. 43, 123 (1974).

49. Demuth, J.E., and Rhodin, T.N., Surf. Sci. 45, 249 (1974).

50. Akimoto, K., Sakisaka, Y, Nishijma, M., and Onichi, M., Surf. Sci. 82, 349 (1979).

51. Papageorgopoulos, C.A., and Chen, J.M., Surf. Sci. 52, 40 (1975).

52. Godbey, D.J., personal communication.

53. Berthelot, M., C.R. Acad. Sci. 62, 905 (1866).

54. Reppe, W., and Schweckendieck, W.J., Liebigs Ann. Chem. 560, 104 (1948).

55. Redhead, R.A., Vacuum 12, 203 (1962).

56. Zaera, F., Ph.D. Thesis, Univ. Calif. Berk. (1984).

CHAPTER EIGHT: CONCLUSIONS

Section 8.1: Overview

The effect of additives on catalysts for the hydrogenation of carbon monoxide and the cyclotrimerization of acetylene has been investigated using both low pressure surface science techniques and high pressure reaction studies. Additives were found to have relatively complicated catalytic behavior, which could be explained with the aid of surface analytical tools such as AES, XPS, TPD, and LEED. Potassium was found to have the greatest effect on both the hydrogenation of CO and the cyclotrimerization of acetylene over all metal catalysts.

Section 8.2: Hydrogenation of Carbon Monoxide

Hydrogenation of carbon monoxide was carried out over Mo, Rh, mixed oxides of Rh and 3d transition metal perovskites.

The hydrogenation of CO on Mo surfaces in the pressure range 1-10 atm and temperature range 520-670 K, primarily produces methane, ethene and propene. The reaction rate exhibits positive order in CO pressure for CH_4 formation unlike other methanation catalysts. The reaction also produces a large fraction of ethene and propene instead of saturated hydrocarbons as observed for other transition metal catalysts (Fe, Re). The addition of K to the surface, at low coverages, causes an increase in the overall rate and a shift in selectivity toward unsaturated products. This has been explained in terms of an electronic effect by which K induces back-donation of electrons into the CO 2 π * orbital, increasing the amount of CO dissociation on the surface. The addition of S to the surface, on the other hand, causes a decrease in the overall rate, but again, an increase in the fraction of unsaturated products. This has been explained in terms of selective adsorption site blocking, preferentially reducing the amount of hydrogen on the surface.

For hydrogenation of CO over Rh polycrystalline foil catalysts, a large equilibrium deuterium isotope effect is observed. The activation energy for the reaction is similar to other methanation catalysts. Also, the pressure dependence of the reaction obeys the rate law:

$$\text{Rate}_{CH_4} = K P^{+1}_{H_2} P^{-1}_{CO}.$$

These observations lead to the conclusion that one of the final hydrogenation steps in the reaction mechanism is rate-limiting.

Over oxides of Rh and La perovskites, the products of the hydrogenation of CO were found to be very dependent on the oxidation state of the transition metal catalysts. The activity is lower for the oxide catalysts relative to clean metal catalysts with the same active metal center. For the transition metal perovskites, the overall activity increases from left to right on the periodic table, from Cr to Co.

Section 8.3: Cyclotrimerization of Acetylene

Acetylene cyclotrimerization over additive-covered Pd(111), (100) and (110) single crystal surfaces at both high (~ 1 atm) and low (~ 10^{-12} atm) pressures has been studied.

At low pressures the reaction was found to have a high degree of structure sensitivity for the formation of benzene, Pd(111) > Pd(110) > Pd(100). At low pressures, additives had large effects of the amount of benzene formed. On Pd(111), addition of P to the surface (0.25 ML) doubled the amount of benzene formed, while K (0.25 ML) greatly reduced the amount of benzene relative to the clean suface (see Fig. 7.19). Benzene formation on Pd(100) increased 15 fold, relative to clean Pd(100), with the addition of 0.25 ML of Si, possibly due to formation of a Pd silicide. The effect of additives on the low pressure stoichiometric reaction can be explained by a combination of surface structure and electronic interactions.

The effect of additives on the high pressure catalytic conversion of acetylene to benzene was much different than on the low pressure stoichiometric reaction. At high pressures, the dominant factor in the rate of benzene formation appeared to be the number of active sites on the surface. The amount of graphite or polyacetylenic carbon on the surface decreased with electron-donating additives (K, Si) on the surface, relative to clean Pd (see Fig. 7.18), and increased with electron-withdrawing additives (S, Cl). The structure sensitivity at high pressures for additive-covered surfaces was found to be in the same order as at low pressures, Pd(111) > Pd(110) > Pd(100), when only the active surface (free of carbon) is taken into account. Much less difference in the overall rate of benzene formation over the three surfaces is observed at high pressures.

APPENDIX: CYLINDRICAL MIRROR ANALYZER SCHEMATICS AND PHOTOGRAPHS

Section A.1: Materials and Suppliers

Schematics for the double pass cylindrical mirror analyzer (CMA) used in the studies discussed in this thesis are shown in Figs. A.1 - A.37 and and Photographs A.38 - A.53. Not shown are schematics for the field terminating plates, which were purchased from the vacuum division of Physical Electronics. The Mu metal shields, shown in Figs. A.19 - A.22 and Photographs A.38,39, were purchased from

Mu Shield Company
121 Madison St.
Malden, MA 02148
(617) 321-4410.

Vacuum feedthroughs were purchased from Varian (Rotary-Varian 954-5151, 10 pin-Varian 954-5033). The channeltron used was purchased from Gallileo (5800 series, high voltage model). The wire meshes used were tungsten 100 X 100 with 0.001 in. wire and 50 X 50 with 0.002 in. wire and purchased from

Unique Wire Weaving
762 Ramsey Ave.
Hillsdale, WI.

All ceramic components are composed of 100% Al_2O_3 and were built in the ceramic shop at LBL by Will Lawrence and Bill Wilkie. All measurements shown in the figures are in units of inches.

Section A.2: Overview of Schematics

Figs. A.1 - A.12 are the schematics for the double pass CMA.

Figs. A.13 - A.18 are schematics for the pivoting aperature for switching from Auger to XPS mode.

Figs. A.19 - A.22 are schematics for the outer Mu metal shielding for the CMA.

Figs. A.23 - A.37 are schematics for the internal electron gun which is used for Auger electron spectroscopy.

Section A.3: Abbreviations Used in Schematics

Be-Cu = Berrilium-Copper

CL = center line

CCF = conflat flange

FH = flat head screw

HEX = hexagonal head screw

IC = inner cylinder

ID = inside diameter

OC = outer cylinder

OD = outside diameter

OFHC = oxygen-free high purity copper

R = radius

SH = socket head

304SST = 304 stainless steel

Vac = vacuum

Section A.4: Figs. A.1 - A.12

The main body of the double pass CMA is shown in Figs. A.1 - A.12. Photographs A.40 - A.43 and A.47 - A.52 show the CMA being disassembled piece by piece.

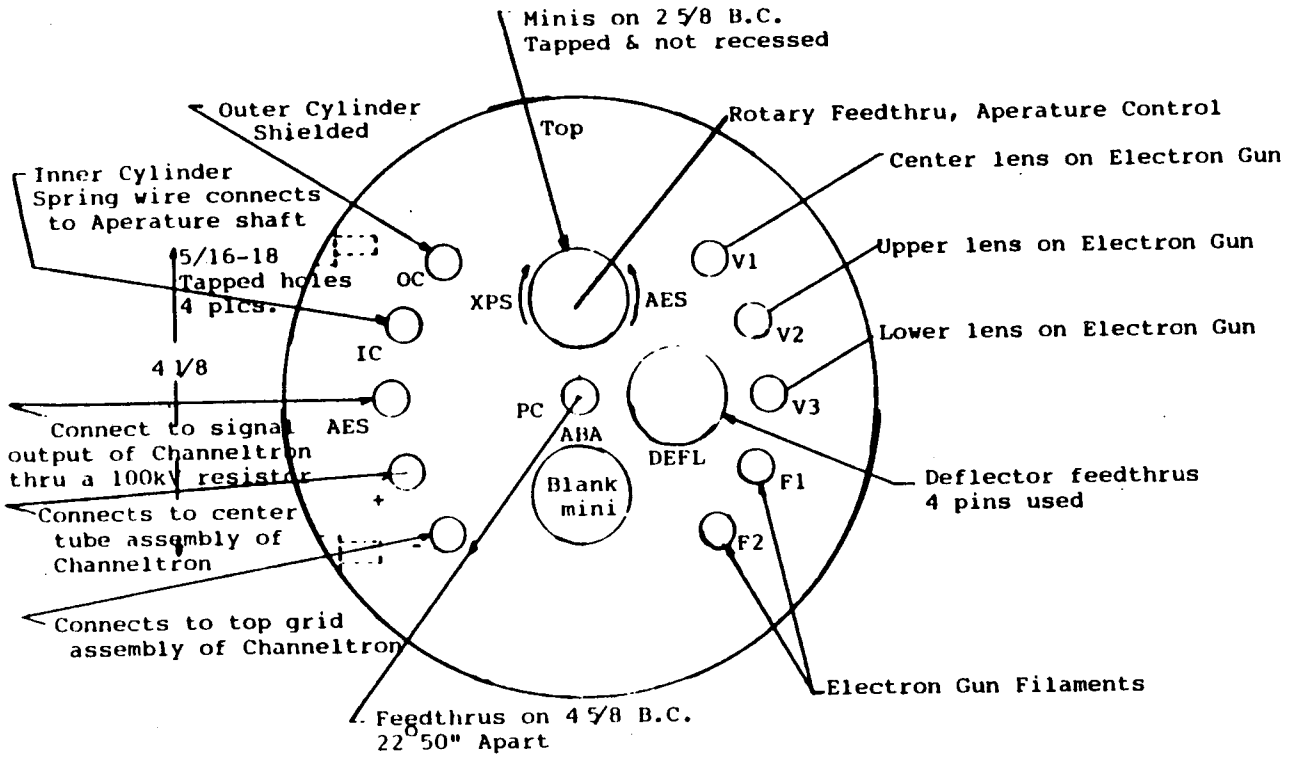

Fig. A.1. 8-in. conflat flange for mounting the CMA to the vacuum chamber has a 10 pin feedthrough mounted on a mini flange, a rotary feedthrough to move the pivoting aperatures (see Fig. A.13 - A.18), and 11 high voltage feedthroughs.

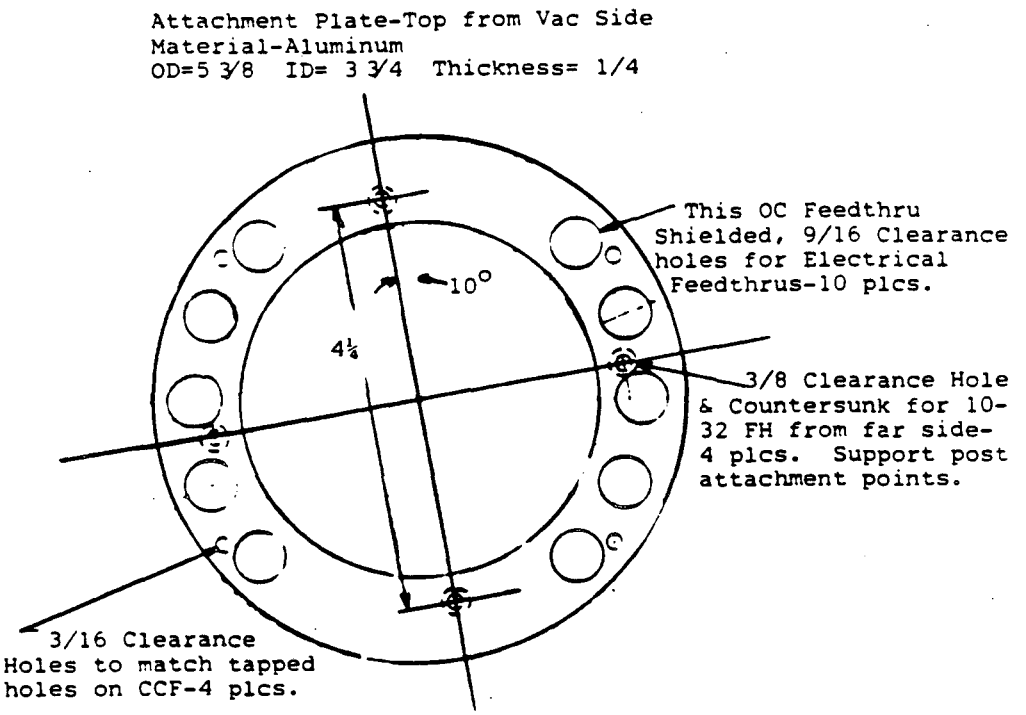

Fig. A.2. The aluminum attachment plate for the support posts is also the attachment point for the OC shielding (see Photograph A.49).

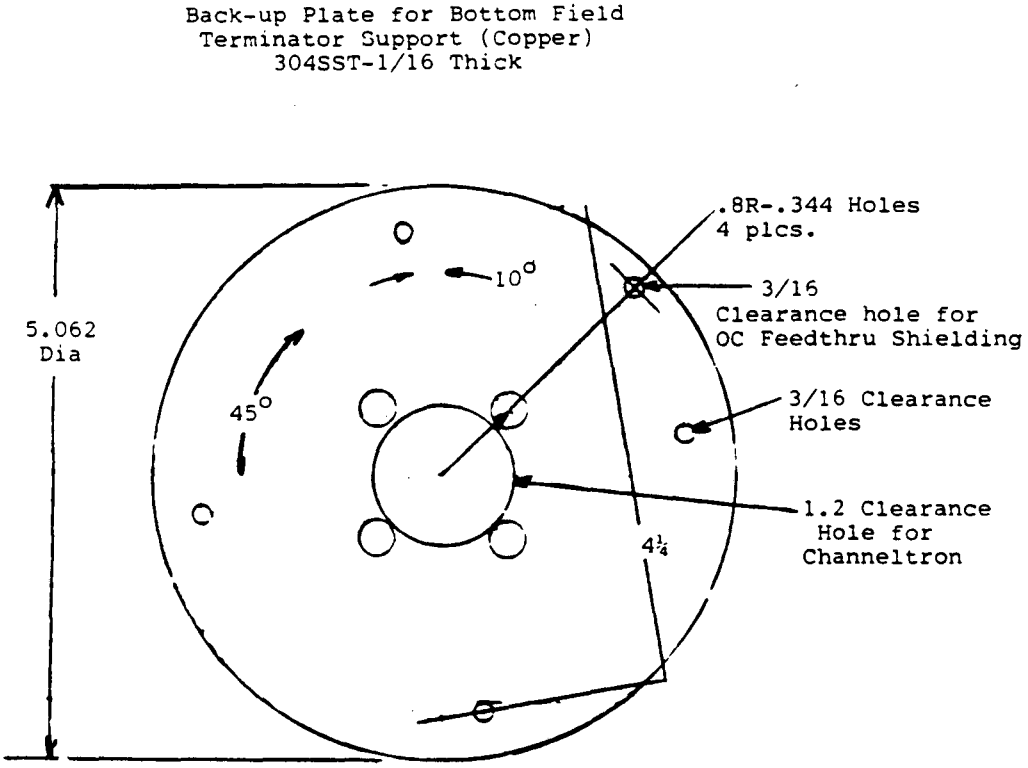

Fig. A.3. The back up plate for the final field terminator support is held above the channeltron by four support posts (see Photograph A.48).

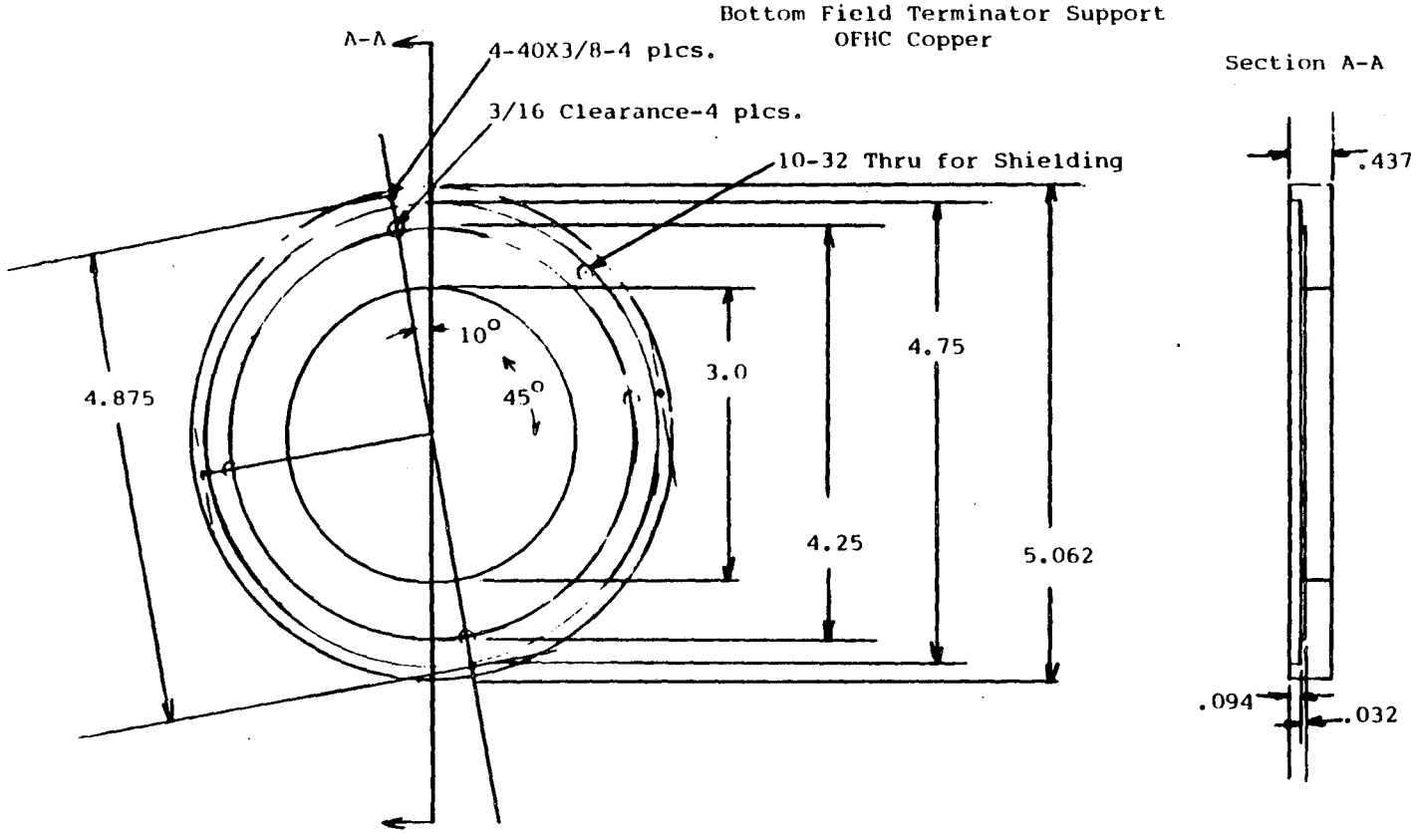

Fig. A.4. The bottom copper field terminator support is attached to the back up plate (see Fig. A.3, Photograph A.48).

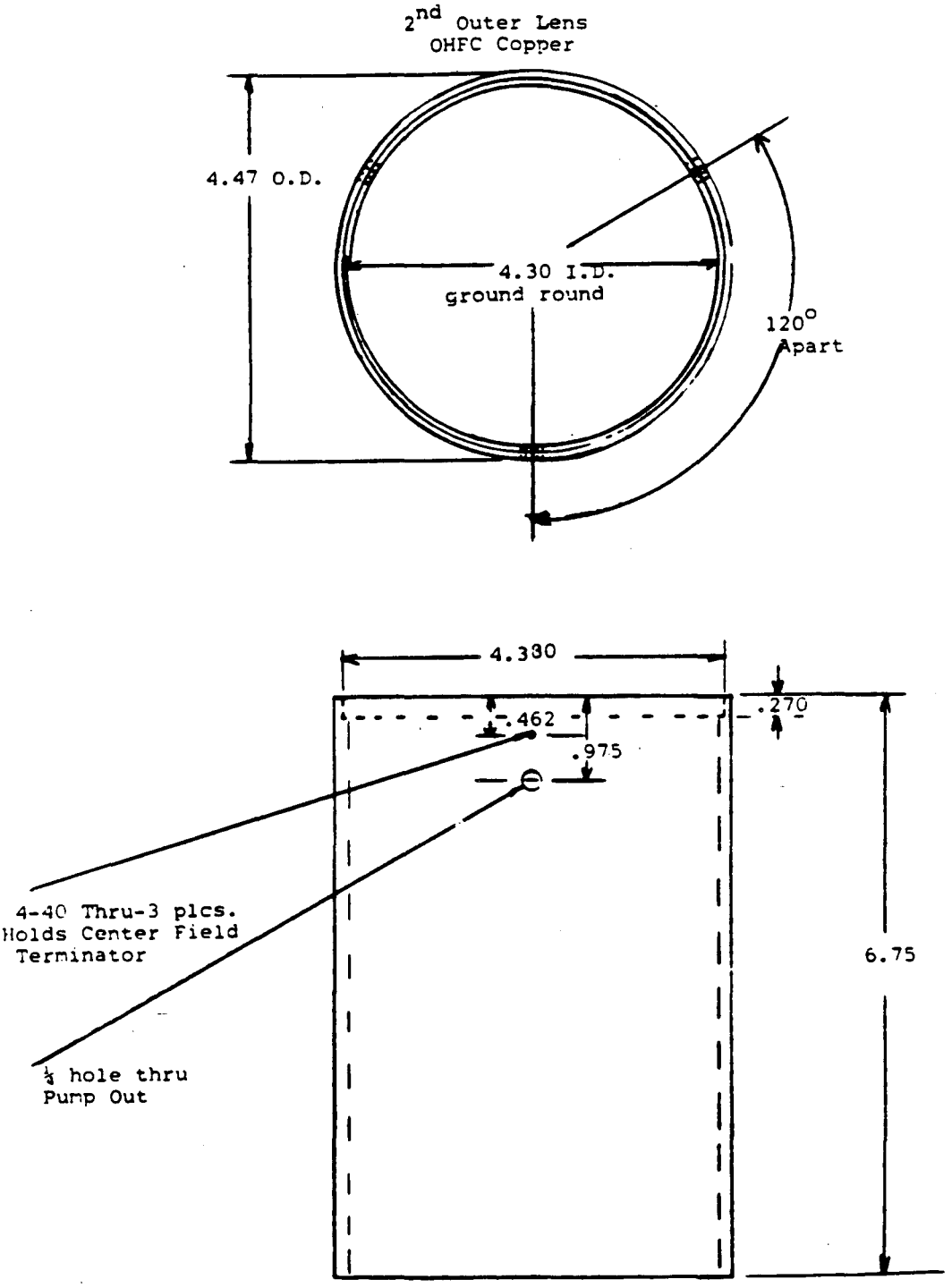

Fig. A.5. The lower oxygen free copper outer cylinder (see Photograph A.41). The middle field terminator is held by three 4-40 allen head screws.

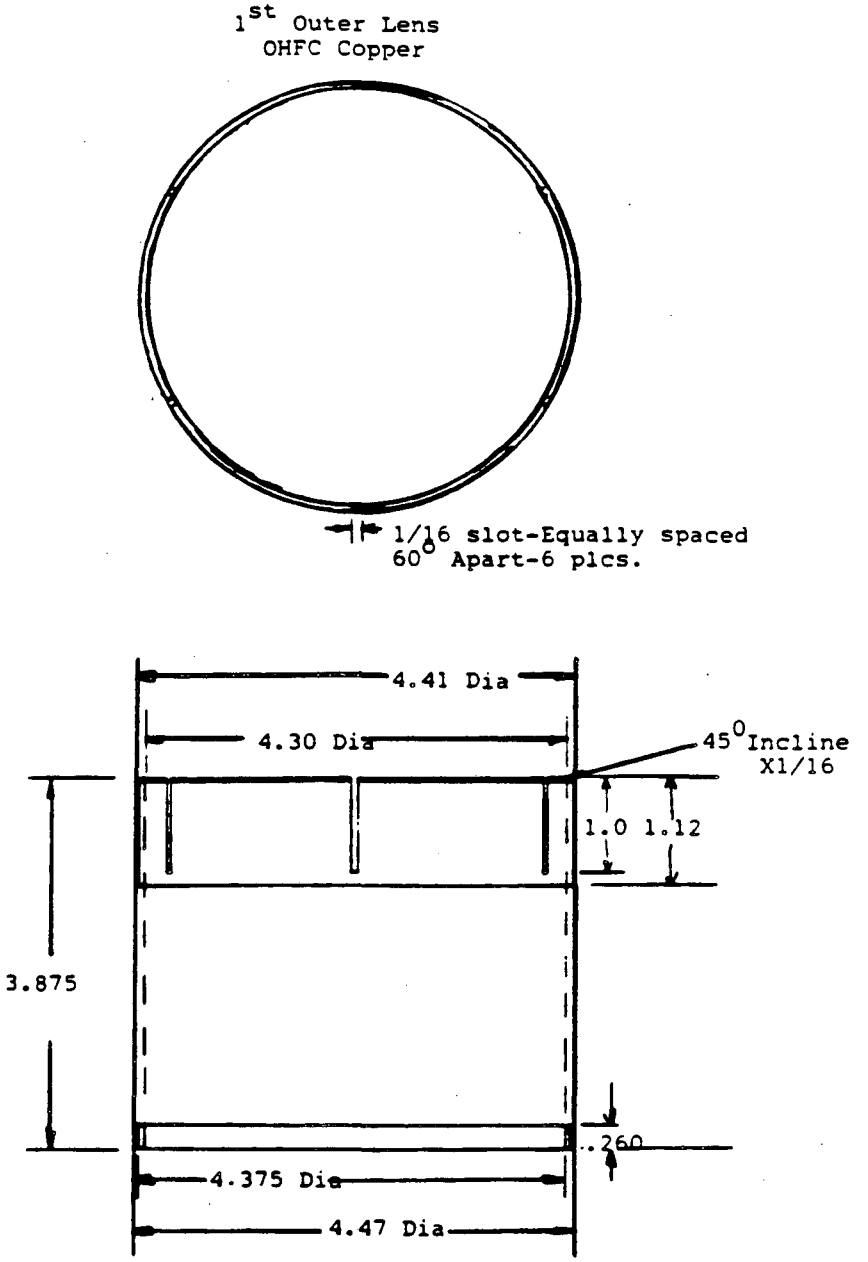

Fig. A.6. The upper oxygen free copper cylinder. The bottom interlocks into the bottom outer cylinder and the top field terminator rests on the slotted top (see Photograph A.40).

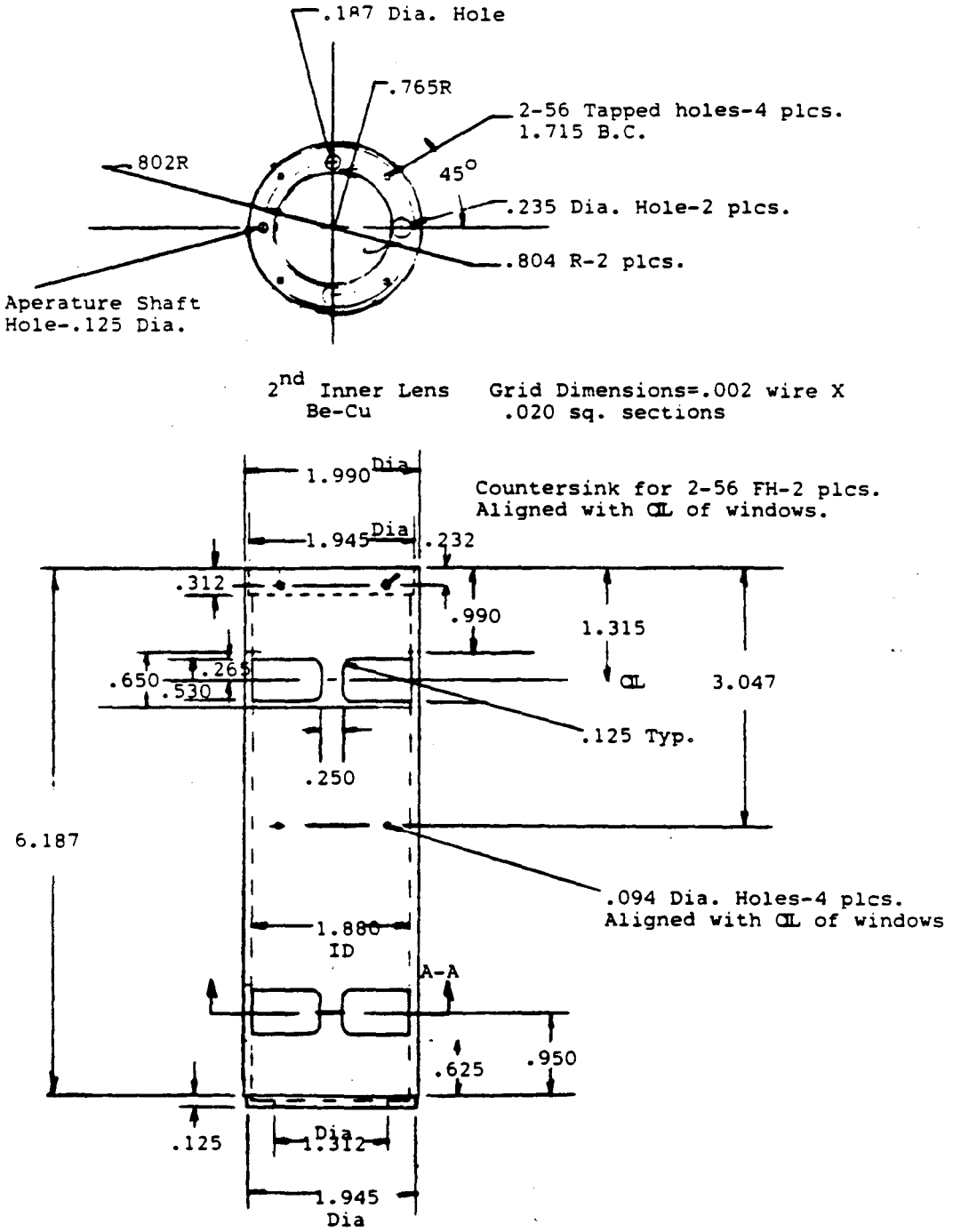

Fig. A.7. The lower Be-Cu inner cylinder with tungsten mesh-covered electron windows (see Fig. A.9). The middle field terminator sits on top of this cylinder and is held in place by the upper inner lens (see Fig. A.8, Photographs A.42,43).

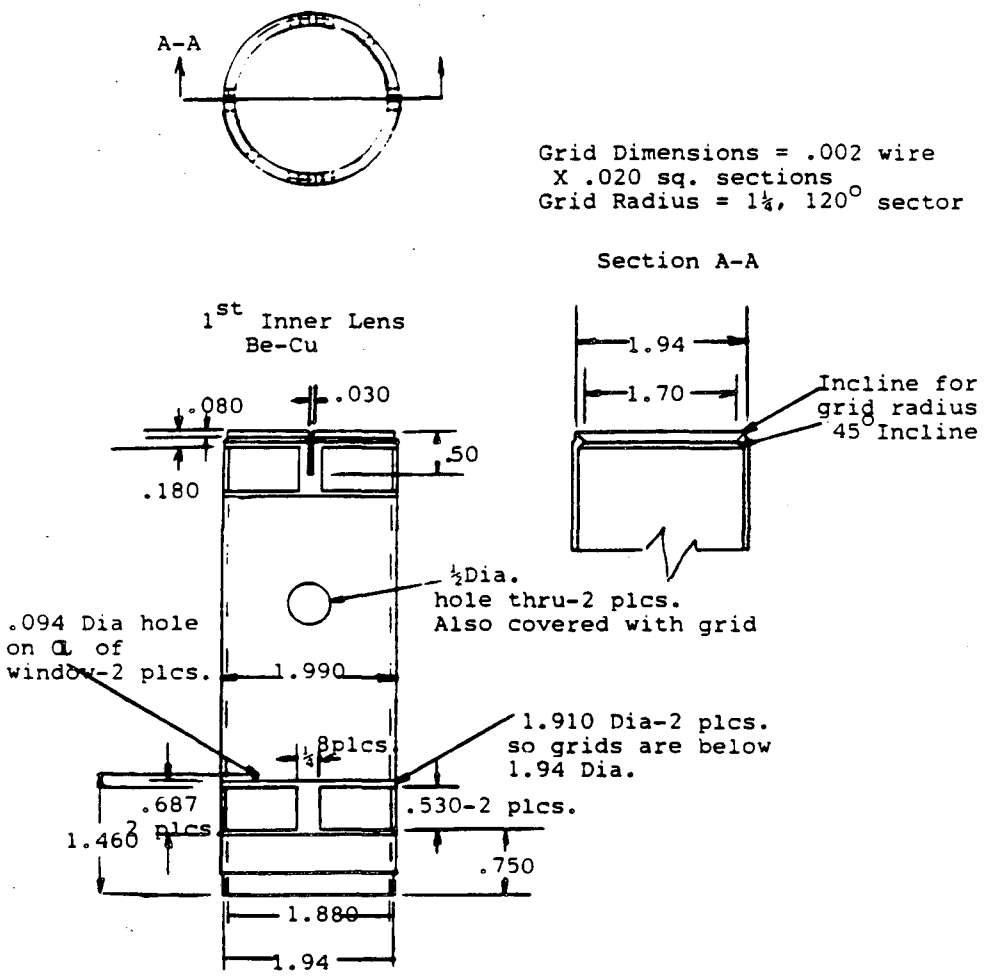

Fig. A.8. The upper Be-Cu inner cylinder. The middle field terminator is held by the long shoulder on the bottom of this inner cylinder (see Photograph A.5l). The top field terminator rests on the top of the cylinder and the electron gun sits between the grid-covered electron windows (see Fig. A.9).

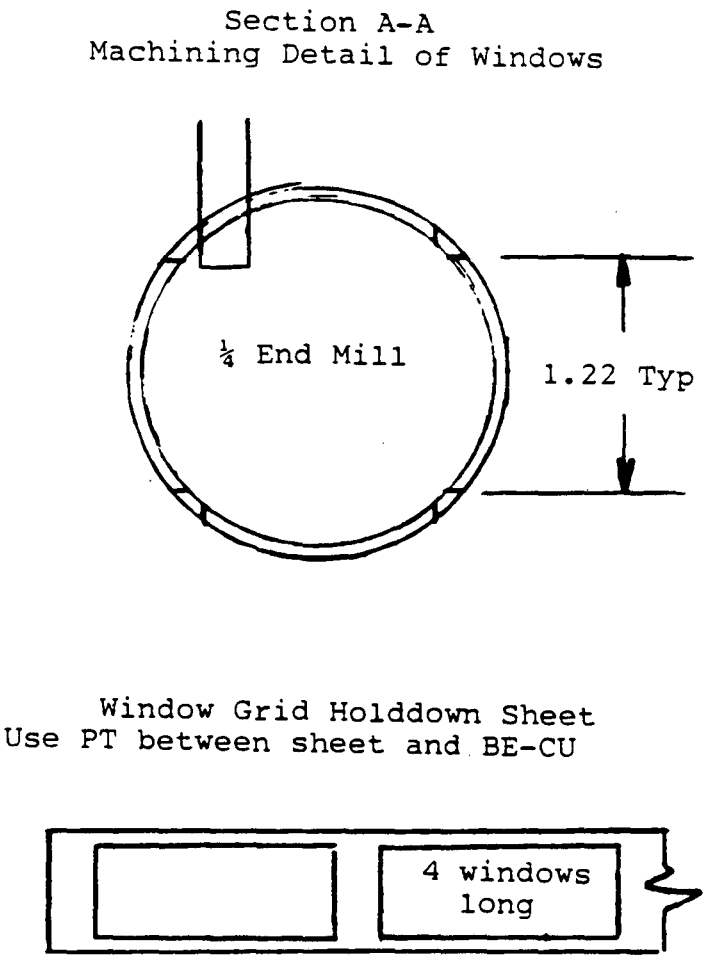

Fig. A.9. Detail of the electron windows for the inner cylinder.

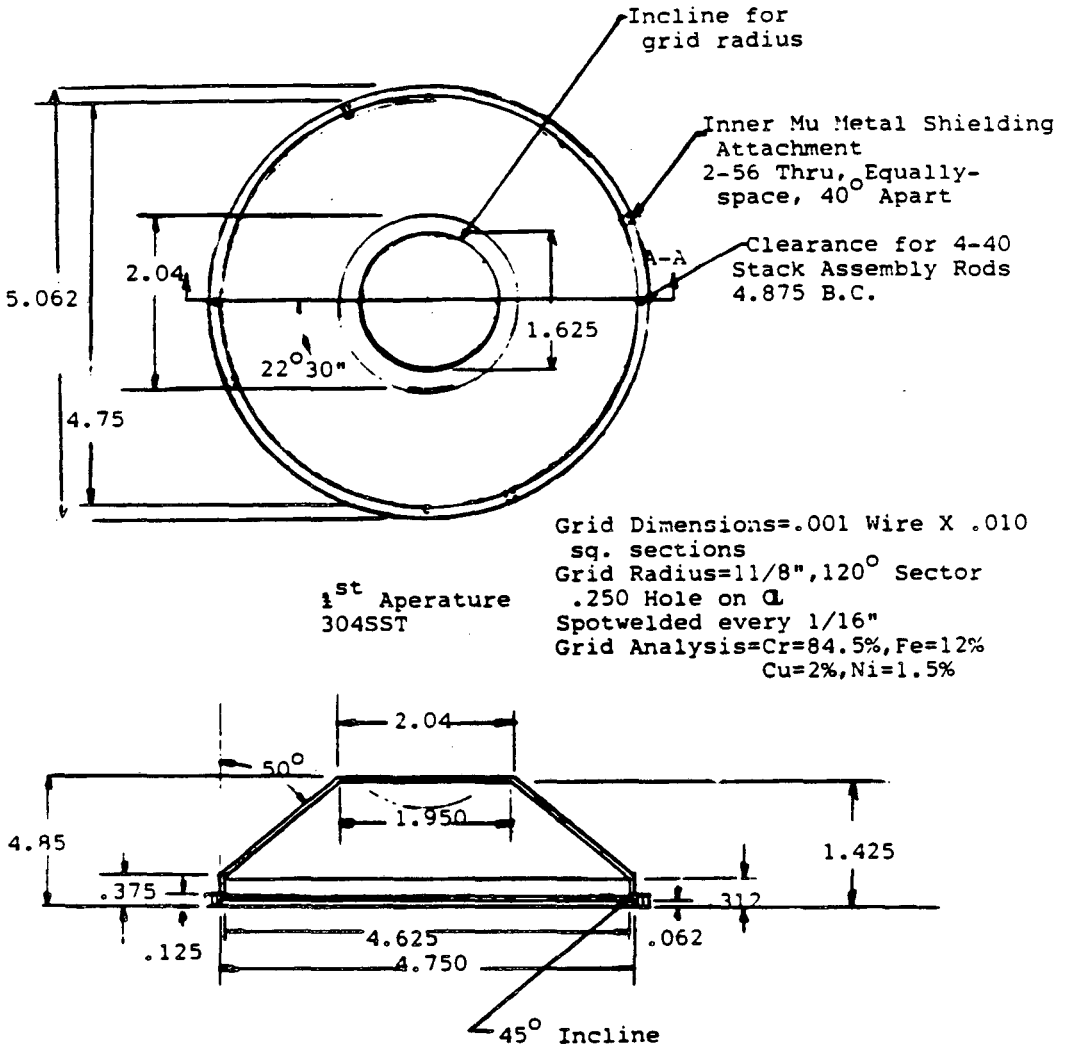

Fig. A.10. The cover shield for the CMA, with attachments for the stack assembly rods (see Fig. A.11), and inner Mu shield. The shield has a hemispherical grid spotwelded on the top (see Photograph A.50).

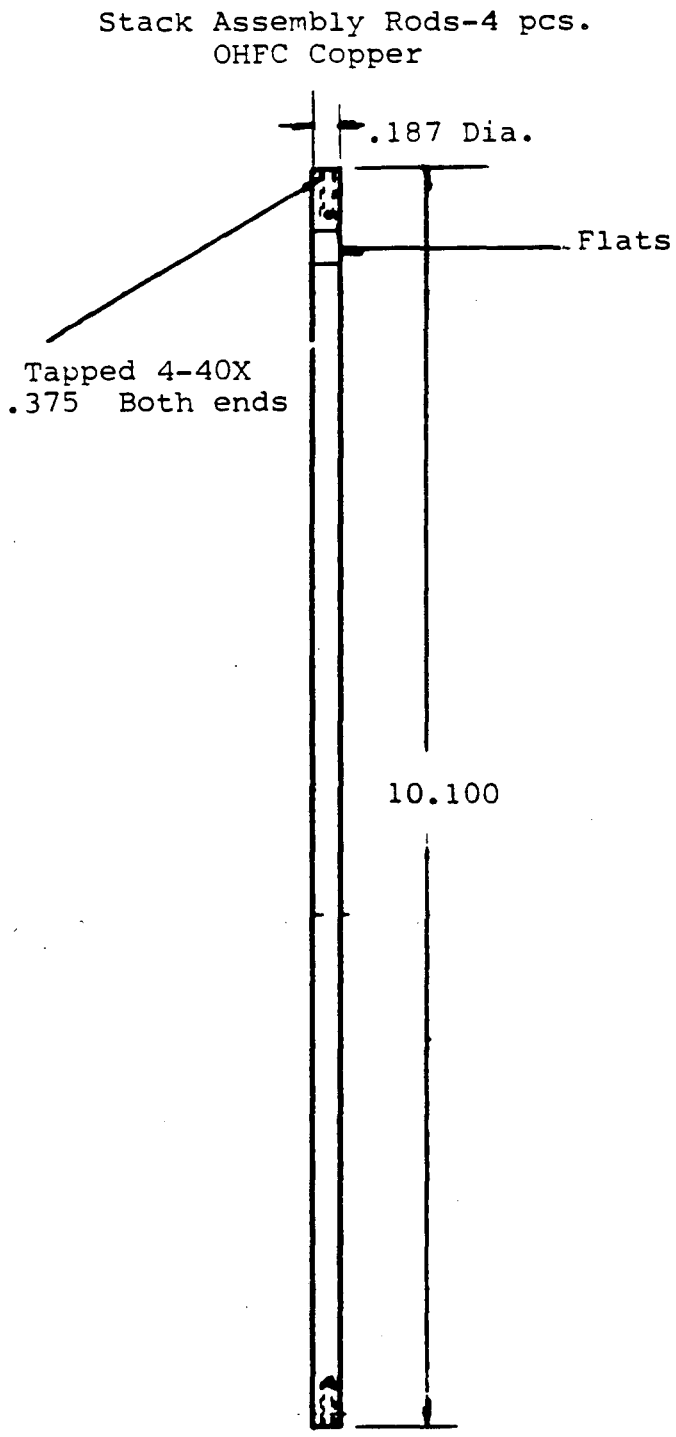

Fig. A.11. The OHFC copper stack assembly rods (see Photographs A.40,41).

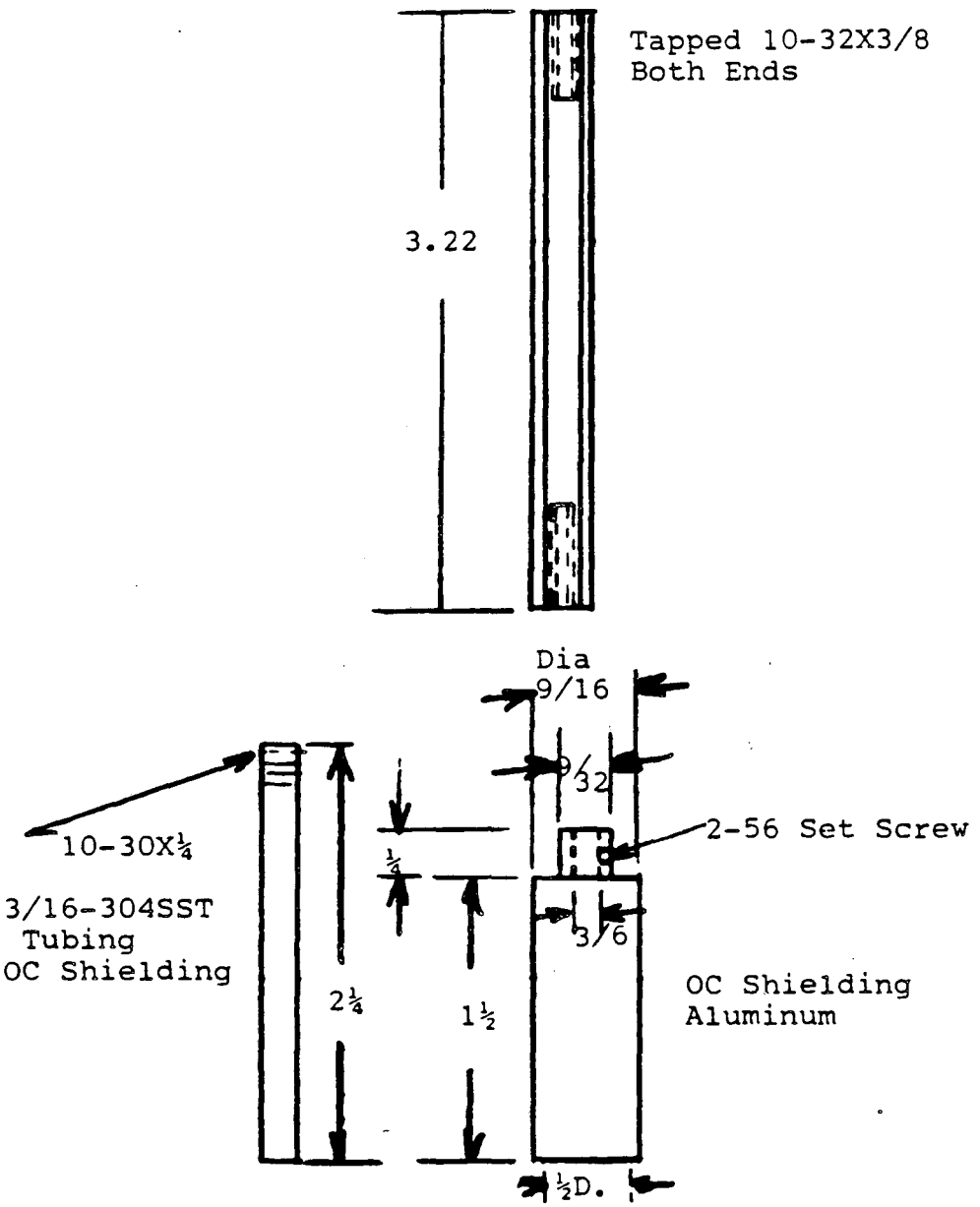

Fig. A.12. The bottom terminator support posts and outer cylinder aluminum shielding (see Photograph A.49).

Section A.5: Figs. A.13 - A.18

The pivoting aperatures are incorporated into the CMA for changing from AES to XPS mode. The electron flux for AES is much higher than that for XPS, therefore, to extend the channeltron lifetime, smaller aperatures are used in the AES mode. The pivoting aperatures are located above the channeltron and at the field terminating plate (at the apexes of the electron flux through the CMA).

Fig. A.1 shows the rotary feedthrough used to move the aperature. The aperatures are connected by a 0.125" stainless steel rod. The rod is inserted through the "aperature shaft hole" in each aperature (see Figs. A.15,16) and moved by the rotary feedthrough on the 8" CCF (see Fig. A.13) moving the pivoting aperature lever arm (see Fig. A.17). The 0.125 rod rotates 45° and is attached to the two pivoting aperatures. The 0.125 rod is attached to the 8" CCF as shown in Photographs A.47,49.

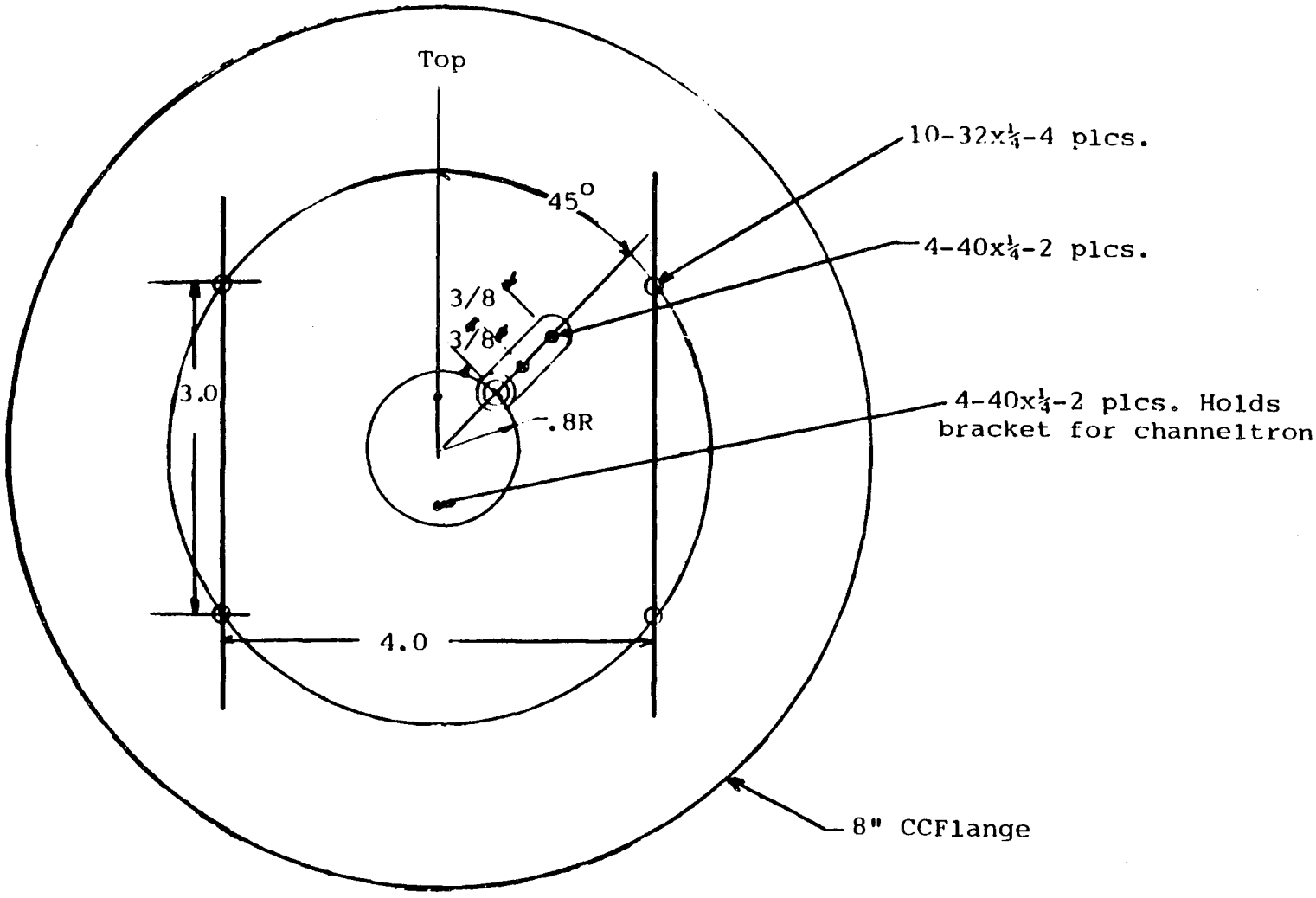

Fig. A.13. The back of the 8" CCF with the pivoting bracket (see Photographs A.47,49).

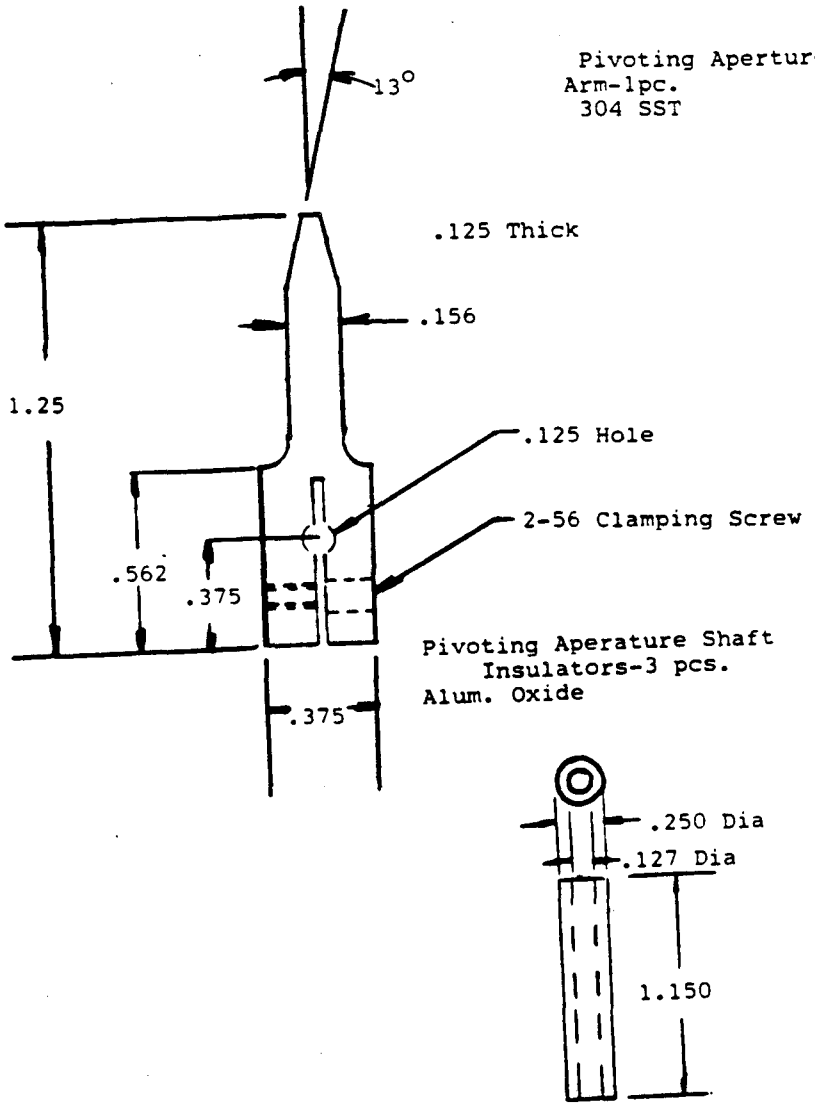

Fig. A.14. The pivoting aperature arm which is activated by the rotary feed-through. The 0.125 rod is attached with the clamping screw (see Photograph A.49) insulators for the 0.125 rod, to go inside the outer cylinder of the CMA.

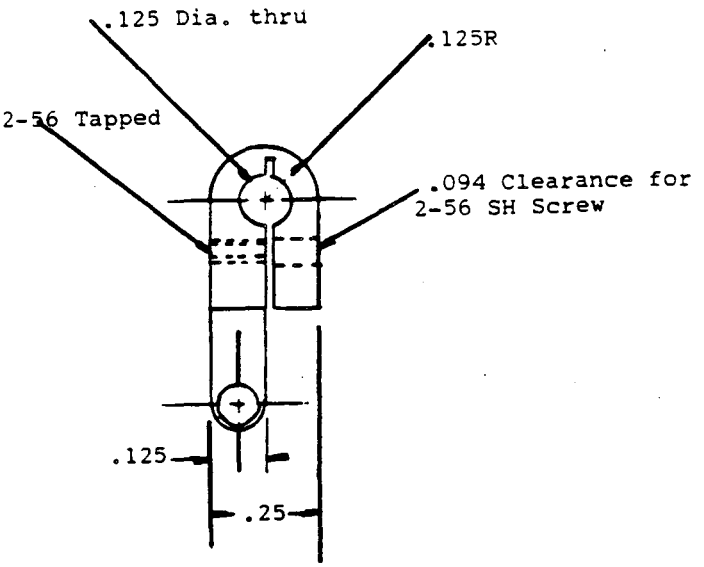

Aperature Pivot Arm

BE-CU 2 pcs.

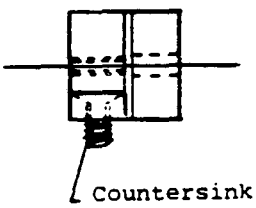

Countersink & Tap Hole for
0-80 FH Screw
Screw to stick down .180

SST-Pivoting Aperature Shaft-.125 Dia X
9.75 Long

BeCu-2 Thrust Bushing=.250 O.D. X .128 I.D. X
.125 Thk
One has 2-56 Tapped hole radially into
.127 I.D. for Set Screw

Fig. A.15. The pivot arm connected to 0.125 shaft is inserted in the oval hole of the pivoting aperature (see Photograph A.45, Fig. A.18).

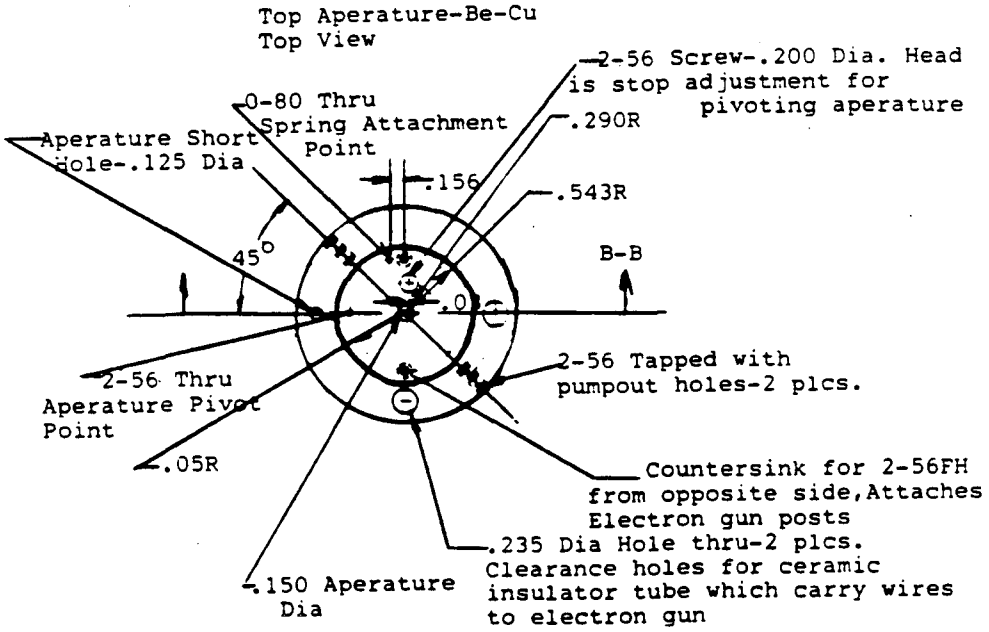

Section B-B

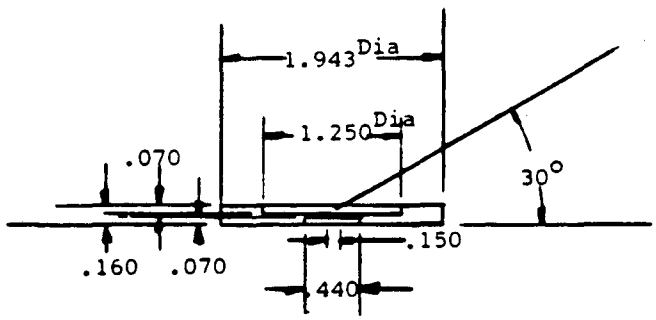

Fig. A.16,17. The top and bottom aperatures each have an aperature hole, spring attachment point and stop to hold the pivoting aperature in the correct position (see Photograph A.45).

Bottom Aperature Top View
Pivoting Aperature Not Shown
Same as Top Aperature

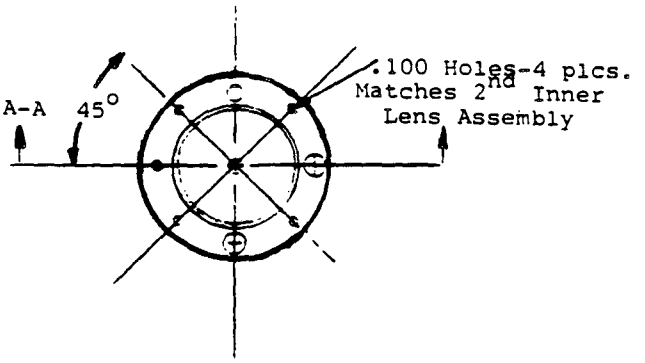

Section A-A

Pivoting Aperature Dia=.062
Grid spotwelded to underside
Grid is .002 wire, .020 square sections

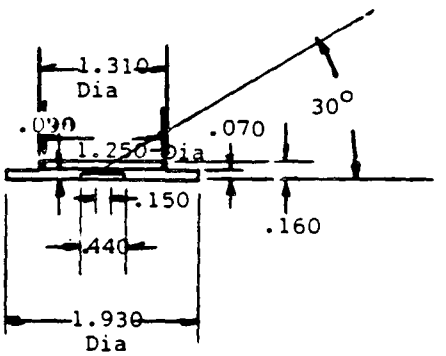

Fig. A.17. See previous figure for description.

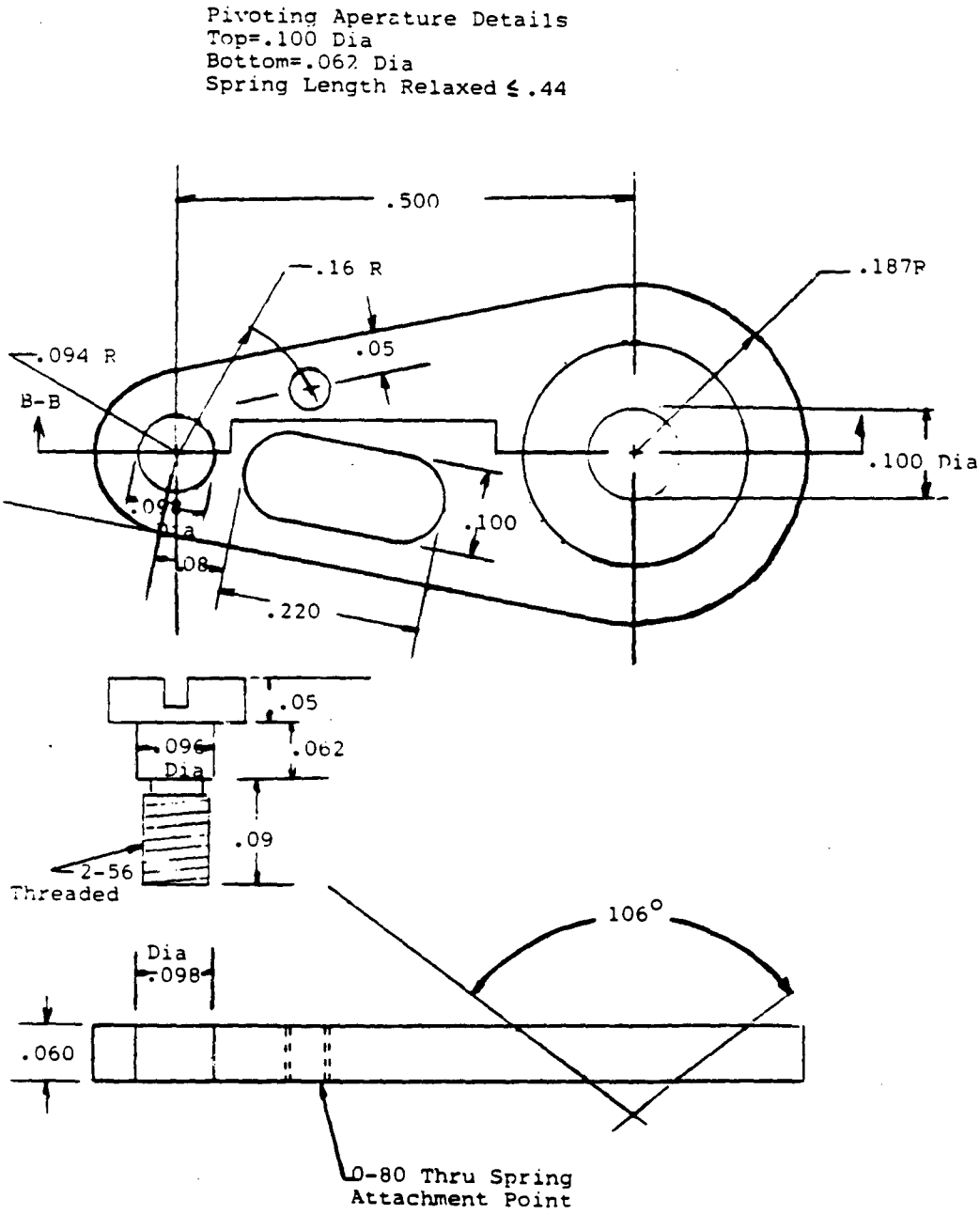

Fig. A.18. The pivoting aperature. The top aperature is 0.100 in diameter and the bottom aperature is 0.062 in diameter (see Photograph A.45).

Section A.6: Figs. A.19 - A.22.

The Mu metal shield shown in Figs. A.19 - A.22 and Photographs A.38,39 insure uniform magnetic fields inside the CMA.

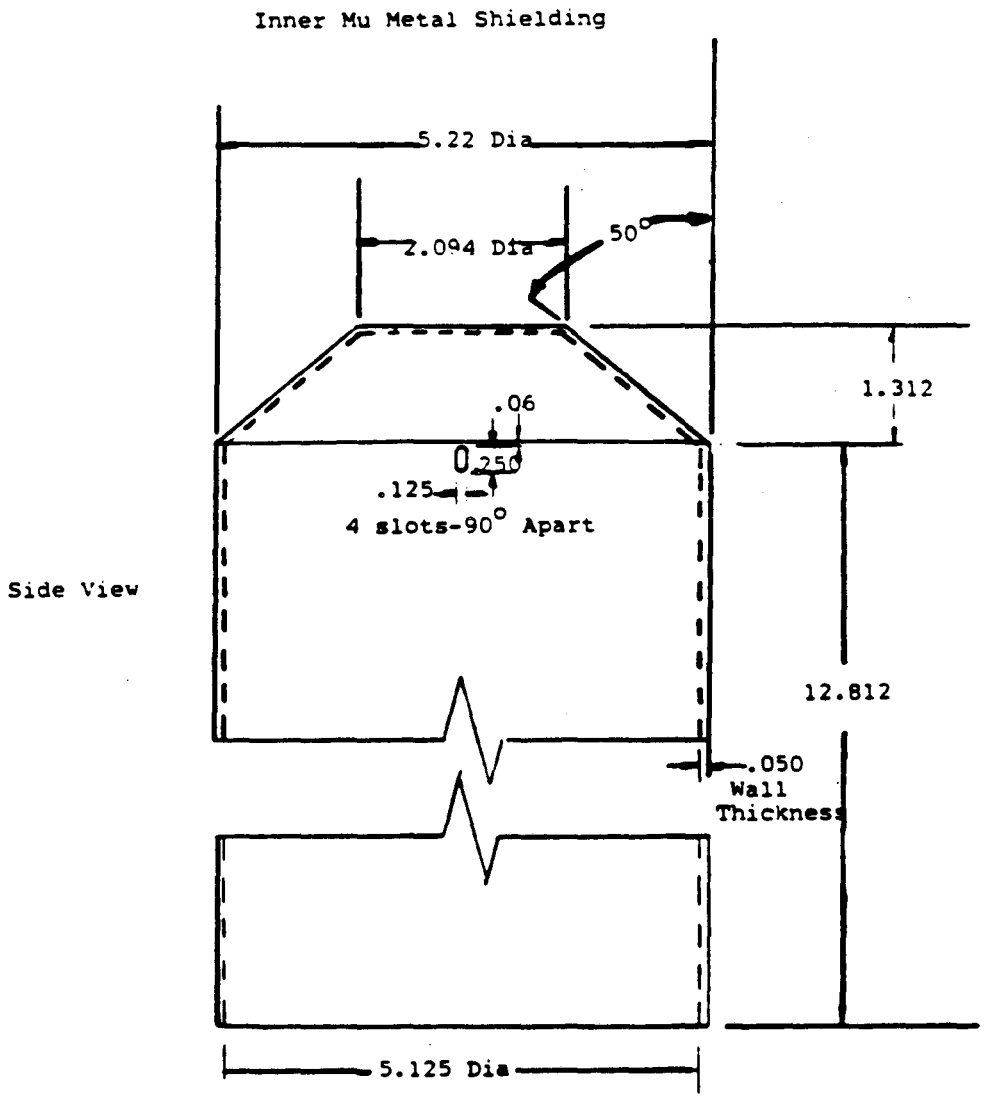

Fig. A.22. Side view of the inner Mu metal shield. The inner and outer shields are separated by 0.090 in. and are parallel with respect to the body of the CMA.

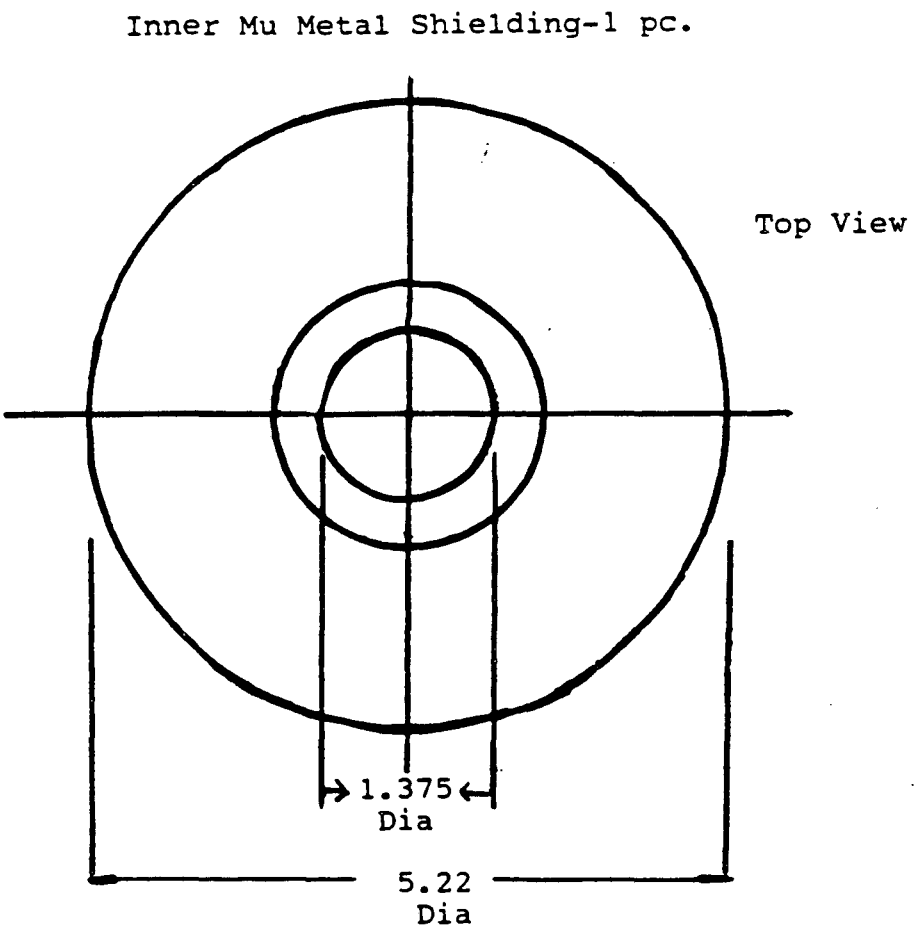

Fig. A.21. Top view of the inner Mu metal shield (see Photograph A.39).

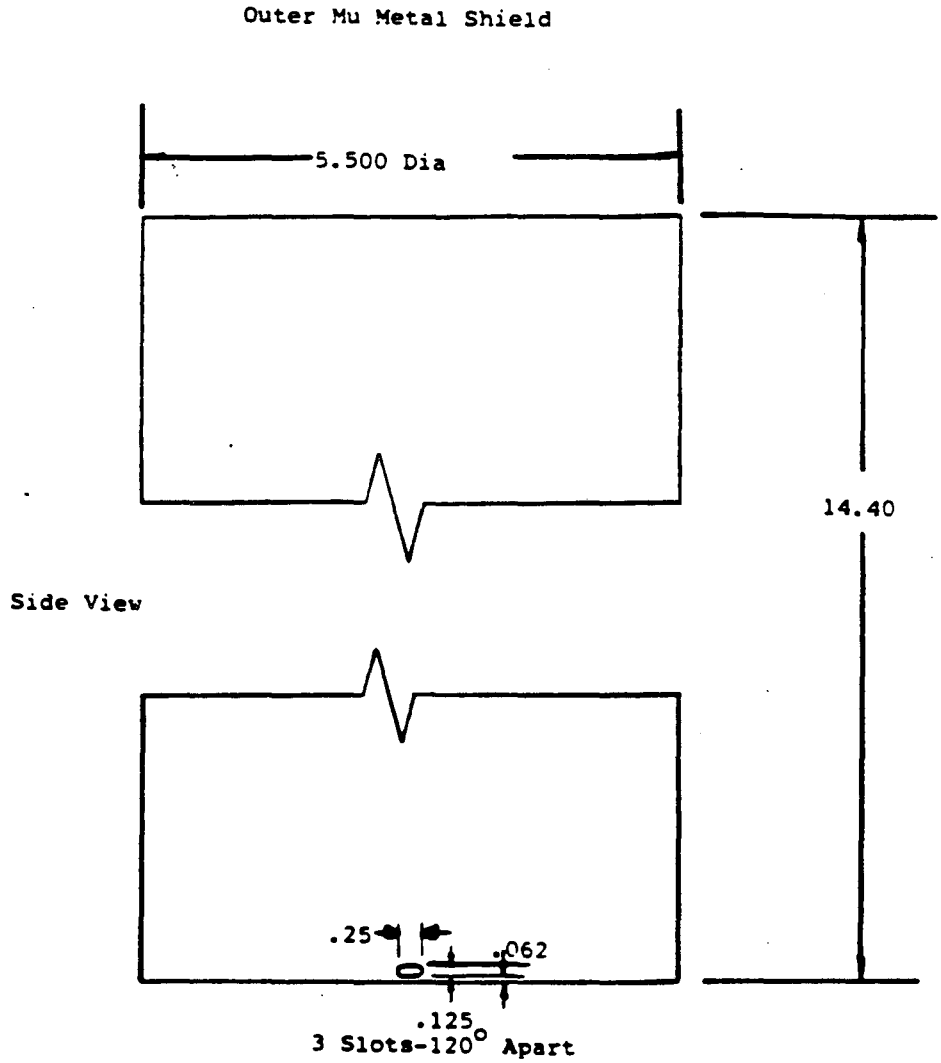

Fig. A.20. Side view of the outer Mu metal shield.

Outer Mu Metal Shielding-1 pc.

Top View

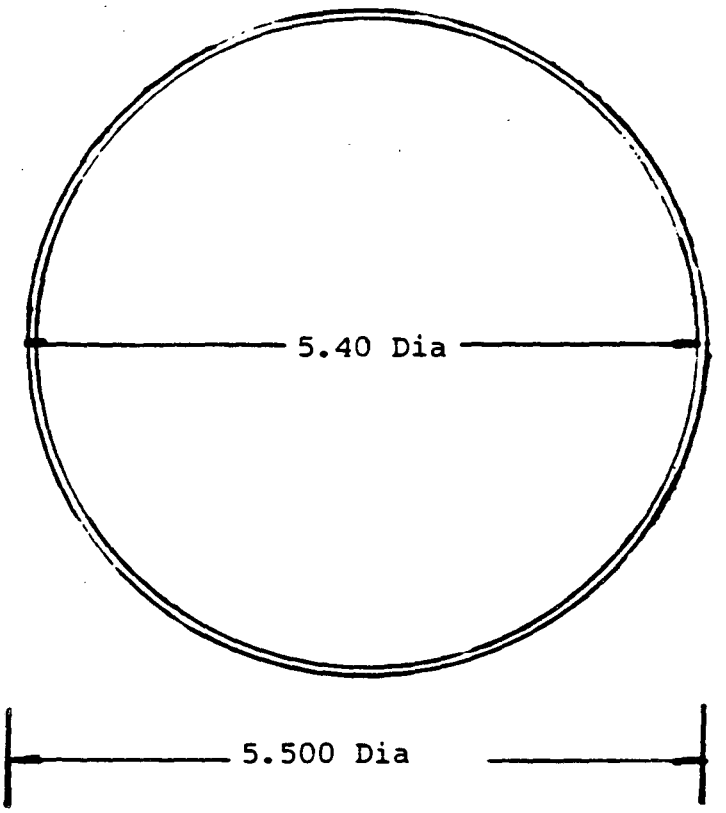

Fig. A.19. Top view of the outer Mu metal shield (see Photograph A.38).

Section A.7: Figs. A.23 - A.37

The internal electron gun is shown in Figs. A.23 - A.37. The gun is taken apart from the bottom to the top. Ceramic insulators, support rods and screws are shown in Figs. A.34 - A.37. Photographs A.44 - A.46 show the actual electron gun from two viewpoints.

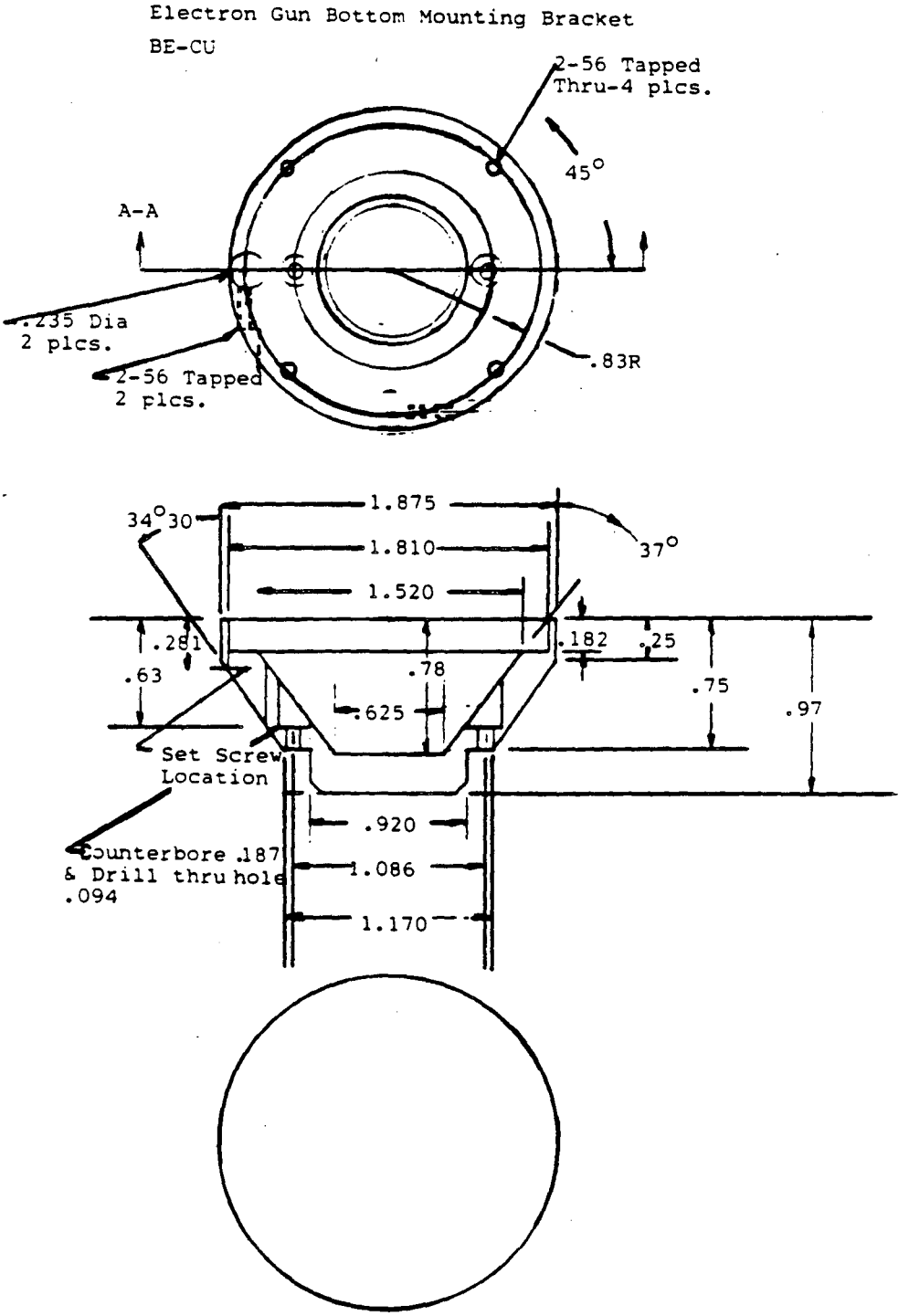

Fig. A.23. Electron gun base with four 2-56 holes tapped to hold the gun together and two counterbored holes for the gun mount on the CMA (see Fig. A.36).

Electron Gun-Plate
304SST

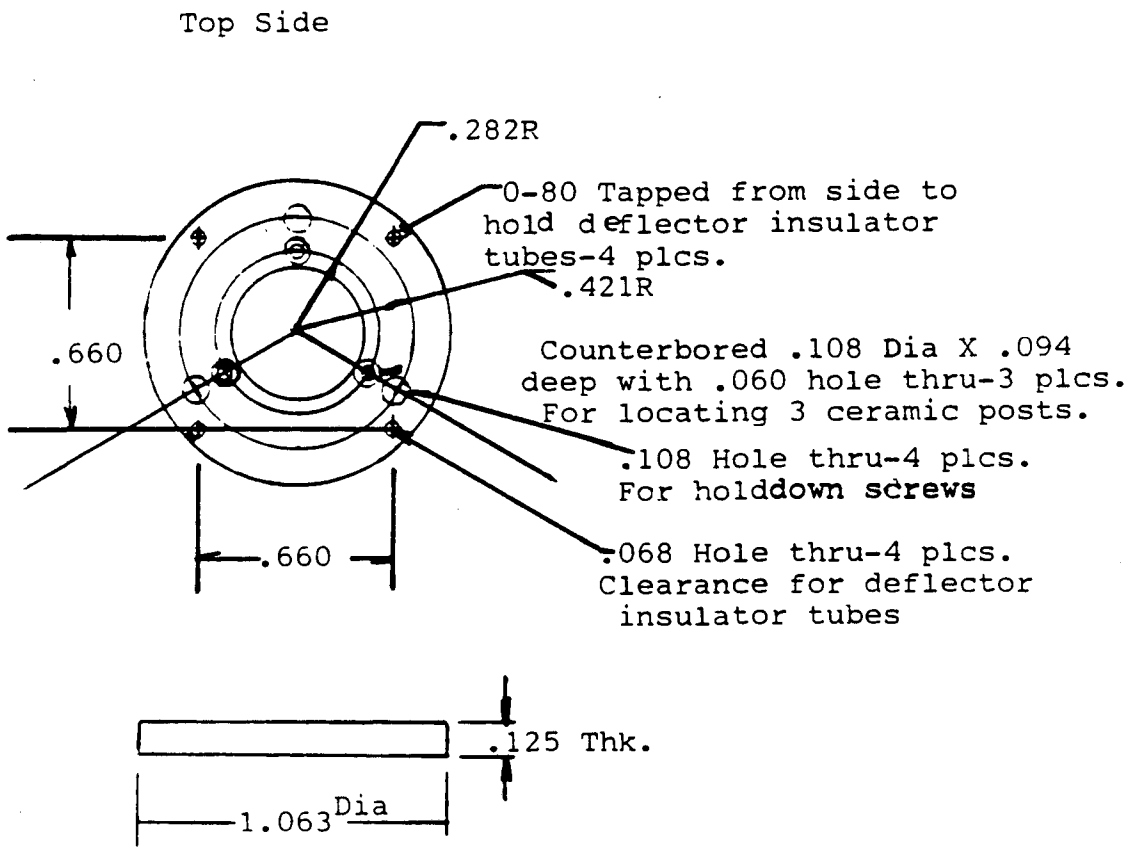

Fig. A.24. Base plate for the electron gun. The internal parts of the electron gun are bolted to this plate (see Photographs A.44 - A.46).

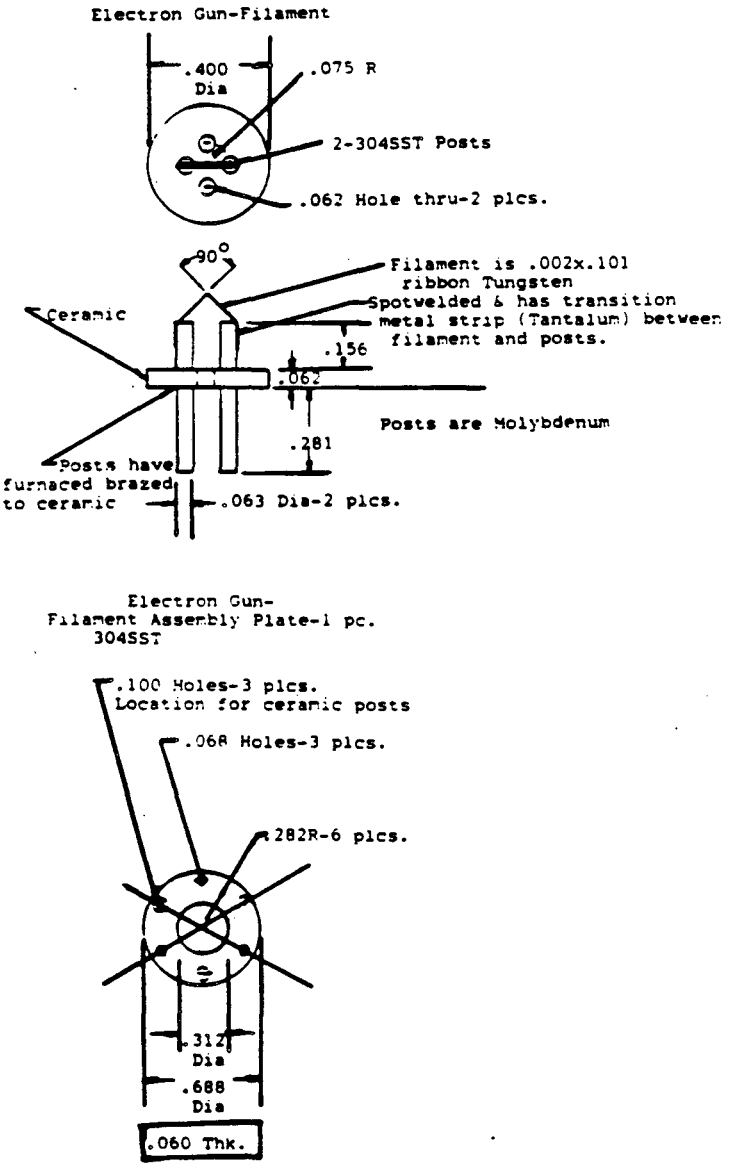

Fig. A.25. Electron gun filament. The tungsten (preferably thoriated tungsten) filament is spotwelded to the Mo support posts using a thin foil of tantalum or platinum. The height of the filament is critical to insure reasonable emission during use. The 2 Mo rods are connected to F1 and F2 on Fig. A.1.

Electron Gun-Filament Assembly Plate-1 pc.
304SST

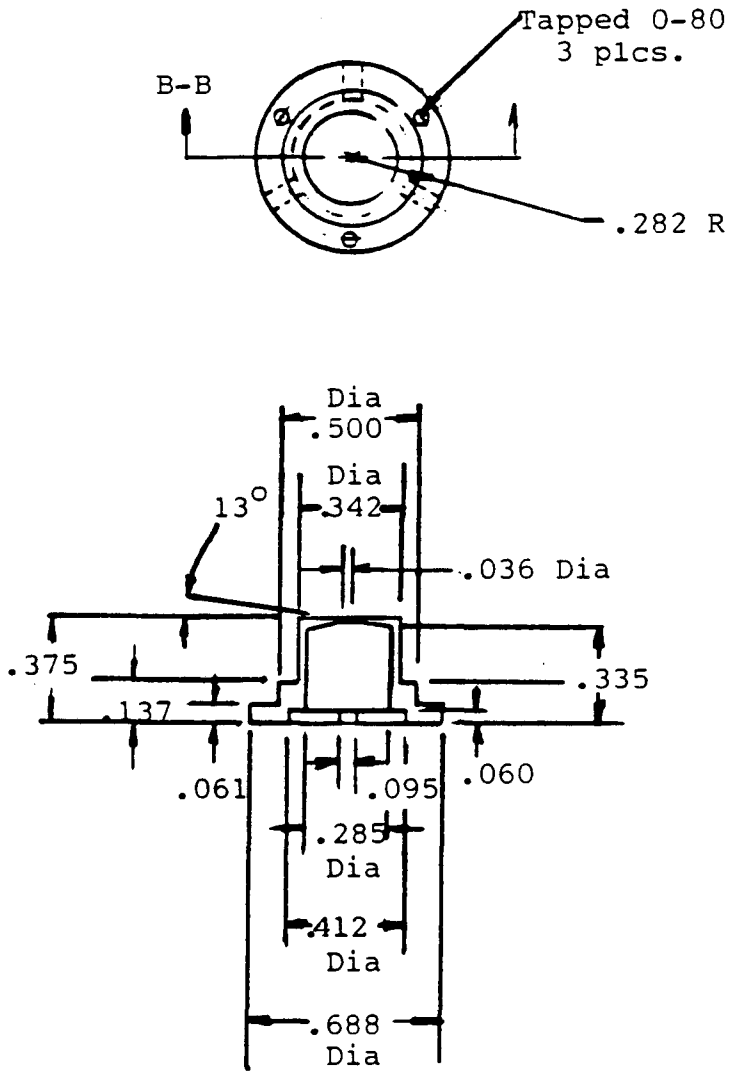

Fig. A.26. Electron filament holder. The filament assembly fits up in the holder such that the end of the filament is lined up with the 0.036 hole at the top and is ~ 0.010-0.002 in. from touching the sides of the hole. The filament holder assembly plate holds the filament in place and is wired to V1 on Fig. A.1. The plate is held away from the electron gun plate (Fig. A.26) by 3 ceramic posts (see Fig. A.37).

Electron Gun Lens
304SST

Top View

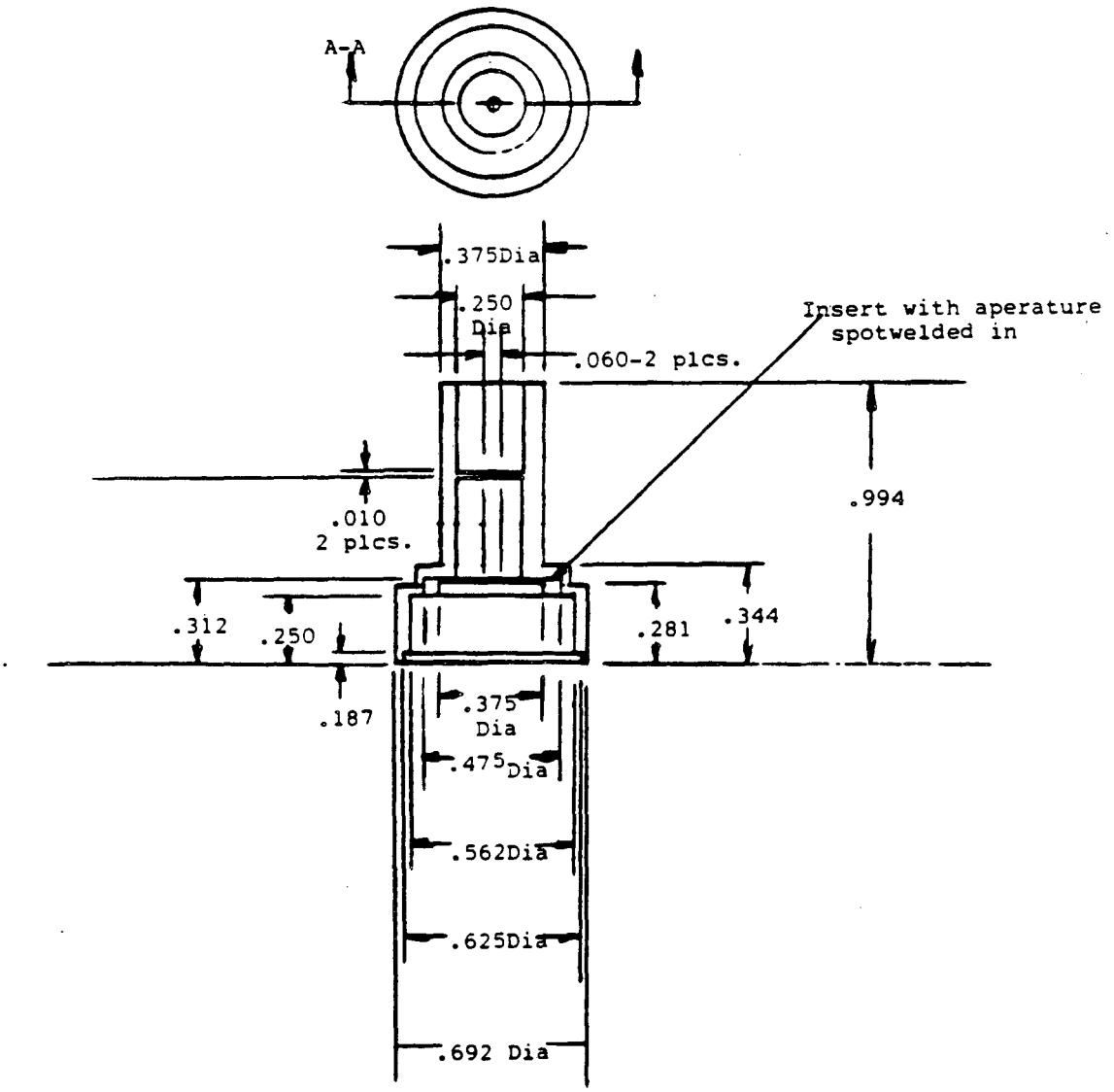

Fig. A.27. The electron beam focusing stage fits on top of the deflector lens assembly and is connected to V2.

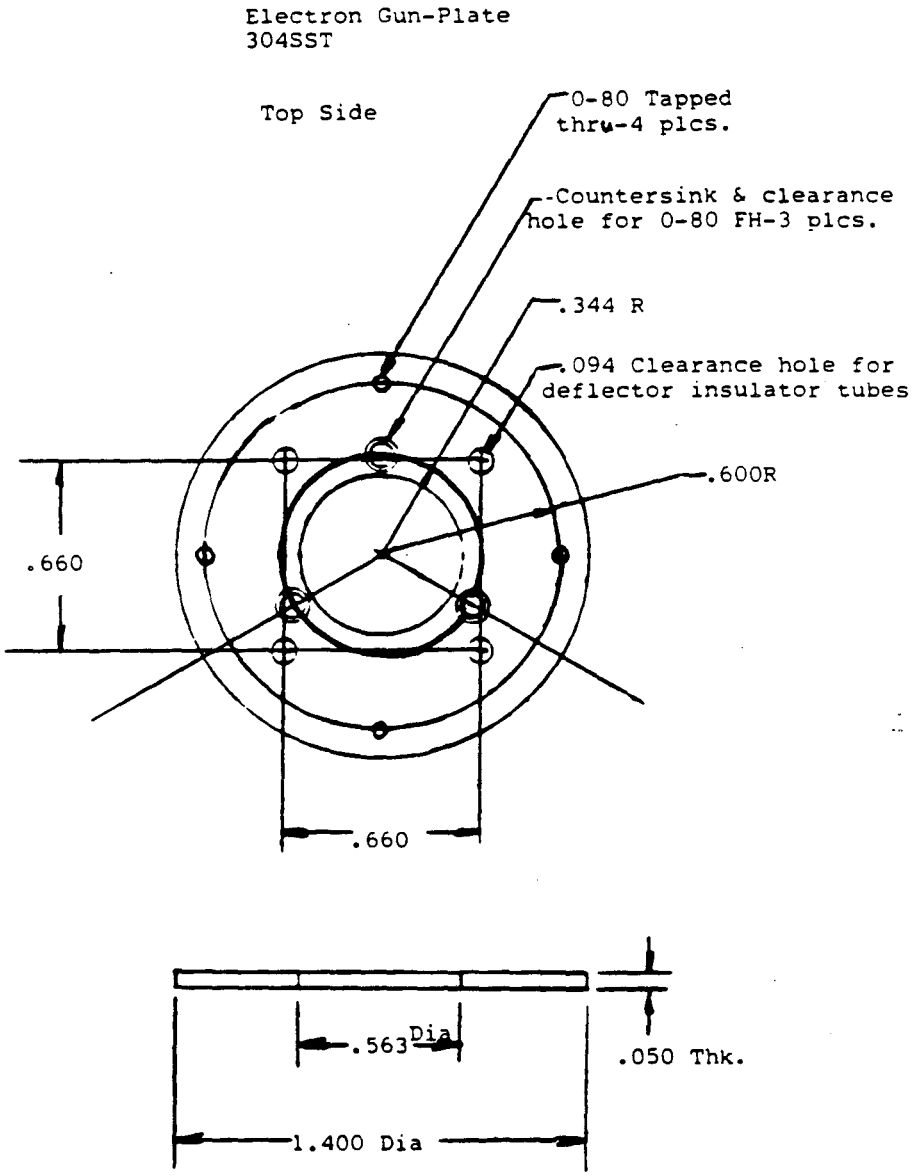

Fig. A.28. The middle plate holding the internal electron gun parts lines up the deflector lens wires and is bolted to the top electron gun plate.

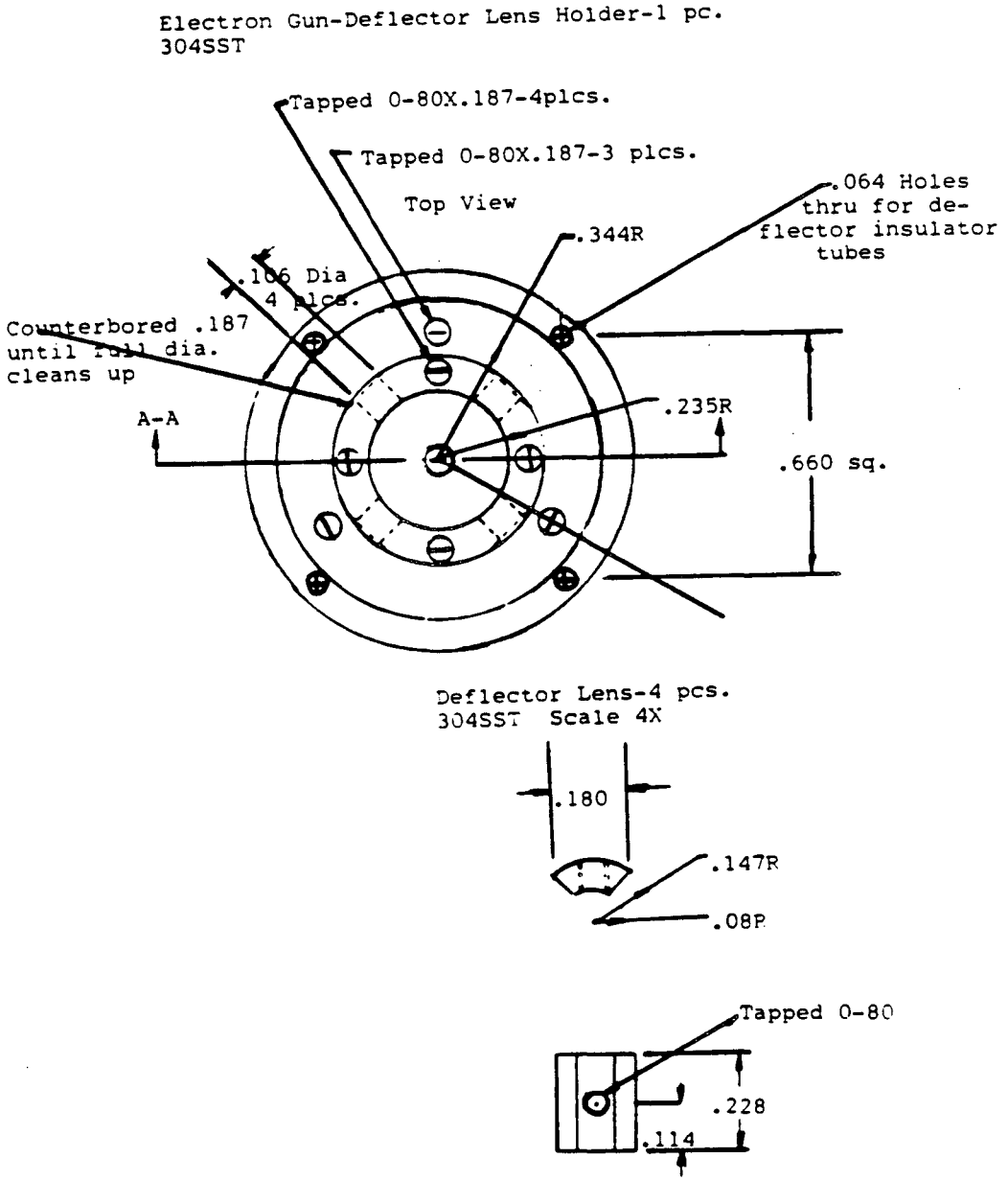

Fig. A.29. The electron gun deflector lens holder is shown from the top (Fig. A.29) and side and bottom (Fig. A.30) views. The deflector plates (see Fig. A.30) are held in place by ceramic isolated screws (see Figs. A.34,36), which are connected to the 10 pin connector in Fig. A.1.

Electron Gun Deflector Lens Holder

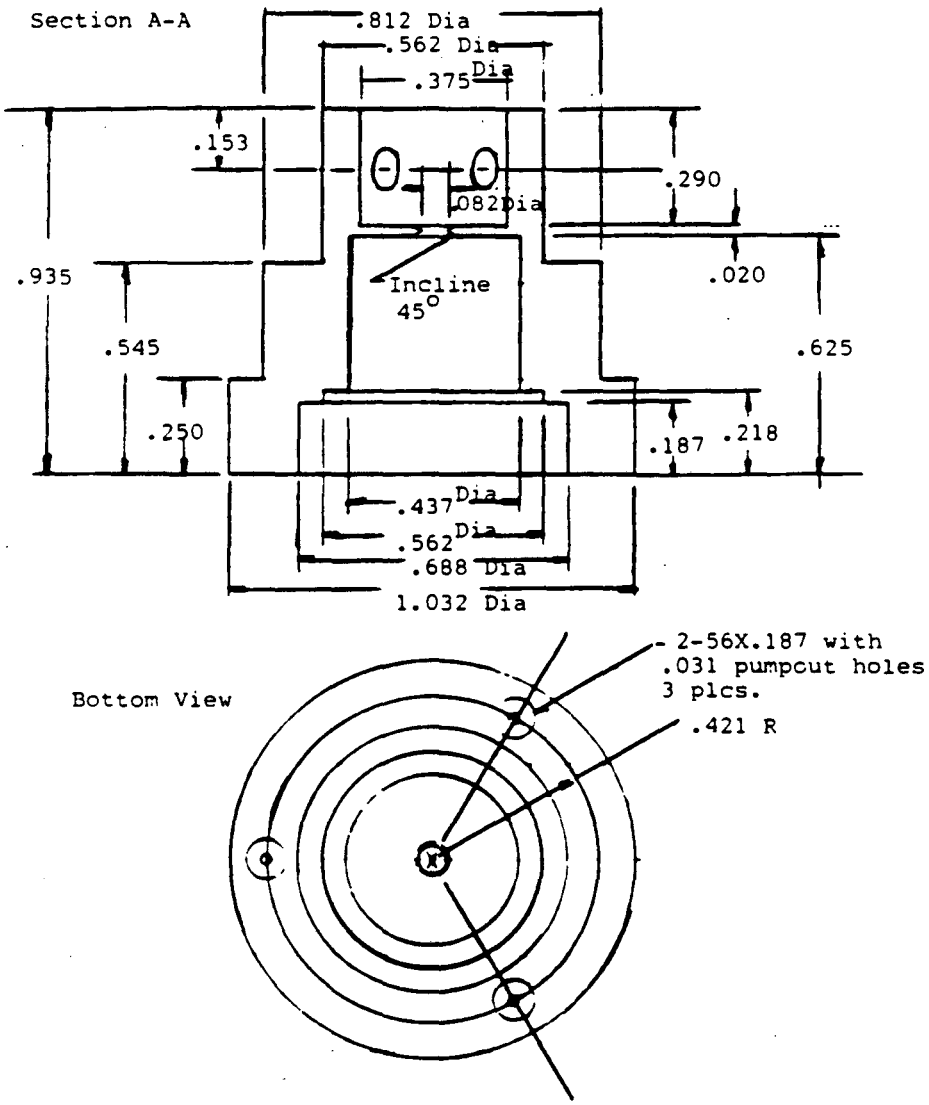

Fig. A.30. See Fig. A.29 for description.

Electron Gun-Final Aperature-1 pc.
304SST

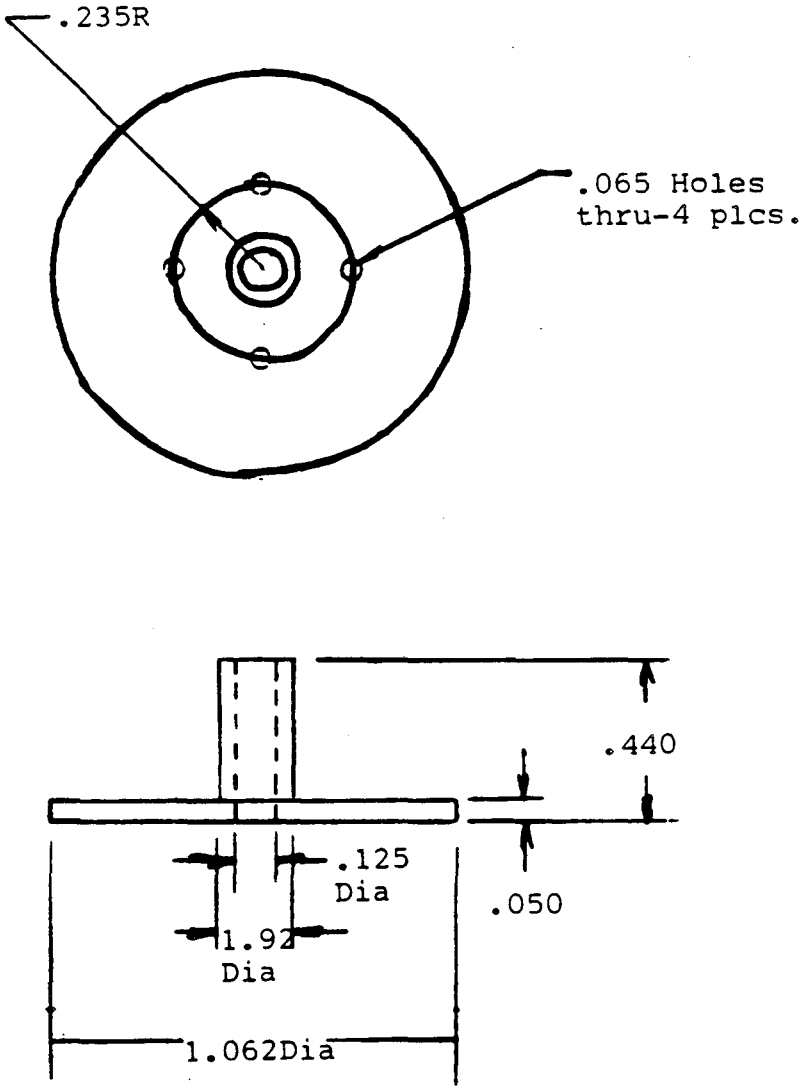

Fig. A.31. The final aperature for the electron beam is 0.125 in. diameter and 0.440 in. long, and usually at ground potential, connected to V3.

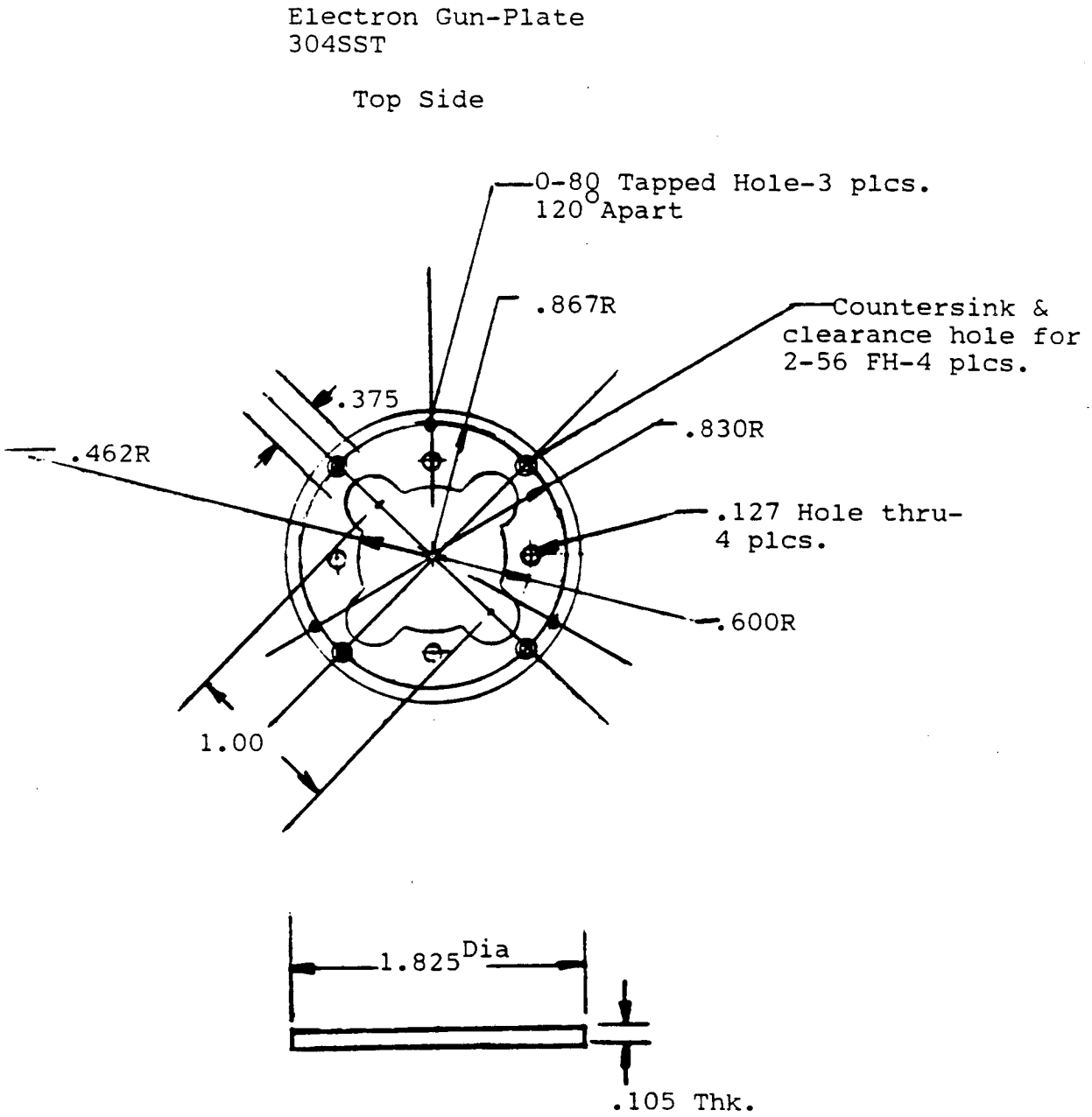

Fig. A.32. The top electron gun mounting bracket holds the electron gun in place and bolts the electron gun together with the gun support posts (see Fig. A.35).

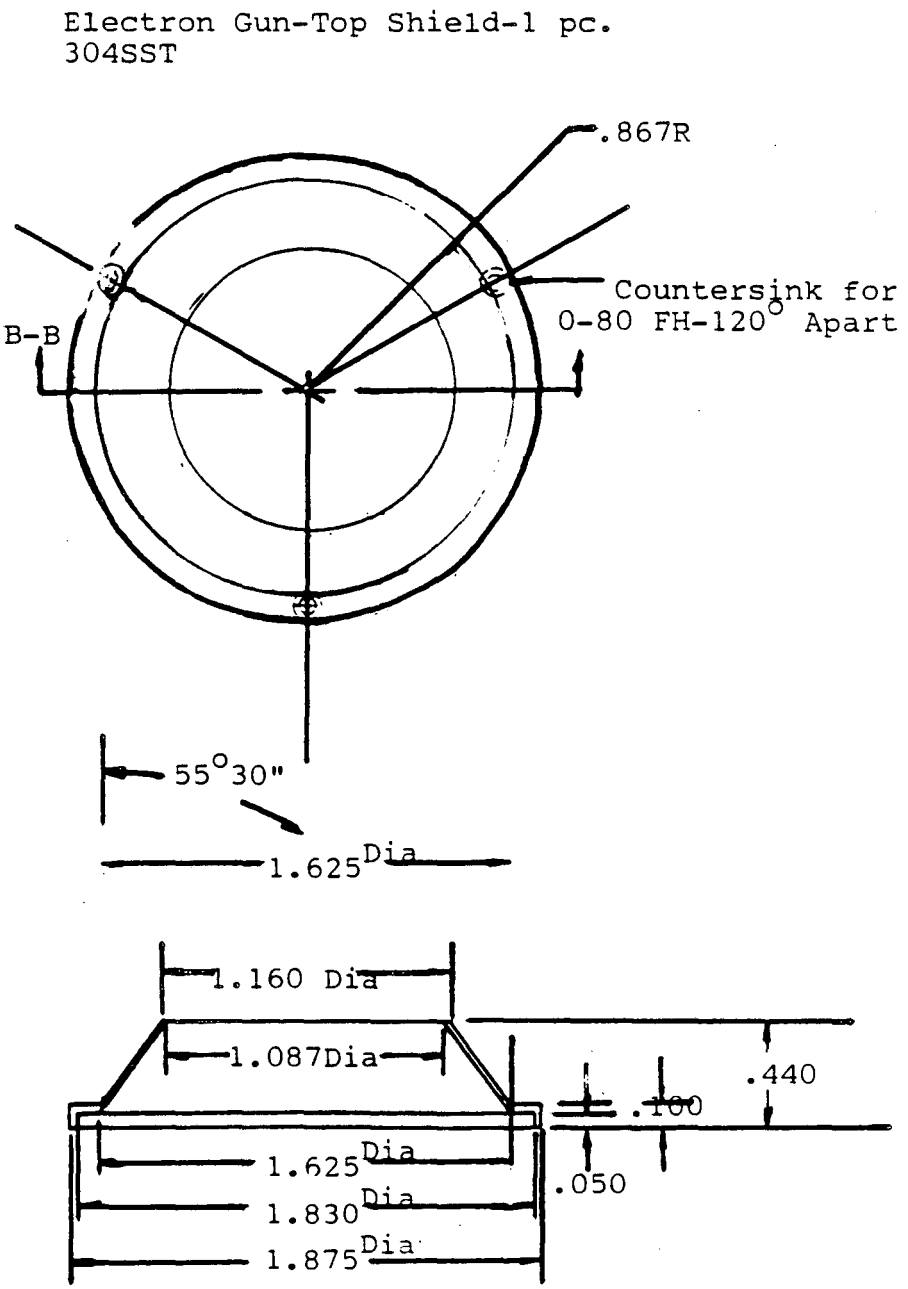

Fig. A.33. Top shield for the electron gun is bolted to the top mounting bracket with three 2-56 screws (see Fig. A.35).

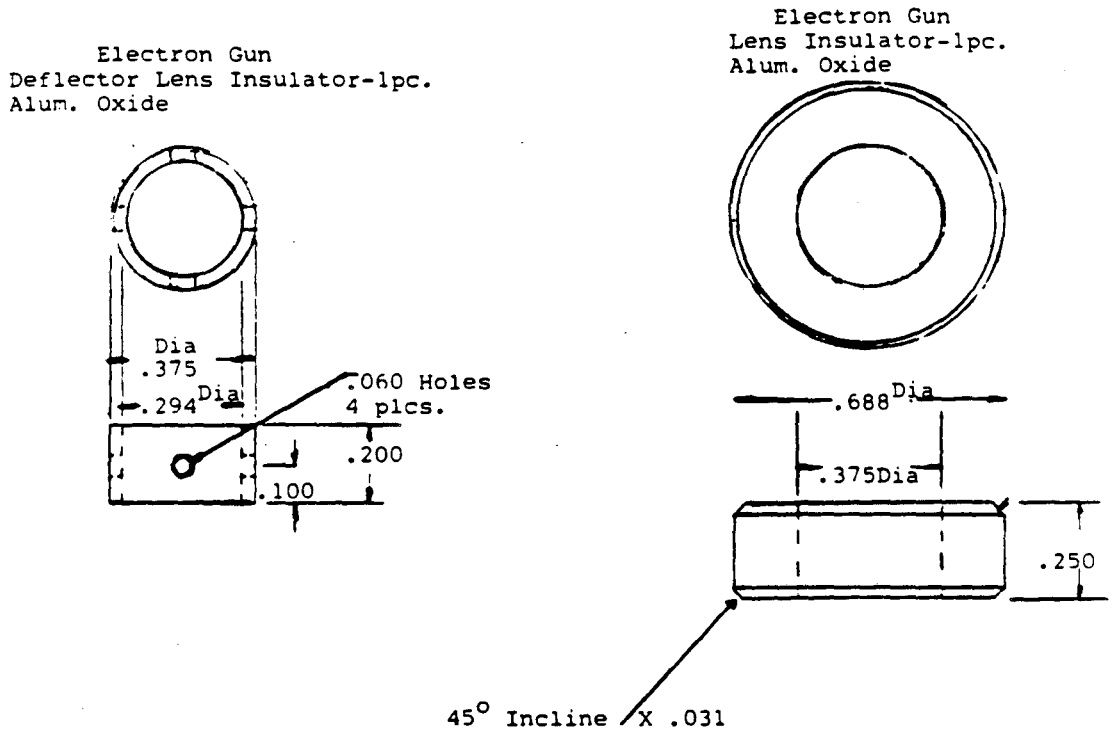

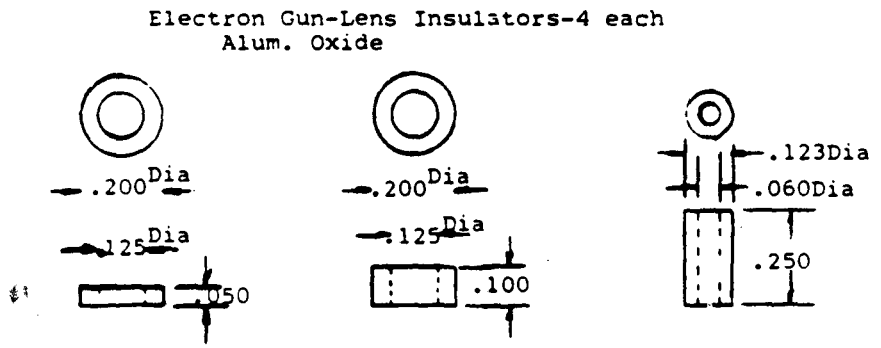

Fig. A.34 - A.37. The assorted ceramics, support posts, screws and wire insulation ceramics in detail.

Electron Gun Assembly Support
Posts- 2 pcs.
OHFC

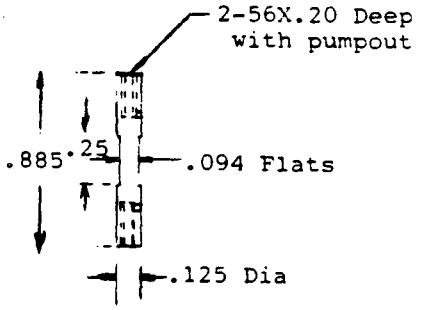

Electron Gun Support Posts-4 pcs.
304SST

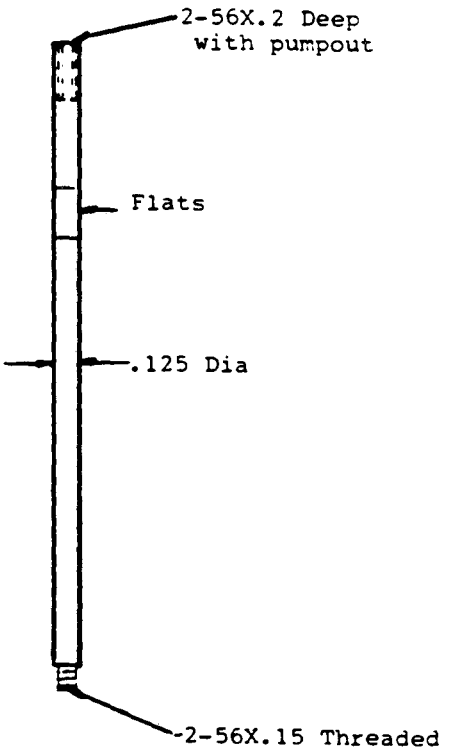

Fig. A.35.

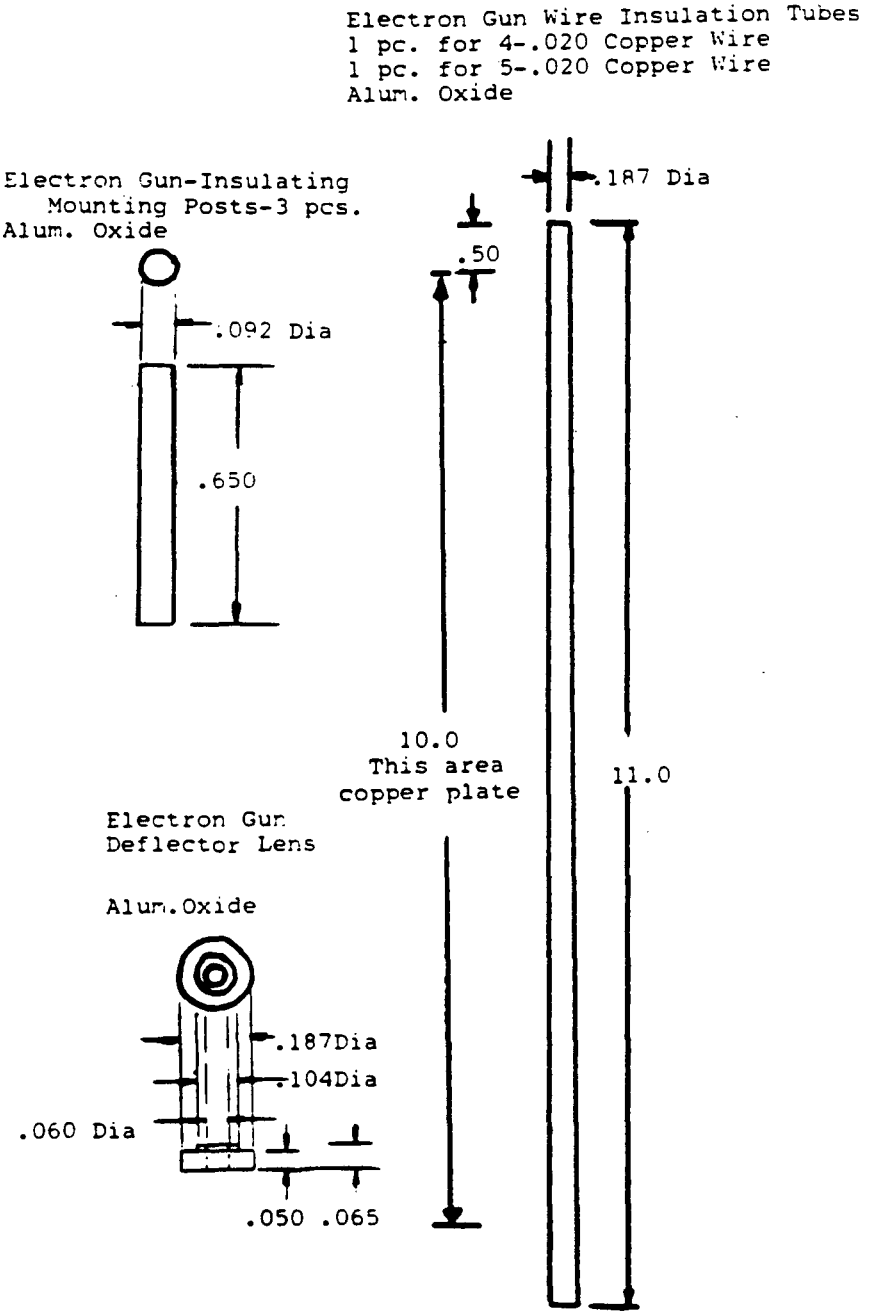
Electron Gun Wire Insulation Tubes
1 pc. for 4-.020 Copper Wire
1 pc. for 5-.020 Copper Wire
Alum. Oxide
Electron Gun-Insulating
Mounting Posts-3 pcs.
Alum. Oxide
.092 Dia
.650
.187 Dia
.50
10.0
This area
copper plate
11.0
Electron Gun
Deflector Lens
Alum.Oxide
.187Dia
.104Dia
.060 Dia
.050 .065

Fig. A.36.

Electron Gun Screws-3 pcs.
304SST

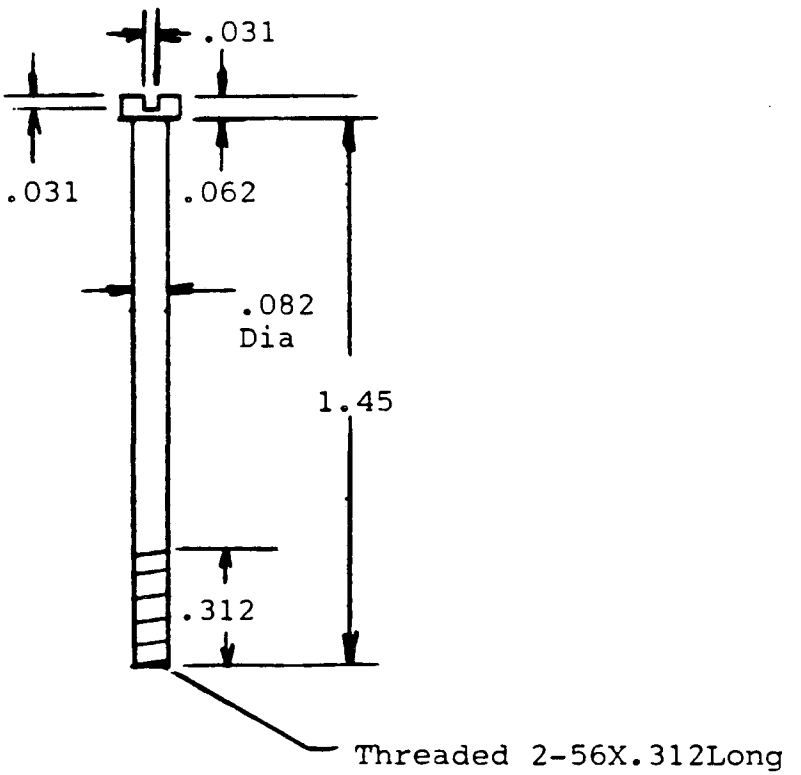

Fig. A.37.

Section A.8: Photographs A.38 - A.52

Photograph A.38. The CMA mounted on its stand, showing the outer metal shield (see Fig. A.19,20). The cylinder is attached to the Al plate (see Fig. A.2) by four allen head screws.

Photograph A.39. The inner metal shield (see Fig. A.21,22). The shield is attached to the first aperature (see Fig. A.10, Photograph A.50).

Photograph A.40. The outer OF copper cylinders are held in place by the first aperature (see Fig. A.10), The bottom field terminator support (see Fig. A.4) and the stack assembly rods (see Fig. A.11).

Photograph A.41. The lower outer cylinder. The middle field terminating plate is held by 3 set screws on the top of the cylinder.

Photograph A.42. The top and bottom inner cylinders with the middle field terminating plate in place (in practice, the lower outer cylinder must be in place prior to putting in the middle field terminating plate).

Photograph A.43. The upper inner cylinder and middle field terminating plate removed to exposed the internal electron gun.

Photograph A.44. A closeup of the electron gun. The four ceramic sleeved wires in the middle are for deflectrion and the other set is for filament current, focusing, accelerating and grounding the various stages of the gun (see Fig. A.23 - A.37).

Photograph A.45. Another view of the electron gun. The pivoting aperature for the top inner cylinder is also shown (see Fig. A.15 - A.18).

Photograph A.46. A top view of the electron gun (see Fig. A.31,33).

Photograph A.47. A closeup view of the lower portion of the CMA. The channeltron is mounted such that it can be replaced without further disassembly (see Fig. A.48). The mounting block for the 0.125 pivoting rod is also shown (see Fig. A.49). The high voltage feedthrus have copper barrel connectors on the vacuum side for easy connection and removal.

Photograph A.48. A second closeup of the lower CMA assembly. The 10 pin feedthru for deflection is clear as well as the channeltron connection.

Photograph A.49. A third closeup of the lower CMA assembly. The rotary feedthru and pivoting arm setup (see Fig. A.13,14) and the outer cylinder Al shielding (see Fig. A.12) are shown.

Photograph A.50. The first aperature (see Fig. A.10) with hemispherical tungsten mesh spotwelded in place.

Photograph A.51. The upper Be-Cu inner cylinder (see Fig. A.8).

Photograph A.52. The top field terminating plate.

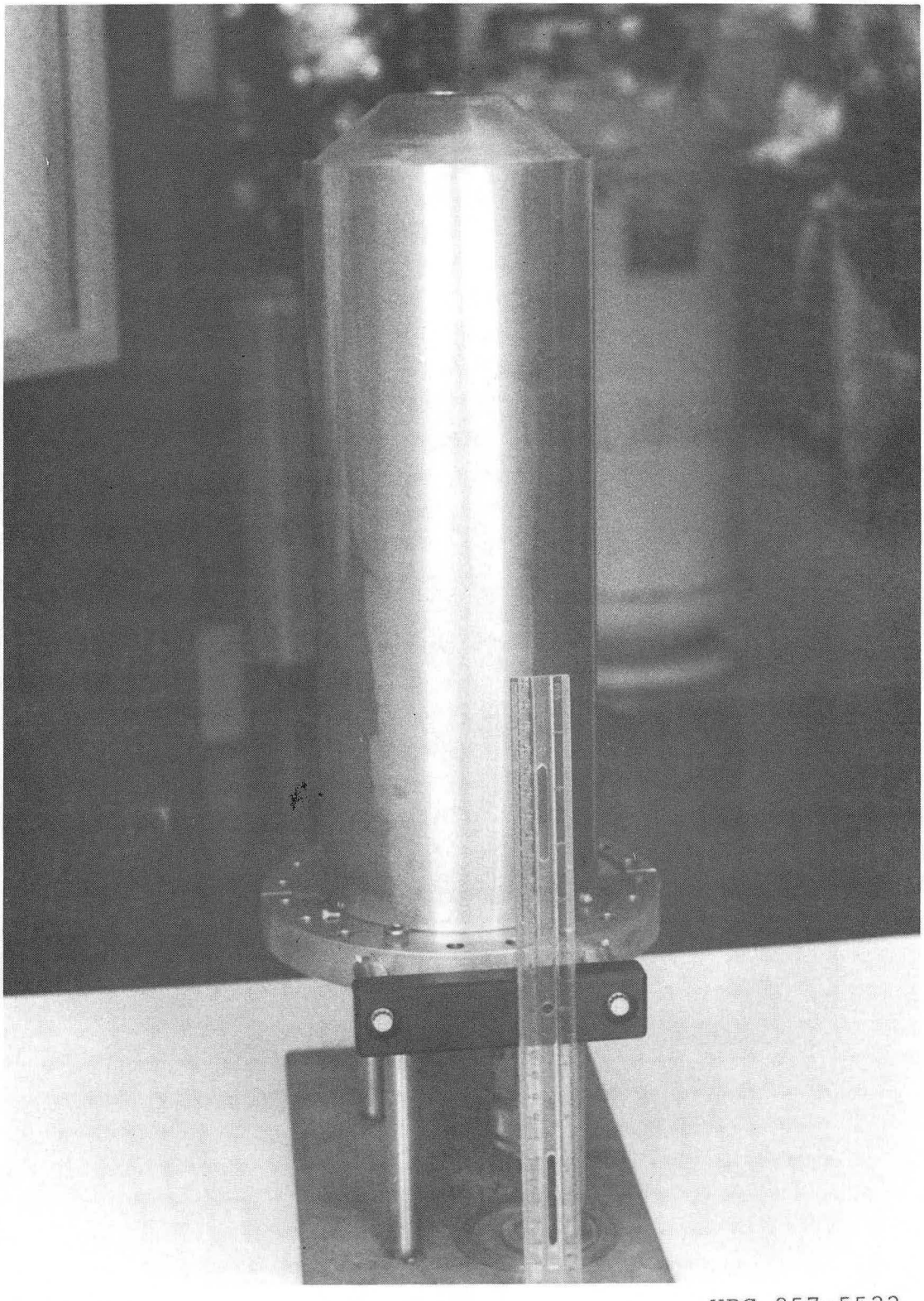

Fig. A.38

XBC 857-5522

Fig. A.39

XBC 857-5523

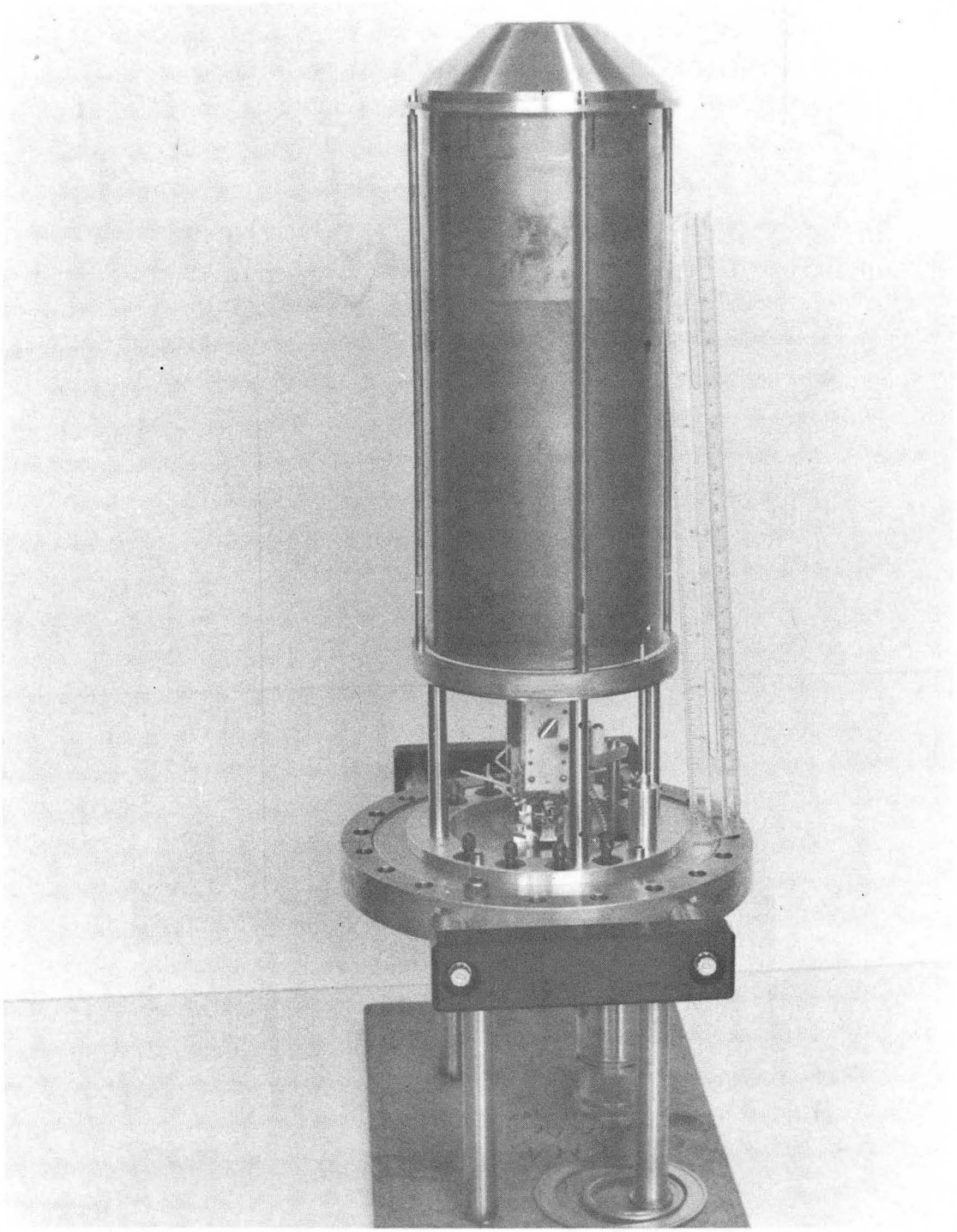

Fig. A.40

XBC 857-5524

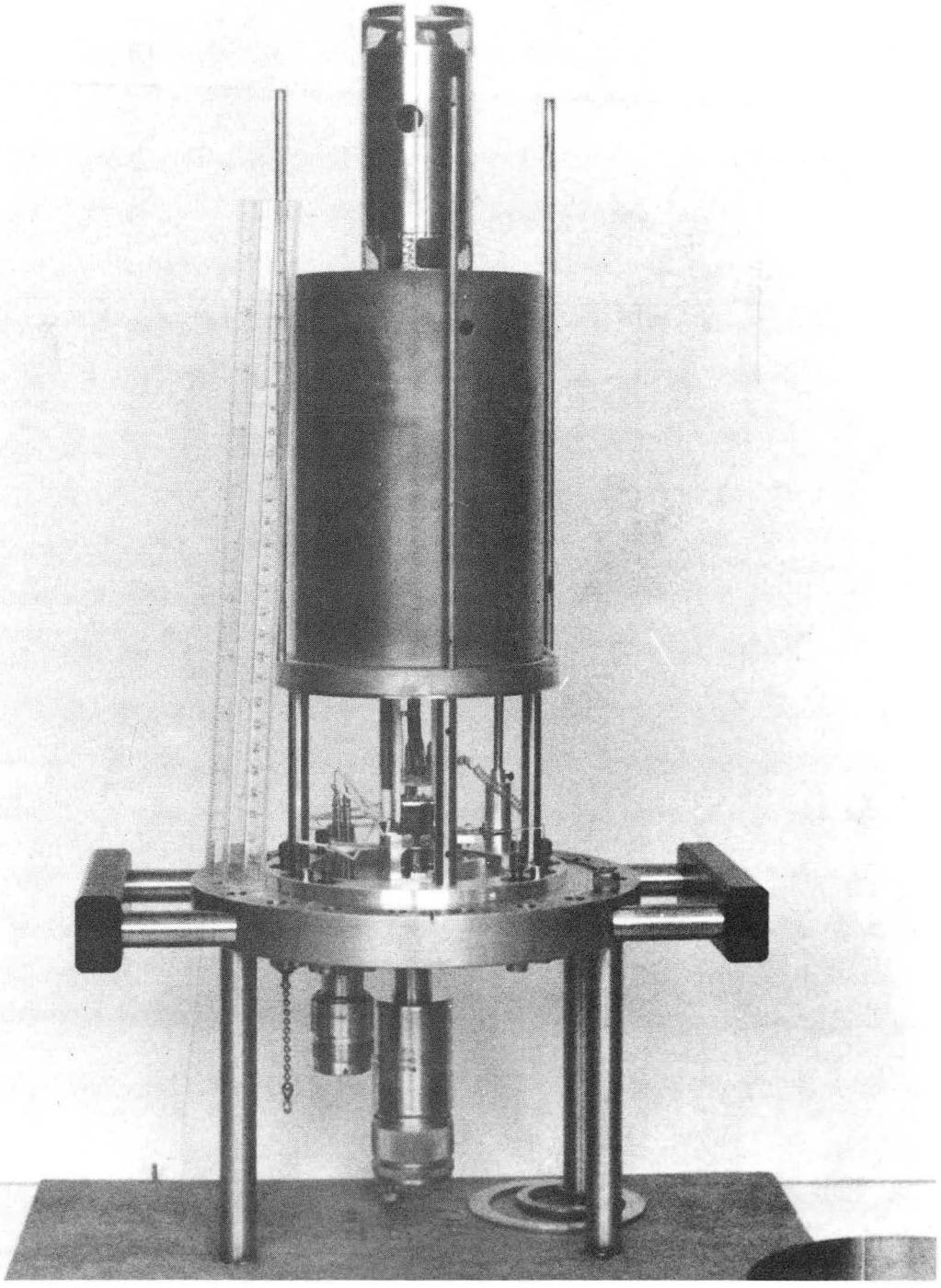

XBC 857-5527

Fig. A.41

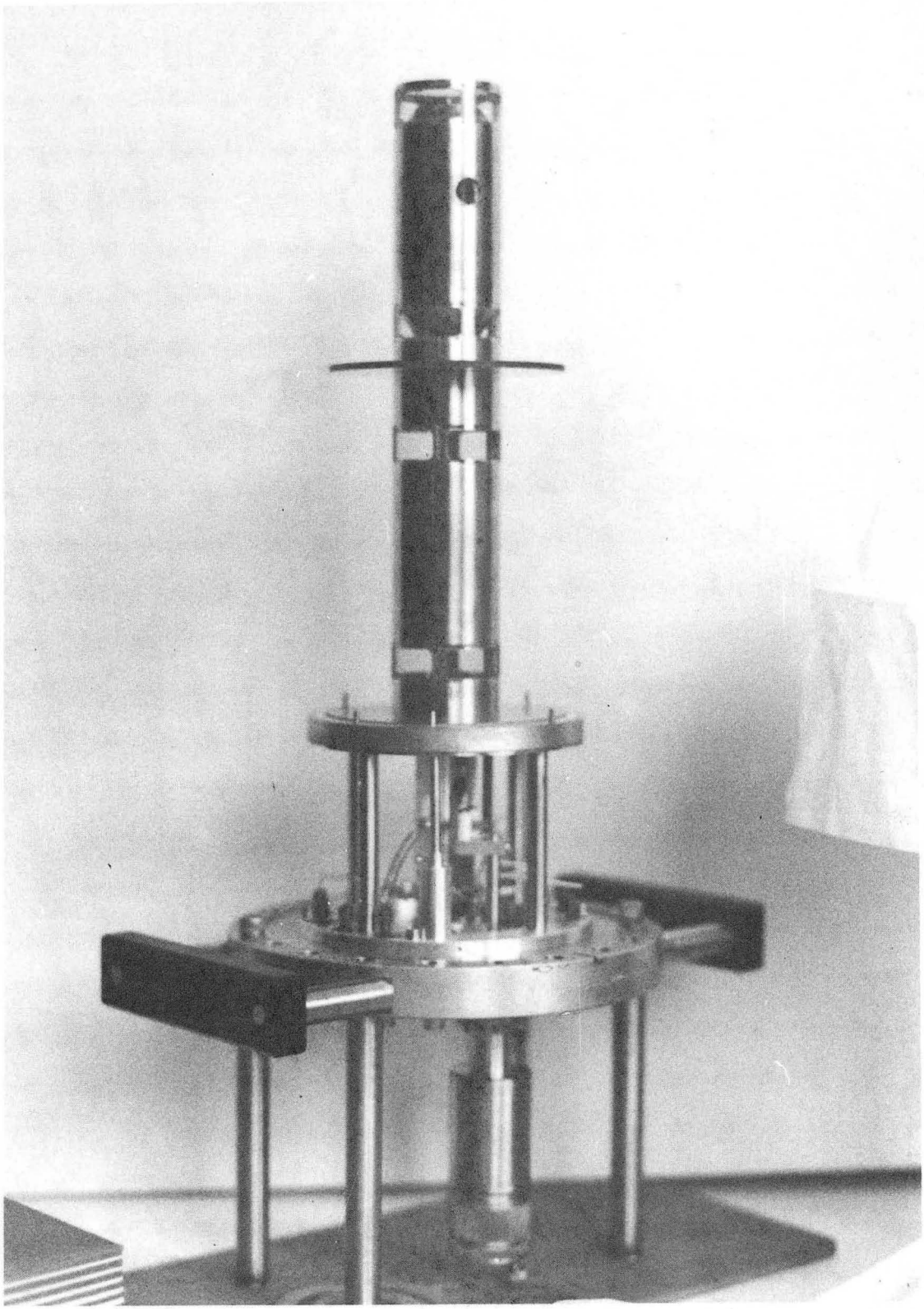

Fig. A.42

XBC 857-5521

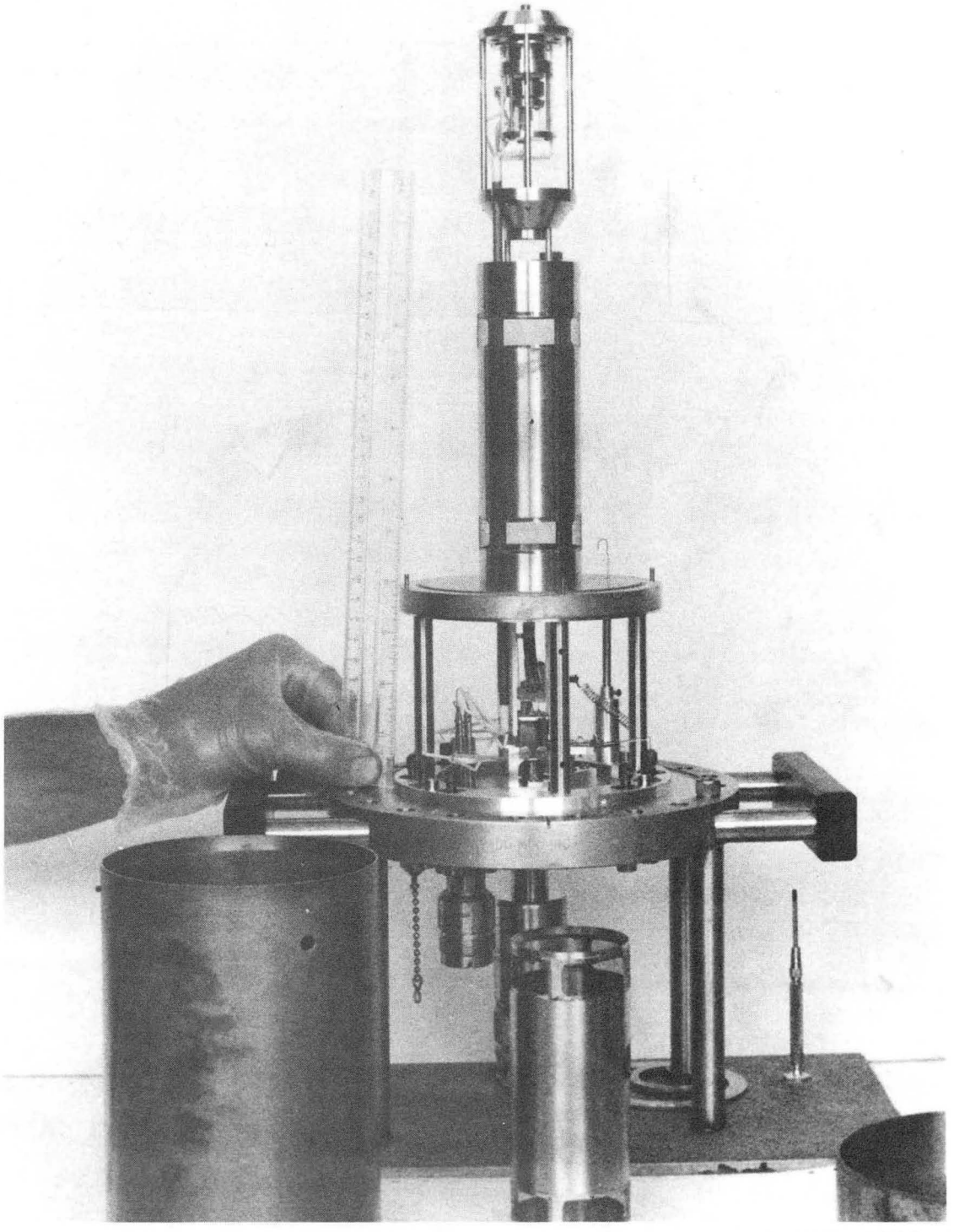

XBC 857-5528

Fig. A.43

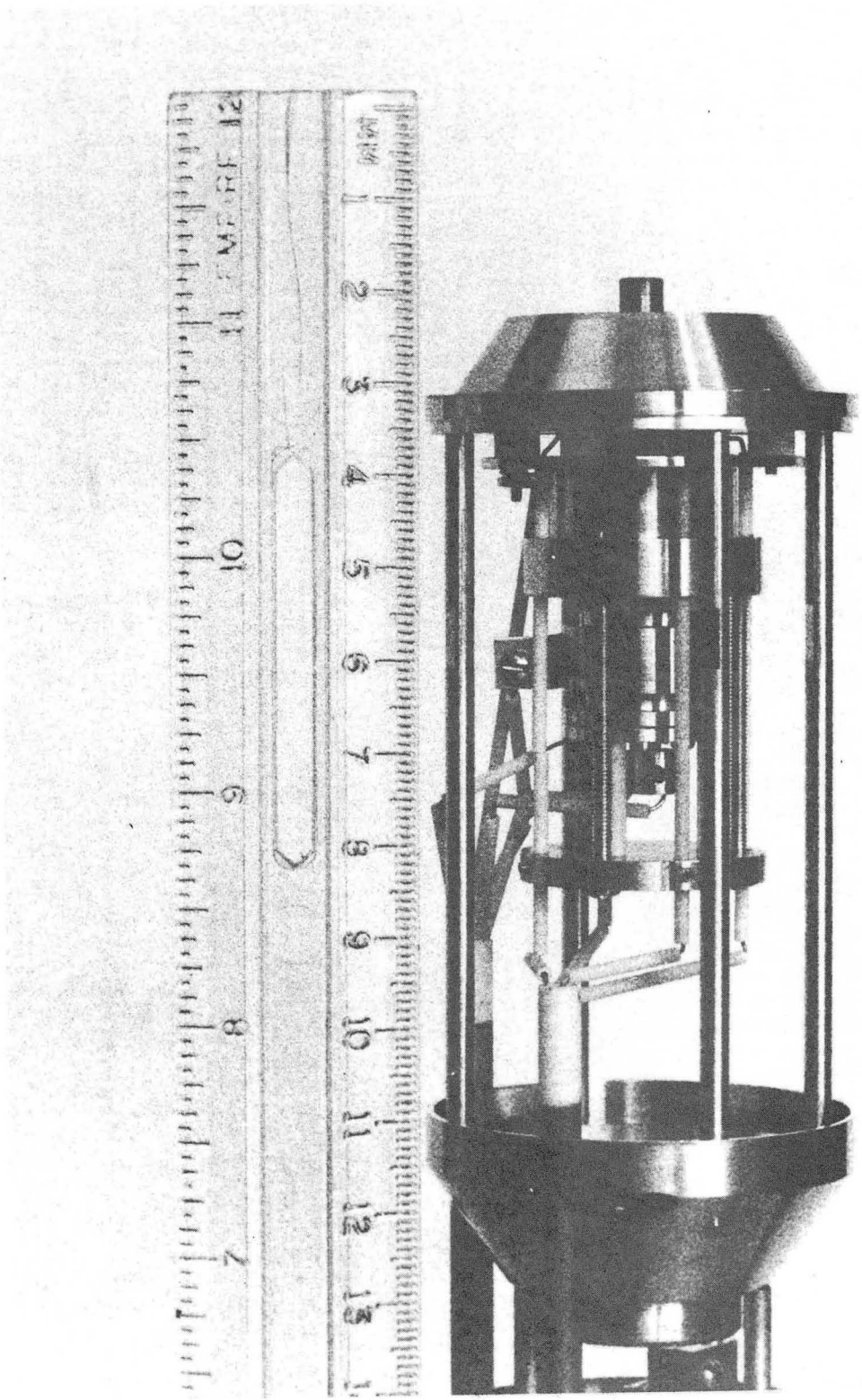

Fig. A.44 XBC 857-5529

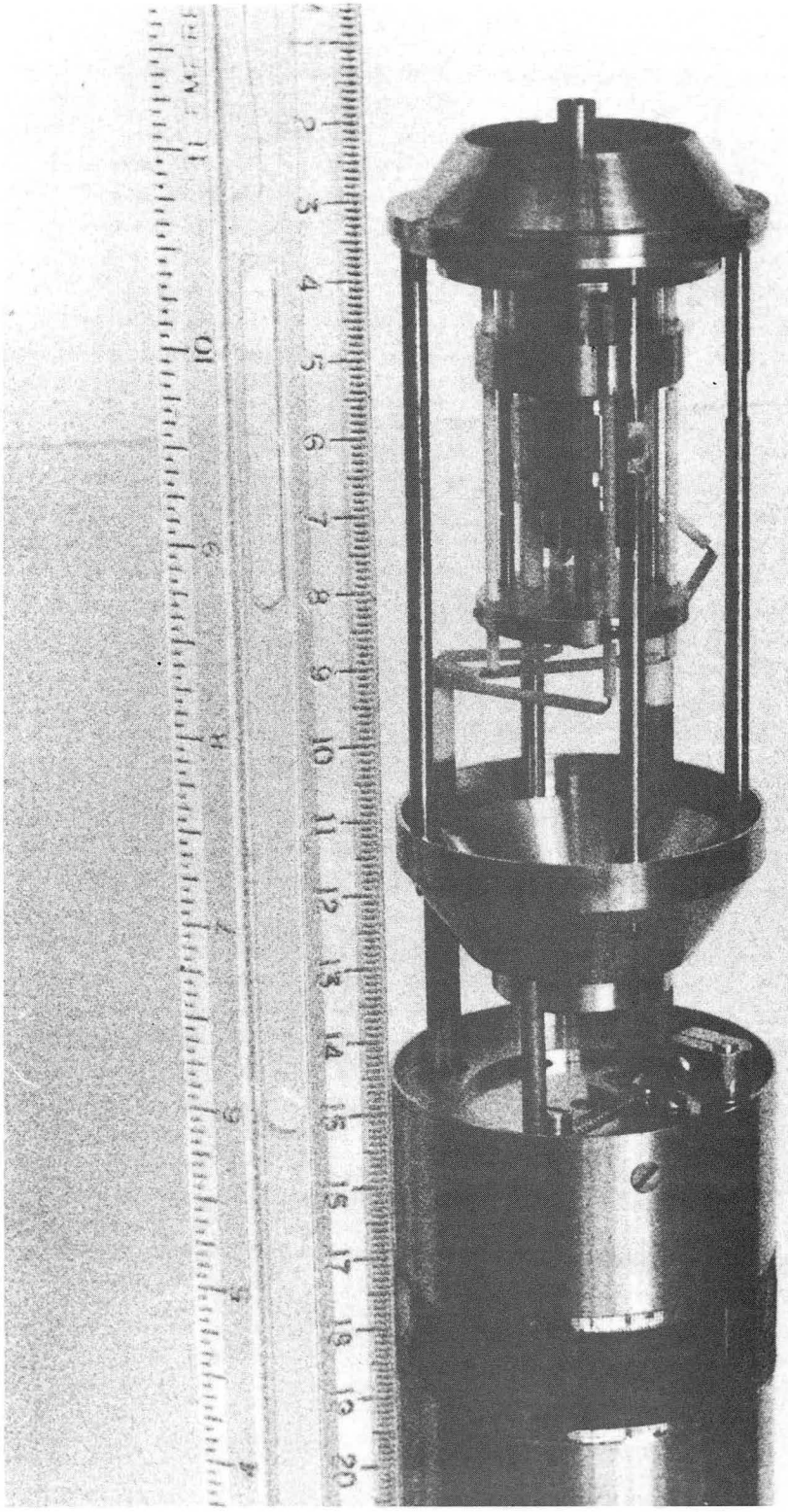

XBC 857-5531

Fig. A.45

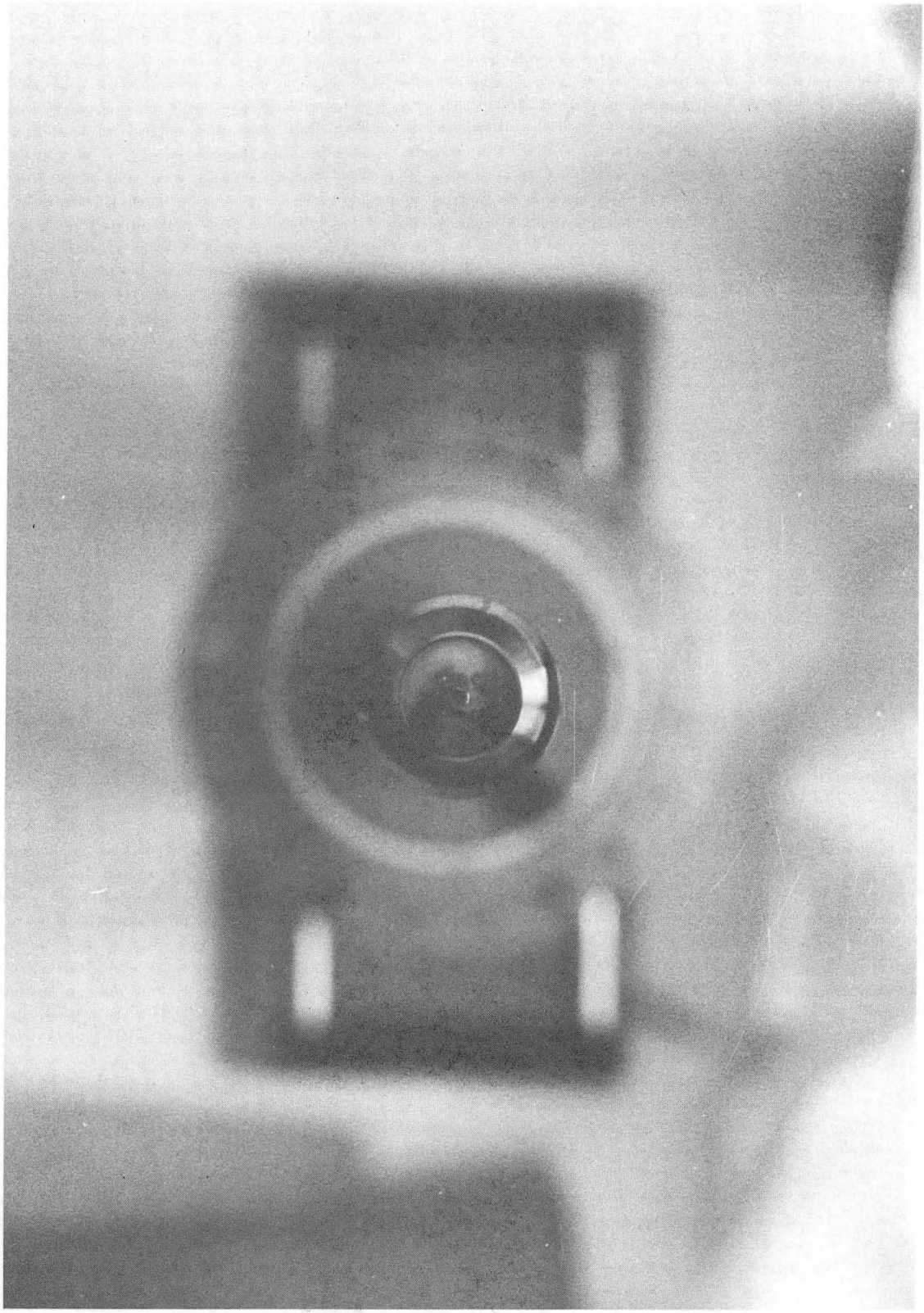

XBC 857-5519

Fig. A.46

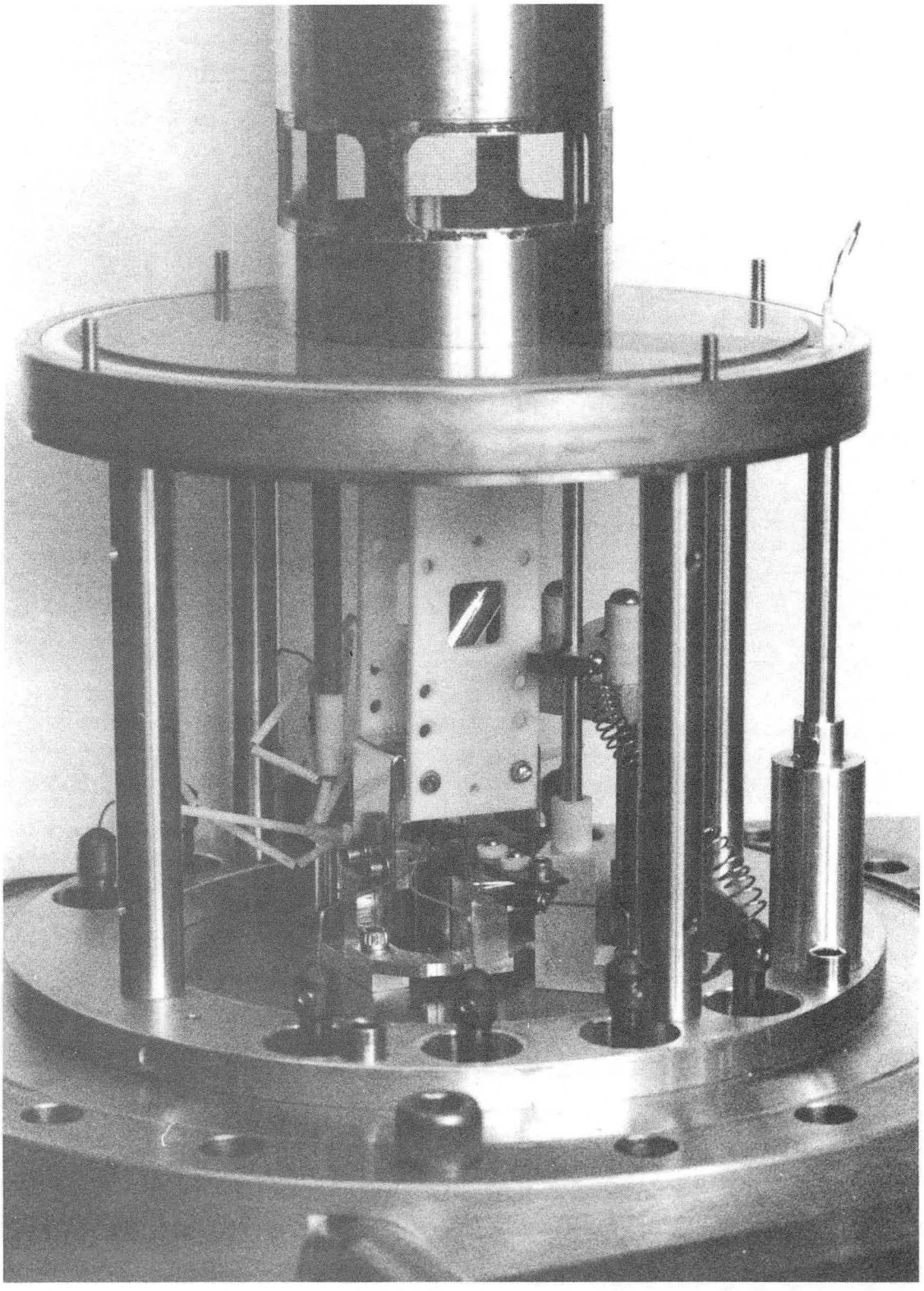

Fig. A.47 XBC 857-5532

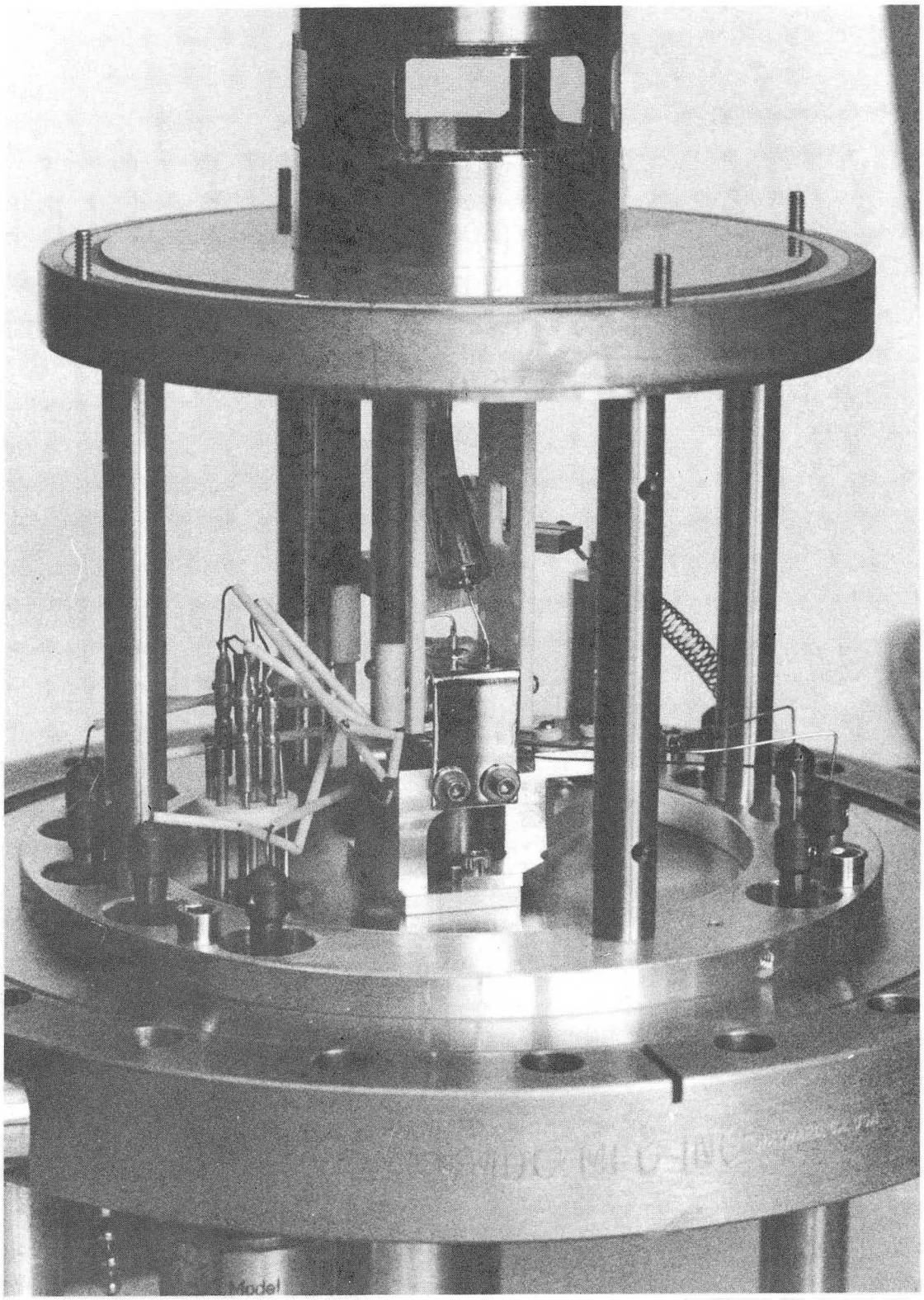

Fig. A.48 XBC 857-5533

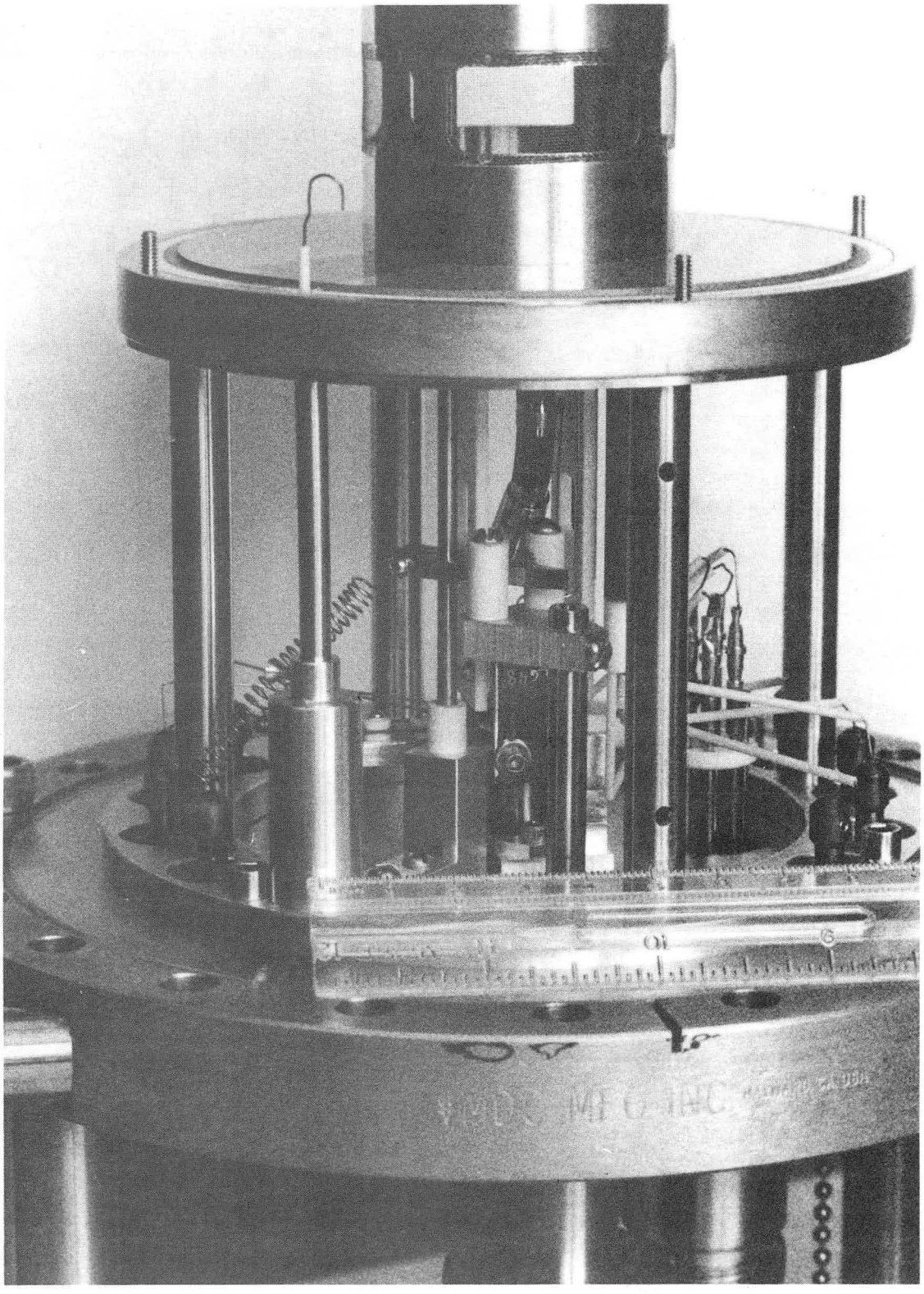

Fig. A.49 XBC 857-5534

XBC 857-5535

Fig. A.50

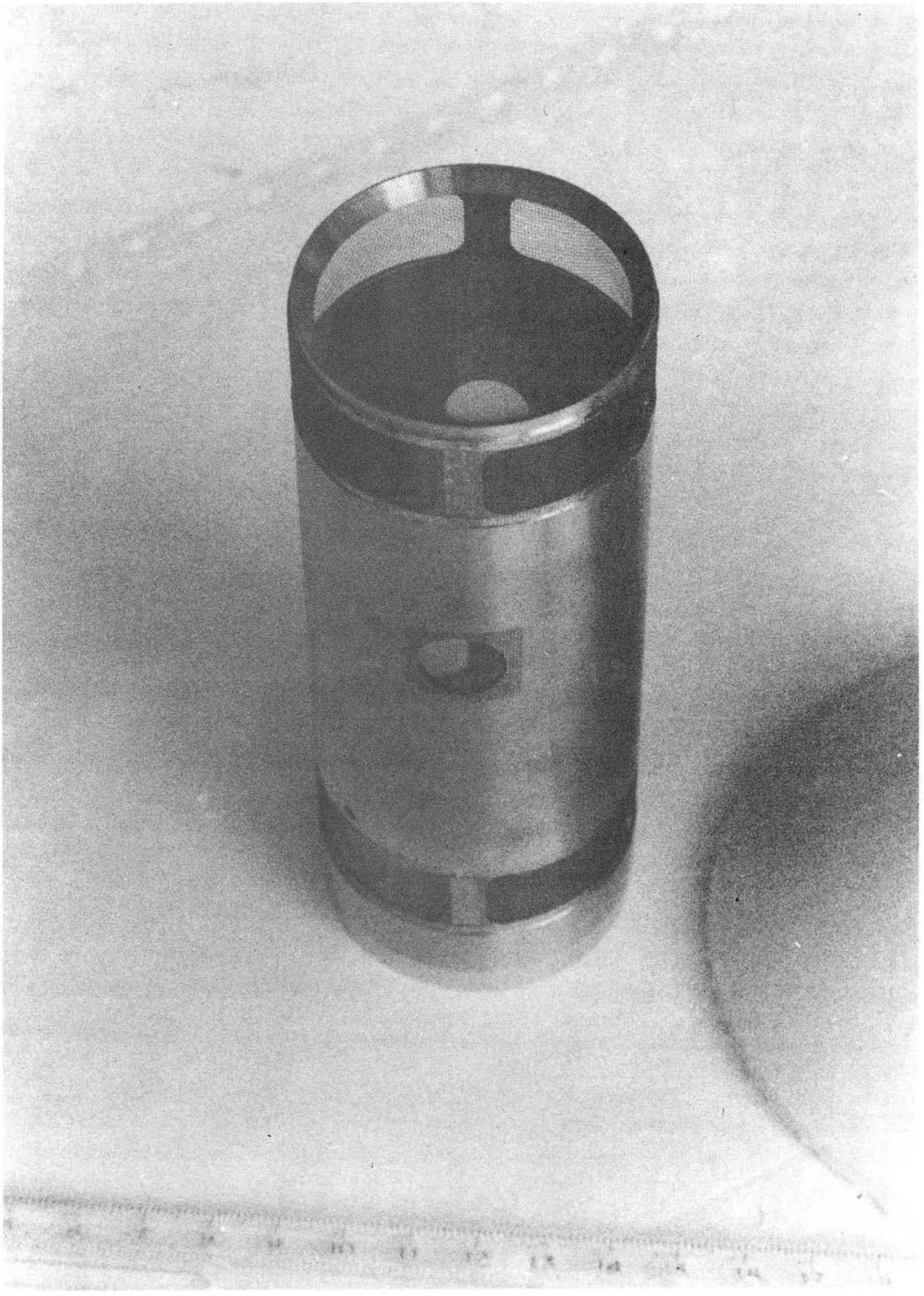

Fig. A.51 XBC 857-5537

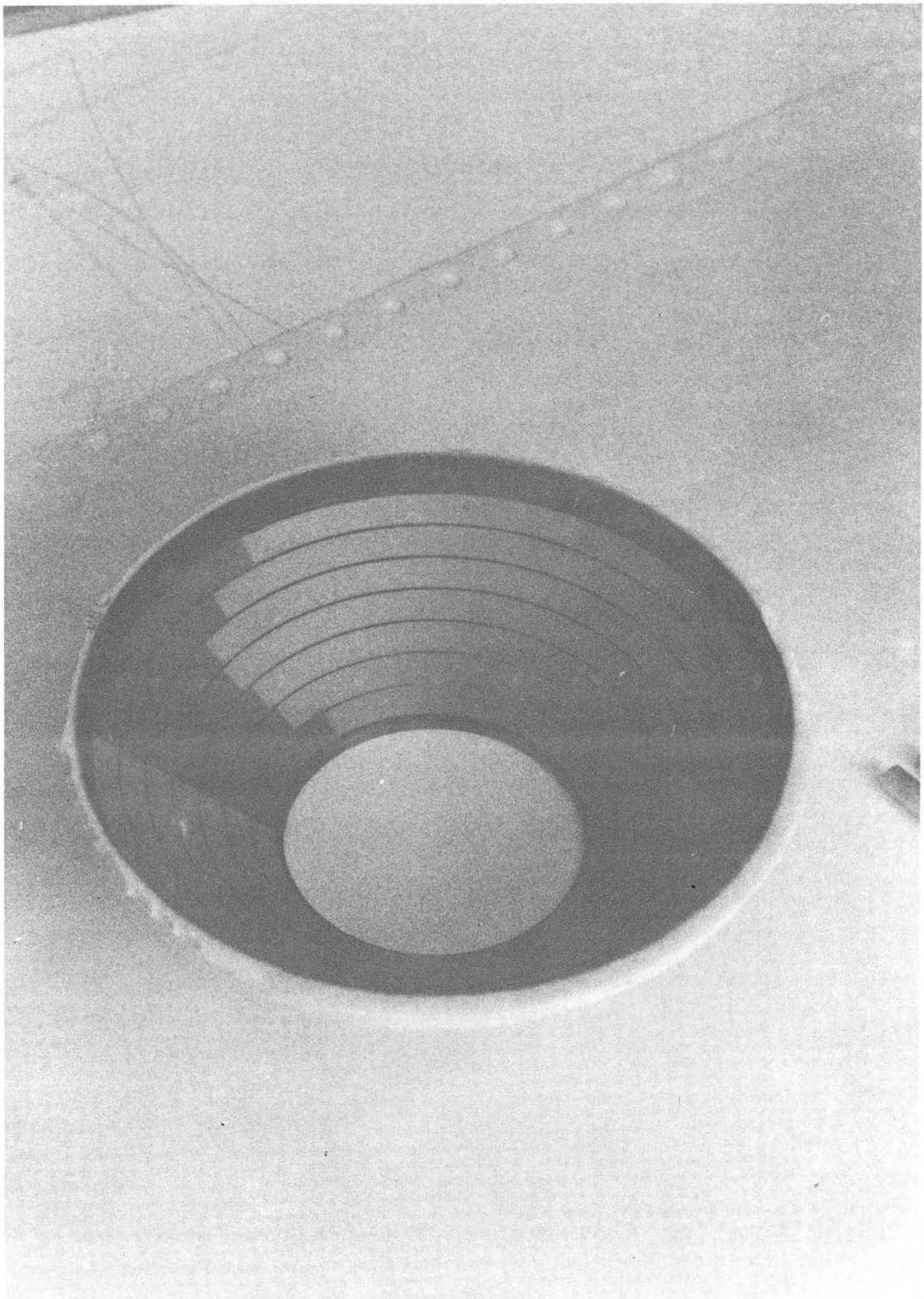

Fig. A.52 XBC 857-5538

This report was done with support from the Department of Energy. Any conclusions or opinions expressed in this report represent solely those of the author(s) and not necessarily those of The Regents of the University of California, the Lawrence Berkeley Laboratory or the Department of Energy.

Reference to a company or product name does not imply approval or recommendation of the product by the University of California or the U.S. Department of Energy to the exclusion of others that may be suitable.

LAWRENCE BERKELEY LABORATORY
TECHNICAL INFORMATION DEPARTMENT
UNIVERSITY OF CALIFORNIA
BERKELEY, CALIFORNIA 94720